VORTEX DYNAMICS IN MAGNETIC AND SUPERCONDUCTING NANOSTRUCTURES

FACULTAD DE
CIENCIAS
UNIVERSIDAD AUTÓNOMA DE MADRID

A Thesis by

Ahmad Awad Awad

Departamento de Física de la Materia Condensada
Universidad Autónoma de Madrid

Submitted in partial fulfillment of the requirements for the degree of
Doctor of Physics Science

Thesis director: ***Farkhad Aliev Kazanski***

September 2012

To my family, for your love, compassion and giving; every single word written here is dedicated to you. Love you so much.

Awad & Mariem (My Parents)
Wisam, Bargita and Randa (Sisters) and Raed (Big brother)
Nemer and the little beloved ones Yara and Leen

ACKNOWLEDGMENTS

Empezaré estas líneas por la persona a quien más quiero expresar mi profundo agradecimiento ***Farkhad G. Aliev***, en primer lugar por ser mi director de tesis que me ofreció la oportunidad de aprender y formarme, y he recibido de él tanto apoyo científico como profesional. Gracias a su dedicación diaria, exigencia y confianza en mí, me ha dado la posibilidad de enfrentarme a los retos y problemas experimentales. Además, quiero agradecerle especialmente su acogida personal y el apoyo humano que me ha dado en todos estos años en España, que me ha tratado como un padre. Muchas gracias Farkhad.

Querria agradecer a todos los miembros del grupo ***MAGNETRANS***. Gracias a ***Rául Villar*** no solo por haberse leído cuidadosamente la tesis, sino también por su buen carácter, siendo tan humilde y preocupandose por nosotros. A ***Arkadi Levanyuk,*** que con sus críticas constructivas y sus preguntas, que nunca eran ¨tontas¨ como él decía, aprendí mucho. Ha sido un placer discutir física siempre contigo. Al señor ***Volodya Pryadun*** por su paciencia, energía y dedicación. De él he aprendido más que hacer cables RF, debido a su infinita humildez, gracias señor amigo por enseñarme también un poco de Ruso y Kalinka. A ***David Herranz*** no solo por corregirme el español ¨simple¨, ni por los piropos y ¨High-level Spanish¨ (la verdad no sé si esto me ha ayudado). Por estar siempre ahí apoyandome dentro del laboratorio y fuera, en los múltiples viajes que hemos compartido. Gracias amigo campeón. A ***Ruben Guerreo*** que me ayudó cada vez que le necesitaba en España y Francia, discutir contigo siempre es un placer. A ***Juan Sierra*** con quien empecé mis primeras medidas a alta frecuencia. Me enseñó todo lo que sabía, me ayudaba siempre tanto en lo profesional como en lo humano. Gracias Juan, te debo mucho. A ***Dennis Dieleman***: me has enseñado más de lo que te enseñé. Colaborando contigo he aprendido muchísimo. Gracias a tus simulaciones tengo muchos colores en la tesis. De el, tengo muy buenos recuerdos. A ***Antonio Lara*** gracias por soportarme hasta el momento y gracias también por todo el trabajo que hiciste en las simulaciones. También ha sido un placer compartir contigo el trabajo y la esquina del laboratorio, gracias por tu apoyo. A ***JuanPe Cascales*** ha sido placer conocerté gracias por tu ayuda y por corregirme el ingles siempre. Ha sido un placer trabajar contigo y escuchar tu arte también.

A todos los miembros del departamento de Física de la Matería Condensada. Especialmente a ***Elsa Fuentes*** por su dedicación y paciencia, por los técnicos especialmente ***Andres Buendía*** que no solo me ayudaba a hacer piezas, también por su simpatía y buen humor, A ***Santiago*** que siempre me hacia las piezas más rápido y mejor de lo que prometía, a ***Jose Luis Romera*** no solo por ayudarme sino tambien por su infinita humildad y su apoyo. Y a la guapa técnica ***Rosa Díez*** por su trabajo y amistad. Y a ***Macarena***, y a los trabajadores del Seginvex.

A mi peludo amigo ***Bisher Kabtoul***; no sé qué decirle, he pasado con él la mayor parte del tiempo en los últimos 7 años, especialmente en mis bajones o borracheras. Hermano del alma te quiero mucho, y te agradezco por ser como eres, estos años han sido de los mejores de mi vida en buena parte porque estuviste a mi lado. Seguro que volveremos a recorrer todo Damasco caminando con más sueños aún.

A ***Amjad Al-Taleb***, por compartir los buenos y malos momentos. Por tu sinceridad y tu apoyo, gracias ¨Angel bárbodo¨. A los de Bajas Temperaturas que compartimos más que trabajar en frio, A los cachondos que siempre están ahí para ayudar: ***Jose Augusto y Roberto***, muchas gracias. Y también ***a Michelle***, ***Manuel, Mohamad, Ana, Prasana, Charalmbos,*** y ***Siya***. Y especialmente a ***Merzak*** que siempre me ha apoyado, gracias amigo por animarme tanto. A ***Tomás***,Por tu humildad y la amistad que siempre has hecho que la comida entre mejor acompañándola con tus chistes. Gracias por todos estos años y lo que vendrán más. A los que ya se han marchado pero han dejado sus huellas ***Eduardo*** (gracias por tu actitud de apoyo y ayuda, y la *bici*), ***Guillermo*** y ***Andrés***.

A mis primeros amigos en España que casi me adoptaron, por los buenos recuerdos cariñosos y alegres que me habies dado, A los maravillosos ***Claudio Polini, Cristina Rodriguez, Carole Brochec, Victoria Khraiche , Sami Benchamekh, Sandra Serbey***, os quiero un monton.

Thanks to all the people in the Nanospintronics group at the IEF, Orsay, France, for their hospitality during my stay there. I would specially like to thank ***T. Devolder*** for receiving me, for his warm hospitality, for offering me all the labs, including me in the group meetings and for offering to me and help me in the experiments. Also I thank ***J-V. Kim*** for his kindness and for trying to clear my doubts concerning multilayer systems. To ***R. Otxoa*** for discussing physics and helping me whenever I needed. I'm happy to have gained such a nice friend; the same to ***S. Petit***. Thanks to ***Y. Lakys*** for his kindness and support. Also I want to thank the people at the University of Poincaré de Nancy for their hosbitality and dedication, especially ***C. Tiusan*** and ***S. Andrieu*** and ***F. Bonell*** for teaching me the epitaxial growth of multilayers.

I want to give special thanks to all the people that I have scientifically collaborated with during the years of my Ph.D. I will just list the people with whom I have had discussions for the published works. In magnetism ***K Y. Guslienko, G.N.Kakazei, B. A. Ivanov, V. Metlushko, M. Garcia Hernández, A Asenjo, S-K. Kim;*** and in superconductivity ***V. V. Moshchalkov, A. Silhanek and Y. M. Galperin***.

To the dedicated teachers of the Damascus University, specially ***Yousef Abou-Ali*** and ***Naaman Sabaag***. They always kept motivating me and I greatly appreciate their confidence in me and friendship. Thanks for your work and dedication. To my friends who always supported me ***A. Samra***, ***H. Samoul, M. Taqui-Eldin, R. Kallol, F. Ganaam and Bisan***. And to those who become my family here ***Amer, Maysa, Eden and Salam*** and my beloved friends ***Mai, A.Abo-Zubida, , H. Khuzam, Amira, Rami Abbas,Liala Mhmad, Laila Tellawi, Naomí Ramírez (¨NaRa¨ gran luchadora), Laura GaliánY Sofia San Millán (grandes de la UAM), Layla y Ussama Jandali, Salvatori, Elena, Sufyan Barhoum y Mohamad Al-Masry (Gran Moe)***; And to ***Malek, May M*** and ***Suhib*** as well.

To the University Autunoma de Madrid, for the financial support and the FPU-UAM grant.

BIBLIOGRAPHY

1) List of publications (related to thesis):

1. F. G. Aliev, J. F. Sierra, **A. A. Awad,** G. N. Kakazei, D. Han, S. Kim, V. Metlushko, B. Ilic and K. Y. Guslienko
“*Spin waves in circular soft magnetic dots at the crossover between vortex and single domain state*”
Physical Review **B79**, 174433 (2009).

2. **A. A. Awad,** K.Y. Guslienko, J. F. Sierra, G. Kakazei, V. Metlushko, and F. G. Aliev
“Precise probing spin wave mode frequencies in arrays of the vortex state circular magnetic dots”
Applied Physics Letters **96**, 012503 (2010).

3. **A. A. Awad**, G. R. Aranda, D. Dieleman, K. Y. Guslienko, G.N. Kakazei, B A Ivanov and F. G. Aliev
“Spin excitation frequencies in magnetostatically coupled arrays of vortex state circular Permalloy dots”
Applied Physics Letters **97**, 132501 (2010).

4. F. G. Aliev, D. Dieleman, **A. A. Awad**, A.A. Asenjo, O. Iglesias-Freire, M. García Hernández, V.M. Metlushko and K. Y. Guslienko
¨Probing ground state in circular magnetic dots: Single vs. double magnetic vortex¨
Proceedings of International Conference on Electromagnetics in Advanced Applications (ICEAA), IEEE- Explore, p.160-163 (2010).
ISBN: 978-1-4244-7366-3, DOI 10.1109/ICEAA.2010.5652137

5. F. G. Aliev, **A. A. Awad**, D. Dieleman, A. Lara, V. Metlushko and K. Y. Guslienko,
“Localized domain-wall excitations in patterned magnetic dots probed by broadband ferromagnetic resonance”
Physical Review **B84**, 144406 (2011).

6. **A. A. Awad,** F. G. Aliev, G. W. Ataklti, A. Silhanek, V. V. Moshchalkov, Y. M. Galperin, and V. Vinokur
“Flux avalanches triggered by microwave depinning of superconducting vortices”
Physical Review **B84,** 224511 (2011).

7. **A. A. Awad**, A. Lara, V. Metlushko, K. Y. Guslienko, and F. G. Aliev
“Broadband probing magnetization dynamics of the coupled vortex state Permalloy layers in nanopillars”
Applied Physics Letters **100**, 262406 (2012).

2) Patent application

8. Solicitud (application number) P201131985
Date: 09.12.2011

Reference (UAM) P00004101/2011 (Spain)
Authors: F. G. Aliev and **A. A. Awad**
Title: ¨Método preciso de desencadenamiento de avalanchas en dispositivos superconductores¨

3) Submitted paper

9. **A. A. Awad**, A. Lara, M. García Hernández, V. Metlushko and K. Y. Guslienko. F. G. Aliev ¨Vortex-vortex spin wave modes and winter magnons in vertically coupled Permalloy dots¨
Submitted to Journal of Superconductivity and Novel Magnetism (proccedings of ICSM 2012 conference).

4) Other publications

10. J.F.Sierra, **A.A.Awad**, G.N.Kakazei, F.J.Palomares and F.G.Aliev
" Broadband magnetic response of periodic arrays of FeNi dots"
IEEE Transactions on Magnetics **44,** 3063, (2008).

11. F. G. Aliev, A. P. Levanyuk, R. Villar, J. F. Sierra, V. V. Pryadun, **A.A. Awad**, V. V. Moshchalkov *"Unusual DC electric fields induced by a high frequency alternating current in superconducting Nb films under a perpendicular magnetic field"*
New Journal of Physics **11**, 063033 (2009).

RESUMEN

El descubrimiento de la magnetorresistencia gigante (GMR), reconocida con el Premio Nobel de Física en 2007, ha revolucionado la tecnología de almacenamiento de información, particularmente los dispositivos magnéticos de alta densidad y alta velocidad de almacenamiento.

La investigación de la dinámica de vórtices magnéticos ha ido adquiriendo una creciente importancia debido a su potencial de aplicación. La tecnología de la información exige la disminución progresiva del tamaño de los dispositivos y la necesidad de mejora de la velocidad de estos dispositivos.

Nuevas propiedades magnéticas y configuraciones no comunes aparecen debido al confinamiento lateral y vertical a escala nanométrica. El vórtice magnético es una de las anomalías topológicas más pequeñas recientemente descubiertas, y está siendo investigado activamente. Esta característica topológica existe en conduciones estáticas o bien puede surgir dinámicamente, por ejemplo, en el movimiento de una pared de dominio ultrarrápido, o en la inversión debida a torque de espín en estructuras magnéticas de forma circular o en forma de línea. El vórtice magnético por sí mismo y la dinámica de su comportamiento son ¨*sistemas-modelo*¨ importantes en el magnetismo fundamental.

El vórtice superconductor es otra de las anomalías topológicas magnéticas que existen. Aparece en el estado mixto de películas superconductoras presentándose en forma de flujo cuantizado al aplicar un campo magnético externo. El estudio de la dinámica de vórtices superconductores es relevante para entender el comportamiento de los superconductores a altas frecuencias. Además, también es de gran importancia para la comprensión del comportamiento de los dispositivos superconductores en presencia de un campo magnético externo. La implantación de los superconductores en una amplia variedad de dispositivos electrónicos de alta y baja frecuencia sigue siendo un gran reto tecnológico. Recientemente, la interacción entre vórtice magnético y vórtice superconductor ha recibido especial atención, debido principalmente a la posibilidad de mejorar el fijamento de vórtices superconductores por vórtices magnéticos. La dinámica conjunta de ambos vórtices (magnéticos y superconductores) con frecuencias en el rango de las microondas, sigue siendo desconocida. En este sentido, una de las motivaciones en esta tesis para estudiar por separado cada uno de estos sistemas de vórtices es obtener un sólido conocimiento inicial sobre

la dinámica de los correspondientes sistemas de vórtices, con el fin de ser utilizada como referencia antes de la investigación ulterior de su respuesta dinámica mutua.

La tesis se divide en tres bloques principales. El primer bloque incluye el ***capítulo I*** y el ***capítulo II*** donde se repasa brevemente el estado actual del tema y se describen tanto los métodos y montajes experimentales utilizados así como la métodología utilizada por otros. La segunda y la tercera parte describen la dinámica de vórtices magnéticos y superconductores correspondientemente.

En el ***Capítulo III*** se investigan las excitaciones del estado fundamental del vórtice en función de la geometría de los puntos circulares en el rango de relación de aspecto moderada. Los resultados están en buen acuerdo con la teoría, en la cual se tiene en cuenta la interacción dinámica entre las ondas de espín y el núcleo del vórtice. Por otra parte, se investigaron las excitaciones del vórtice cuando el vórtice está desplazado, por el campo magnético externo, aplicado en el plano de los puntos circulares de permalloy. Se encontró que los modos azimutales de ondas de espín "sobreviven" aproximadamente hasta el campo de nucleación del vórtice. Además, se observó nuevo tipo de excitación, fuertemente localizada cerca del núcleo del vórtice desplazado y se investigó para campos de excitación paralelos al campo externo aplicado.
El ***Capítulo IV*** presenta el estudio de las ondas de spin en el estado meta-estable de doble vórtice en los puntos circulares de Py, que aparecen en los puntos durante la inversión de la magnetización antes de alcanzar el estado de un vórtice. La dinámica de magnetización ha sido estudiada en función del campo magnético, tanto en el estado de vórtice individual, así como en el estado de doble vórtice compuesto de dos vórtices acoplados, conectados indirectamente a través de las paredes de dominio conectando los núcleos del vórtice con los medios antivortices en el borde. Se encontró que los modos excitados de onda de espín son oscilaciones de flexión de las paredes de dominio del tipo "magnones de Winter" que son análogas a las ondas de desplazamiento de las cuerdas.

El ***Capítulo V*** explora el efecto de acoplamiento entre puntos circulares idénticos de Permalloy (Py) en los espectros de excitación, con acoplamiento lateral o vertical. Se estudiaron puntos con diferentes separaciones laterales. Ademas se han investigado nano-pilares con dos espaciadores que corresponden a intercambio de canje y acoplo dipolar entre las capas. El estudio muestra que la influencia del acoplamiento en el estado vórtice para las matrices de puntos magnéticos 2D es bastante diferente de lo que se encontró antes para puntos de mono dominio magnético o puntos en el estado saturado. La influencia de la interacción dinámica magnetostática, en los puntos circulares en el estado vórtice, en las ondas de espín ha sido estudiada y descrita en términos de componentes tanto dipolares como cuadrupolar del acoplo, las ondas en las capas nanopilares con dos tipos de acoplamiento (acoplamiento dipolar y de intercambio de ancalje) también son investigados. La influencia del campo externo, aplicado en el plano, en los modos propios y la transformación de estos modos en otros nuevos, una vez el vórtice esta desplazado, ha sido estudiada en detalle. Los resultados experimentales obtenidos en este bloque han sido apoyados por simulaciones micro-magnéticas dinámicas (hechas en el grupo MAGNETRANS o en colaboración con el profesor Kim de Universidad de Seúl - Corea del Sur). Además, los modelos de análisis fueron realizados por el prof. K. Guslienko (Universidad de País Vasco España) y prof. B. A. Ivanov (IM-Kiev, Ukraine) con el fin de apoyar y confirmar los resultados experimentales.

En el **Capítulo VI** se presenta la dinámica de vórtices superconductores en el rango de microondas. Uno de los parámetros más importantes que afectan a la dinámica del vórtice, la frecuencia de desenganchamiento ¨depinning¨ del vórtice, ha sido obtenida de la permeabilidad de microondas en función de la frecuencia y la potencia de microondas *rf* aplicada. Nuestro método permite la detección directa de múltiples frecuencias de desenganchamiento ¨depinning¨ a través de la detección de avalanchas de vórtices desencadenadas por rf- de banda ancha.

La parte final queda reservada a la síntesis de los trabajos abordados y las conclusiones más relevantes.

Este proyecto de tesis ha sido co-financiado en parte por proyectos de investigación de Gobierno de España y por la Universidad Autónoma de Madrid a través de una beca propia FPU-UAM (2008-2012).

ABSTRACT

Discovery of the giant magnetoresistance effect (GMR), recognized by awarding the Nobel Prize in physics 2007, has revolutionised the information storage technology, particularly magnetic high density and high speed storage.

The investigation of magnetic vortex dynamics has gained increasing importance due to its potential applications. Information technology demands progressive shrinking of the devices size and the need to improve the velocity of such devices. New unusual magnetic properties and configurations emerge due to the lateral and vertical confinement at nanoscale. The magnetic vortex is one of the smallest topological anomalies recently discovered which is being actively investigated. This topological feature exists in static's or may emerge dynamically, for example, in ultrafast domain wall motion, or spin torque switching in magnetic circular or line structures. This magnetic vortex by itself and its dynamics behaviour are also an important toy models in fundamental magnetism.

Superconducting vortex is another topological magnetic anomaly which exists in the form of flux quanta emerged in the mixed state of superconducting films under the application of external magnetic field. The knowledge of superconducting vortex dynamics is relevant for understanding of the behaviour of the superconductors at high frequencies. In addition, it is also of great importance for understanding of the behaviour of superconducting devices in the external magnetic field. Implantation of superconductors in a wide variety of high and low frequency electronic devices remain one of the challenges.

The interactions between magnetic vortex and superconducting vortex have recently received special attention, mainly due to the possibility of enhanced pinning effect of the superconducting vortex by the magnetic one. The mutual dynamics of coupled magnetic and superconducting vortices at microwave frequencies still remains unknown. In this respect, one of the motivations to study separately each of these different vortex systems in this thesis is to gain initial solid

knowledge on the dynamics of corresponding reference vortex systems before further investigation of their mutual dynamic response.

The thesis can be divided in three main blocks. The first block includes ***Chapter I*** and ***Chapter II*** were we briefly review current status and describe the experimental methods used along with experimental setups and methods used by others.
The second and the third blocks describe the dynamics of magnetic and superconducting vortices; respectivlly.

Chapter III investigates ground state excitations of the magnetic vortex as a function of the circular dots geometry in a moderate aspect ratio range. The results are in a good correspondence with theory which takes into account dynamical interaction between spin waves and vortex core Moreover, excitation in the linear regime when the vortex state is displaced by external in plane magnetic field in the circular Permalloy dots have been investigated. It was found that azimuthal spin wave modes “survive” approximately until vortex nucleation field. Besides, new kind of strongly localised near shifted vortex core excitations was observed and investigated with drive field parallel to the external bias field.

Chapter IV presents the investigation of spin waves in the metastable double vortex state in the circular Py dots. The double vortex state was found to emerge in the dots during the magnetization reversal proccess before reaching the single vortex state. The magnetization dynamics has been studied as a function of the magnetic field both in the single vortex state as well as in the double vortex state. The later composed of two coupled vortices connected via domain walls through edge half-antivortices. The excited spin wave modes are found to be flexural domain wall (DW) oscillations of “Winter´s magnon” type which are analogous to the displacement waves of strings.

Chapter V explores the effect of interdot coupling on the excitation spectra for either lateral or vertical coupling between identical circular Permalloy (Py) dots. Different lateral separation for the laterally coupled dots and two different spacer thicknesses corresponding to dipolar and interlayer exchange coupling for layered pillars where explored.
The study shows that influence of coupling in the vortex state for the 2D magnetic dot arrays is quite different from one found before for the saturated or single domain dots. Influence of the dynamical magnetostatic

interaction, in the circular dots in the vortex state on spin waves has been studied and described in terms of both dipolar and quadrupolar components,
Spin waves in the layered nanopillars with two types of coupling (dipolar coupled and exchange) have also been investigated. The influence of the in-plane bias field on the eigenmodes and transformation of those modes into to the new once in shifted vortex state has been studied in details.
The experimental results obtained in this block have been supported by dynamic micromagnetic simulations (done in the MAGNETRANS group and in collaboration with prof. Kim group from Seoul University, South Korea). In addition, analytical models were done by prof. K. Guslienko (Universidad de Pais Vasco, Spain) and prof. B. A. Ivanov (IM-Kiev, Ukraine) in order to support and confirm experimental findings.

In chapter VI the microwave dynamics of the superconducting vortices is presented. One of the most important parameter affecting the vortex dynamics - the vortex depinning frequency- has been obtained from the microwave permeability as a function of rf frequency and power. Our method allows direct detection of multiple vortex depinning frequencies via broadband detection of rf-triggered avalanches.

The final part of the thesis summarised the work

The thesis project has been partially supported by research funds from Spanish government and by the Universidad Autónoma de Madrid through scholarship FPU-UAM (2008-2012).

TABLE OF CONTENTS

Chapter Page

CHAPTER I: THEORETICAL BACKGROUND

1.1 Introduction

The challenge of making devices smaller and faster pushes the investigation in magnetism of nanomaterials to understand the magnetization dynamics on a progressively smaller time and length-scales. These challenges also lead to great advances in nanolithography which have provided a variety of novel nanostructured magnets. In those nanostructures unusual magnetic properties and configurations have emerged due to the lateral confinement. Interesting and unexpected structure arising at submicron scale is magnetic vortex, which appears in circular, elliptic, triangular nano dots, or during domain wall motion or as a result of the spin current switching in magnetic nanostructures and in spin torque oscillators. In the all the above cases the investigation of vortex high frequency properties is crucial due to the need to control the precessional and relaxation processes and characteristics times for application and fundamental research.

As to the superconducting devices, they also have got a wide spectrum of applications due to their unique properties including an extremely low dissipation and energy handling as well as their behaviour in the external magnetic field. Relevant applications range from transformers, power storage devices, electric power transmission, electric motors, magnetic levitation devices and Superconducting Quantum Interference Devices (SQUIDs) capable of measure extremely small magnetic fields or voltages. Moreover, superconductors are widely implemented in high frequency devices such as those used in particles accelerators and high frequency filters and telecommunications.

External magnetic field penetrates into thin superconducting films in form of flux quanta, also called vortices. Understanding and controlling the superconducting vortex motion, pinning and depinning is one of the most important challenges both for fundamental and applied physics.

In this chapter we will introduce briefly the magnetization dynamic as well as the vortex dynamics; trying to describe the state of the art of the magnetic and superconducting vortex.

1.2 Magnetization dynamics

The dynamics of a macroscopic magnetic moment, induced by an effective field H_{eff} is described by the Landau-Lifshitz (LL1) equation [1]:

$$\frac{dM}{dt} = -\gamma\mu_0\left[M \times H_{eff}\right] \tag{1.1}$$

where γ is the gyromagnetic ratio $\gamma = g|e|/(2m_e)$ g is the Lande-factor or g-factor, e the electron charge and m_e the electron mass.

The equation (1.1) presents an undamped precession with a constant angle around the H_{eff} which does not describe the experiments in real magnetic materials. Landau and Lifshitz [1] added a phenomenological dissipation to avoid the above inconsistency, transforming the dynamic equation (LL2) in the following form:

$$\frac{dM}{dt} = -\gamma\mu_0\left[M \times H_{eff}\right] - \frac{\lambda}{M_s^2} M \times \left[M \times H_{eff}\right] \tag{1.2}$$

Here the phenomenological damping constant $\lambda > 0$ has the dimension of frequency. Afterwards Gilbert added to the equation of dynamics a dimensionless damping parameter converting the LL equation to the Landau-Lifshitz-Gilbert [2] (LLG) equation:

$$\frac{dM}{dt} = -\gamma\mu_0\left[M \times H_{eff}\right] + \frac{\alpha}{M_S}\left[M \times \frac{dM}{dt}\right] \tag{1.3}$$

where α is the dimensionless Gilbert damping parameter. The LLG can be written into a form similar to the LL2 equation:

$$\frac{dM}{dt} = -\frac{\gamma\mu_0}{(1+\alpha^2)}\left[M \times H_{eff}\right] - \frac{\gamma\mu_0\alpha}{M_S(1+\alpha^2)} M \times \left[M \times \frac{dM}{dt}\right] \tag{1.4}$$

From both LLG equations:

$$\gamma_{LL} = \frac{\gamma_{Gilb}}{(1+\alpha^2)} \tag{1.5}$$

The Eq (1.3) can be interpreted as follows: the first corresponds to the precession of the magnetization around the effective field, and determines the spin precession frequency (Larmor frequency). The second term in the Eq(1.3) presents the energy dissipation due to damping mechanisms which will be discussed later. The effect of damping can be seen as illustrated in Figure 1.1b.

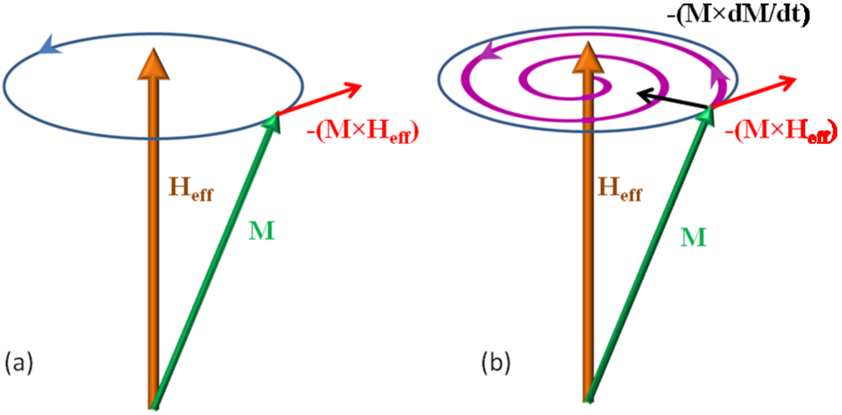

Figure 1.1 (a) The magnetization M precesses counter-clockwise around the effective field $\mathbf{H}_{\mathrm{eff}}$ following the Landau-Lifshitz equation (b) Magnetization precession after adding the phenomenological damping term.

The magnetization spirals down until it becomes aligned with the field. The damping parameter determines the rate at which the magnetization relaxes towards the effective field H_{eff}. This dimensionless factor typically has values much smaller than 1 and situated in the range between 0.01 and 0.1. The damping term also causes the precession frequency to decrease slightly, as it lowers the effective gyromagnetic ratio to the value presented in Eq(1.5). The damping term will be discussed further in details.

1.2.1 Ferromagnetic resonance in thin films

Ferromagnetic resonance (FMR) is the main phenomena in the magnetization dynamics that included both the precessional and the relaxation behavior of the ferromagnetic material, which depends on the material parameters as well as on the sample shape and to some limit on the sample size.

The first observation of FMR in magnetic films was reported by Griffiths in 1946 [3]. In 1948 Kittel developed the theory of the FMR [4]. Kittel also pointed out the importance of the demagnetizing field to define the resonant condition. Due to the demagnetizing field, the internal magnetic field inside the sample may be different from the applied external magnetic field. The demagnetizing factor of the sample is $N = (N_x;N_y;N_z)$, so the field components could be written in the form:

$$H_x^i = H_x - N_x M_x;\ H_y^i = H_y - N_y M_y;\ H_z^i = H_z - N_z M_z$$

Here H^i denotes the internal magnetic field; H is the applied magnetic field.

In order to obtain the resonance frequency it is supposed that the applied magnetic field is directed along the z axis; see Figure 1.2. To the first order approximation one imposes condition (dM/dt=0) and M_z=M. Solving the LLG equation one obtains [5]:

$$\begin{aligned} \frac{dM_x}{dt} &= -\gamma\mu_0\left[M_y H_z^i - M_z H_y^i\right] = \gamma\mu_0 M_y\left[H + (N_y - N_z)M\right] \\ \frac{dM_y}{dt} &= -\gamma\mu_0\left[M_z H_x^i - M_x H_z^i\right] = -\gamma\mu_0 M_x\left[H + (N_x - N_y)M\right] \end{aligned} \tag{1.6}$$

In order to solve the above system of coupled equations one can suppose that the solution is time dependent and is proportional to ($e^{-i\omega t}$) with $\omega=2\pi f$. The resonance condition is:

$$\begin{vmatrix} i\omega & \gamma\mu_0\left[H+(N_y-N_z)M\right] \\ -\gamma\mu_0\left[H+(N_x-N_y)M\right] & i\omega \end{vmatrix} = 0$$

One can obtain the ferromagnetic resonance frequency in the applied field H:

$$f_0 = \frac{\gamma\mu_0}{2\pi}\sqrt{(H+(N_y-N_z)M)\cdot(H+(N_x-N_y)M)} \tag{1.7}$$

In the special case shown in Figure 1.2, where the applied magnetic field H is in the xz-plane of a thin film with $\{N_x=N_z=0;\ N_y=1\}$, the resonance frequency of the uniform mode will be:

$$f_0 = \frac{\gamma\mu_0}{2\pi}\sqrt{H(H+M)} \tag{1.8}$$

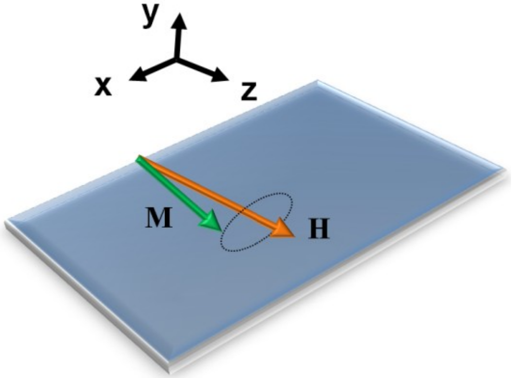

Figure 1.2 Scheme of the FMR

Usually a uniaxial anisotropy field H_k is created during the sample growth, or due to crystalline or surface or shape anisotropy. By taking into account the anisotropy, as an example the resonance frequency in the thin films with uniaxial anisotropy is given by the expression:

$$f_0 = \frac{\gamma\mu_0}{2\pi}\sqrt{(H+H_k)(H+H_k+M_S)} \tag{1.9}$$

The field swept line width is described by the following equation [6]:

$$\Delta H = \Delta H_0 + 4\pi \frac{\alpha}{\gamma_S} f \tag{1.10}$$

While the line width in frequency coordinates is [6]:

$$\Delta f = (\gamma \Delta H_0 + 4\pi \alpha f)\sqrt{1 + \left(\frac{\gamma \mu_0 M_S}{4\pi f}\right)^2} \tag{1.11}$$

In the high frequency limit this equation may take a simple form: $\Delta f = \alpha \gamma \mu_0 M_S$ and the resonance field can be presented as [7]:

$$H_r = \sqrt{\left(H_0^2 + 4\pi M_s^2\right)} - 2\pi M_s \tag{1.12}$$

For the special case of magnetic dots with cylindrical shape introducing the demagnetizing factors gives [7]:

$$H_r = \sqrt{H_0^2 + \frac{M_s^2\left(N_z(r) - N_y(r)\right)}{4}} - \frac{M_s\left(N_z(r) + N_y(r) - 2N_x(r)\right)}{2} \tag{1.13}$$

1.2.2 Magnetic damping

The typical time of the magnetization relaxation is one of the most important parameters of interest for FM systems. Experimentally measuring the resonance linewidth is one of the main methods used to investigate this phenomenon. In a FMR experiment, the linewidth of the resonance ΔH, consists of intrinsic and extrinsic contributions. The intrinsic contribution is always present in a particular material and cannot be suppressed. It is present even in a perfect crystal and originates from interactions of free electrons with phonons and magnons. The extrinsic contributions can vary from one sample to another, depending on preparation and structure. They arise from the microstructure imperfections or from finite geometry or interfaces. They could, in principle, be suppressed.

1.2.3 Exchange coupling between magnetic layers

Since its observation in 1986 [8], [9],and [10] interlayer exchange coupling has been the subject of many studies [11]. We will limit the discussion to the case of interlayer exchange coupling e.g. a typical trilayer system is composed of two ferromagnetic layers interacting through an intervening nonmagnetic interlayer. Initially, the experimental data were fitted with a bilinear coupling; in this case the magnetizations in the ferromagnetic films trend to be either parallel to each other (ferromagnetic coupling) or antiparallel (antiferromagnetic coupling). Ruderman, Kittel, Kasuya, Yoshida interaction (RKKY) (which describes a coupling mechanism of nuclear magnetic moments essentially proposed to explain some unusual broad in the nuclear spin resonance), had been used to explain this kind of coupling. This phenomenological model has been adapted to explain the exchange coupling with ferromagnetic/antiferromagnetic coupling oscillation. In this case the bilinear coupling it is due to indirect exchange through conduction electrons of the intermediate layer. It is now well established that in addition to this bilinear coupling, there is a biquadratic coupling [12], where the magnetization have perpendicular configuration between each other.

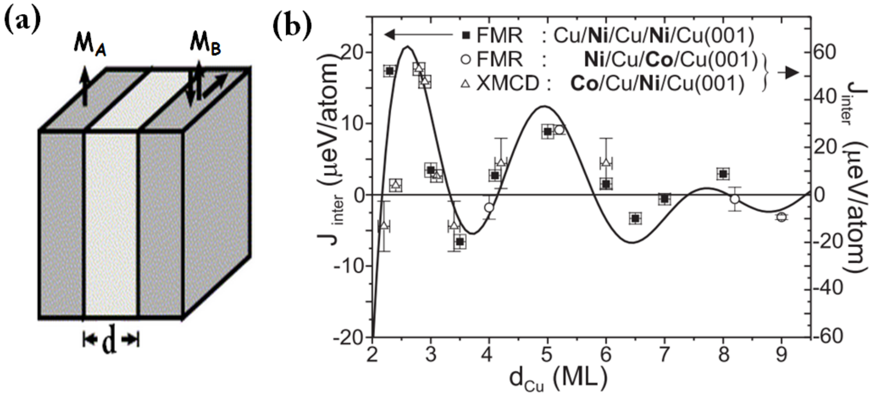

Figure 1.3 (a) Scheme of coupled ferromagnetic trilayer. (b) the exchange coupling oscillation (adapted from Lindner et al.,[13]**)**

The exchange energy can be written:

$$E_{ex} = -J_1 \frac{M_A \cdot M_B}{M_A M_B} - J_2 (\frac{M_A \cdot M_B}{M_A M_B})^2 = -J_1 \cos\varphi - J_2 \cos^2 \varphi$$

where φ is the angle between the magnetizations of the two ferromagnetic (FM) layers. Here M_A and M_B are the magnetizations of the layers A and B; while J_1 and J_2 are, respectively, the bilinear and biquadratic coupling parameters. The first term in the equation is called the bilinear coupling and the second the biquadratic coupling. Coefficients J_1 and J_2 describe the type and the strength of the coupling. When the bilinear term dominates, the energy minimum corresponds to FM coupling for $J_1>0$ and antiferromagnetic (AF) coupling for $J_1<0$. On the other hand, when biquadratic coupling is the main term and is negative, one gets a 90° coupling. As it has been mentioned above, the microscopic mechanism which explains the bilinear exchange coupling J_1 has the same physical origin as the RKKY interaction. As to the biquadratic coupling, J_2 could in principle be also could be describe in the RKKY framework.

The resonance frequency of the coupled system can be presented [14] in a simple case as for symmetrical layers (A=B), and bilinear exchange coupling (J_1=J):

$$\omega^4 - \omega^2 \begin{bmatrix} 2\gamma_A^2 H_1^A H_2^A + J\left(\dfrac{2\gamma_A^2 H_2^A + 2\gamma_A^2 H_1^A}{t_A M_A}\right) \\ + J^2\left(\dfrac{4\gamma_A^2}{(t_A M_A)^2}\right) \end{bmatrix}$$

$$+\gamma_A^4 \left[(H_2^A)^2 + J\left(\frac{2H_2^A}{t_A M_A}\right)\right] \times \left[(H_1^A)^2 + J\left(\frac{2H_1^A}{t_A M_A}\right)\right] = 0$$

And:

$$H_1^A = H\cos\alpha + 4\pi M_A + 2K_A / M_A$$

$$H_2^A = H\cos\alpha + 2K_A / M_A$$

where, α is the angle of the applied field in respect to x-axis, t_A is the ferromagnetic material thickness, K is the magnetic anisotropy constant.

1.3 Magnetic vortex

1.3.1 Magnetic nanodots

Reducing the dimensions of thin films to nano-scale permits to tune their physical properties. This leads to a variety of phenomena that had opened and still opens new horizons in science for both fundamental investigation and application. At nanoscale dimensions we get a wealth emerging magnetic properties and structures which are of great scientific and technological interests.

Indeed recent developments in nanotechnology and electron beam lithography techniques with the ability to create magnetic dots of well defined forms, have strongly enhanced interest to these systems both from fundamental points of view and due to its potential applications such as in magnetic recording media and spintronics. At nano-scale new magnetic configuration arises due to the interplay between different energies as the dipolar, the exchange and the anisotropy energy. As the magnetization changes from in-plane to out of plane and vice versa, the creation of exotic magnetic configurations may be expected.

- **Magnetization configuration in magnetic dots**

The magnetic dots in this thesis referee to submicron magnetic disks with thickness in the nanometer scale. In those magnetic discs magnetic vortex emerges as the ground state due to the competition between the dipolar and the exchange energies. From one side, reducing dipolar energy minimizes the magnetic charges forcing the magnetic moments to follow the shape of the disk borders. From the other side, the exchange energy keeps the moments to be aligned parallel to each other, except the nanometers zone proximity to the dots centre where the cost to keep the magnetic moment aligned parallel to each other is too large and magnetic moments point out of plane to avoid head to head alignment. This creates so called vortex core (Figure 1.4)

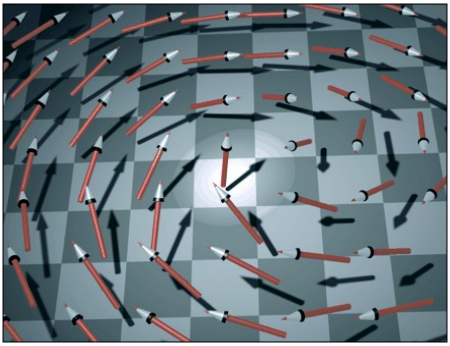

Figure 1.4, Schematic representation of the vortex core (adapted from ref[15] **).**

The vortex core has dimensions of approximately the exchange length of the material which is defined as

$$L_{ex} = \sqrt{\frac{2A}{M_S^2}} \tag{1.14}$$

where A is the exchange stiffness and M_S is the saturation magnetization.

1.3.2 Magnetic vortex

The internal magnetization configuration of the mentioned vortex structure (with small core having a perpendicular component (M_z) has been initially observed indirectly only [16]. Soon after, these magnetic nanostructures were investigated by using magnetic force microscopy. Shinjo et al [17] quantified vortex core by imaging circular dots of Permalloy with 50 nm in thickness and 0.3 to 1 µm in diameter. More recently, the image of the vortex core in nano-islands of iron using spin-polarized scanning tunnelling microscopy, capable of resolving structures down to the atomic scale [15] has been reported. Figure 1.5 shows the images of the vortex in circular dots reported in [17] and [15]. In such a system (with the core sometimes referred to as a magnetic soliton) we can characterize those vortices by two binary properties (‘‘topological charges’’): a chirality (counter-clockwise vs. clockwise directions of the in-plane rotating magnetization) and a polarity (the up or down direction of the vortex core’s magnetization). Controlling and switching between those parameters could allow using those structures as a four-level memory device.

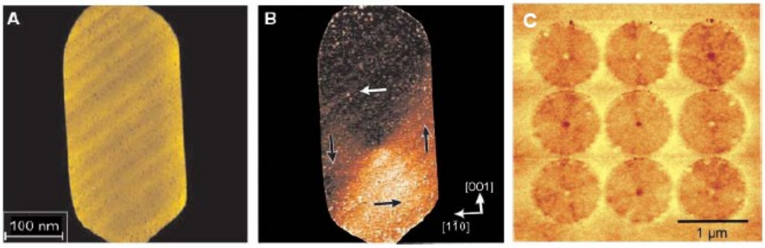

Figure 1.5 (A) Topography and (B) domain image obtained with spin-polarized scanning tunnelling microscopy of a single nanoisland of Fe. The arrows indicate the orientation of the domains. (C) Magnetic force microscopy image of an array of Permalloy dots with 1 μm of diameter and 50 nm thick. The central dot in each disk shows the evidence of the vortex formation. Figure adapted from refs. [17] **and** [15].

- ## Phase diagram

The magnetic vortex mentioned in the previous paragraph emerge in the magnetic dots in a certain range of geometry, depending on the material parameters. It is convenient to introduce magnetic phase diagram as a function of normalized dimensions (by material exchange length L_{ex}) proportions of a circular magnetic disk/cylinder in the absence of external magnetic field is shown schematically in Figure 1.6. This diagram has been calculated using the vortex state energy and the energies of single-domain (in-plane and out-of-plane) states[18].

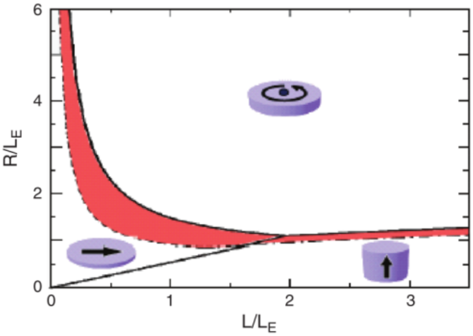

Figure 1.6 The magnetic phase diagram of the circular magnetic dot. The insets are shown in perspective, i.e. they are circles, not ellipses[19].

The calculations show that stability of the ground state depends on three parameters which define the magnetic structure of a dot: (i) the dot radius R, (ii) the dot thickness L and (iii) the exchange length of the vortex state (see refs. [19–21]). This phase diagram is universal for soft magnetic dots in the coordinates of (R, L) normalized by the exchange length see Figure 1.6.

1.3.1 Magnetic vortex in the applied magnetic field

For cylindrical dots with aspect ratio corresponds to vortex ground state (see Figure 1.6.). Upon the application of high enough field the dots saturate in a single domain configuration. The magnetization reversal occurs starting with vortex nucleation followed by displacement and then annihilation of magnetic vortex Figure 1.7.

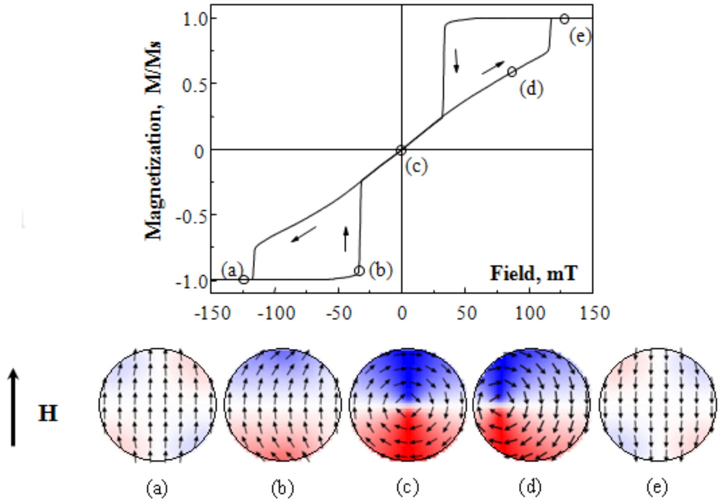

Figure 1.7 Sketch of a hysteresis loop of the single vortex state, the insets show snapshots of the magnetization configuration (adapted from Guslienko et al.,[18]).

This reversal with vortex happen as the applied field aligns the magnetization near the vortex extending the zone ¨domain¨ in which the magnetization is aligned along the applied field direction forcing the vortex to move across the dot perpendicular to applied magnetic field, till the is expelled totally out of the dot at the field value called the “vortex annihilation field” (H_{an}). The vortex returns to enter/form into the dot when the magnetic field is decreased from saturation at a field value called the "nucleation field" (H_n). The dots size dependence of vortex annihilation (H_{an}) and nucleation (H_n) fields has been studied theoretically and experimentally for 2D arrays of soft magnetic dots and treated in some references [22], [23] as an off-centered rigid vortex structure. This rigid vortex model provides analytical expressions for the size-dependent initial susceptibility and the vortex nucleation and the annihilation fields.

1.3.2 Vortex dynamics

After introducing a picture of the vortex state, we can procced introducing its dynamics at high frequencies. The understanding of the high frequency spin wave excitation modes in ferromagnetic dots in the vortex state is of special fundamental and applied interest because knowledge of these modes allows controlling the magnetic vortex switching (see for example [24]) characteristic times and fields [25] [26]. This fact has stimulated most of the fundamental studies of the vortex state devoted to understand the magnetization dynamics in such systems. Short magnetic field pulses are usually applied perpendicular or parallel to the dots plane to achieve the magnetization reversal and to excite vortex related spin wave modes (see for example [27]).

A rich variety of spin eigenmodes could be excited in the magnetic dots systems specially those related to the magnetic vortex which can be divided in low frequency modes in the range of hundreds of MHz, where the vortex core moves as a whole (the so-called translational mode [28]) and high frequency modes, in the GHz range, which correspond to radially and azimuthally symmetric oscillations of the vortex magnetization. These excitations of the dot magnetization are mainly localized outside the vortex core and named radial and azimuthal modes due to their magnetization profile symmetry.

- **Translational mode (gyrotropic mode)**

The spin eigenmode frequencies in micron and submicron size dots are determined mainly by magnetostatic interaction. The translation (gyrotropic) vortex mode was predicted in ref. [29] and has been detected by direct imaging with time resolved magneto-optical effect [30] and by the photoemission electron microscopy technique [31]. The dependence with the aspect ratio was measured by Novosad et al. [32].

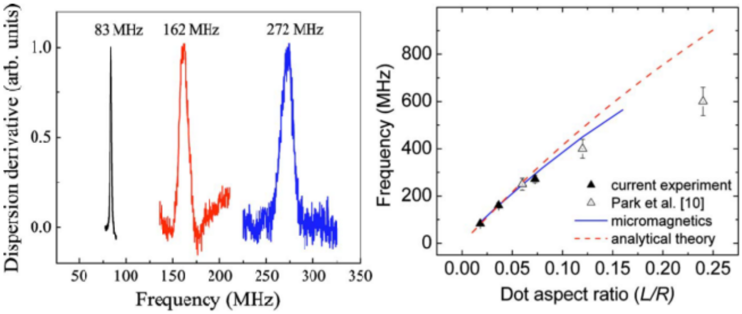

Figure 1.8 Vortex translational mode: comparison between experiment, micromagnetic calculations, analytical theory as function of aspect ratio the dot aspect ratio=L/R (adapted from Novosad et al.[32]**).**

The gyrotropic mode frequency[33] can be expressed as function of the dots aspect ratio as: $\omega_0 = \gamma M_s (20/9) L/R$ and the line-width [34] $\Delta\omega = 2\,d\omega_0$; where $d = \alpha_{LLG} F(L,R)$. A simple relation in which this linewidth [34] can be expressed as [see, for example, Vogel et al, [35]]: $\Delta\omega = 2\,\omega_0 \alpha \left[1 + \frac{\ln R/R_c}{2}\right]$. Here L and R are the thickness and radius of the dots as mentioned earlier and R_c is the thickness-dependent vortex core radius.

- **High frequency (azimuthal and radial) modes**

Highest frequency spin waves generated in the circular dots are the radial and azimuthal modes. Observation of these modes was first reported in 2004 by Buess et al. [36] . The analytical theory explained the experimental results afterwards by Guslienko et al., [37]. To obtain discrete set of vortex high-frequency modes, the linearized equation of motion of dynamic magnetization components at the vortex ground state was used [29]. Both radial and azimuthal modes explored by Buess [36] are mainly determined by magnetostatic interactions [37]; and belong to the GHz range with eigenfrequencies proportional to the aspect ratio $(L/R)^{1/2}$ (see for example ref[18]) for thin soft ferromagnetic dots. An example of both modes is shown in Figure 1.9.

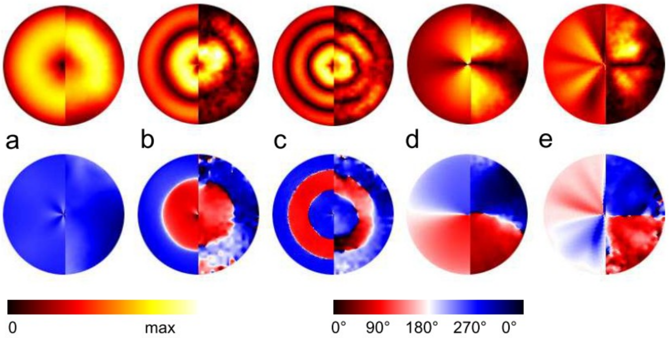

Figure 1.9 Fourier transform images and simulation (right/left respectively) The Fourier magnitude (up) and Fourier phase (down) a) to (c): Axially symmetric modes showing concentric nodes (n= 1, 2, 3, m= 0). Mode, (d)-(e): These modes have nodal lines going across the image. (d): one azimuthal node (1, 1). (e): two azimuthal nodes (1, 2). (This figure is adapted from[36]**)**

Solving the problem assumes that the magnetization inside the circular dot is spatially and time dependent: $m(\rho,t)=m_0(\rho)+\mu(\rho,t)$. The spin wave modes can be labelled by the number of nodes n and m along the radial ρ and the azimuthal φ directions respectively, with $\omega_{n,m}=2\pi\cdot f_{n,m}$ being $f_{n,m}$ the eigenfrequency. For a fixed *n* a splitting of azimuthal modes occurs for values of *m* with the same absolute value and different sign (sign denote the direction of rotation of the dynamical magnetization clockwise or counter clockwise). This effect has been studied theoretically and splitting of the vortex azimuthal modes with indices $m=\pm|m|$ was observed experimentally in refs.[38], [39]. The model depending on linearized set of Landau-Lifshitz equations in[40] gives a considerably lower value of the splitting in comparison with the experiments. This splitting is a result of interaction of the high frequency spin-waves with the vortex core. The effect of the core was verified experimentally by Hoffman et al.[41], where they suppress the splitting by removing the vortex core (removal of the magnetic material at the central part of the dot).

As far as these spin wave modes originate from magnetostatic interactions [37], they will depend on the dot aspect ratios. There were reports on corresponding spin wave frequencies using time domain measurements. The reported mode excited by in-plane microwave field are spin wave azimuthal modes with indices n=0, m=±1 for circular Permalloy dots and with small aspect ratio thickness/radius β (below 0.06) [39]. It was found that the simulated eigenfrequencies and their corresponding splitting values are considerably higher than the experimental ones. Zhu et al.[38] reported on the lowest spin excitation frequencies for the dots with aspect ratio β=0.087 only. Later Hoffman et al.[41] also measured the azimuthal eigenmode frequencies (n=0, m=±1) for dots with small aspect ratio (<0.03) and reported on the values which are substantially different from those measured by Park and Crowell[39]. Those previous reports on the aspect ratio dependence of the spinwave modes are limited to small aspect ratio β.

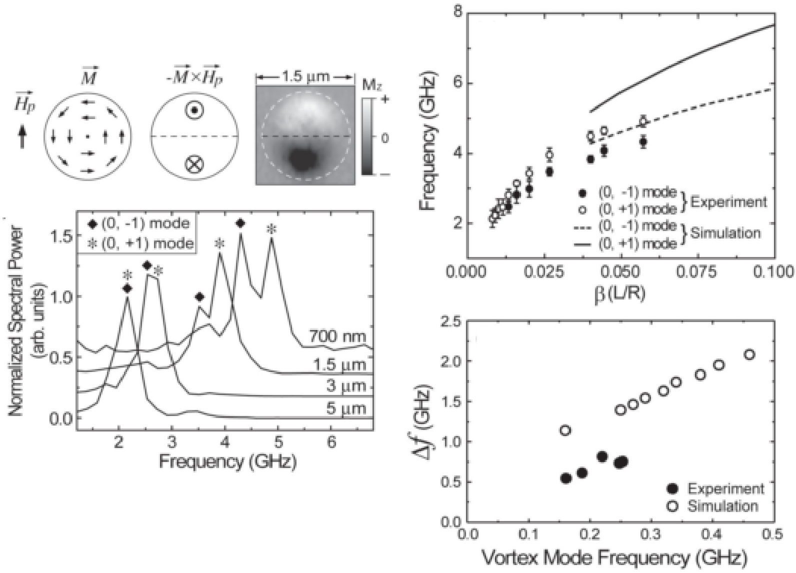

Figure 1.10 (left) The measured signal and the eigenfrequencies (Up right) of the (0,1) modes are shown and its function of L/R. The symbols are experimental data and the curves are the results of micromagnetic simulations. (Down right) The splitting f of the (0,1) modes is shown as a function of the vortex mode frequency figure is adapted from Park and Crowell et al., [39].

- **Vortex dynamics in the applied in-plane field**

Understanding of the dynamics of the shifted in the applied magnetic field vortex is important for physics of switching of the vortex as well as for the spin-polarized current-induced switching of the free layer in nanopillar devices [24]. The shifted vortex in the applied magnetic field has not been investigated theoretically. The present models are mainly based on the rigid vortex model (see for example Guslienko review[42]) and the calculation of the high frequency azimuthal modes is done for centered vortex with symmetric in-plan magnetization, which is obviously not the case for the shifted vortex with applied field. There have been some initial studies of the spin waves in the vortex state under bias field using Py disks by FMR and time resolved scanning Kerr microscopy[43], [44]. These studies seems to be incomplete yet, as the description of the data in terms of azimuthal modes with indices (n,m) as being unchanged between cylindrical (zero field) and fully broken (near annihilation field) symmetries.

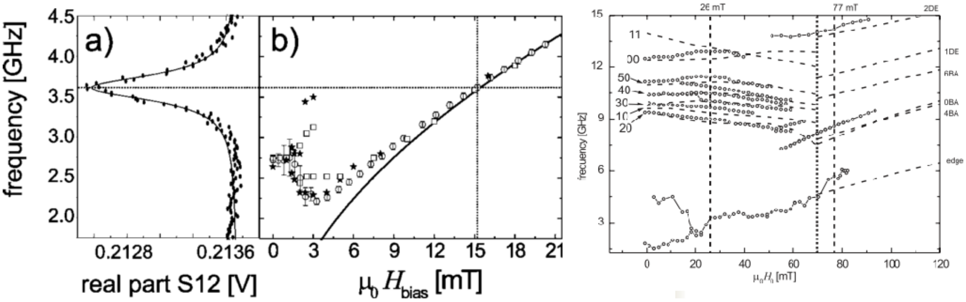

Figure 1.11 (a) Real part of the vector network analyzer (VNA) raw data. (b) spectra obtained by VNA-FMR measurements (open circles), by micromagnetic simulations (open squares) and by frequency sweeps using scanning kerr microscope (FMR-SKEM) measurements (stars). The data points were obtained from an up-sweep (increasing the bias field starting from zero field). The fit to the Kittel equation is represented by the solid line in (b). (Figure at the right) Experimental data from VNA-FMR (open circles) together with calculated frequencies (dashed lines) for the Permalloy disks as a function of the external bias field H_0. The vertical doted line at (H=70mT) assigns the transition from the vortex to the saturated state. The calculated lines are labelled by (n = number azimuthal nodes, m = number of radial modes)figures adapted from ref [43], [44].

What was unclear is why some of the modes continuously ¨survived¨ between the vortex state and the saturated state as shown in Figure 1.11 .

This observation leaves an open question about the nature of the conversion from those present in the centred vortex into the uninform and spin modes in saturated state.

• Vortex dynamics with out of plane magnetic field

In contrast to the in-plan case presented in the previous paragraph, there are only few studies concerning spin waves in this perpendicular to the plain configuration. A microwave spectroscopy using magnetic resonance force microscopy MRFM [45], of individual vortex-state magnetic nanodisks, revealed that there is a splitting induced by H on the gyrotropic frequency of the vortex core rotation [45]. This splitting is related to the existence of the two stable polarities of the core. This enables to detect the core polarity. The core polarity is reversed at value of the bias magnetic field H_r negative respect to the core see Figure 1.12. The frequencies of the two stable rotational modes (corresponding to each core polarity) are proportional to field H and to the aspect ratio of the disk [45].

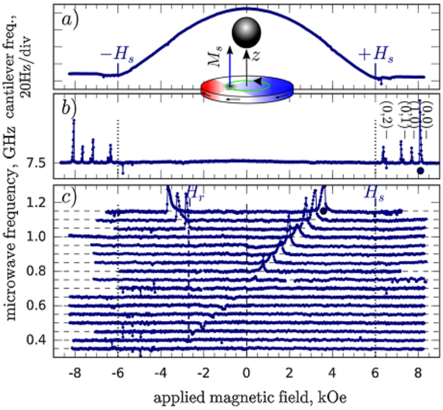

Figure 1.12 (a) The cantilever frequency, proportional to Mz, the vertical component of the static magnetization of the R1= 130 nm NiMnSb nanodisk, as a function of the perpendicular bias magnetic field H. Inset shows detection scheme (figure is adapted from ref [45]**).**

1.3.3 Metastable states for magnetic vortex in circular dots

As mentioned above the vortex state is the ground state of magnetic dots, for a certain aspect ratio, other states exsist for such dots those states are metastable. Generally speaking metastability has been found in many systems and is characterized by some property that is likely to remain nearly unchanged until a transition to another metastable or stable state occurs.

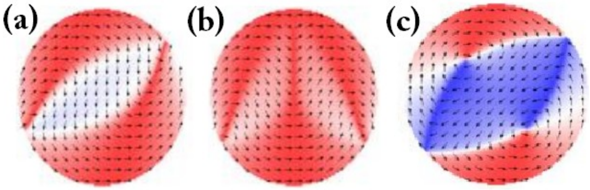

Figure 1.13 Metastable states (a) S-state, (b) triangle state and (c) The double magnetic vortex state (color = M_x).

The metastable (MS) states that may appear in the magnetic nanodisk dots could be classified as the S-state, the triangle state and the Double Magnetic Vortex (DMV), sometime referred also as “diamond” state see Figure 1.13 .

In the DMV there are two vortices both having an M_Z component, similar to one in the single vortex state. Generally, a random configuration of core polarities P1 and P2 can be expected. Metastable states can be described as trapped for some time in local energy minima. Magnetic system can be trapped for a very short or very long time period before it eventually falls back to its ground state. The height of the energy barrier that a system needs to overcome in order to jump out of the local minimum determines stability of that state. Existence of the metastable states in the magnetic dots depends essentially on the dots size [46], [47] . In the part (a) of the Figure 1.14, adapted from Vaz et. al [47], three metastable states can be distinguished. It may be seen that the ground state is the vortex state as it is the lowest in energy. The energies of the different magnetic states depend on the dots thickness. So, for the smallest dots the energy difference between different metastable states is reduced. A schematic representation of metastability can be drawn as in Figure 1.14**b**.

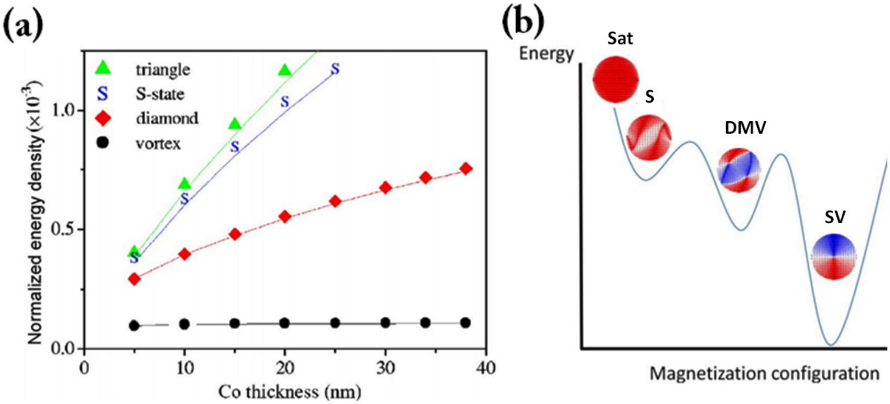

Figure 1.14 (a) Total magnetic energy density for the different metastable states as a function of dots thickness of Co disk with diameter 1.65µm. The diamond state one called the DMV state in this thesis (adapted from ref[47]**). (b) Schematic representation of metastability of a nanodot.**

In Figure 1.1b the system goes from a higher energy state (in this case a saturated state) to the magnetic ground state (the single vortex). Typically the path from a higher energy state to the ground state is not a straight slope. i.e. a local minima may exist, like sketched in the Figure 1.14b.

• Double magnetic vortex state

A very important factor of the metastable state is relation between its lifetime and characteristic time window of the experiment. Some materials (e.g magnetic bits in a hard disk drive) maintain their MS state unchanged during at least a few tens of years. Sufficiently long lived MS states may permit experimental study of their properties by investigation linear response to small external perturbations, i.e. the determination of the dynamic eigenmodes.

It is a challenge, however, to exploit the dynamic properties of short-lived (nano/microsecond long) MS states. Also, MS states with a very short lifetime have (definition) a low energy barrier to keep the system trapped. So, relatively small perturbation can push the system out from the MS state, making it difficult to study the dynamic response of such a system. Though the lifetime of the MS states in a magnetic disks could be small, there were possibilities to find them either in the hysteresis loop or by visualization mainly for hard magnetic dots as Co[48], [49] and for soft magnetic dots as Permalloy[47]. Evidently, it is easier to find MS states in simulated hysteresis loops as a states being prior to the nucleation of the single vortex[47], [50], [51].

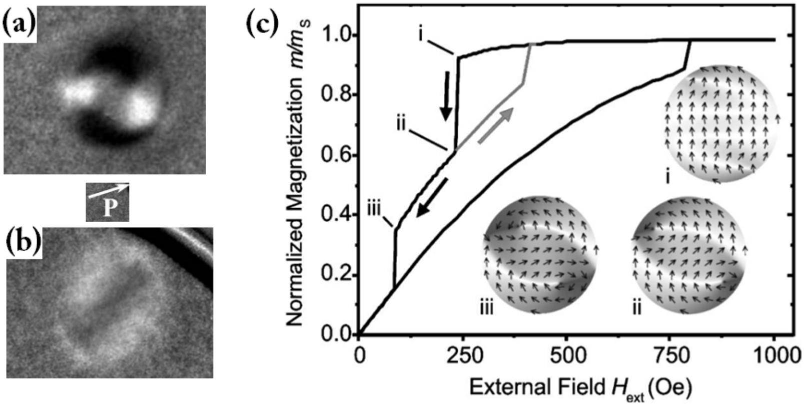

Figure 1.15 (a), (b) PEEM DMV images of the 29 nm fcc Co epitaxial disks and 10 nm Permalloy NiFe polycrystalline disks respectively the inset shows direction of the light polarization P, which is the same easy axis in (a), (c) the simulated hysteresis loop for 40-nm-thick Permalloy disk of 700nm diameter. Parts (a),(b) have been adapted from Vaz et al,[47] **Part (c) has been adapted from Rahm et al.**[51]

In spite of that there have been previous observations of the double magnetic vortex state in Permalloy dots, so far there were no reports on the dynamic response in the DMV state in circular dots. However, some of the spin waves detected in the FMR spectra might correspond to the DMV excitations see, for example, Pechan et. al.[52]. This work used 40 nm thick dots and changed the diameter between 100 and 1000 nm. Their main proof for the existence of a double vortex state was the appearance of remanence at zero fields for large dots diameters beside the simulated hysteresis. Pechan et. al.[52] did not investigate dynamics of the DMV neither experimentally nor by simulations.

1.3.4 Coupled magnetic vortex dynamics

- **Laterally coupled vortices**

For two laterally coupled circular dots in the vortex state four different combinations of the magnetic states are possible. This is due to presence of two independent parameters, namely two vortex chiralities C_1, C_2 and two possible polarizations P_1, P_2 of the magnetic vortex core. In contrary to what has been analytically predicted (in ref [19], [53]) that the gyrotropic eigenmode of vortices in coupled dots (dipolar lateral coupling) should spilt in four eigenmodes see Figure 1.16 **.** Recent experiments[35], [54] and analytical model[55] shows that the coupling splits the gyrotropic mode just in two modes due to different combination of core polarity (parallel and anti-parallel).

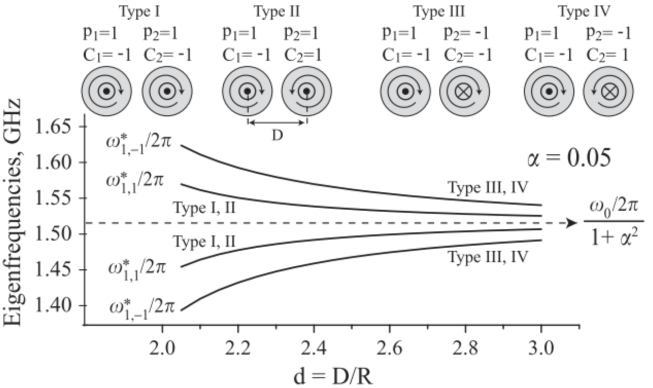

Figure 1.16 Schematic diagram of vortices for various combinations of polarizations p and chiralities C (upper figure). Analytically estimated eigenfrequencies for a weak damping 0.05 (lower figure). The computational material parameters are typical for Permalloy with radious R = 0.1 µm. D is the dots centre to centre distance (figure adapted from ref.[19] **).**

Vogel et al. investigated experimentally magnetization dynamics in arrays of coupled Py disks with different interdot distance *d* [35]. It was found measurable gyrotropic mode splitting for small *d* (i.e. strongly coupled dots, see Figure 1.17). Calculation has suggested that interdot coupling integral has $1/d^6$ dependence. This dependence, however, does not agree with more recent analytical calculations by Sukhostavets et al., [55] neither fits well into more recent experiments and simulations made by Sugimoto et al.[54] where the measured mode splitting is larger for

P_1P_2 =-1 than for P_1P_2=+1, and the frequency spectrum (splitting of the modes) does not depend on the vortex chiralities C_1C_2, which is confirmed in the analytical calculations[55].

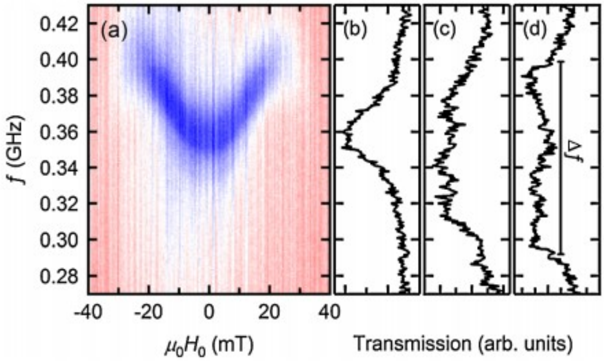

Figure 1.17 (a) FMR transmission spectra of an array of permalloy disks (R = 500 nm and d =1.6 µm). The bias field along the signal line is successively increased from μ_0H_0=-40 mT to 40 mT. The dark (blue) color corresponds to reduced transmission. Spectra at zero bias field for a center-to-center distance of (b) d = 1.6 µm, (c) d = 1.2 µm, and (d) d = 1.1 µm are shown (adapted from[35]**).**

- **Perpendicularly coupled magnetic vortices**

Another form of coupling between vortices is the vertical coupling which can be engineered controlling the spacer between vortex state ferromagnetic layers.

These layered magnetic usually referred to as magnetic nanopillars consisting of ferromagnetic (F) and nonmagnetic layers (N) are becoming the main “building blocks” in spintronics [56]. As to the vertically coupled magnetic vortices in F/N/F nanopillars, the scarce knowledge on dynamics is mainly restricted to investigation of the interlayer coupling effect on the vortex low frequency gyrotropic modes [57], [58] and little is known on the influence of the character of the coupling [59] (dipolar vs. exchange) on the excited high frequency spin wave modes[60]. Besides, the major part of the studies of the vertically coupled vortex state dots has been done in asymmetric conditions by using the dots made of different magnetic materials (typically Co and Py)[59], [61]. If the F-layer thicknesses and radii are relatively small, the dots are in in-plane single domain state and only edge localized modes can be detected in the low frequency part of the spin wave excitation spectra [60]. The experiments showed that some conditions should be satisfied to stabilize a remanent double vortex state in F/N/F stack [62]. The related phase diagram, Figure 1.18, was calculated by Buchanan et. al [63] and the hysteresis loops where simulated and measured for a wide range of symmetric trilayer dots of Py. Visualization of the magnetic state also had been done [63]. The hysteresis shows [63] that for double vortex state (i.e. single vortex in each layer) with a centered vortex in the ground state correspond to a vortex-like hysteresis. This type of hysteresis is valid for the magnetization configuration with the vortex chiralties with the same phase (parallel configuration) and with 180° phase difference (antiparallel configuration), see the inset of Figure 1.18b.

.

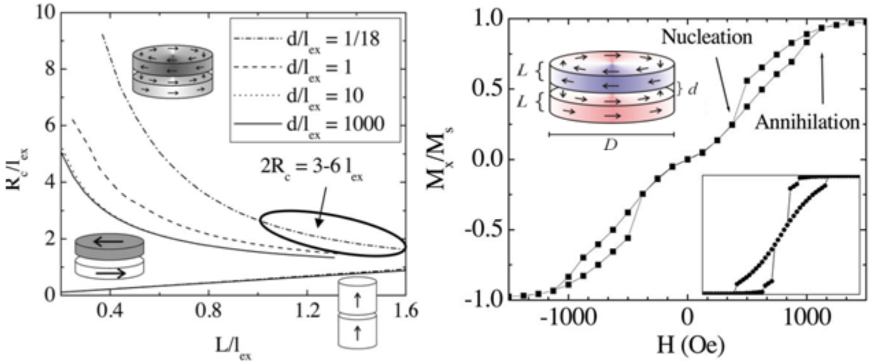

Figure 1.18 (a) Magnetic phase diagram for trilayer F/N/F cylindrical dots for spacer thicknesses ranging from the single dot limit down to l_{ex}=18 or 1 nm. For the F layers and spacer thicknesses considered here the critical diameter 2Rc is 6lex or less. (b) Hysteris loop of a double vortex with antiferromagnetic chirality (and ferromagnetic chirality the inset). Figure is adapted from[63].

Detailed study of the magnetization dynamics of Py/Cu/Py nanopillars in the perpendicularly saturated state was recently reported by means of a magnetic resonance force microscope [64].

As mentioned before, the research on vertically coupled vortex dynamics has been mainly restricted to the investigation of the coupled vortices gyrotropic modes[32], which has been predicted to have a splitting [58] to a low frequency mode in the range of several MHz. These modes present the oscillation of the mean position of the cores around the disk center. The second (a higher frequency mode) in sub GHz range presents in-phase gyration of the vortex cores around their equilibrium centre.

1.4 Vortex dynamics in superconductors

1.4.1 Introduction to superconductivity

A century had been passed since the discovery of superconductivity. In 1911 Kamerlingh Onnes observed that the electrical resistivity in Mercury and of some other elements fells sharply to zero at a critical temperature T_c [65]. This fascinating phenomena and their potential applications have attracted a huge number of physicists both experimentalists and theoreticians. Intentions to understand the physics behind superconductivity and the search for new superconductors have made this field one of the most important and most awarded branches in physics. K. Onnes in 1913. J. Bardeen, L. Cooper and J. Schrieffer in 1972. I. Giaever and B. Josephson in 1973. G. Bednorz and A. Müller in 1987, and finally A. Abrikosov, V. Ginzburg and A. Leggett in 2003 were awarded the Nobel Prize in physics for advances in the superconductivity. These facts underline the importance of this phenomenon from both theoretical and experimental physics points of view.

Intense research has been done towards the understanding and the description of the electrodynamics and thermodynamics properties of superconductivity both on the microscopic and the macroscopic scales. In general, the macroscopic behaviour of superconductivity is described by the well-known London theory developed by the brothers F. and H. London in 1937 [66]. The microscopic properties of superconductivity are described by the well-known BCS theory developed by Bardeen, Cooper and Schrieffer in 1957.

Superconductors are not just ideal conductors but also ideal diamagnetic, as discovered in 1933 by Meissner and Ochsenfeld [67]. This property means that a magnetic field cannot penetrate a bulk superconductor as it is cooled below the critical temperature T_c (see Figure 1.19). In these experimental conditions the magnetic field is expelled from the superconducting sample. This phenomenon was described theoretically by the brothers F. and H. London in 1935 [66].

Later, in 1950, V. Ginzburg and L. Landau developed a phenomenological theory capable of describing the superconducting state in the presence of a magnetic field [68] this approach is called the Ginzburg-Landau (GL) formalism.

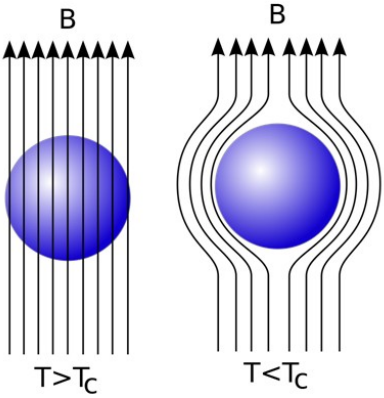

Figure 1.19 Meissner effect in superconducting sphere called in a constant applied magnetic field. Adapted from [C. Kittel [5]**]**

Bardeen, Cooper and Schrieffer explained the microscopic mechanism (BCS theory) [69]. The GL theory [68] describes the normal-superconducting transition by expressing the Gibbs free energy density F as a function of a complex order parameter Ψ. This Ψ can be interpreted as pseudo wave function for superconducting electrons. The local density n_{sc} of the superconducting quasiparticles is given by the square of this function (amplitude), i.e. $|\Psi|^2= n_{sc}$ (in the normal state $n_{sc}=0$). The GL theory was used by Abrikosov [70] to predict a new quantum mechanical state named type-II superconductivity [70] in which external magnetic fueld penetrates in form of flux quanta, vortex.

- **Classification of superconductors**

Superconductors could be classified by different criteria. The most often used classification is due to their behaviour in an external magnetic field. *Type I* completely expels external magnetic fields if the strength of the applied field is below single critical field H_c, above which all superconductivity is lost. Alternatively, superconductors can be of *type II* meaning they have two critical fields: H_{c1}, H_{c2}, between which a partial penetration of the magnetic field is allowed in the form of magnetic flux quanta which is called superconducting vortices.

Other classifications are also used upon introduction of the physical theories that explain origin of their superconductivity. Superconductors can be classified as *conventional or unconventional* (depending if they are explained within the BCS theory or its derivatives such as magnon assisted coupling etc,). Also superconductors could be classified by the values of their critical temperature, namely as *low and high superconductors* (with $T_c > 77$ K). Finally, classification could be due to materials used (element, alloy, ceramic, etc).

- **Parameters describing superconductor**

One of the main characteristics of the superconducting state are two important scales introduced within the GL formalism: the penetration depth λ(T) and the coherence length ξ(T). The first one determines the distance at which external magnetic fields are screened from the interior of the superconductor. The second one determines the typical distance along which the modulus of the order parameter Ψ(r) can be changed. Both characteristic lengths depend on the temperature in the following way:

$$\xi(T) = \frac{\xi(0)}{\sqrt{1-\frac{T}{Tc}}} \quad ; \quad \lambda(T) = \frac{\lambda(0)}{\sqrt{1-\frac{T}{Tc}}}$$

The ratio between the two characteristic length scales λ(T) and ξ(T) define the Ginzburg-Landau parameter κ

$$\kappa = \frac{\lambda(T)}{\xi(T)}$$

In the bulk superconductors, the κ parameter is a dimensionless, temperature independent number, whose value determines the distinction between type-I and type-II superconductors. The critical value of $\kappa=1/\sqrt{2}$

determines crossover from positive to negative surface energy (mentioned in the GL model). Abrikosov [70] found that when the surface energy of a superconductor is negative this will drive to maximize possible normal-superconducting interfaces/boundaries (or quantum flux tubes – vortices). This is the case of type II superconductors where for H in-between the critical fields ($H_{c1} < H < H_{c2}$), the magnetic field penetrates the superconductor in the form of vortices; and the corresponding state is named the mixed state. This state persists until the external magnetic field reaches the second critical magnetic field value H_{c2}, which is dependent on the coherence length $\xi(T)$: $H_{C2} = (\varphi_0)/(2\pi\xi^2(T))$.

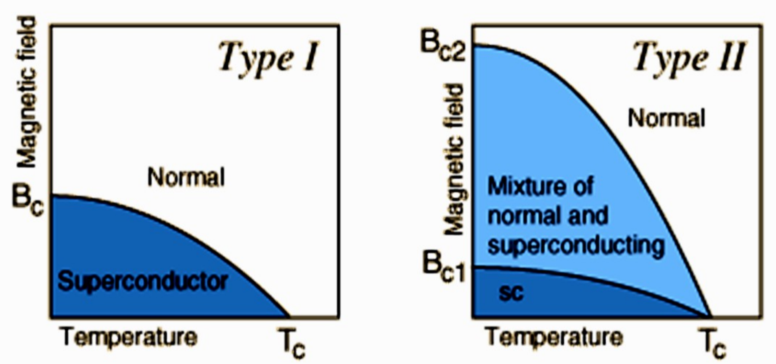

Figure 1.20 Schematic phase diagram drawn for type-I (a) and type-II (b) superconductors

For the other case where $\kappa < 1/\sqrt{2} \Rightarrow \sigma_{ns} > 0$ one speaks about a type-I superconductor. The difference between both superconducting materials type would be presented as H-T phase diagrams, shown in Figure 1.20.

The mentioned above tubes predicted by Abrikosov [70] should penetrate in a regular arrays each one carrying a flux quantum $\Phi_0 = h/(2e) = 2.07 \cdot 10^{-15}$ T m^2 . Within each unit cell of these flux lines there is a vortex of supercurrent concentrating the flux towards the center. Firstly, Abrikosov [70] predicted a square vortex array to be formed. Later, however, it was shown that he had a numerical error in his predictions and the real geometry minimizing the free energy of the system corresponds to a triangular array of vortices (see Figure 1.21)

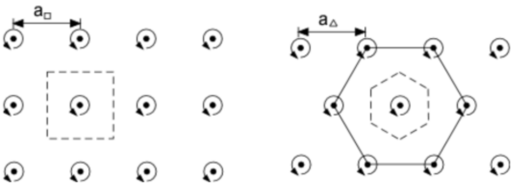

Figure 1.21 The Abrikosov vortex lattice. In left the square vortex lattice predicted by A. A. Abrikosov is sketched In the right part the real triangular vortex lattice which will have with a slightly lower energy is shown.

The single vortex can be presented schematically as consisting of a normal core encircled by superconducting screening currents (see Figure 1.22). The three graphs show the radial distribution of the local magnetic field (B), the current density, J and the local density of superconducting electrons, n_{sc}.

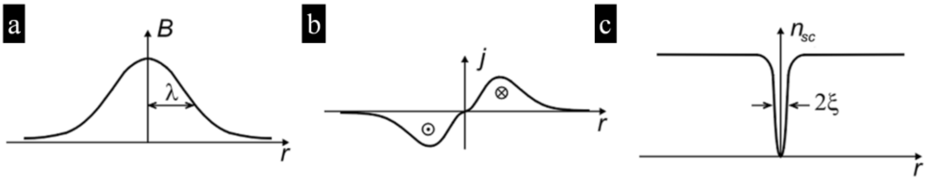

Figure 1.22 (a) Magnetic induction B, (b) current distribution J, (c) and the local density of the superconducting order parameter n_{sc} close to the superconducting vortex (adapted from thesis J. Sierra[71]**)**

In infinite thin films this picture is modified. The vortex structure in finite size real films turns to be Pearl vortices described by Pearl [72] and vortex interaction [73] mediated mainly by the magnetic stray field that exists outside the film.

1.4.2 Superconducting vortex dynamics

One of the main characteristics of the superconducting state is the possibility to transport an electric current without energy dissipation. When a flux quanta exist in the superconductor due to the interaction between the applied current (with density J) and the magnetic flux quanta φ_0 in the superconducting vortex, a force will act on the vortex leading to the vortex motion. A vortex moving in magnetic field creates an electric field **E=B×v; v** being the vortex velocity. The superconductor will therefore show a finite longitudinal resistivity ρ=E/J because a finite voltage appears along the current direction, which will make the current transport to be dissipative. Fortunately, in real superconductors the vortex interacts with defects that serve as pinning sites.

To describe the vortex dynamics one can introduce three main regimes: (i) pinning, (ii) creep, and (iii) vortex flow.

(i) *Pinning regime*: If the pinning is sufficiently strong, the vortex motion can be made small enough so that the superconductor behaves much like a perfect conductor.

(ii) *Vortex creep*: vortices jump from one pinning site to another due to the thermal activation. In some cases this hopping occurs at measurable rate, which is called creep rate.

(iii) *Flux flow:* The vortices move in a rather steady motion, at a velocity limited mainly by a viscous drag. This happens if the pinning is rather weak compared to the driving force. This flow will give rise to a flow resistivity which sometimes is comparable to the normal state resistivity ρ_n.

The vortex motion implies moving normal cores. This motion is accompanied by dissipation proportional to the velocity. This dissipation can be described by an effective viscosity, and the velocity **v** is determined by the balance between the Lorentz force and the viscous force. Therefore a free vortex lattice would move as a whole with a constant velocity. We can write down the global dynamic equation for the balance of forces exerted on a single vortex (per unit length) [69], [74–76]:

$$\eta v + \alpha_H n \times v + \nabla U = \Phi_0 [n \times J] + F_{thermal} \qquad (1.15)$$

where the first terms are: **v** is the vortex velocity, η is the viscous drag coefficient related to the relaxation processes of the quasiparticles. Cooper pair converts to quasiparticle and vice versa with the moving vortex. Dissipation energy is due to the fact that not all energy is restored due finite relaxation time[77].

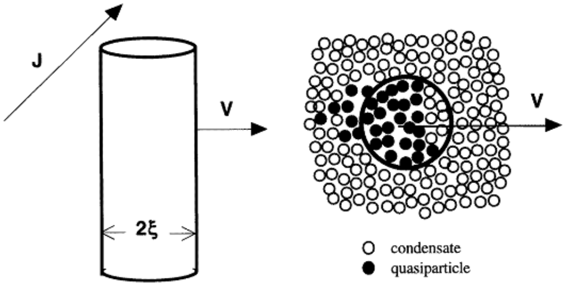

Figure 1.23 A vortex moves under the action of the transport current J. The right-hand side shows a cross section of the moving vortex. On the front of the moving vortex the condensate is converted to quasiparticles (normal electrons), while on the rear of the vortex the quasiparticles are converted back to condensate (adapted from Golosovsky [74]**).**

The second term is the perpendicular (Hall) force acting on a moving vortex, $\alpha_H[\mathbf{n} \times v]$. Here the Hall coefficient is α_H and **n** is a unit vector in the magnetic field in the direction along the vortex. Due to this contribution, the superconducting vortex moving with velocity v experiences driving force along the current.

The third term in equation 1.15 is the pinning force due to pinning potential U(r) that has minimum around r = 0. Any displacement from the equilibrium position gives rise to a restoring force on the vortex. The pinning potential is quantified by the so-called Labush constant $\alpha_L = (\partial^2 U/\partial r^2)_{r=0}$, which in some references is referred as the pinning constant k_p when its described in terms of single pinning. This force is the result of interaction between pinning centers and vortices, including collective interaction of the ensemble of pinning centers and the vortex matter, including the vortex system properties too. So, the pinning constant contains much of the physics of the vortex matter. In all real superconductors the flux lines interact with material defects that act as pinning sites and hamper their motion. Besides the pinning barriers that arise from rather inevitable structural irregularities such as vacancies, dislocations, grain boundaries, etc., there exists a rich zoo of artificially introduced pinning sites like magnetic inclusions, phases of weaker/stronger superconductivity, lithographically patterned “antidots”, magnetic dots, etc.

An electric current exerts a Lorentz force on the vortex at rest. This force can be expressed as $F_L = J \times \Phi_0 n$, where J is the current density. This force drives the vortex perpendicular to the current. In addition to the Lorentz force F_L due to external current, thermal fluctuations can induce flux movement over the pinning background, allowing potentially flux jumps between energy minima. The Anderson and Kim model for flux creep [78] describes this effect in terms of a thermally activated jump rate. In traditional superconductors (with high ξ and low T_c), the flux creep can appear only if the Lorentz force is sufficiently high to nearly overcome the barrier, i.e. for $J \sim J_c$. This mentioned dynamics hold for both DC and AC currents.

- **Vortex resistivity models**[*]

There are different approaches to model the vortex resistivity or the flux flow resistivity; dealing with alternating current density J with frequency ω. It has been described in relation with the depinning frequencies starting from Gittleman-Rosenblum [75] simple model to a recently proposed unified model by Pompeo [79]. The above models extract the vortex parameters from the high frequency measurements. We present first a brief description of the model by Gittleman-Rosenblum (GR); then proceed with brief introduction of other more general approaches.

The GR model for the vortex electrodynamic response [75] neglects Hall effect and therefore the flux creep equation (1.15) is reduced to the form: $\eta v + k_p x = F_L$ with $\rho_v = B\Phi_0 v/J$ the vortex resistivity:

$$\rho_v = \frac{B\Phi_0}{\eta} \cdot \frac{1}{1 - i\omega_d/\omega} \qquad (1.16)$$

$$\omega_d = \frac{k_p}{\eta} \qquad (1.17)$$

---

[*] This paragraph has just comparative relevance to our measurements. It has been introduced to shed more light about depining frequency along with depinning frequency models for comparison reason.

Equation (1.16) indicates that pinning forces dominate at low frequencies, while frictional forces dominate at high frequencies. The depinning (crossover) frequency ω_d delineates the low- and high-frequency regimes.

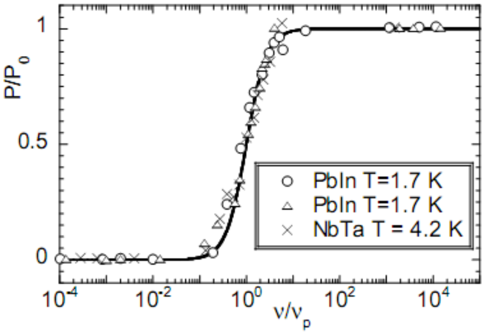

Figure 1.24 Normalized power dissipated in different type-II superconductors as a function of the angular frequency normalized to the depinning frequency. The line shows the fitting to Eq (1.16), (adapted from[75]**).**

According to equation (1.16), at high frequencies **($\omega \gg \omega_d$)** the vortex resistivity is real, $\rho_v = B\Phi_0/\eta$, and the vortex motion is highly dissipative. At low frequencies **($\omega \ll \omega_d$)** the vortex resistivity is imaginary, $\rho_v = -i\omega B\Phi_0/k_p$, and the vortex motion is almost non-dissipative. The different regimes of the vortex resistivity are shown schematically in Figure 1.25.

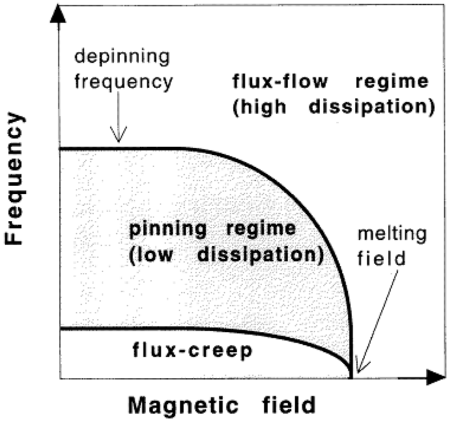

Figure 1.25 A schematic field–frequency diagram. In the pinning regime the vortex resistivity is primarily inductive and is determined by pinning. [adapted from ref [74]**]**

At low fields, each vortex is pinned individually; thereby the pinning constant and the depinning frequency are field-independent. At high fields, pinning is collective and weak, and the depinning frequency is lower due to the decrease of the pinning constant with the magnetic field.

Coffey and Clem (CC) model [80] introduces additionally the flux creep and considers sinusoidal pinning potential U(x). The vortex resistivity derived from their model can be rewritten[80] as:

$$\rho_{\mathrm{v}} = \frac{B\Phi_0}{\eta}\frac{\varepsilon + i\omega/\omega_d}{1 + i\omega/\omega_d} \tag{1.18}$$

Here, the flux-creep factor is ε, which also includes the sinusoidal potential. In the limit of neglecting the above factors the model returns to the GR approximation.

On the other hand, Brandt [81] introduced even more complicated model by considering a phenomenological thermally relaxing pinning constant k_p, that depends on the depinning characteristic time. In this approximation the microwave resistivity has the following form[81]:

$$\rho_{\mathrm{v}} = \frac{B\Phi_0}{\eta}\frac{\varepsilon' + i\omega\tau}{1 + i\omega\tau} \tag{1.19}$$

The surface pinning could bend the flux lines. This bending would give rise to the second oscillatory mode in addition to the $k_p/\eta = \boldsymbol{\omega_p}$, namely is $\boldsymbol{\omega_{ps}}$. By summing it with the classical pinning frequency, so that the depining frequency is $\boldsymbol{\omega_d = \omega_p + \omega_{ps}}$, one arrives to the so called two-mode (TM) model [79]

$$\rho_{\mathrm{v}} = \frac{B\Phi_0}{\eta}\frac{1}{1 - i\dfrac{\omega_p + \omega_{ps}}{\omega}} \tag{1.20}$$

When surface pinning is negligible, the above equation coincides with the GR expression for a single oscillation frequency. A “universal expression” which unifies all the previous expressions [79], proposing an effective creep as a measure of the “weight” of creep phenomena.

• Measurements of the depinning frequencies

All the previous studies of the vortex depinning frequency and related pinning parameters [74], [79] used the above mentioned approaches by fitting the surface impedance Z which is related to the complex penetration length λ.

The main physical quantity directly measurable in the microwave experiments is the effective surface impedance Z_s which is given by:

$$Z_s = R_s + iX_s \tag{1.21}$$

R_s and X_s are the surface resistance and reactance which account for dissipation and energy storage, respectivlly.

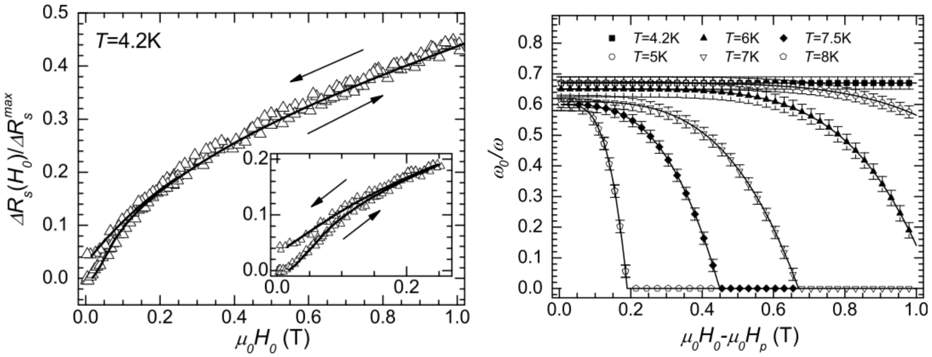

Figure 1.26 (a) Field-induced variations of R_s at T=4.2K. The $\Delta R_s=R_s(H_0)-R_{res}$ R_{res} is the residual microwave surface resistance at the lowest temperatures, and ΔR_s^{mas} is the same difference but with the sample in the normal sate. (b)Magnetic-field dependence of the depinning frequency, obtained by fitting the experimental curves at different temperatures. Figure is adapted from [82].

Recent examples of the calculation of the depinning frequency by Bounara [82] used the complex penetration depth from the Coffey-Clem model calculated from the surface resistance

$R_s = \mu_0 \omega \mathrm{Im}[\tilde{\lambda}(\omega, B, T)]$ where R_s is calculated from the quality factor and the geometry of the a single frequency, ω, resonator.

1.4.3 Critical state

In the critical state of a superconductor close to its edges/ interfaces the current density reaches the maximum possible (critical) value J_c. The critical state occurs under application of a current or if the superconductor is exposed to an external magnetic field. So, the critical state is marked by the limit of the loss-free current density (i.e. critical current density J_c) which in real films depends on the geometry and mainly on the types of the pinning and the vortex-vortex interaction. The evaluation of the critical current requires summation of vortex-vortex interactions and all elementary pinning forces, which all together is a rather unfeasible task. According to the critical state model [83], the stationary distribution can be found from Ampere's law with the condition that the current density at each point is equal to its local critical value $J_c(B,T)$ which is the spatial derivative of the magnetic induction. The easiest case is to consider the current density inside the superconductor to be equal either to 0 or to J_c, as done within Bean model [83].

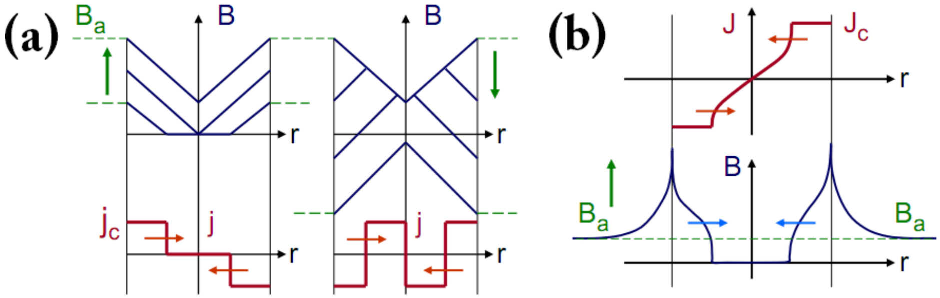

Figure 1.27 (a) Bean's critical state in a cylinder with parallel field, The upper part shows to internal field profiles for increasing (left) and decreasing (right) field and the corresponding current densities (down). (b) Modified Bean's critical state. Current density (up) and internal field profiles (down) for increasing field, adapted from [E.M. Brandt talk[84]].

The original model considered superconducting bodies as long cylinders or slabs. When the field is increased, it penetrates in the film with zones of superconductivity with the current as shown in Figure 1.27. The same Figure also shows the case when the field is decreased. Here the flux decays from the centre to the edges where the superconductivity zone is recovered. In the 2D case a modified Bean critical state model has been introduced with sharp penetration at edges [85], [86] as shown for the perpendicular field case in Figure 1.27(b)

1.4.4 Vortex avalanches

One of the characteristics of the critical state in type II superconductors is the avalanche penetration of the magnetic field at low enough temperatures. Avalanches are commonly observed in the critical state of various physical, chemical or biological systems [87]. These metastable vortex states in type II superconductors have recently been a favourite object for testing the nonequilibrium theories of avalanche dynamics. Vortex avalanches in superconductors consist of sudden large-scale redistributions of the flux penetration that involve up to millions of vortices (see review [87]) due to total collapse of the critical state. Without any external stimulus, avalanches are stochastic processes emerging at the superconductor edge. Most of the experiments observe irreproducible avalanches that are not desirable for applications of superconductors in power electronics and other devices.

To understand the collapse of the critical state we recall that the critical state, emerging from the balance between the Lorentz and the pinning forces, is metastable. Even a slow increase in the external magnetic field may lead to avalanches. Such dramatic events, observed experimentally as abrupt drops in the magnetization.

Vortex avalanches are observed in form of dendrite, and this occurs only at temperatures lower than a threshold below T_c , (see Figure 1.28). While the experiments show clear evidence for the vortex avalanches, the nature and robustness of the resulting avalanche size distributions have been a subject of intense debate. Two different activation mechanisms for vortex avalanches in superconductors have been discussed extensively: of dynamic and of thermal origin.

The first mechanism is supposed to be the intrinsic mechanism in the formation of the critical state and can be a result of the self-organized criticality (SOC) of the system. SOC theories and models predict power-law size distributions for avalanches P(s) ~ $\mathbf{s}^{-2a}$, with P(s) being the probability to find an avalanche event with **s** vortices suddenly on move. Exponent **a** is a critical exponent describing the underlying dynamics of many systems with universal exponents [87]. Analysis shows that robust, well-defined power laws are somewhat elusive [see for e.g review[87]] which weakens the SOC mechanism. Even that, for some experimental results the speed of dendrite propagation even exceeds the velocity of sound in the material [88]. This raises questions about possible non-phonon heat conduction mechanism with speed of dendrite propagation in YBCO being up to 180 km/s [88]. A different mechanism of flux avalanche emerges when a thermomagnetic instability occurs [89], [90]. This mechanism has become now a commonly accepted explanation of the avalanches (see review by Yurchenko et al. [91]) where the link between the avalanches and the sample parameters, as well as threshold field and dependences on the sample and current parameters are explained within the frame of the thermal instability analytical theory. The speed of the dendrite propagation has been also resolved recently by simulation[†] taking into account the thermal instability mechanism.

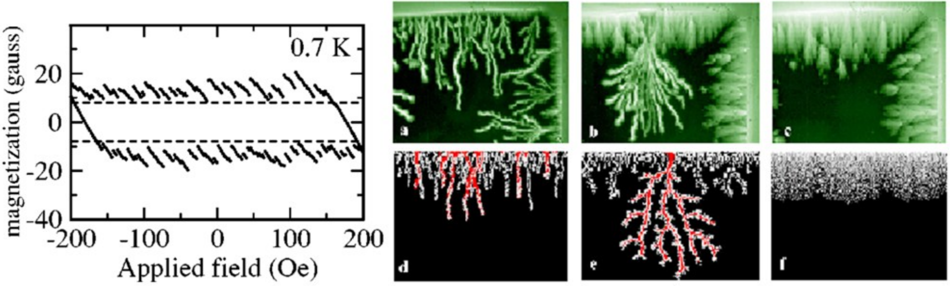

Figure 1.28 Development of avalanche process from magnetization curve[Pb at 0.7K adapted from [92]**], and dendrite avalanches in MgB2 visualized by MOI at different temperature and by vortex dynamics simulations ¨lower panel¨ [adapted from** [87]**]**

To summarize, recently, the avalanches are ascribed to the thermomagnetic instability mechanisim, where the local heat dissipation

---

[†] Private communication by Yu. Galperin.

associated with vortex motion reduces the pinning, which in turn facilitates further vortex motion. With this positive feedback, a small perturbation can quickly evolve into a flux avalanche (see Nowak et al., [93]).

The observed dendrite fingers shape of the avalanches maybe explained as dendrites that have a strong tendency to avoid overlapping. As discussed in relation to the work of James et al. [94], this effect is probably a result of the long-range action of the repulsive force between vortices in thin films. The same ‘‘explosive’’ force could also be responsible for the branching itself, although the mechanism for selecting these seemingly random bifurcation points is not yet clear. Aranson et al.[95] suggest that vortex ‘‘micro-avalanches’’ can be triggered by a hot spot and that the temperature distribution can evolve in a branching manner.

Despite there has been substantial progress in understanding the avalanche processes, it still not fully clear to what extent one can control the intermittent flux dynamics of type-II superconductors (see for example[87]). There exist several ways to trigger avalanches controllably, e.g., by laser[96] or current pulses[97], due to microwave fields in superconducting resonators or coils [98–100], etc. The common feature of these methods is that the instability is triggered by a normal hot spot generated by the external perturbation.

• Thermal stability of the critical state

To further shed light on the above mentioned thermal instabilities. We review the thermal stability of the critical state which can be expressed as the stability of the simple critical state model i.e. Bean state. The thermal stability of the critical state can be defined as the ability of the superconducting system to decay the local temperature raise due to dissipation of energy. The origin of the energy dissipation is mainly due to the heat generated from vortex motion. In the critical state the flux jump would be considered as a rapid heating affecting the superconductor with the magnetic flux distributing (pinned and interacting) in it.

The mentioned heat generation due to vortex motion Q_{vm}, would be balanced by heat absorption within the sample and heat removal through the substrate. The ratio between those two quantities correspond to the stability parameter β. When β>1, the critical state is unstable and small perturbation destabilize the critical state initiating a flux jump. Meanwhile, at high temperatures, near T_c, β «1 and a large heat capacity serves to stabilize the Bean state.

The heat absorption by the sample and heat removal through the substrate can be expressed as γCΔT, and C_sΔT, respectively. Here ΔT is the peak temperature raise during a flux jump and C, and C_s are the heat capacity of the superconductor and the substrate respectively. The size of the jump is related through $J_c(T,B)$ to the temperature at which heat from vortex motion is balanced by the heat capacity and cooling [93]. The instability is also related to the field and temperature from C(H,T) dependence, which for a superconductor increases with H (see ref. [93]). In these conditions we get $\beta = Q_{vm} /(\gamma C+C_h)\Delta T$; where in ref.[93], β is derived for ring geometry with hole inside having the substrate with C_h (here h denotes the hole inside the ring).

- **RF induced avalanches**

The origin of the rf induced avalanches could be understood by the fact at high frequency, vortex depinning occurs (thermally or RF driven) and the vortices enter in the strongly dissipative dynamic response after increasing the drive frequency. Recent experiments showed the possibility of rf induced avalanches either by single high frequency pulses [100] or emerged due to flux shaking provided by radio frequency currents in superconducting resonators near characteristic resonant frequencies [101].

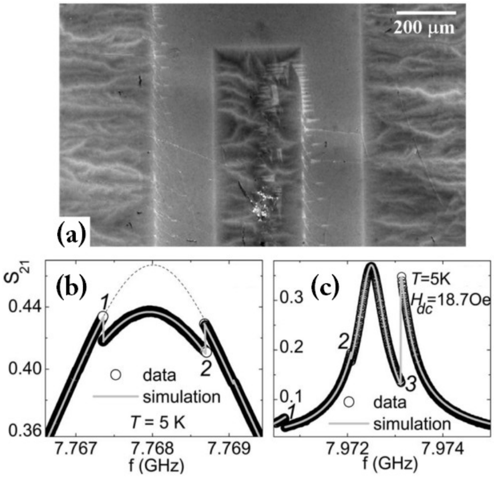

Figure 1.29 (a) Magneto-optical image of the dendritic flux penetration in the coplanar resonator at T=5.6 K and H_{appl}=218 Oe, in the absence of the microwave signal. Brighter gray levels correspond to higher magnetic flux density regions, while black zones inside the sample correspond to regions in the Meissner state. (b) and (c) Resonance curves show how weak links and avalanche have effect on the resonating frequencies (adapted from ref. [101] **and** [102]**).**

The origin of such avalanches in strip line resonators is the thermal instability. One of the main findings [102] is the recovery of supercurrents at the resonator edge after the avalanche occurrence and the flux freezing inside the strip line. However, the complication of the microwave induced avalanches, still due mainly to the microwave vortex depinning as the depinning process is a complex process in the presence of different pinning sources in real sample. Also, for high T_c superconductors, there is important influence of thermal creep that could be involved also in triggering avalanches.

1.5 Problems within the objective of this thesis

1.5.1 Magnetic Vortex dynamics

- ✓ Dependence of high frequency vortex spin wave modes on the dots aspect ratio, especially at relatively large aspect ratios.
- ✓ Detailed field dependence of the vortex spinwaves and their behaviour near transition to the saturated state.

- ✓ Spin waves in the metastable vortex states in Py dots .
- ✓ Influence of lateral coupling effects on the high frequency modes at vortex state.
- ✓ The effect of interlayer coupling on the spin wave frequencies.

1.5.2 Superconducting vortex dynamics

- ✓ The effect of the microwave power and frequency on the avalanches.
- ✓ Influence of different pinning sources on vortex depinning frequency.
- ✓ The origin of the RF induced avalanches
- ✓ The possibility to control avalanches by microwave stimulation.

CHAPTER II: EXPERIMENTAL SETUP

2.1 Introduction

The high frequency magnetization dynamics and superconducting vortex dynamics studies date to more than six decades. Many new measurements techniques have been introduced and developed especially in the last two decades, ranging from classical techniques using inductive methods to a variety of techniques that use novel concepts to detect vortex dynamics. This chapter provides short review of the most known measurement techniques. The vector network analyzer ferromagnetic resonance (VNA-FMR) technique, which is used in this thesis, will be further explained along with the measurements setups and the evaluation methods used to obtain physical parameters.

2.2 High frequency characterization techniques

2.2.3 Ferromagnetic resonance (FMR) techniques

- **Conventional FMR technique**

Up to now, the Ferromagnetic Resonance (FMR) technique has been one of the most often used techniques to study the magnetization dynamics (conventional FMR technique). Historically it was the first technique to study the FMR effect [4]. Normally, the magnetic sample is placed in a high frequency resonant cavity working at its own resonance resonant frequency. The microwave signal is provided from either a klystron or a Gunn diode with a frequency in the GHz range. Depending on the shape of the cavity and the way it's coupled to the microwave source, this will determine the type of Transverse Electromagnetic (TEM) (normally named TEM_{mn}) mode, with m and n being the horizontal and vertical nodal planes of the resonance mode. Normally, the sample is placed in a way to be located at maximum of the magnetic field component. Also, depending on the position, different RF pumping geometries could be used [103] (see Figure 2.1b). The detection of the resonance is done by monitoring the absorbed power, which will increase when the resonance condition is met and can be measured as a reduction of the reflected power. This absorbed power depends on the susceptibility of the sample [104]. In the FMR experiment the general conditions of the detection of the FMR are essentially that the pumping field h_{rf} creates a torque on the magnetization and the total dynamic magnetization has a nonzero projection in the direction of the pumping field. The resonant condition can be expressed as nonzero time averaged absorbed power [103]:

$$P_{tot} = \left\langle h_{rf} \frac{dm_{tot}}{dt} \right\rangle_t \neq 0$$

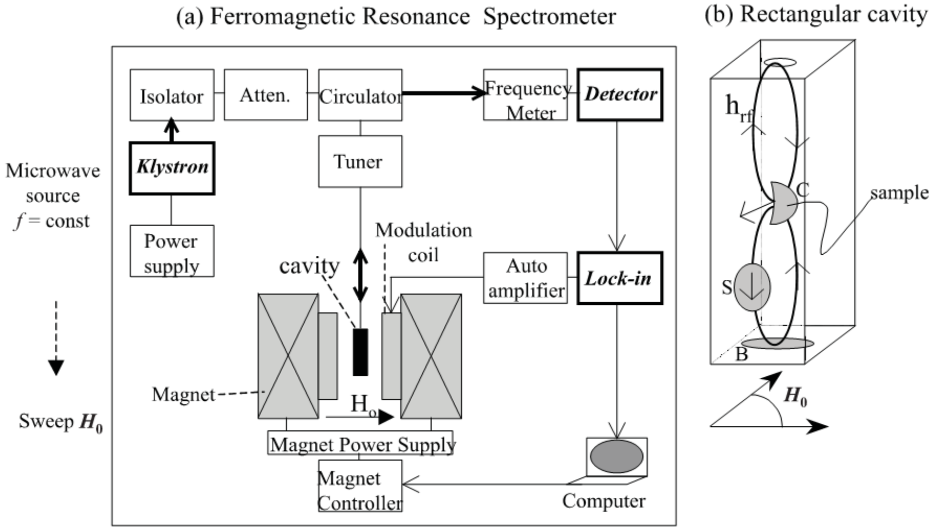

Figure 2.1 Schematic diagram of the conventional FMR with cavity, (b) the RF cavity with possible sample positions (noted by B, S, C) used to realize different pumping field configurations (adapted from[103]**).**

The magnetic field is swept by an external electromagnet till the ferromagnetic resonance condition is met.

- **Pulsed Inductive Microwave Magnetometer (PIMM)**

The pulsed inductive microwave magnetometer (PIMM) technique has been developed by Dietrich et al [105] in the 1960's. A pulsed magnetic field is created by the coplanar waveguide (CWG) due to voltage step from the pulse generator. Free induction decay (FID) in the magnetic sample placed faced down on the CWG induce a voltage detected by fast oscilloscope on the time domain. The signal can be transformed to the frequency domain using Fourier transform which allows to obtain the parameters of the ferromagnetic material [106]. Figure 2.2 shows a schematic diagram of PIMM technique [6] where set A and set B are Helmholtz coils used to saturate magnetically sample and to take a reference measurement respectively.

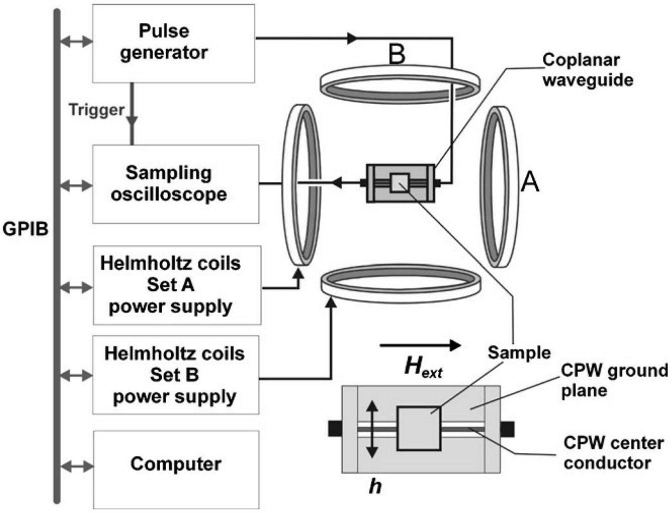

Figure 2.2 Schematic diagram of the pulsed inductive microwave magnetometer. [adapted from[6]]

- **Vector network analyzer-FMR**

Vector network analyzer (VNA-FMR) is another, relatively new, inductive technique which takes the advantage of the VNA devices and high frequency circuits components. The VNA-FMR technique operates over a wide frequency band (to several tens of GHz) and yields FMR parameters from standard scattering parameters (S-parameters see appendix A for more details) measurements as function of frequency and field. Figure 2.3 shows a diagram of the system. The microwave drive is created by means of a coplanar waveguide CWG excitation structure, with the sample placed faced down on it. The static magnetic field is provided by a set of Helmholtz coils. The measurements are typically done by sweeping the frequency in the desired range in a fixed magnetic field and by recording the signal and then changing the magnetic field and repeating the sequence.

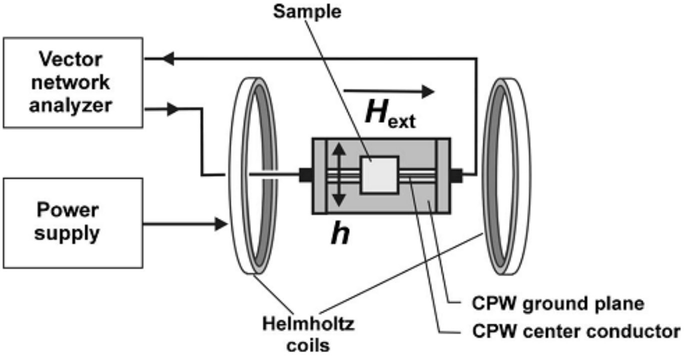

Figure 2.3 Schematic representation of the VNA-FMR setup [adapted from ref[107]**]**

As we mentioned, VNA provides the scattering parameters (S-parameters). There are several models that evaluate the permeability or the susceptibility of the magnetic materials from S-parameters. The main relative approaches are discussed later in this chapter.

• Brillouin Light Scattering

Time-domain magneto-optical measurements offer two more possible advantages compared to the conventional microwave measurements. The first is the very high bandwidth due to the ultrafast laser pulse as it has the ability to deliver this bandwidth optically. The second is the spatial resolution obtained also due the optical detection ability. This converts Brillouin light scattering (BLS) spectroscopy to be a very powerful measurement tool. The BLS effect is due to the interaction between light and the spin waves (photon-magnon scattering). This scattering is inelastic: the photon may lose energy and momentum to create a magnon (Stokes process) or gain momentum and energy by destroying one (anti-Stokes process). The scattering produces shift in the photon frequency known as the *Brillouin shift* which is equal to the energy of the interacting magnon. The Brillouin shift also depends on the wave vector q which is commonly measured by a Brillouin spectrometer based on a Fabry–Pérot interferometer (see Figure 2.4). So the BLS merits lie in the determination of the frequency and the wave vector of magnetic excitations in large frequency range [108] in the measured two-dimensional spatial distributions intensity of the dynamic magnetization, as well as ability to analyze the temporal evolution of magnetic processes with a typical time resolution below 1 ns. An example of such studies in magnetic dots could be found in ref. [109].

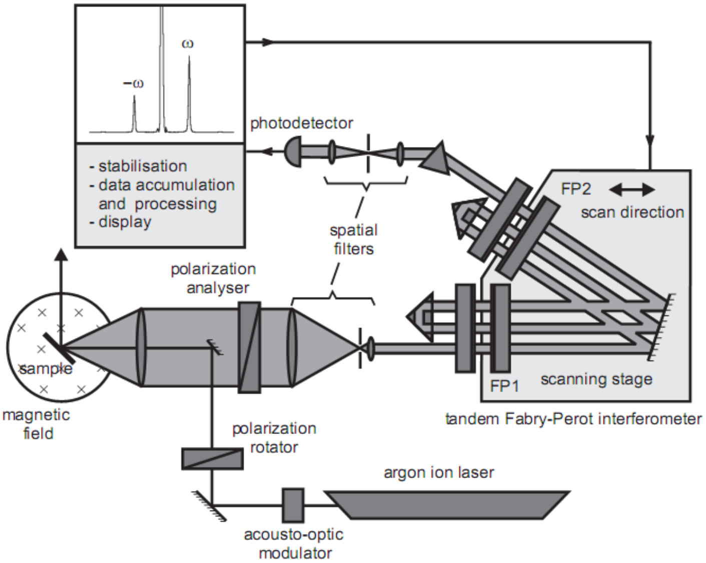

Figure 2.4 Schematic view of a Brillouin light scattering setup [adapted from Demokritov et al., in ref [103]**]**

• Time Resolved Magneto Optical Kerr Effect microscopy

In magneto-optic Kerr effect (MOKE) the light reflected from a magnetized material suffers slightly rotated plane of polarization. This technique has been implemented since the early 1970s. Argyle et al [110] carried out an experimental study of the vortex dynamics with the simplest form of this technique using a continuous-wave light source illuminating a ferromagnetic cross sample. The magnetic contrast can be obtained by various contrast mechanisms as the Kerr effect, Voigt effect, Faraday effect or Cotton-Mouton effect[108]. The development of the technique and its importance have been greatly stimulated by the development of modern pulsed laser sources [111], [112]. A detailed review of this experimental approach has been done by Freeman and Hiebert in [103]. In the pump-probe measurement geometry [103] two pulses are used to reconstruct the magnetization dynamics in a stroboscopic way. The first pulse ¨pump pulse¨ creates a small magnetic field pulse [typical field strengths does not exceed values from 50Oe to 100Oe] disturbing the magnetization from its equilibrium. This can be achieved by using a Schottky Barrier or by creating an electrical field pulse using a photo-switch which traverses a micro-coil or a micro-strip line [see the Figure 2.5]. The second pulse is the probe one which is directed at the sample probing the magnetization state via the change of the polarization due to the Kerr effect.

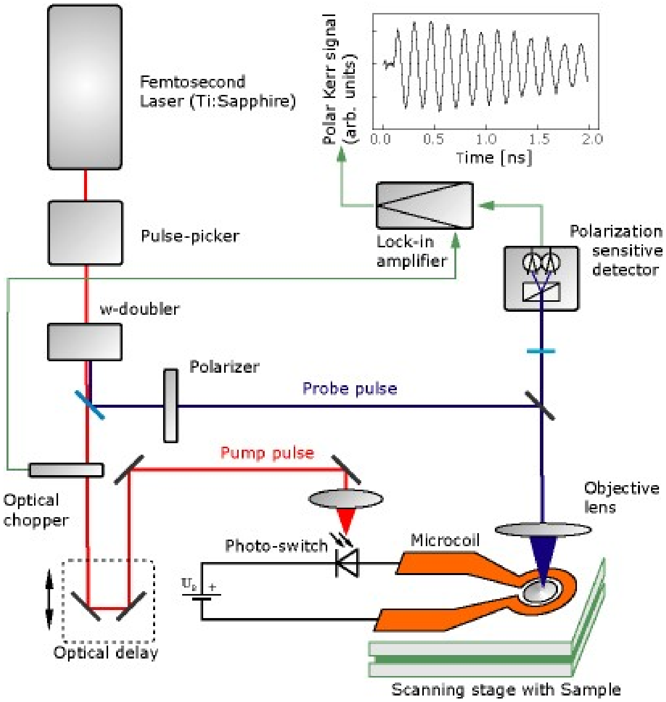

Figure 2.5 Experimental TR-MOKE setup. The magnetic sample (dot) is placed inside a microcoil [adapted from [43], [113]**].**

Tamaru et al.,[114] demonstrated that using a sinusoidal high-frequency (hf) field created by a RF source with a single frequency replacing the pulse field, enables to directly investigate the eigenmode spectrum of a magnetic system in the frequency domain; still benefitting from the spatial resolution of the Kerr setup. So, one can reconstruct the mode spatial distribution making local Fourier-transform process for each position in the space. The time-domain signal is extracted from the magnetic image sequence as shown in the images presented in the introduction to vortex dynamics (seeFigure 1.9).

- **Ferromagnetic Resonance Force Microscopy**

The Ferromagnetic Resonance Force Microscopy FM-MFM technique relies on the coupling between resonating moment **m**(r,t) and a magnetic local probe via the force interaction. The force F(r,t) would affect a displacement of the resonator via the change in the resonant frequency of the cantilever [108]. The importance of FM-MFM is the possibility of imaging the resonating modes locally which permits spatial mapping of magnetostatic modes [108] with spectra presented as function of the probe position.

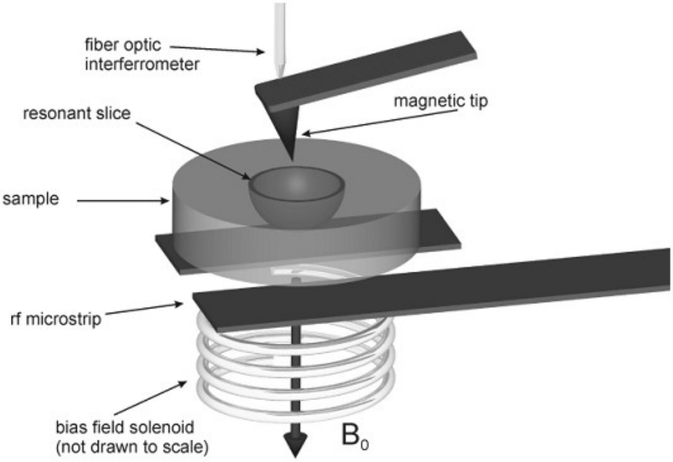

Figure 2.6 A schematic view of the FM-MFM dives (adapted from ref.[108] **).**

- **Synchrotron radiation technique**

Synchrotron radiation technique has been adapted in the last few years to investigate properties of magnetic thin-film and nanostructures. The attractive properties of synchrotron radiation are mostly that their capabilities allow measurements in resonant conditions at an absorption edge allow studying the properties of selected components with define material/element in the sample as long as radiation energy is tunable. For example, X-ray magnetic circular dichroism (XMCD) is a quantum mechanical effect that causes the absorption of circularly polarized X-rays by a magnetized medium to depend on the direction of the magnetization [115], [116]. This capability is important in addition to time-resolved measurements in sub-nanosecond timescales via stroboscopic pump and probe experiments. Basically the synchrotron-based techniques are similar to the optical techniques both working for small patterned samples (for review of application of this technique to magnetic dots see Back et al., in the ref [108]).

2.2.4 Superconductor high frequency measurements techniques

The most common techniques used to study the high frequency properties of the superconductors are briefly reviewed below. Those are essentially the resonating cavity and the Corbino disc. There are other techniques which will be not be reviewed such as bolometric technique, rf coil and rf SQUID which are less relevant to our measurement setup; due to the volume limitation of the manuscript.

- **Cavities**

A cavity is an electromagnetic resonator, typically consisting of a defined volume of conducting walls made of almost ideal conductors such as copper or even superconductor itself [117]. For the measurements of the superconducting films, the sample could be mounted inside a cavity, typically cylindrical or box shaped (see for example[118]). Also sample could be used as one of the walls of the cavity (see for example[119]), or may totally form a resonator itself as in so-called parallel-plate resonators PPR [120]. Here the penetration depth can be calculated from the resonance linewidth and the quality factor Q of the PPR, microstripline [121] (see Figure 2.7). The surface resistance R_s can be calculated from the measured Q and the resonating frequency f_o. Normally the coupling with the high frequency source is done via a capacitive approach (see Figure 2.7d).

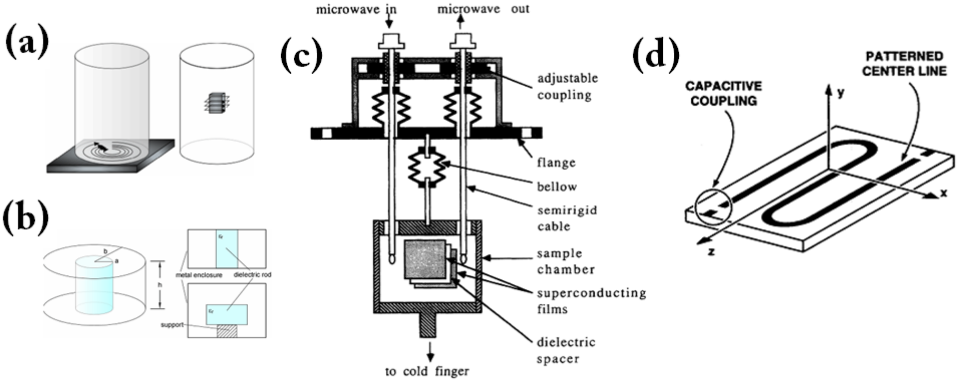

Figure 2.7 Schematic picture of cavities (a) metallic with the sample forming wall or inside the cavity, (b) Dielectric cavity[both adapted from [122]**] (c) Parallel-plate resonator spectrometer[adapted from** [120]**], (d) Superconducting strip-line resonator (adapted from**[121]**).**

The cavity has well-defined resonance frequencies corresponding mainly to the TEM modes and in general only one of those is used considering the major excitation scheme and the pumping direction for the measurements. The signal in the cavity could be studied by measuring the reflected or transmitted signals. By sweeping the frequency of the applied microwave, the resonance frequency and the linewidth are obtained. Both are affected if a sample is introduced into the cavity. By measuring these two quantities, from complex surface impedance Z_s (obtained provided the size and shape of the sample are well known) and the surface resistance one obtains the penetration depth. In this way, through use of the models of the surface resistivity one can obtain the superconductors properties.

- **Corbino disk**

This technique uses the Corbino geometry connected to network analyzer. The technique is widely used to measure different types of materials starting from semiconductors (see for example [123]) to magnetic materials (see for example[124]). Corbino geometry was implemented to study superconducting films by Booth [125]. The design of the Corbino disc setup is very simple as shown in Figure 2.8. It is done by terminating a coaxial cable with the sample with metallic contact being deposited on the surface. Thus, the microwave signal is reflected by the sample and returns to the network analyzer through the same coaxial line as shown in Figure 2.8.

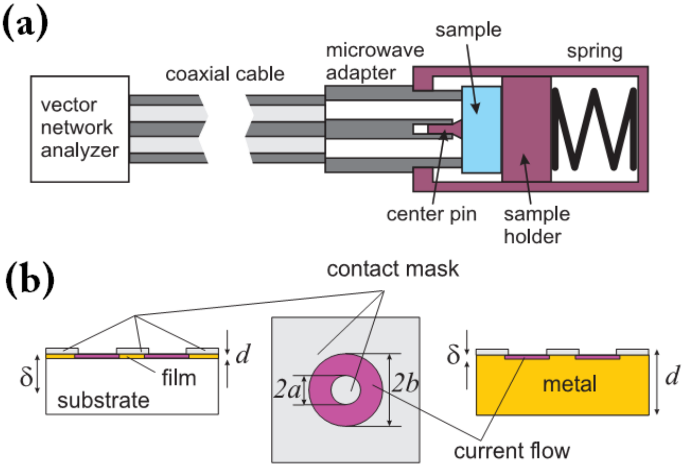

Figure 2.8 Schematic picture of a broadband microwave spectrometer that employs VNA with Corbino disc geometry (adapted from [123]**).**

Knowing reflection coefficient at the input of the cable one can obtain the reflection coefficient Γ_0 at the sample and then the sample surface impedance using the following expression (see for example [126]):

$$Z_s(\nu) = Z_0 \frac{1+\Gamma_0(\nu)}{1-\Gamma_0(\nu)}$$

Here Z_0 is the characteristic impedance of the material filling the cable. The coaxial cable supports the TEM mode.

2.2.5 Comparison of the techniques and methods

Cavities in both conventional FMR and superconducting measurements techniques have the advantage of the high sensitivity due to the fact that small changes of a resonant structure, such as introducing sample, strongly affect the resonance. Furthermore, frequency shifts and the change of the transmission/reflection due to the absorption can be measured easily with a high accuracy. This provides high sensitivity of the conventional FMR measurements despite its drawback of being fix frequency technique.

Signal to noise ratio (SNR) is very high for the FMR techniques. The VNA-FMR with its broadband capabilities also has relatively high SNR. On the other hand, the TRMOKE has a small SNR comparing to FMR and VNA-FMR mainly due to reduced probe area [43]. The detection limit is high for the TRMOKE down to $7.7\times10^6\mu_B$ meanwhile it is in the order of $10^{12}\mu_B$ for inductive FMR techniques [43]. The PIMM technique has a low SNR and the detection limit is also comparable to the FMR and VNA-FMR values.

The BLS technique has the capability to provide the frequency-wave vector dispersion. The limitation of the optical setups is (valid also for the synchrotron techniques) the relatively large probe area as they are limited to the optical focus limitation. The time domain measurements have reduced number of the measurement points, comparing to the other frequency domain techniques where the sweep bandwidth and sweep steps can be predefined down to Hz. As we mentioned above, the disadvantage of the conventional FMR is essentially the limitation to the single frequency. Tuning of this frequency is linked to the dimensions of the cavity. All techniques detect FMR resonance with the same value of the frequency see ref [6], [43], while the linewidth somewhat varies from a one technique to another. For example, the linewidth of the optical technique is less than the inductive one primarily due to the small area probed [6].

Corbino disc method has the advantage of the wideband measurements but its disadvantage is the sample preparation limitation due to the inclusion of the contacts pads. Even more essential issue is calibration which is somewhat challenging due to the need to fix the sample prior cooling. Besides, changes of the properties of the cable as a function of temperature may give contribution which is comparable to the one of the sample.

2.3 Measurements setup

In the course of this thesis we used room [127] and low temperature[128] versions of VNA- FMR developed at MAGNETRANS-UAM group, Madrid. We also developed new low temperature VNA-

FMR insert working down to 1.8K and up to 60 GHz, as well as upgraded RT-VNA-FMR capabilities from 8.5 to 40 GHz. A home-developed LabView based control the complete measuring sequence: setting external bias field, controlling and measuring the VNA parameters and writing data to data sheets and subsequently analyze the measured data. LabView programs improving experimental possibilities and analyses; were also created in the course of this thesis. Below we provide details of these setups.

2.3.1 Room temperature Vector network analyzer VNA-FMR

This set-up was upgraded to work till 40GHz by the using new Agilent network analyzer (PNA E8363C) and by the implementation of new set of Rosenberger commercial cables with 2.92mm connectors working to 40GHz. In addition, two types of interchangeable setups were created. We can list them depending on how one connects the coaxial cable to the coplanar geometry:

- The first one has U shaped CWG which existed previously in the Lab. This relatively large grounded CWG with connection to the high frequency cable made by mechanically fixed endlaunch (commercial 2.92mm endlaunch Southwest Microwave) connectors. The CWG was fabricated from Rogers commercial laminates with a gold Gladding conductor with an inner conductor thickness of 375 μm and a gap distance between inner and outer conductor of 140 μm. The insulator material is a glass reinforced hydrocarbon/ceramic laminate with dielectric constant of $\varepsilon_r = 3.66$. Additionally, in order to have a good ground connection, an array of micro-holes was designed surrounding the ground planes on the CWG. A detailed image of this CWG along with the calculated excitation field h_{rf} around the central conductor is shown Figure 2.9.

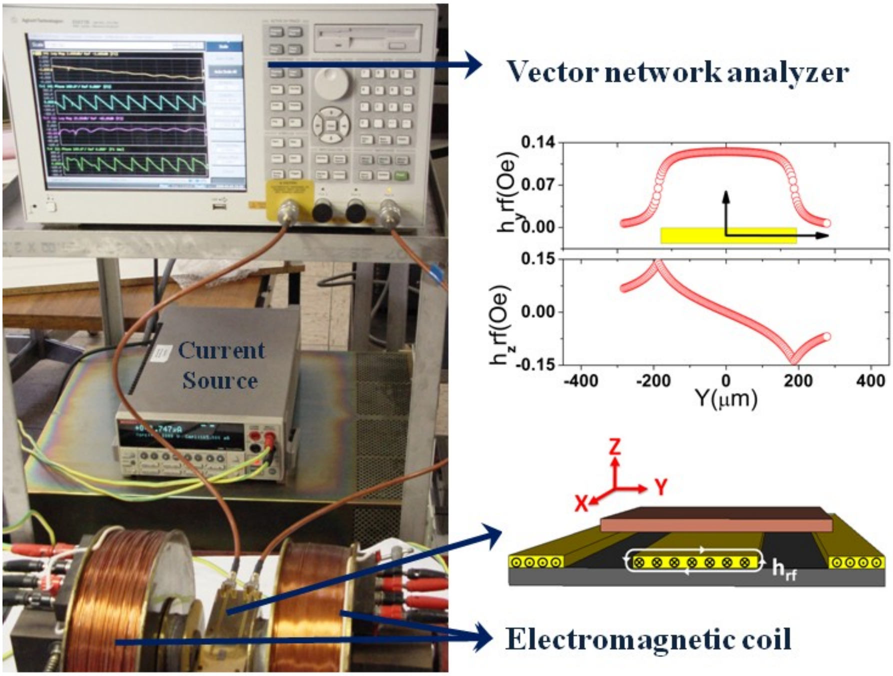

Figure 2.9 The photograph is the VNA-FMR transmission setup with the coplanar wave guide CWG orientation and the field created. The plots are U shaped CWG rf field excitation calculated around the central conductor using the equations [129]**.**

- The second (see appendix B) CWG is made using microwave commercial nonmagnetic custom Picoprobe probes (K-type with tips in a GSG (Ground-Signal-Ground) geometry and 150 μm pitch size (separation between Ground-Signal pads) (see Figure 2.10). These microwave coaxial probes, lead to a low insertion loss. They are similar to the K-type cables and work up to 40 GHz.

We employed two xyz manipulators (non-magnetic also) one to adjust the probe (Picoprobe) and the other to mount the sample/calibration substrate to avoid the displacement of the probes and the cables preventing changes of phase due to their displacement after calibration.

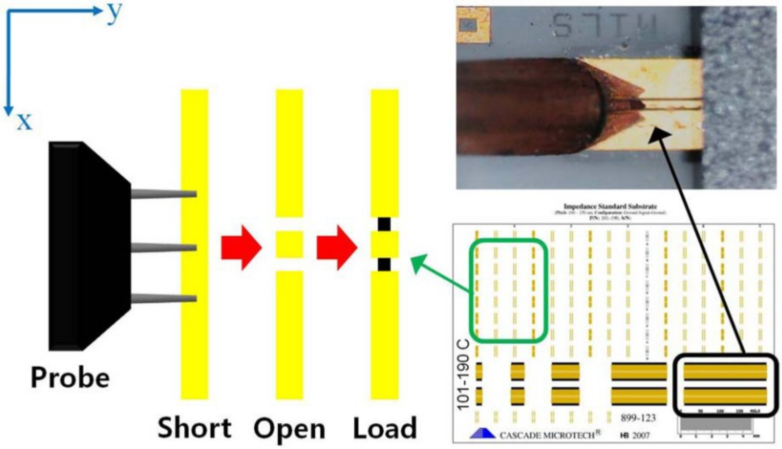

Figure 2.10 Reflection setup showed be changed cause its now adapted from[130]**.**

Both coplanar setup were built over a copper plates and mounted between the poles of a homemade calibrated electromagnet. The external bias field can be applied using an electrical current provided by a Keithley 2800/2400 multi-meters or Kepco BOP 100-10MG power supply with a maximum DC field 350mT.

2.3.2 Low temperature VNA-FMR

- **Cryogenic System**

The ultra low loss ^{4}He gas flow JANIS-2002 cryogenic system can carry out both high and low frequency (AC or DC) measurements on magnetic or superconducting films through use of universal- compatible inserts. The cryostat is equipped with 9T superconducting magnet.
All low temperature measurements presented in this thesis were done using low temperature insert working down to 1.5K (LT-FMR I). This setup works till 12 GHz. In addition, a new setup working till 40GHz and down to 1.8K was created in the course of elaboration of this thesis.

The cryostat (Janis Research Co.) ^{4}He system has an inner ^{4}He flow system with a variable temperature insert, inserted inside a 50 liters ^{4}He reservoir containing a superconducting magnet. Both ^{4}He parts are thermally isolated from their environment by vacuum shielding. Besides, the outer reservoir has a liquid N_2 thermal protection shield. The temperature inside the variable temperature insert is controlled by changing the pressure in the He-flow system with a vacuum pump and by using a LakeShore-340 temperature controller with two thermometers.

A Cernox resistor thermometer sensor (CX-1050-SD, serial: X20466, calibrated from Lakeshore) register He flow temperature and the temperature is controlled by a 25 Ohm heater coupled to the flow valve. The second thermometer is installed in the microwave insert near the sample. For the LT-FMR I insert a Silicon diode standard thermometer from Lakeshore. Meanwhile for the second insert (LT-FMR II) the thermometer is Cernox resistor thermometer (CX-1050-SD, serial: X44217, calibrated by means of other commercial calibrated Carbon-Cermamic CCS/A2 from 1.3-300K) see appendix B.

The LakeShore-340 controls the temperature in the gas-flow system through a mechanically manipulated capillary. A proportional integral derivative controller (PID) between temperature reading (Lake Shore) and temperature controlling (butterfly valve) results in a temperature stability better than 1mK for the temperature range between 1.5K and 10K and around 10mK from 10K to room temperature. The cryostat design permits to exchange the inserts without the need of heating up the whole cryostat. This permits to maintain the experiments running up to 10 month/year.

The magnetic field is provided by a superconducting (SC) magnet consists of a twisted multifilamentary NdTi/Cu solenoid. The SC magnet is operating in a DC mode by current supplied from a power source (American Magnet System) works up to 100A and 5V, which allows creating DC magnetic fields up to 9T.

- **VNA-FMR Setup**

For the high frequency measurements at low temperatures a commercial Agilent E-5071B (ENA series) working in the frequency range from 300 kHz up to 8.5GHz is used with VNA connected to the homemade microwave insert.

The microwave insert have three different parts. Below we mention list of the common parts between the two inserts (LT-FMR I, LT-FMR II):

The top part (head) includes the Aluminum predesigned head to have the connection to the VNA and to the temperature controller as well as to multimeters for DC measurements (Figure 2.11). In addition to high frequency connectors, the DC pin connectors are hermitic. The middle part (body) include essentially the main support bar made of aluminium installed on it aluminium plates to reflect the heat radiation to insure a good temperature gradient to the bottom part. The bottom part includes a sample holder located along with the heat coupler and heater. The sample holder is a Cu piece containing the previously mentioned calibrated thermometers. CWG is fixed at the sample holder with the sample put on CWG top (2 at Figure 2.11). The sample is further fixed mechanically by means Cu flexible plate clamp (see 3 at Figure 2.11).

A commercial Hall probe [AHP-H1G from AREPOC (with sensitivity >700mV/T at nominal current of 5mA) is installed in both LT-FMR I, LT-FMR II inserts.

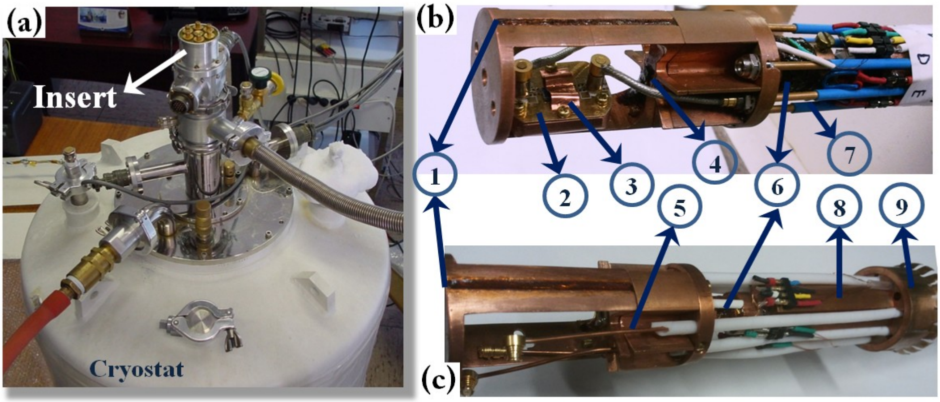

Figure 2.11(a) Photograph of the upper side of the Cryostat, (b) , (c) Microwave insert I and II respectively; the parts: 1-thermometer hole, 2-CWG with its SMP connectors, 3-cupper fixing finger, 4-Hall probe, 5-Cable UT-47-C, 6-Heater, 7-Cable UT-85-B-B, 8-Heat sink rod, 9- cylindrical crown shaped heat sink Copper plate.

Once the sample has been properly placed on the CWG; the sample holder is closed with a protective cylinder made of Teflon/Copper. This part is mounted directly below the 25Ω heater constructed as twisted coil made of manganine wire turned directly over the copper rode and fixed permanently with low-temperature varnish. The lowest part of the insert (sample holder and the heater) is connected thermally to the Copper heat sink rod (8 at Figure 2.11). On the Copper heat sink rod upper part a cylindrical crown shaped heat sink Copper plate is fixed (9 at Figure 2.11).

We further mention differences between the two inserts:

The first microwave insert (LT-FMR I):

The microwave part was made using special low temperature high frequency semi-rigid coaxial RF cables UT-85-B-B with a beryllium copper BeCu center conductor and jacket. *The selection of the cables was made to the best trade-off between the desired small thermal conductivity to minimize the thermal link to the room temperature connectors at the head of the insert, and the good metallic conductivity. Discussion concerning the selection of cryogenic cables can be found in ref.* [123]. *In addition,* UT-85-B-B *cables are non-magnetic.* As long as we study the superconductor properties under applied field, the *superconducting cables should be excluded from the selection* due to the effect of the magnetic field on the properties of such cable. The cables have 0.51/2.20mm inner/outer conductor diameter. The cables connectors with sample holder area are SMP (Sub Miniature version P). A high frequency coaxial connectors with 50 Ω impedance capable to work up to 40GHz.. Those SMP connectors are fixed on the final part of the insert. The connection between these cables and the CWG was done using small hand deformable coaxial cables with 50 Ω impedance working till 26GHz. These cables are from Fernell QF86 with central conductor being Silver plated copper clad steel, and Teflon (PTFE) as dielectric material. The outer conductor is Tin soaked braid. These cables were homely ensembled with SMP connectors.

The second microwave insert (LT-FMR2):

The second insert is a newer microwave insert setup developed during this thesis (see appendix B). It incorporates some important structural elements of the LT-FMR I insert and was constructed with support of SEGAINVEX- the mechanical workshop unit at the University; and the participation of the Department technician A. Buendia.

A new cables implemented are UT-047-C Low Loss semi-rigid 1.8m long coaxial RF cables. These cables have a low density PTFE dielectric for improved insertion loss, the electrical phase stability and increased temperature range. The silver-plated copper wire is the central conductor. The presence of Copper jacket was taken into account in the selection of the cable as for the previous insert LT-FMR1. Meanwhile one has an improved thermal conductivity respect to the UT-85-B-B, it also gets an improved conductivity in addition to the low density dielectric material. This leads to lower losses along with small diameter of the cables *0.29/1.19mm inner/outer conductor diameter* comparing to the UT-85-B-B in the previous version.

The cables have 50Ω impedance, and have SMP (Female) and 1.85mm (Male) connectors capable to work up to 40GHz. Other improvements of the LT-FMR1 insert are that the cables connect directly to the CWG without the need of the hand formable cables which exist at the previous version (see Figure 2.11). Besides, there is possibility to remove and to install new cables, along with the possibility to make DC measurements using up to 6 pairs of copper wires installed in the insert and reach the bottom part of it.

The CWG:

- Due to the reduced dimensions of the cryogenic zone at the bottom part we used specially designed CWGs (see Figure 2.12). The CWGs have reduced size to fit within the sample holders for both LT-FMR inserts. The CWGs are made of Rogers laminates [131] with a Copper Gladding (RO4350 10MIL/ RO4003C 8MIL) conductor. The inner conductor width of 375 μm/343 μm and a gap distance between inner and outer conductor is 140 μm/133 μm. The thickness of the metallic gladding is 66 μm and the coplanar were gold plated to improve conductance. The insulator material is a glass reinforced hydrocarbon/ceramic laminate with dielectric constant of $\varepsilon_r = 3.66/3.55$ [132]. Additionally, in order to have a good ground connection, an array of micro-holes was designed surrounding the ground planes on the CWG. The CWG can be seen as in Figure 2.12.

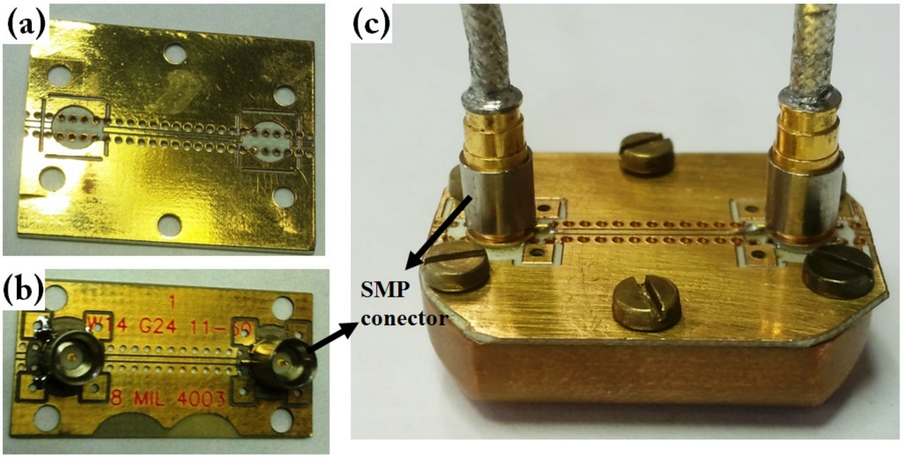

Figure 2.12(a) CWG with etched area for Rosenberger SMP endlaund connector ;(b) CWG made from Rogers RO4003C 8MIL laminate with SMP endlaund connectors soldered on it. (c) One of the CWG made from Rogers RO4350 10MIL laminates fixed on its holder and connected to the RF cables.

The two SMP male launch connectors were soldered to the CWG by Tin at the CWG board edge (the CWG length is almost 25 mm). Coplanar were ensemble to adapt those connectors by drawing and then etching mechanically afterwards, the copper from the drawn footprint of the SMP connectors over the CWG circuit (see Figure 2.12).

2.4 Analysis models

Appendix A includes a brief review radio frequency concepts used in the model.

- **Transmission VNA-FMR technique**

Recently few evaluation methods for different physical parameters to be obtained from VNA-FMR have been proposed and compared with other extraction methods. A very good example of such comparisons are presented by Kalarickal et al.,[6] and Bilzer et al.[133]. Below we will briefly introduce some of these methods.

Kuanr et al.[134] evaluate the resonance frequency and the linewidth from the amplitude of the transmitted signal S_{21} directly. The contribution of the connections and the substrate were subtracted from a spectrum at a field where no response is detected.

Kalarickel et al.,[6] presented a evaluation of an uncalibrated effective microwave permeability parameter by neglecting reflections. Using only the transmission S_{21}-parameter of the measurements and the measurements in the reference field with parallel pumping for which no response in the case of uniform magnetization exists, provides the uncalibrated effective microwave permeability parameter as, according to Kalarickel et al.,[6]:

$$U(f) = \pm \frac{i \ln\left[S_{21-H}(f)/(S_{21-ref}(f))\right]}{\ln\left[S_{21-ref}(f)\right]} = \pm i\left(\frac{\ln\left[S_{21-H}(f)\right]}{\ln\left[S_{21-ref}(f)\right]} - 1\right) \qquad (1.22)$$

This equation presents simplified relation that will lead to additional offsets and resonance shape distortions which can be corrected by introducing additional fitting parameters as shown by Kalarickel et al.[6]. In this approach -Im(U(f)) corresponds to the loss profile of the resonance and the sign in the equation of U(f) is chosen to have the U(f) negative around the resonance peak, meanwhile Re[U(f)] shows the dispersion of the resonance.

Another important approach has been made by Bilzer et al.[133], which provides value proportional to the complex susceptibility and permittivity for the ferromagnetic sample with additional corrections due to sample placement and dimensions. The above approach uses the de-embedded scattering parameters (both the reflection and transmission parameters).

- **Reflection VNA-FMR technique**

One port open circuit reflection measurements have a simplified analysis model proposed by Bilzer et al [135]. The measurements itself is more simplified and faster than the two ports due to the measurements of a single reflection parameter as well as simplified calibration procedure for single port.

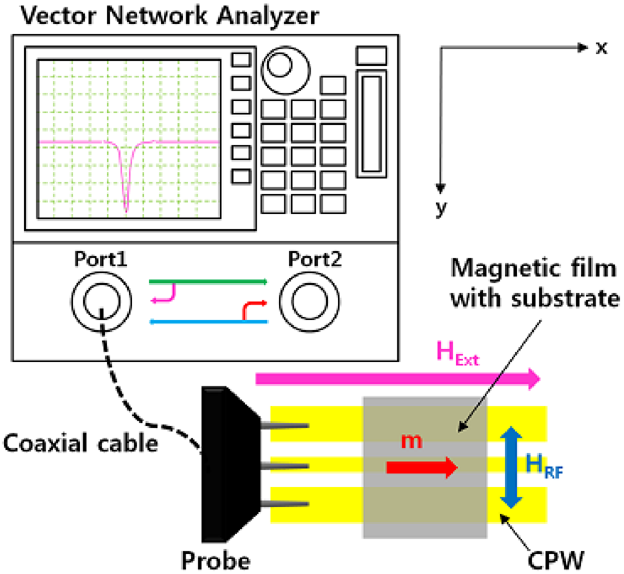

Figure 2.13 Schematic drawing of the one port open circuit VNA-FMR measurement system (adapted from[130] **).**

The one port system is composed of the open circuit CWG shown in Figure 2.13. The expression for X is a value proportional to the susceptibility of the ferromagnetic film[135]:

$$X = \frac{\ln(S^{R}_{11,mea})}{\ln(S^{R}_{11,ref})} - 1 \tag{1.23}$$

The FMR frequency and the linewidth are extracted from X.

For the two ports measurements all mentioned evaluation methods provide the resonance within 1% relative error as well as the open port technique. At the same time, the relative error in the linewidth varies between the discussed above methods. The Kuanr [134] method has the highest relative error followed by Kalarickel[6]. which reaches up to 10% for both methods at low fields (i.e. corresponding to low frequencies) and decreases at high frequencies to around 4% [133]. The open port evaluation method shows relative error in the evaluation of the linewidth below 6% as reported by Bilzer et al., [135].

2.5 Measurement of FMR in films

Before presenting our experiments, it is important to mention that in this thesis we investigated magnetic structures made of Permalloy, an alloy with about 80% Ni and 20% of Fe, This alloy has a high saturation magnetization and very low coercivity. In addition to low damping and small grain size and extremely low anisotropy, all these properties made Permalloy one of the "classic" ferromagnetic materials for investigation of spin dynamics and static's. In addition to the fact that it is widely used in applications, e.g. recording head sensors. Typical parameters of Permalloy in the literature are: M_s= [730×10^3 to 860×10^3] A/m, the exchange stiffness is of about A =13×10^{-12} J/m, α~0.004 to 0.15 (neglecting anisotropy).

The setup and the evaluation analysis methods which we will use mostly in this thesis has been tested on a thin magnetic film in order to explore the capability of our VNF-FMR technique. The measured sample is a thin film Permalloy[‡] ($Ni_{80}Fe_{20}$; or Py), the film has d=36nm thickness. The external bias field was applied in the **x** direction while the pumping field (h_{rf}) was generated by the CWG in the **y** direction as shown in Figure 2.9. The measurements are made at frequencies from 50MHz to 17 GHz. The access to ferromagnetic resonance frequency is limited by the available electromagnet which creates the magnetic field (300mT). We can obtain the spectra of the VNA-FMR using the mentioned Kuanr evaluation method. Figure 2.14 shows 3D contour plot of the obtained results, two peaks in the studied frequency range were observed. The first and the lowest in frequency peak is the FMR and the higher in frequency is the first order perpendicular standing spinwave (PSSW) [Demokritov et al., en ref. [103]]:

[‡] The Py thin film was prepared in the group of professor Peter de Groot, in the University of Southampton. The Py was deposited over a 4nm layer of Cr deposited on a single crystal substrate of GaAs with crystal orientation [100].

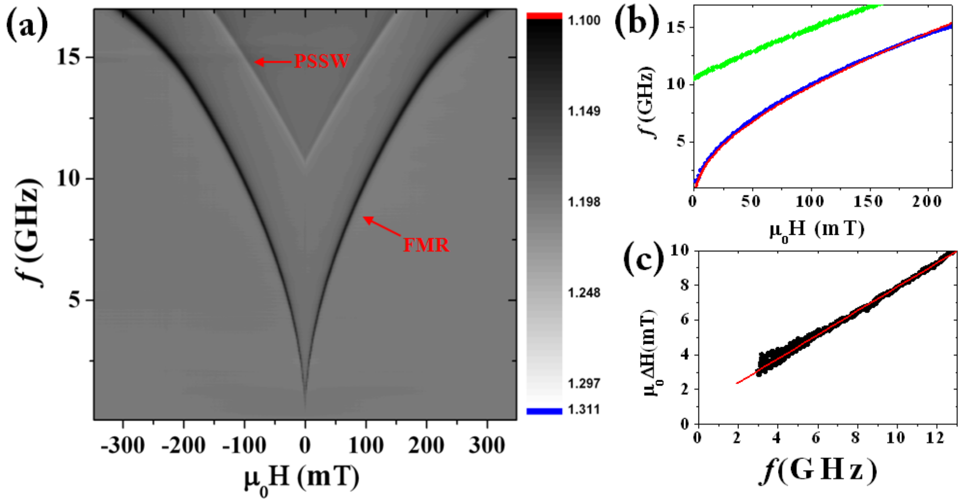

Figure 2.14(a) Counterplot of the magnitude of the normalized transmission parameter, (b) resonance frequency extracted peaks as function of the applied field the red curve present fitting to the ferromagnetic resonance Kittel formula, (c) Measured linewidth as function of field, the red line is the linear fitting.

The measured FMR frequency follows Kittel formula (see Chapter 1) which for film with in-plane applied field H_{app} and perpendicular excitation can be written as:

$$f_0 = \frac{\gamma\mu_0}{2\pi}\sqrt{H_{app}(H_{app} + M_S)}$$

Fitting this relation to the results shown in Figure 2.14 (b) gives directly [considering the gyromagnetic ratio: $\gamma = 1.76\times10^{11}$ Hz/T] value of saturation magnetization $M_S = 794.39\times10^{3} \pm 2.37\times10^{3}$ A/m which is in agreement with values obtained in the literature. The resonance linewidth Figure 2.14(c) can be presented as a function of frequency f as (see chapter 1):

$$\Delta H = \Delta H_0 + 4\pi\frac{\alpha}{\gamma}f$$

The slope obtained Figure 2.14(c), provides the apparent damping parameter: $\alpha=0.0096$, while $\Delta H_0=1.048$ mT is additional broadening of the linewidth and is related to magnetic inhomogenties, grain boundaries, defects, etc.

As we mentioned above, the first (low frequency) peak is the FMR, while the second peak higher in frequency is an exchange-dominated thickness or perpendicular standing spinwave (PSSW)[136] which is described by the relation [Demokritov et al., en ref[103]]:

$$f_{PSSW}^{2}=\left(\frac{\gamma\mu_{0}}{2\pi}\right)^{2}\left[H_{appl}+M_{eff}+\frac{2A}{\mu_{0}M_{S}}\left(\frac{\pi P}{d}\right)^{2}\right]\times\left[H_{appl}+\frac{2A}{\mu_{0}M_{S}}\left(\frac{\pi P}{d}\right)^{2}\right]$$

Here we detect the lowest order PSSW, which corresponds to number of the nodes of the mode profile along the film thickness (here we have the lowest so P=1). M_{eff} includes the contributon of the surface anisotropy. Those modes are important due to the possibility that they offer the extraction of the exchange stiffness constants A of the sample material.

CHAPTER III: VORTEX DYNAMICS IN SINGLE MAGNETIC DOTS

3.1 Introduction and motivation:

Ferromagnetic dots in magnetic vortex ground state [25] have attracted increasing interest in the last years due to the possibility of using the vortex state as a key element of a new type of information storage media as well as the importance of vortex spin excitations for operation of spin current driven spintronic devices and of logic operation devices[26], [137]. Implementation of the vortices in information storage assumes using both the vortex core magnetization direction (up or down) and vortex chirality (i.e., clockwise or anticlockwise rotation direction of the in-plane dot magnetization). Switching between these well defined states, which is expected to be done by either external field, electric current or their combined action, is accompanied by excitation of the spin waves which influences the switching time. Additionally, it has been shown recently that the selective excitation of eigenmodes permits effective switching of the vortex core in the single dot [24]. Therefore, precise mapping of the high frequency spin excitation eigenmodes, and the eigenmodes breaking axial symmetry, is of great importance as those modes are expected to define the vortex switching characteristic times and roots to reduce critical currents for dots in the ground state and in presence of magnetic field.

In this chapter we describe results on the linear spin dynamics of the vortex state in Permalloy cylindrical dots namely the azimuthal and radial spin wave excitations of the vortex ground state and then in the presence of in-plane bias magnetic field. Results on dots with aspect ratio (β =height over radius) varied from 0.03 to 0.1 will be presented.

For the ground state excitations we find that for β exceeding approximately 0.05, variation of the spin wave eigen-frequencies with β deviates from the predicted $\sim \sqrt{\beta}$ dependence. The frequency splitting of two lowest azimuthal modes was observed. The experimentally observed dependence of the frequency splitting on β was reasonably well described by dynamic splitting model accounting the spin-waves and, vortex gyrotropic mode interaction.

For the in-plane bias magnetic field we demonstrate experimentally by a broadband VNA-FMR technique and by simulations that breaking the cylindrical symmetry of the magnetic vortex gradually changes and suppresses the azimuthal spin eigenmodes below the vortex nucleation field, and leads further to the appearance of new eigenmodes. We also show that the parallel microwave field pumping is a unique tool to observe spin excitation modes localized near the strongly shifted vortex core for the bias field between the vortex nucleation and annihilation fields. Meanwhile, the perpendicular field pumping, which excites the spin waves throughout the entire dot, reveals a crossover between two dynamic vortex regimes near the nucleation field.

3.2 Samples preparation

The nanofabrication technologies of the high-quality patterned magnetic nanostructures with lateral extensions in the submicrometer, and nanometer scales have substantially improved during the last few years. Patterned magnetic structures are fabricated mainly using self-organized growth or by lithographic patterning procedures of thin films.

The patterning processes commonly involve electron beam lithography (EBL) [138], X-ray lithography (XRL) [139] and laser interference lithography (LBL)[140].

For our study; the samples[§] were grown by using the EBL technique. The main fabrication steps of EBL are the photoresist film deposition, the electron beam exposure, etching, and finally the sample growth. The arrays of polycrystalline Permalloy dots were fabricated on silicon substrates using lift-off techniques. Figure 3.1 shows the fabrication steps carried out. A double layered resist spin coating on top of a silicon substrate was exposed to a focused electron beam (a). The bottom layer is more sensitive to the electron beam than the top layer, therefore, the bottom layer forms an undercut profile when developed (b). After this

---

[§] Samples were growth by *Vitali Metlushko* [Department of Electrical and Computer Engineering, University of Illinois at Chicago, Chicago, Illinois, USA]; and *Gleb N. Kakazei* [Departamento de Física da Faculdade de Ciências, IFIMUP and IN-Institute of Nanoscience and Nanotechnology,Universidade do Porto, Portugal].

step, the magnetic film can be deposited on a water-cooled substrate from a Permalloy target with a growth ratio of 1Å/s (c). Although EBL is a relatively slow process, the technique is very convenient in order to fabricate arrays of dots with different diameters and inter-dot distances within a limited area of substrate.

Nearly identical properties of magnetic material, grain sizes, distribution and film thickness may be obtained over the whole sample. Finally a lift-off process of the double spin coating layers is carried out. (d). After the sample growth, samples were cut in small pieces and covered by a very fine (few microns) layer of photoresist material to prevent the direct contact with the coplanar wave guide in the set-up.

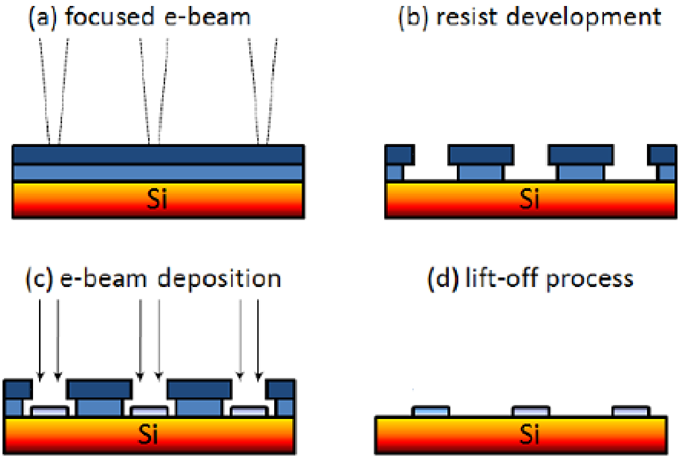

Figure 3.1 Successive steps in the EBL technique: (a) the focused electron beam is applied on the double layered photoresist spin coating layers. (b) After that, a photoresist development is done. (c) With the fabrication of the pattern, the process continues with a magnetic film deposition with a growth ratio of 1Å= s. (d) A lift-off process of the double layered resist.

Following this procedure, two sets of square arrays of Py circular dots were fabricated on a standard Si(100) substrate (explained also elsewhere [27], [141], [142]). The first set includes three samples with thickness L=50 nm, diameter D=1000 nm and the dot´s lattice parameters (center-to-center distance, d_{CTC}) of 1200, 1500 and 2500 nm. The second set included two sets of arrays of Py dots with thickness L=25, 20, 15 nm and diameters of D=1035 nm (d_{CTC}=2000 nm) and of 572 nm (d_{CTC} =1000 nm). In order to check the size and shape of the dots, images of the samples have been obtained using scanning electron microscopy (SEM) technique see also appendix B. The inset Figure 3.2 illustrates the image of one of the arrays of dots. One can observe the good quality of the dots edge. The patterned area had dimensions from 2×2 to 10×10 mm^2.

3.3 Experiment and simulations

The VNA-FMR technique provides precise detection of the spin waves (SW) modes in the vortex state in frequency domain. In addition, the VNA-FMR provides the ability of averaging multiple spectra taken with relatively small excitation field as well as the ability to measure the response of dots in an array [43] that increases the signal to noise ratio in comparison with thetime resolved magneto-optic Kerr effect (TRMOKE) experiments. We note that in our VNA-FMR setup, sketched in Figure 3.2, in addition to the main azimuthal modes (having $m = \pm 1$) some radial (n=0, 1…, m=0) modes could be also excited [44]. This is because the studied samples are wider than the waveguide, and a perpendicular component of the RF field is effective for the dots situated close to the edge of the CWG.

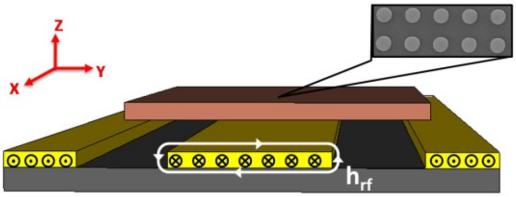

Figure 3.2 (a) Sketch of the experimental setup and the coordinate system used. The insert shows a typical SEM image of an array of Py dots. The bias magnetic field is directed along the x or y axes.

The excited spin waves have been studied at room temperature by the VNA-FMR [see Methods]. The set-up allows to apply RF field either in perpendicular configuration ($\mathbf{h}_{rf\perp}$) where $\mathbf{H}_{bias} || \mathbf{x}$ and $\mathbf{h}_{rf} \perp \mathbf{x}$ as shown in Figure 3.2, or with parallel pumping scheme ($\mathbf{h}_{rf||}$) when $\mathbf{H}_{bias} || \mathbf{x}$ and coplanar wave guide (CWG) rotated perpendicularly with respect to the in-plane static bias field, providing $\mathbf{h}_{\mathrm{rf}} || \mathbf{x}$. The data were analyzed on the basis of transmission model described in Methods chapter and developed under the assumption that the dominant CWG mode is the TEM mode and also neglecting the effect of reflection.

Besides the experimental studies, the micromagnetic simulations [see http://math/nist.gov/oommf] were carried out for a circular Py dot having the thickness of 25 nm and the diameter of 1035 nm. The physical parameters of the individual cells of $5\times5\times25$ nm^3 used were: the exchange stiffness constant $A = 1.4 \text{ x } 10^{-11}$ (J/m), the saturation magnetization $M_s = 830\times10^3$ A/m, $\gamma/2\pi = 2.96$ MHz/Oe taken from the measurements [141], and the Gilbert damping constant of $\alpha = 0.01$.

3.4 Single vortex dynamics

3.4.1 Brief outlook

As we explained in the Introduction chapter, *in the absence of the bias field* multiple spin eigenmodes in the magnetic vortex state can be excited by an external perturbation and the dynamical response in the linear regime is described by their superposition. The lowest frequency excitation corresponds to the gyrotropic mode when the vortex moves as a whole around an equilibrium position [30], [32], [33], [143], meanwhile the higher frequency modes correspond to the spin waves excited mainly outside of the vortex core [36], [37], [39], [40], [43], [44], [52], [142], [144], [145]. The spin waves having radial or azimuthal symmetry with respect to the dot center are described by integers (*n, m*), which indicate the number of nodes of the dynamic magnetization components $\propto \sin(m\varphi - \omega t), \cos(m\varphi - \omega t)$ along the radial (*n*) and azimuthal (*m*) directions (φ is the azimuthal angle in the dot plane, ω is the spin wave frequency). The spin wave eigen-frequencies $\omega_{n,m}$ are quantized due to strong pinning boundary conditions on the dot lateral edges. For in-plane magnetic excitation field the azimuthal spin waves $m = \pm1$ and the gyrotropic mode are expected to be excited [43], [44], [142] because only these spin modes have non zero average in-plane magnetization and can interact with the uniform inplane *rf* driving field. For micron and submicron size dots these spin eigenmode have frequencies which are mainly determined by magnetostatic interaction, therefore they depend on the dot aspect ratio. There were previous reports on the time domain measurements of spin wave azimuthal modes with indices n=0, m=±1 for circular Permalloy dots with small aspect ratio thickness/radius β (below 0.06) under bias in-plane magnetic field [39]. It was found that the simulated eigenfrequencies and their splitting values were considerably higher than the experimental ones. Zhu et al.[38] reported on the lowest spin excitation frequencies for the dots with aspect ratio β=0.087 only. Recently Hoffman et al.[41] also measured the azimuthal eigenmode frequencies (n=0, m=±1) for dots with small aspect ratio (<0.03) and reported on the values which are substantially different from those measured by Park and Crowell [39]. Meanwhile the previous investigations mainly focused on spin waves in the absence of bias magnetic field (as in refs. [30], [32], [36], [37], [39], [40], [52], [145]), i.e. when the vortex is localized in the dot center, just few studies of the spin waves in the vortex state under the influence of an in-plane bias field were conducted [43], [44].

Broadband ferromagnetic resonance (VNA-FMR) results in the applied magnetic field were reported for circular dots with a large aspect ratio (the dot thickness L to radius R ratio was L/R=0.15) in Ref. [43], where up to 8 modes were observed in the vortex state. Then, Neudecker et al. [44] investigated dots with a large diameter (4μm) and very small aspect ratio (L/R=0.01). Two excitation modes were observed up to vortex annihilation field $H<H_a$ by FMR-SKEM (scanning Kerr microscopy)[44] and it was found that the low frequency spin mode transforms to the Kittel´s mode increasing the bias field. The FMR-SKEM optical technique allows getting spatial images of the dynamic magnetization distributions, but it is only applicable (i) to large in-plane size dots (near the border of the single vortex state stability) because the light spot must be much smaller than the dot diameter and (ii) only to few low-frequency spin wave modes, which have a relatively small number of nodes of the dynamical magnetization. The spatial resolution of the optic probes (>300 nm, Ref.[44]) is not sufficient for a clear spatio-temporal observation of all the excited modes in dots with diameter of about 1 micron and below. Applying the VNA-FMR technique, Neudecker et al. [44] observed just one spin wave mode due to the dense mode spectrum and insufficient frequency resolution for such thin, large-diameter dots (the inter-mode separation is proportional to $(L/R)^{1/2}$). For instance, they were unable to resolve the zero-field splitting of the azimuthal modes, which being proportional to L/R is very small (0.15 GHz) and is beyond their experimental resolution of about 0.5 GHz. We also note that the authors of Ref.[43], [44] never used parallel pumping scheme, which should be effective to detect the excited localised spin modes in the vortex state.

Resuming, the previous VNA-FMR results [43], [44] are not sufficient to understand the real field dependent spin wave spectra of the biased vortex dots. The FMR-SKEM results obtained for a very special case in Ref.[44] cannot be generalized to describe smaller dots due to the absence of scaling of the spin eigen-frequencies, when decreasing the in-plane dot sizes. Other existing technique, namely X-ray imaging based on the magnetic circular dichroism effect [146], has a sufficient spatial resolution, but is not fast enough to resolve the spin wave modes with frequencies about 5-10 GHz and is currently employed only to detect the low-frequency gyrotropic vortex modes (hundreds MHz frequency range).

3.4.2 Objectives

As we could see in the Introduction, despite of a huge current interest in the manipulation of the gyrotropic mode in the centred (unshifted) vortex ground state, there is little understanding concerning the spin waves excited in Py dots with larger aspect ratio and in a strongly shifted nonuniform magnetic vortex state. This unexplored (shifted vortex) regime, however, is not only of fundamental interest, but is also of great importance for potential applications in magnetic recording and spintronics. For instance, a precise knowledge of the spin-wave modes in the biased vortex state is crucial for the spin-polarized current-induced switching of the free layer in nanopillar devices and also permits switching of the vortex in single dot [24].

This chapter describes the spin dynamics of the single vortex in the ground state as function of the dots aspect ratio and in the strongly nonuniform (shifted vortex) asymmetric state of Py magnetic dots with a moderate aspect ratio L/R ~ 0.05–0.1.

3.5 *Results*

3.5.1 Static magnetization

The remnant state of all studied dots is a vortex state (see the phase diagram in the introduction). The micromagnetic simulations done by OOMMF confirm this fact (see Figure 3.3b shows a typical dependence of the magnetization (***M***) of the dots array on the in-plane magnetic field during the hysteresis cycle for the positive field branch.

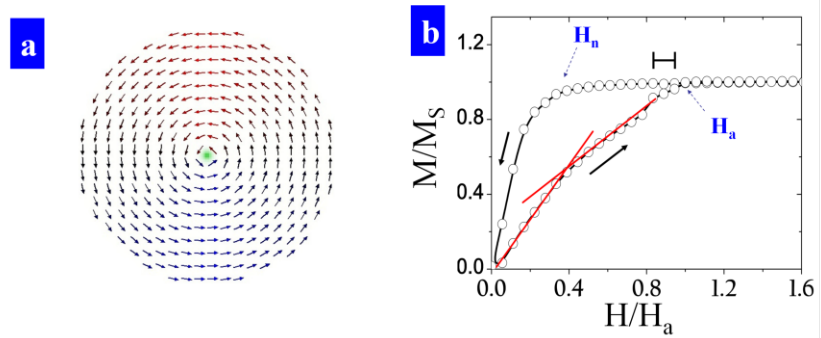

Figure 3.3 (a) Sketch of the simulated ground state of Py dots. (b) Magnetization vs. magnetic field normalized by the vortex annihilation field (Ha =360 Oe Py 1035, 25nm). The annihilation and the nucleation field are indicated. Error bar evaluates the uncertainty in vortex annihilation field. Red lines indicate the change in the slope of the M (H) dependence near H_n.

We can identify the vortex nucleation (H_n) and annihilation (H_a) fields, marked by the arrows for the dots having the vortex remanent state. These fields approximately describe a range of field stability of the vortex ground state [37]. In order to compare the static and dynamic measurements we normalized the external field by H_a.

3.5.2 Vortex dynamics

We performed the broadband VNA-FMR experiments on the arrays of Py dots, using measurements at high magnetic field as reference field. We also simulate the experiment using OOMMF (see Methods) by applying a short pulse (1Oe Gaussian 1ps in plane field pulse) to the magnetic dot in the ground state. So we can obtain the ground state excitation spectra and we can compare the experimentally observed SW modes and micromagnetic simulations.

The Figure 3.4 compares the broadband vortex response of the dot array with *L*=25 nm and *R*=518 nm (β=0.0483). Both the curves are normalized by the frequency of the lowest mode. The origin of a small (of about 10%) difference between the simulated and the detected frequencies (for example, the lowest simulated azimuthal mode is 5.62 GHz, whereas it is 5.05 GHz in the experiment) could be a weak dipolar coupling between the dots. Other possible reasons include the fact that simulations are done at T=0 K and an error in saturation magnetization value taken in the simulations.

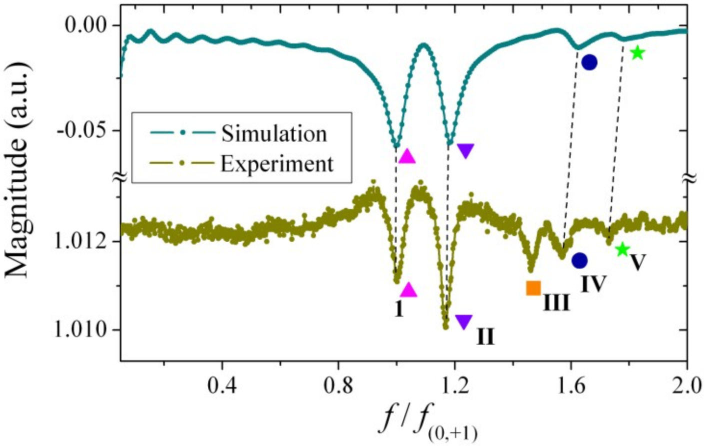

Figure 3.4 Dynamic magnetic response simulated and measured for Py dots with aspect ratio β= 0.048 normalized by the frequencies of the first mode. Vertical dotted lines and symbols show relation between the simulated and measured eigenmodes #1, II, IV, V.

Four experimentally detected modes (#1, II, IV, V) correspond well to four simulated azimuthal modes (*n*=0,1; *m*=±1). The mode #III situated between the first (*n*=0, *m*=±1) and second (*n*=1, *m*=±1) doublets of the split azimuthal modes is absent in the simulations. The azimuthal modes profiles obtained by the simulation (*n*=0, *m*=±1) and second (*n*=1, *m*=±1) is shown in Figure 3.5.

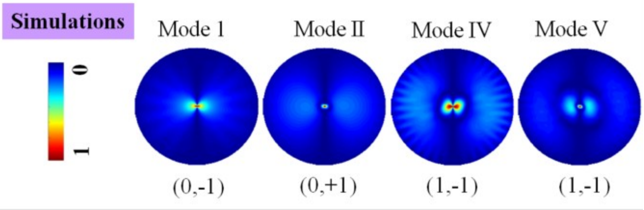

Figure 3.5 2D-snapshots of the relative magnetization ΔM_x amplitude (a.u.) presenting the spatial distributions of the modes (#1, II, IV, V) spin eigenmodes.

The correspondence in the sign of *m* to lower/upper frequency in the azimuthal doublet depends on the vortex core polarization. So we can assign the sign of *m* just for the simulation case as the vortex core is defined meanwhile for the experiment there is a distribution of core polarities so that the sign will have no physical meaning.

Mode #III is, most probably, a radially symmetric mode. This mode has a node in the dynamical magnetization profile in the middle of the dot with respect to the radial coordinate see Figure 3.6. We suggest that mode #III is excited by the small perpendicular field component created in the waveguide due to finite size of the central conductor (see Methods).

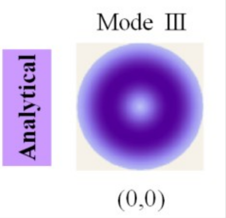

Figure 3.6 2D-represntation of spatial distributions of dynamical magnetization the mode (#III).

The field dependence of the modes #IV, V is well described by simulations, in which consider only in-plane rf driving field. This supports interpretation of the mode #III as a radial mode and the modes #IV,V as azimuthal modes for β=0.048. The field dependence of modes will be treated later in this chapter in the part dealing with the vortex dynamics in the applied magnetic field.

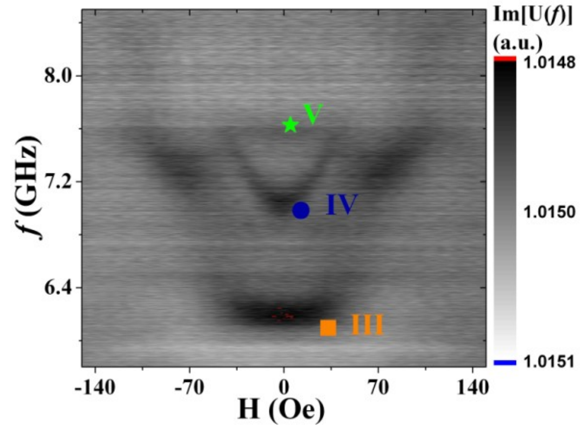

Figure 3.7 (c) Intensity plots of the measured spin wave spectra for magnetic field below the vortex nucleation field. The magnetic field is applied along [11] dot array lattice direction and is perpendicular to the RF field (h_{rf})

Figure 3.7 shows modes #III, IV, V intensity plots of the measured SW spectra for the magnetic field below the vortex nucleation field (β=0.04). The second doublet of the azimuthal modes (*n*=1, *m*=±1) indicated by green stars and blue circles shows reduced intensity in comparison with the first doublet due to existence of a node of the dynamic magnetization along the radial direction. We find that the lower azimuthal mode (*n*=1) frequency shows strong parabolic dependence, while the upper one is influenced weakly by the magnetic field. For the aspect ratios β=0.03 - 0.1 the frequency of the main radial mode (0, 0) is always close to the frequencies of the second azimuthal doublet (*n*=1, *m*=±1).

More detailed analysis of the mode #III,IV,V intensities (the azimuthal doublet modes should have almost equal intensities) shows that the mode #III is radial for the samples with β= 0.04, 0.048, 0.067, and 0.083, but the radial mode is the high frequency mode #V for the samples with β= 0.1. This means that the dependence of the radial mode frequency $\omega_{0,0}(\beta)$ vs. β has a higher slope than the similar dependencies for the azimuthal modes $\omega_{1,\pm1}(\beta)$ as we shall see in the next paragraph. There were just one single mode above the first frequency doublet for Py dots with β=0.03 and 0.05 (*L*=15 nm).

3.5.3 Dependence of spin wave modes on the aspect ratio

The main experimental findings as a function of dots aspect ratio are summarized in Figure 3.8. The results on (n=0, 1; m=±1) azimuthal eigenmode frequencies and their splitting (which will be detailed later) are in a good agreement with the calculated frequencies within a theoretical model (see dashed dotted lines in Figure 3.8).

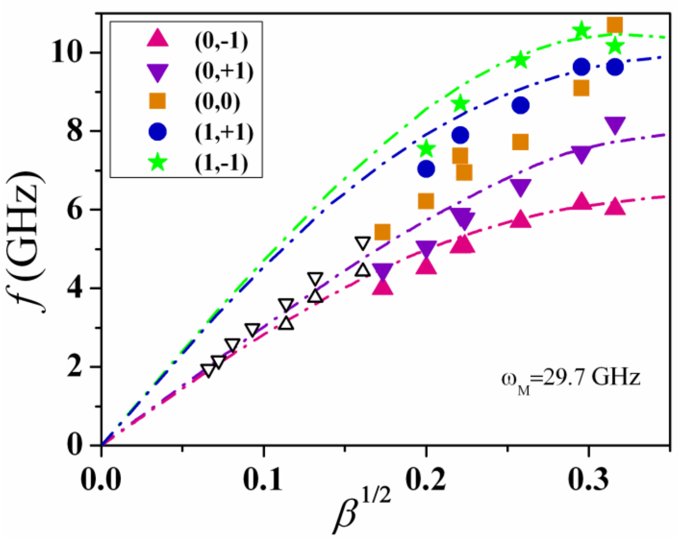

Figure 3.8 The measured spin wave mode frequencies vs. square root of the dot aspect ratio β. The dashed dotted line represents theoretical values described in the text. Open triangles show the lowest azimuthal mode frequencies from ref. [41] **measured for very thin dots with β < 0.03. All experimental data are taken for maximum interdot separation in the Py dot arrays.**

The details of the model will be described in the next paragraphs. The second doublet (n=1, m=±1) frequencies for the different aspect ratio and their splitting have been observed for the first time. In our broadband experiments the (n=1, m=±1) azimuthal modes were clearly detected only for samples with the dot thickness of 20, 25 and 50 nm. The presence of modes splitting proves the concept of the moving vortex interaction with all the azimuthal SWs (n=0, 1,...) having the same azimuthal symmetry (m=±1) as the vortex gyrotropic mode.

Figure 3.8 demonstrates that for β<0.05 the low frequency azimuthal modes (*n*=0, *m*=±1) follow predicted theoretically [31] and observed experimentally ~ $\beta^{1/2}$ dependence vs. β (the open triangles data in Figure 3.8 are taken from the Ref. [41]), whereas for β exceeding 0.05 both (*n*=0, *m*=±1) modes show downwards deviation from the linear dependence ~ $\beta^{1/2}$ mainly due to decreasing of the *z*-component of the dynamic magnetostatic field. We measured the dot arrays with different (random) core polarizations, so this sign has no direct physical sense, and is used just to number the azimuthal modes in the spectra.

We attribute small mismatch between present and previously measured for small β (<0.03) azimuthal mode frequencies (Figure 3.8) to differences in the saturation magnetization of Permalloy dot arrays. We note also that the lowest azimuthal eigenmode frequencies (*n*=0, *m*=±1) measured for the single value of β= 0.087 by Zhu et al.[142] are also in reasonably good agreement with the present VNA-FMR data.

3.5.4 Vortex modes splitting vs. dots aspect ratio

Figure 3.9 shows dependence of the measured and calculated frequency splitting of the first azimuthal mode on the dot aspect ratio.

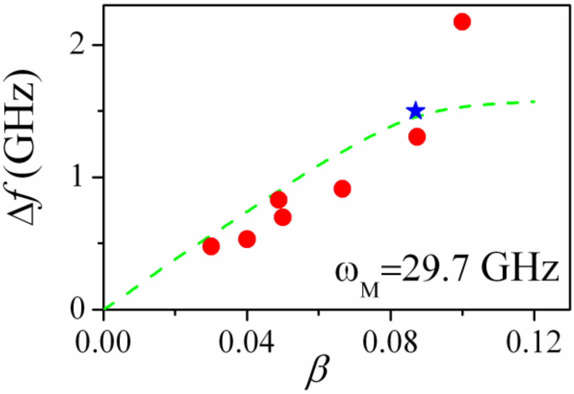

Figure 3.9 Measured splitting (solid circles) of the first azimuthal mode (*n* = 0, *m* = ±1, red and blue triangles in Figure 3.8). Blue star shows the lowest azimuthal mode splitting measured in Ref. [142] **. The dashed line represents theoretical values described in the text.**

The splitting of the first azimuthal mode (n=0, m=±1) shows nearly linear dependence on the dots aspect ratio almost in the all range of β studied; and in a good agreement with the calculated splitting within a theoretical model (dashed lines in Figure 3.9).

The theoretical model (the main contribution of K. Guslienko to ref. Awad et al. [147]), starts with considering the Landau-Lifshitz equation of motion:

$$\frac{M_s}{\gamma}\cdot\frac{\partial m}{\partial t}=m\times\frac{\partial w}{\partial m} \tag{3.1}$$

where w is the energy density $w=-\mathbf{M}\cdot\mathbf{H}_m/2$, $\mathbf{H}_m$ is the magnetostatic field. This equation of motion has this shape by introducing the reduced magnetization $\mathbf{m}(\mathbf{r},t)=\mathbf{M}(\mathbf{r},t)/M_s$, $\mathbf{m}^2=1$, and assumes that **m** does not depend on z-coordinate along the dot thickness. To find the vortex high-frequency modes, the linearized equations of motion of dynamic **m** over the vortex ground state $\mathbf{m}_0(\rho)$ are solved. They are linearized by the substitution $\mathbf{m}(\boldsymbol{\rho},t)=\mathbf{m}_0(\rho)+\boldsymbol{\mu}(\boldsymbol{\rho},t)$, where small $\boldsymbol{\mu}=(\mu_\rho,\mu_\varphi,\mu_z)$, $|\boldsymbol{\mu}|<<1$ corresponds to SW excitations, and ρ,φ are the polar coordinates. The $\boldsymbol{\mu}$-components are used in the form of waves $\mu_\rho(\boldsymbol{\rho},t)=b(\rho)\sin(m\varphi-\omega t)$, $\mu_z(\boldsymbol{\rho},t)=a(\rho)\cos(m\varphi-\omega t)$ travelling in azimuthal direction, where a, b are the SW amplitudes and $\mu_\varphi=0$. In zero-bias field case only the eigenmodes with m=±1 can be excited by uniform in-plane rf field. Neglecting the small dynamic exchange interaction the problem is reduced to eigenvalue problem for the integral magnetostatic operator [37]. The solution of this problem for a thin dot yields a discrete set of magnetostatic SW eigenfunctions $a_n(\rho)$, $b_n(\rho)$ and corresponding eigenfrequencies $\omega_{n,m}$, which are well above the gyrotropic mode eigenfrequency. The azimuthal SW modes with $m=\pm1$ have the same angular dependence as the vortex gyrotropic mode, and this leads to a considerable frequency splitting of the degenerated SW $m=\pm1$ modes due to moving vortex core Ref. [148].

The second azimuthal mode (n=1, m=±1) splitting reveals non monotonous behaviour with clear maximum for β around of 0.05 (see

Figure 3.10). Such behaviour is due to change of the SW mode radial profiles with increasing β.

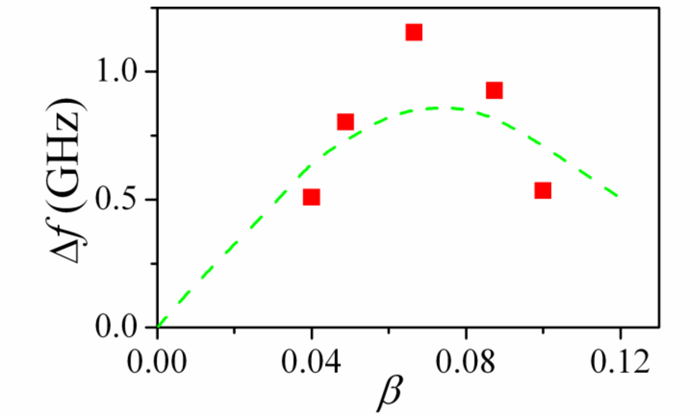

Figure 3.10 Second azimuthal doublet frequency splitting (*n* = 1, *m* = ±1, dark blue circles and green stars in Figure 3.8). The dashed line represents theoretical values described in the text.

Generalising the results of ref. [148] to the case of arbitrary radial index *n* of the azimuthal SW frequency (*m*=+1/-1), the splitting is calculated as using the overlapping integral of the vortex gyrotropic mode and the SW eigenmodes ω_{n1}, (for more details [147]).

The SW magnetostatic frequencies for $(|m|=1)$ are $\omega_{n1}^2 = \omega_M^2 F(L/R)$, where the function *F(β)* depends only on β and on the magnetization distribution of the *n*-eigenmode $\boldsymbol{\mu}_n(\boldsymbol{\rho})$, and $\omega_M = 4\pi\gamma M_S$. The function *F(β)* to a good approximation is linear in *β*=*L*/*R* and, therefore, we get the simple relations for the $\omega_{n1} \propto \beta^{1/2}$ and $\Delta\omega_{n,\pm1} \propto \beta$ at *β*<<1. The splitting of $m = \pm 1$ modes is a result of interaction of the high frequency SW with the moving vortex core. The calculation of the azimuthal SW frequencies allows to explain quantitatively the experimental data presented in Figure 3.9 for mode (*n*=0 and *m*=+1/-1) and in Figure 3.10 for the mode indexes (*n*= 1 and *m*=+1/-1). The frequency splitting for *n*=1 is approximately twice smaller than for *n*=0 azimuthal modes due to decrease of the overlapping integral of the vortex gyrotropic mode and the SW eigenmodes with increasing *n*.

The radial (*m*=0) mode frequencies can be described by the equation $\omega_{n0}^2 = \omega_M^2 f(\beta\alpha_{1n})$, where α_{1n} is the *n*-th root of the equation $J_1(x)=0$ the first order Bessel function [37]. The value of $\omega_M = 4\pi\gamma M_s$ =29.7 GHz was used to calculate the frequencies, which is an average of ω_M extracted from fitting the FMR spectra of the saturated dot arrays with different β.

3.5.5 Vortex dynamics in the applied in-plane magnetic field

In the previous paragraphs we have studied the spin waves excited in the ground state. Here we proceed to investigate the spin waves in the vortex state, being subject to the applied in plane magnetic field. The experiments (Figure 3.11 a,b) and simulations (Figure 3.11 c,d) of the spin dynamics in Py dots with thickness of 25 nm and diameter of 1035 nm were done by using either parallel ($\mathbf{h}_{\mathrm{rf}||}$) or perpendicular ($\mathbf{h}_{\mathrm{rf}\perp}$) rf drive and were carried out *with increasing bias field from zero to above annihilation field*. Similar results have been also obtained for other dot arrays with the aspect ratio thickness/radius (*L/R)* varying from 0.05 and 0.1 revealing ¨extra¨ higher frequency modes appearing in the measured spectral window for smaller *L/R*. The dynamic response remains qualitatively unaffected by the interdot dipole-dipole interaction with more than 2-fold change in the interdot distance ensuring that we observe a single dot eigenmodes. The influence of small dipolar coupling will be considered in detail in chapter V.

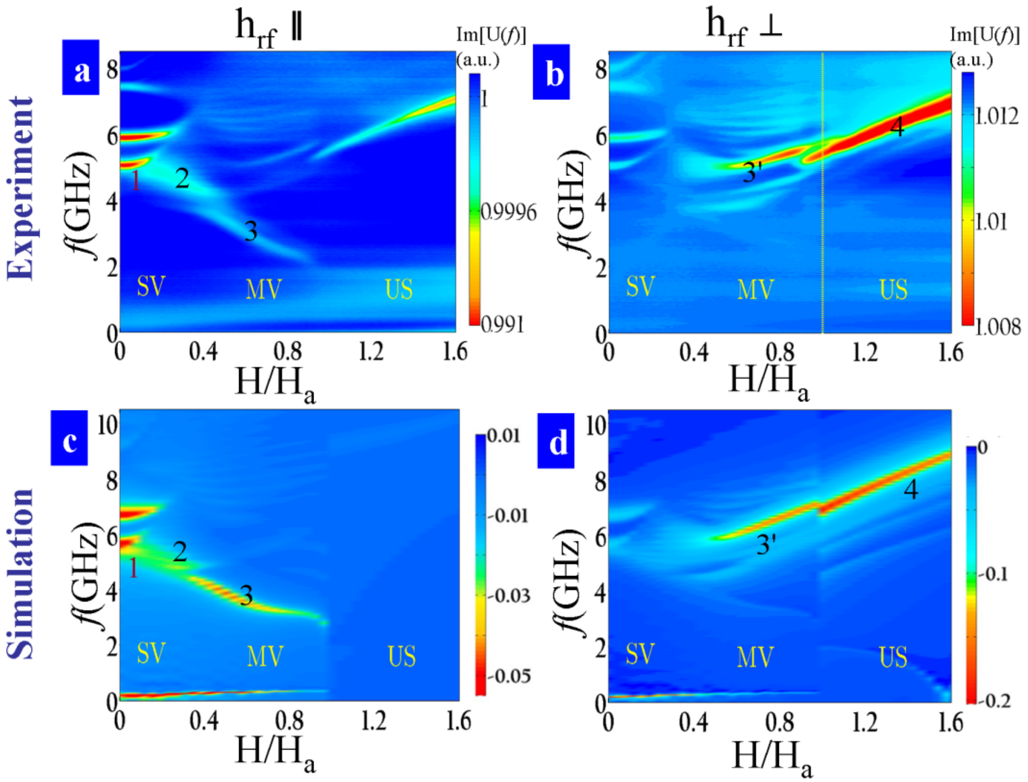

Figure 3.11 Intensity plots of the measured [a,b] and simulated [c,d] spin-wave spectra for the Py dot arrays with thickness 25 nm and 1035 nm diameter for the driving rf field (a,c) parallel and (b,d) perpendicular to the increasing bias magnetic field. Numbers 1, 2, 3, 3´, and 4 label the spin-wave eigenmodes discussed in the text.

Let us first discuss the experimental results (Figure 3.11 a, b). Applying the uniform rf field $\mathbf{h}_{rf}$ we excite only the spin eigenmodes localized in the areas where the torque $\mathbf{h} \times \mathbf{M}_0 \neq 0$ ($\mathbf{M}_0$ is the static magnetization).

In the small field regime $H<H_n$ (further- stable vortex SV) two doublets of the spin eigenmodes are observed with the eigen-frequencies being independent of the orientation of the rf field (see Figure 3.11 a, b). These low-field doublets can be described [148] as azimuthal spin waves with the indices ***n*=0, *m*=±1** indicated in Figure 3.11 as (1), and with the indices ***n*=0, *m*=0** and ***n*=1, *m*=±1**. The later modes have much lower intensity and will not be discussed in this paragraph. In accordance with recently developed model [148] of the dynamical vortex core – spin wave

interaction the zero-field splitting of the doublet eigenfrequencies is about 1GHz, as was mentioned earlier in this chapter.

We note that previous works [43], [44] described the data in terms of azimuthal spin wave modes with the indices (*n,m*) as unchanged between the cylindrical (zero field) and fully broken (near the vortex annihilation field) symmetries of the magnetization ground state. However, this assumption obviously has no sense from the symmetrical point of view, and interpretation of these modes and the mode indices should be corrected because the azimuthal modes cannot survive up to the vortex annihilation field. The spin wave eigenmodes (*n,m*) classification is strictly applicable to the zero-field case. The authors[43], [44] assumed that the modes keep their indices having sense only for cylindrical symmetry (H=0) for the entire field region, up to the annihilation field, H_a. However, our experiments show that the mode classification can be used only approximately up to $H \approx H_n$.

At small H one can excite the spin eigenmodes with indices m=0, ±2, whose intensities are proportional to H^2. The first mode is not observed in our simulations (see below), whereas the m=±2 (n=0) modes are responsible for the formation of the spin wave branch (2) observed with parallel pumping. We note that the spin wave mode localization discussed here is a result of the non-uniform ground state, whereas the mode localization at the dot edges discussed in Ref.[149] is due to a non-uniform internal field for quasi-uniformly magnetized dots. When the vortex core is sufficiently shifted from the centre of the disk (further strongly shifted ¨metastable¨ vortex, MV) the consideration of MV is taken just for formal notation. Indeed, there are two energy minima in the MV field region corresponding to shifted vortex and quasi-uniform magnetization states [150].

There is an essential area of the dot where the static magnetization $\mathbf{M}_0$ is parallel to the bias field $\mathbf{H}$. Here we specially underline the *fundamental importance of the parallel pumping* [151] *which excites only the modes localized close to the strongly shifted vortex core.* This is indeed contrary to the usually employed perpendicular pumping scheme, which provides a much broader spin wave spectrum because the microwave field is strongly coupled to different spin eigenmodes throughout the whole dot. This explains the importance of the parallel pumping to provide information on the spin wave modes localized near the vortex core (mode n.3). We observed that the “soft” mode (3) exists also only with parallel pumping when the vortex core is close to the dot edge at $H_n < H < H_a$.

Increasing the bias field with the perpendicular pumping also suppresses the azimuthal modes $|m|=1$ at $H>H_n$. The perpendicular pumping scheme in the strongly shifted vortex state provides a much broader (than parallel pumping) spin wave spectrum because the microwave driving field is strongly coupled to different modes throughout the sample. Increasing H with $\mathbf{h}_{rf\perp}$ reveals a crossover between three main field regions in the excitation spectra: from stable vortex (SV) state ($H<H_n$), where the eigenmodes classification is still applicable, to the strongly shifted (MV state) with a much broader spin wave spectrum and, finally, to the quasi-uniform or saturated state (US).

It is important to underline that *the parallel or perpendicular pumping field can excite fundamentally different spin modes in the MV state* ($H_n<H<H_a$). Indeed, the frequency of the localized near vortex core mode (3) observed for the MV with the $\mathbf{h}_{rf||}$ configuration (see Figure 3.11a,c) decreases with increasing magnetic field. In contrast, using $h_{rf\perp}$ in the MV state excites a dominant parabolic-like mode marked as (3′), accompanied by multiple satellites (Figure 3.11b,d), which transforms abruptly near the annihilation field H_a into the almost uniform precession mode (4) existing at $H>H_a$ in the US. Only edge modes are excited with the parallel pumping in US (Figure 3.11 b,d).

Figure 3.11 shows clearly other fundamental difference of the detected spectra for parallel (part a,c) and perpendicular (part b,d) rf excitations. While for the parallel excitation both the azimuthal modes merge close to the vortex nucleation field with a new mode (2) excited at the transition between the stable and metastable vortex states, the field dependence of the modes excited with perpendicular pumping is very different. One clearly sees a vertical zone presented in the dynamic response close to the vortex nucleation field, with no modes excited. Measurements conducted in this specific field range between the stable and metastable vortex states clearly show that the spin wave modes excited with perpendicular pumping in the MV state (like the mode 3′) do not represent a continuous transformation of those modes excited in the symmetrical (almost symmetrical) vortex ground state ($H<H_n$). We note that in Ref. [44] only 1 mode was found by VNA-FMR with

perpendicular pumping, and the indices (n=0, m=1, our notations) were assigned to it for the entire field region from zero to the field well above H_a, whereas we clearly established that there are at least 4 intensive azimuthal modes with the indices n=0, m=+1/-1,0 and n=1, m=+1/-1 having a significant frequency splitting. All the modes exist only below H_n.

An analysis of the linewidth of the spin wave modes presented in Figure 3.11 reveals that the lowest (n=0; m=±1) azimuthal modes observed in small magnetic fields are characterized by a relatively narrow linewidth of about 250±50 MHz, being almost field independent in the SV state. The observed linewidth for both the pumping schemes is close to the one measured in the uniform state near the border between the MV and US states. The spin wave modes (2), (3) and (3`) detected in the MV state are characterized, however, by much a broader linewidth of about 800±300 MHz, with the error bar attributed to weaker signals. The mode (2) linewidth reveals a maximum at H_n (parallel pumping), whereas the mode (3′) linewidth reaches its maximum values just below H_{an}. We note that qualitatively different results were reported in ref [44] for perpendicular pumping, where the sharp maximum in the VNA-FMR linewidth of the single observed mode (interpreted as the first azimuthal mode with n=0, m=1) as a function of magnetic field was observed between H_n and H_{an} in the vortex state and was attributed to possible variations in the dots dimensions and to the integrative nature of the VNA-FMR technique.

- ## Micromagnetic simulations

To understand in details the excited spin eigenmodes in the frequency domain at a given bias field, we analyze the conducted[**] micromagnetic simulations by applying the field to the vortex-state dot along the x-direction in the range from 0 to 1000 Oe with steps of 20 Oe. Our numerical results provide an annihilation field of 500 Oe. The difference with the experimentally measured value could be due to the weak dipolar

---

[**] The simulation is made in collaboration with the group of prof. Kim, Seoul National University, South Korea.

coupling between the dots and to the fact that the simulations are done at T=0 K. Both the $\mathbf{h}_{\mathrm{rf}||}$ and $\mathbf{h}_{\mathrm{rf}\perp}$ pumping schemes were explored by applying a sine-field of variable frequency and with amplitude of 1 Oe. Figure 3.11 shows also the simulated Fourier power spectra in a wide frequency range as a function of the bias field normalized by H_a for parallel (part c) and perpendicular (part d) pumping schemes, which are in rather good agreement with experiments (Figure 3.11 a,b).

As we have mentioned earlier, we attribute the small (<10%) disagreement between the experimental and simulated spin eigenmodes to:

(i) An influence of the interdot dipolar interaction (will be studied further in details in chapter V).
(ii) The presence of a small out-of-plane rf component (see Methods in chapter 2).
(iii) to the thin (about 2 nm) Py oxide layer[152], which influences the dot thickness and therefore the spin eigenfrequencies [37].

- **Vortex spin wave modes profiles**

Below we discuss in detail the simulated spatial distributions of the dynamic magnetization in the parallel ($\Delta M_x/M_s$) and the perpendicular ($\Delta M_y/M_s$) pumping schemes for the most intensive excited modes (marked as 1-4 in Figure 3.11) at some specific frequencies and normalized fields. We selected the frequency/field points, where splitting of the eigenfrequencies occurs at each frequency branch.

- ## Mode 1

The lowest (n=0, m=+1) azimuthal mode (1) is observed in zero bias field, as seen from Figure 3.12. The sign is positive as the mode is rotating counter clockwise CCW taking into account a vortex with positive core polarization.

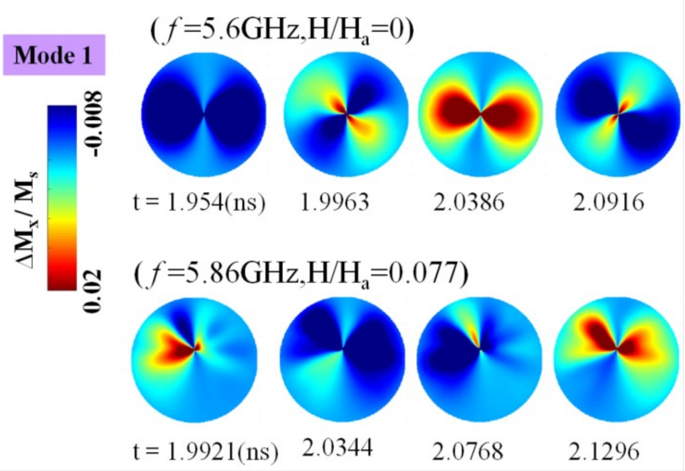

Figure 3.12 Simulated spatial distributions of the magnetization component $\Delta M_x/M_s$ (in the form of time sequences with the step of about ¼ oscillation period) of the vortex dynamic in the SV with parallel pumping for mode 1 in Fig. 3.11. The number in brackets (f, H/H_a) shows the eigenmode frequency, and the normalized magnetic bias field.

The application of a weak field (e.g., H/H_a=0.077) smoothly breaks the vortex state cylindrical symmetry but maintains the character of the mode (1).

- **Mode 2**

As pointed above, the mode (2), splitting out from the lowest azimuthal mode has *a qualitatively new character* described approximately as a superposition of the azimuthal spin wave modes $m=\pm2$ rotating around the vortex-core in the opposite directions (clockwise, CW and counter-clockwise, CCW).

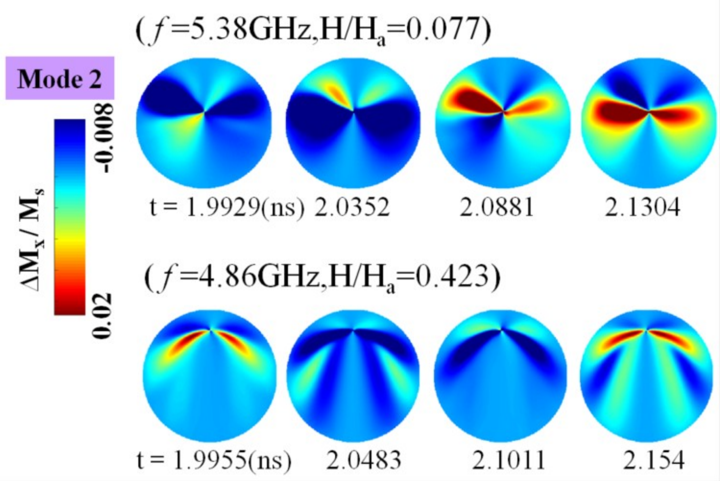

Figure 3.13 Simulated $\Delta M_x/M_s$ for mode (2) for parallel pumping (in the form of time sequences with the step of about ¼ oscillation period) spatial distributions of the vortex dynamic magnetization in the SV region.

Given the vortex core shift in the positive *y*-direction, the modes start from the positive *y* semi-axis, propagate, meet each other and disappear at the negative *y* semi-axis. When the bias field is further increased (4.86 GHz, H/H_a=0.423), the mode (2) also shows a similar qualitatively new motion but with more nodes in the disturbed azimuthal direction (Figure 3.13).

We can distinguish two different regions in the dynamical ***M***-images. In the first one, close to the vortex core, there is a superposition of the CCW and CW motions. In the second region (far from the vortex core, the lower part of the dot) *standing-like spin wave modes dominate* (Figure 3.13, mode 2, $f=\omega/2\pi$=4.86 GHz). The increase of the bias field expands the second region.

- **Mode 3**

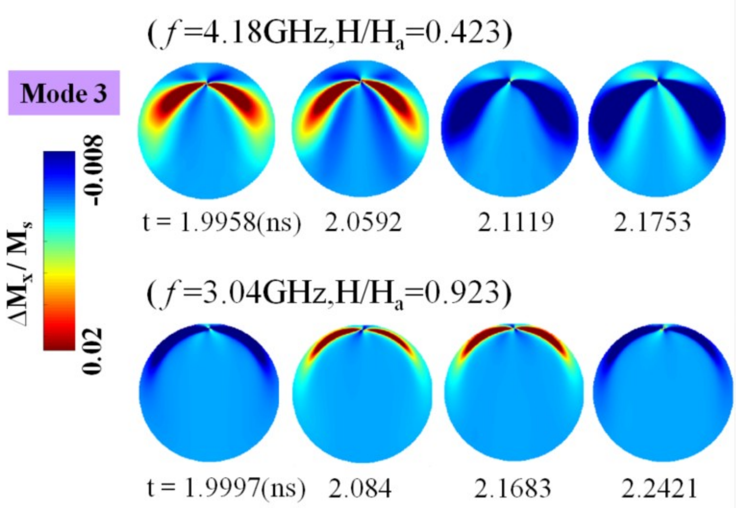

Figure 3.14 Simulated spatial distributions of the vortex dynamic magnetization in the MV region $\Delta M_x/M_s$ for mode (3) for parallel pumping (in the form of time sequences with the step of about ¼ oscillation period).

In the MV range one can see that there is a clear standing whisker-like dominating pattern for the lower frequency mode (mode (3), 4.18 GHz, MV). These modes are localized near the deformed vortex core (where the static magnetization component M_y has a significant value) and the reduced area occupied by the modes gradually decreases with increasing of the bias field (compare the images for H/H_a=0.423 and 0.923 in Figure 3.14). This spin mode (3) can be approximately described for low fields (just around H_n) as having a wave vector along the bias field **H** (analogy to the backward volume magnetostatic spin waves in continuous films) because the nodal planes are perpendicular to the *x*-direction.

- **Mode 3’**

When one applies the perpendicular drive, the response in the low field region (SV) is the same as in the parallel case. In the MV region the high frequency mode (3′) is more intensively excited compared to the parallel pumping case (the mode (3)). The mode (3′) is localized mainly outside the vortex core in the domain magnetized parallel to the bias field. In general, the mode (3′) dynamic **M**-images are similar to those observed for the mode (3) for weaker fields in the MV state (5.84 GHz, 0.423), but become more complicated close to the boundary with the US increasing the bias field (6.88 GHz, 0.923).

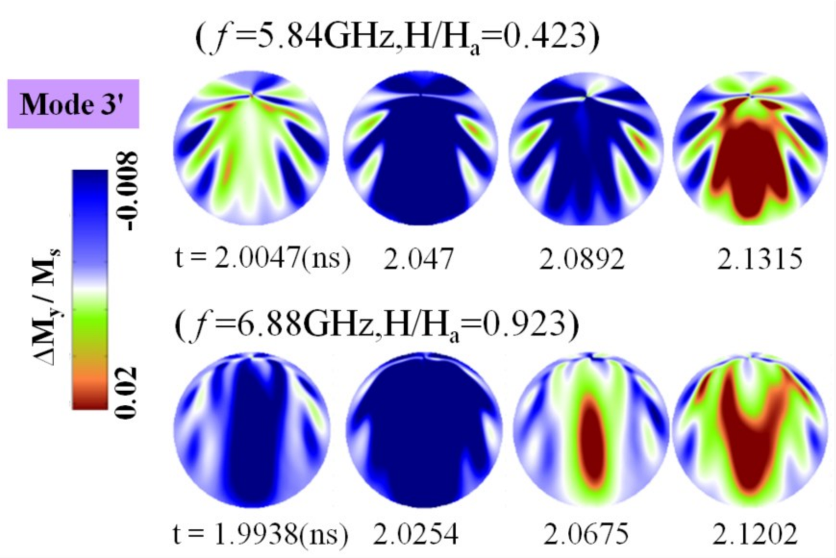

Figure 3.15 Simulated spatial distributions of the vortex dynamic magnetization in the MV region $\Delta M_y/M_s$ for mode (3′) excited with perpendicular pumping (in the form of time sequences with the step of about ¼ oscillation period).

- **Mode 4**

We note that the transition to the US regime suppresses abruptly the (3)-mode, but the quasi-uniform Kittel-like mode (4) is a continuation of the (3′)-mode, not of the (n=0, m=1) azimuthal mode as stated in Ref.[44].

3.5.6 Summary & perspectives

By extensive dynamic measurements and simulations we have investigated the spin wave response of the vortex ground state. The main SW eigenmodes could be detected in the VNA-FMR. For dots with moderated aspect ratio the first and the second azimuthal mode are clearly detected and the splitting has been studied. The SW study of the shifted magnetic vortex state in the 3D-plots has also been investigated as a function of in-plane magnetic field, providing a clear frame for unambiguous identification of the spin wave excitation spectrum.

We show that independently of *rf* pumping orientation the azimuthal modes survive only below vortex nucleation field. With parallel rf pumping we identify new unexpected eigenmode in the weakly shifted vortex state and new recently predicted localized near strongly shifted vortex core spin wave mode [151]. With perpendicular pumping, which excites modes in the whole Py dot, we clearly observe crossover in the spin wave dynamics of the shifted vortex near the vortex nucleation field.

The main finding of this chapter, however, is not just the observation of the differences between spin wave modes excited with the parallel and perpendicular pumping schemes, but also that these modes transform in a fundamentally different way, when the magnetic vortex is displaced by the in-plane bias field. Our results are important for understanding the dynamics in different vortex systems in confined biased conditions, e.g., in arrays of vortex nano-oscillators excited by a spin-polarized current[153].

3.6 Conclusions:

In Conclusion, the main SW eigenmodes namely the first and the second azimuthal mode, for dots with moderated aspect ratio, and their splitting are in a good agreement with the theoretical model accounting the hybridization of the SW modes with the gyrotropic mode. The second azimuthal mode shows a maximum of splitting as function of the dot´s aspect ratio. We found that spin wave eigenmodes (*n,m*) classification based on the number of nodes in radial and azimuthal directions could be applicable to the vortex shifted by magnetic field, but only below the vortex nucleation field. Microwave excitation in different directions with respect to the bias field reveals unique information on spin wave dynamics in the strongly shifted vortex state, particularly on the modes localized near the vortex core.

The perpendicular and parallel excitation schemes do not just reflect the coupling of rf field to the different modes, but what is more critical, the excited spin wave mode frequencies vary in qualitatively different way as the vortex is shifted from the dot centre to the dot edge for the parallel and perpendicular excitations. The new insights into the spin wave dynamics in the magnetic vortex state presented above can be summarized as follows. We supply an experimental proof that the main azimuthal modes (with the indices $m=\pm 1$) exist only in low fields, below the vortex nucleation field H_n. We also present the first observation of a new spin mode of the shifted vortex observed by using parallel pumping (the mode 2). This mode splits out from the lowest azimuthal mode (with $m=+1$) and *has a qualitatively new character* described approximately as a superposition of the azimuthal modes with the indices $m=\pm 2$ rotating around the vortex core in the opposite directions. Furthermore, the high-field soft mode (3) localized near the vortex core for parallel pumping was observed for the first time. This mode (3) can be approximately described as having a wave vector along the bias field and is stable up to H_a. Finally, we present the first observation of the fundamental differences in the field dependence of spin wave modes excited with *perpendicular* (abrupt change between the SV and MV regions, broad spin wave response in the MV state) and *parallel* (the spin wave spectrum more continuously transforms, a single localized mode in the MV state) pumping.

We enumerate new observations presented in this chapter:

1) We present the main SW eigenmodes, the first and the second azimuthal and the first radial SW modes dependence on the dot aspect ratio in moderated range (0.03 - 0.1).
2) We verify that the observed splitting of the degenerated azimuthal doublets ($n=0,1$, $m=\pm 1$) is in good agreement with the model of the magnetostatic modes in the vortex state dots that takes into account dynamical origin of the azimuthal modes frequency splitting.
3) We show that contrary to the previously reported results [43], [44], the spin wave modes with azimuthal symmetry (having non-zero azimuthal indices m) do not survive up to the vortex annihilation field. They transform to fundamentally new spin wave modes, when the bias magnetic field shifts the vortex core from the dot centre.

4) We identify for the first time a fundamentally new spin wave mode localized near the shifted vortex core (mode 3) in relatively high magnetic fields.

5) We present the first observation of fundamental differences in the field dependences of the spin wave spectra excited with perpendicular and parallel pumping.

CHAPTER IV: DYNAMICS OF THE METASTABLE DOUBLE VORTEX STATE IN PY DOT

Introduction and motivation:

Vortex forms are found in a variety of physical systems, ranging from superfluids and superconductors to tornadoes. Special interest in the confined magnetic vortices is inspired by the possibility of excitation or switching of the vortex core [146], [154] which has been suggested as a potential new road to the creation of nanoscale memory and spin torque vortex oscillators [155]. To achieve the possibility of implementing those spin torque oscillators in applications it has been shown that synchronization offers substantially improved power [153]. Vortex based oscillators already have improved power and synchronization of multiple vortices through the mediation of antivortices is possible way of lock-in the vortices oscillation [156].

In spite of the important potential applications of magnetic vortex, very little is known about spin dynamics in its higher energy (metastable) states. In fact, just preliminary reports have been published on the observation of double vortex [further double metastable vortex-DMV] in either circular or elliptic shape [47], [51],[63], [157] dots. Spin wave excitation in such system remain unknown.

Circular dots provide a unique opportunity to investigate the spin wave dynamics of both the DMV and single vortex (SV) configurations by reducing or increasing the external magnetic field below or above the vortex nucleation field, H_n. In this system, the vortex cores can be pinned by microstructure related defects, intergrain boundaries, etc.[158], thereby trapping the system in the metastable DMV state. Provided the perturbation is small enough, the dot can stay in its metastable state for at least the duration of the measurements. In addition to the application interest, the DMV presents a model experimental system for the study of interacting solitons, in which each vortex being a topological soliton.

In this Chapter we will describe our investigation of the magnetization dynamics in circular Py dots with DMV presented in the form of a two spatially separated magnetic vortices interconnected by domain walls (DWs). We create this metastable state in the dots with reduced thickness and by sweeping magnetic field downwards from saturation.

4.1 Samples, experimental setup and simulations

Investigated dots were the same used and explained in the previous chapter. Circular Py dots with thicknesses *L*= 50, 25, 20 and 15 nm with diameter 2*R* = 1035 nm and 20 nm thick dots with 2*R*=570 nm. The micromagnetic simulations were carried out also using OOMMF code [159] for circular Py dots with a diameter of 1035 nm and thickness of 20 nm, with simulated cell size 5 x 5 x 20 nm^3, $\gamma/2\pi$ = 2.96 MHz/Oe, the exchange stiffness constant A = 1.4 x 10^{-11} J/m, and the Gilbert damping constant α = 0.01. The excited spin waves have been studied at room temperature by broadband spectrometer based on vector network analyzer (see Methods). The parallel pumping scheme was used, ($\mathbf{h}_{\mathrm{rf}||}$) with $\mathbf{H}_{\mathrm{bias}}$ || **x** . This configurations was previously explained in Methods chapter. For the experimental sketch we refere also to the previous chapter.

We excite the dots by applying small (0.14 Oe) in-plane driving fields created by a co-planar waveguide (CWG), parallel to the magnetic bias field (see the coordinate system XYZ and corresponding indications in the previous chapter Figure 3.2). This technique ensures small precession amplitudes of the magnetization around the effective field. In this experimental scheme, the rf drive field excites mainly small in-plane deviations (ΔM_X; ΔM_Y) of non-uniform in-plane magnetization M; Small out-of-plane rf field component, created in the waveguide due to finite size of the central conductor (see also sketch in Methods indicating the directions of the CWG and the exciting magnetic field), could also excite the perpendicular to the dot plane magnetization component ΔM_Z. The data was analyzed on the basis of the transmission model, under the assumption that the dominant CWG mode is TEM mode and by neglecting the effect of reflection (see Methods, Figure 2.9).

4.2 Double vortex dynamics

4.2.1 Brief review

As explained in the introduction, the nanodisk could have remanent magnetization in the DMV state. Decreasing the external magnetic field from saturation, circular nanomagnets are known to have two intermediate metastable states: the so-called S-state and the double magnetic vortex (DMV) [47]. Recent reports show that circular magnetic dots with reduced thickness, and therefore enhanced pinning, may accommodate the DMV as a long-living state. This state contains two magnetic vortices connected via a domain wall (DW) to edge localized half-antivortices (AV)[47], [48], [51], [160]. As for the single magnetic vortex (SV) state in confined geometry, its first observation already revealed the coexistence of a SV and domain walls (DW), which connect the SV with the vertices of a triangular nanomagnet[161].

It is now well established that *coexisting vortex-DW configurations* are formed in the ground states of magnetic rectangles, triangles or ellipses [157], [161–164], before the single-domain state appears upon decreasing the particle size[162]. Although excitations of the confined DW or SV states are well understood [29], [36], [165–167], the nature of the *spin waves excited in nanomagnets involving both vortices and domain walls* remains unclear.

4.2.2 Objectives

As we could see from the Introduction chapter and the review paragraph, despite of a huge current interest in magnetic vortex, there is little understanding concerning the metastable states especially the double vortex state and the spin waves excited in a strongly coupled double vortex magnetic state. This unexplored regime, however, has not just great importance for potential applications in spintronics; but also is of fundamental interest, particularly due to excitation of coupled solitons (vortex cores) and coupled vortex-domain wall excitations. We shall explore the region and the parameters where we can find this metastable and shall try to find the possible coupled oscillation of the vortices and the interconnecting DW between them as well as study the excitation of this state at high frequencies.

4.3 Results

4.3.1 Double vortex state

- **Magnetization vs. field and dot thickness:**

Static magnetization hysteresis loops of all Py dots arrays were measured at room temperature by using a SQUID magnetometer. The measurements were done by saturating the samples by an in-plane magnetic field of 1500 Oe and measuring the magnetization between -1500 and 1500 Oe with steps of 1 Oe (see Figure 4.1). The analysis of the normalised room temperature remanence of the studied dots shows that $M(0)/M_S$ increases rapidly below 20-25 nm, as can be seen in the Figure 4.1a. This is an indirect indication of the possible change of the magnetic groud state of the dots. While for single vortex ground state the remanence magnetization is expected to be small, the finite values of the remanent magnetization observed for thinnest dots indicate either a shifted out of center single vortex state or other metastable (S or DMV) states.

Further we analyse changes in the vortex nucleation and annihilation processes with dot thickness. We define the nucleation field (H_n) as the magnetic field value at which the Py dots leave the saturated state with decreasing magnetic field by nucleating either a single or a double vortex. Correspondingly, we define the annihilation (H_a) field value as the magnetic field at which the Py dots return to the saturated state.

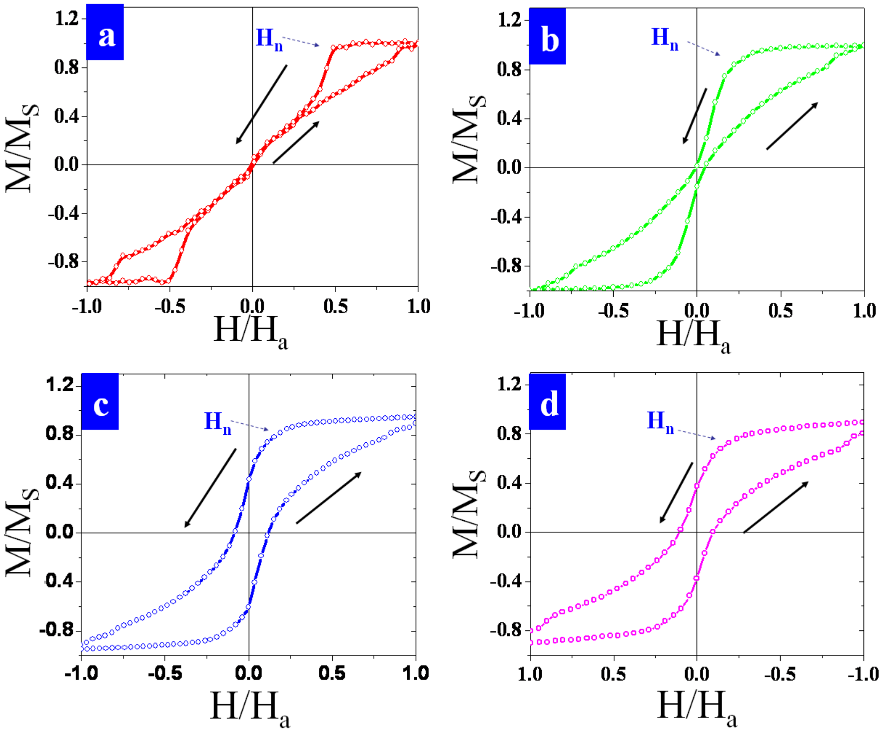

Figure 4.1 Hysteresis loops for the Py dot, a,b,c,d present the magnetization loops for dots with 1000nm diameter and 50, 25, 20 and 15nm thickness respectively. The fields are normalized by their respective vortex annihilation field H_a.

Both the nucleation and annihilation fields decrease with the dots thickness as shown in Figure 4.2b, most probably due to reduction of the corresponding energy barriers. Interestingly, while H_n weakly changes with decreasing thickness below 25 nm, the annihilation field is much stronger dependent on thickness. This could be an indirect indication of the nucleation of some metastable vortex state and the annihilation from the vortex ground state.

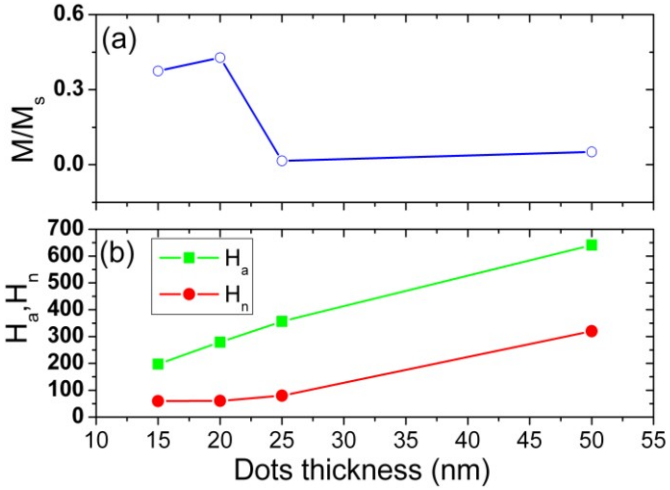

Figure 4.2 (a) Remanent magnetization and b) vortex nucleation and annihilation fields as a function of Py dots thickness. (diameter 1000nm).

- ## Metastable states during relaxation of magnetization: simulations

The simulations (with the participation of the Master student Dennis Dieleman) were performed using an extension [168] on the original OOMMF code [159] that augments to the LLG equation a highly irregular fluctuating field, so the resulting equation is a stochastic differential equation of the Langevin type[169]. The micromagnetic simulations were carried out for circular Py dots with a diameter of 1035nm and thickness of 25nm and 20nm, with simulated cell sizes of 5 x 5 x 25nm^3 and 5 x 5 x 20nm^3, respectively, $\alpha = 0.5$, $\gamma/2\pi = 2.96$ MHz/Oe, the exchange stiffness constant A = 1.4 x 10^{-11} J/m.

We first saturate the dot, using an in-plane field of 1000 Oe. After releasing the field in one step to zero, in agreement with [47], the dot relaxes by means of two clearly defined steps that have a slope of energy vs. time of almost zero (Figure 4.3). These steps are two metastable magnetic states which we identify as first the S-state and afterwards the DMV state. For our simulations these states remain stable for about 10 ns only. This can be attributed to the fact that we neglected the local magnetic anisotropy and all the defects and imperfections that the real samples usually have. To break the deterministic characteristic of OOMMF, we used a different set of random fluctuation for each run that we made, as can be seen in Figure 4.3.

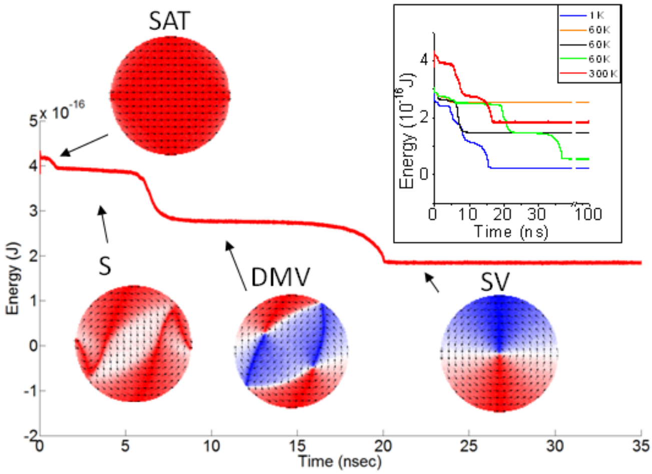

Figure 4.3 Total energy as a function of time at T=300K after the 1000 Oe saturation field is turned off abruptly. After saturation, three different levels can clearly be distinguished corresponding to the S-state and the DMV state respectively as indicated by the snapshots of the magnetization at the indicated time, with a colour coding for M_x. (dot: 1035x25nm at 300K). The inset shows different runs of the same simulation, using a different temperature and different random fluctuations. The line in black shows a run where the DMV remains stable for the duration of the simulation.

• Vortex core size vs. dots thickness

As can be seen in Figure 4.4, in agreement with analytical approach [170], the vortex core sizes decrease with decreasing dot thicknesses. This makes the core in thinner dots to be more susceptible to pinning and thus may lead to stabilize metastable state. The stability of the metastable state in defect-free magnetic devices is mainly determined by energy barriers between topologically different magnetic states. In the real dots, pinning of the vortex cores [171] is an additional factor that prevents the system from attaining the ground state. In our Py dots with a grain size around 4 nm and surface roughness below 1 nm, as estimated from transmission electron microscopy. The strong pinning implies that the vortex core size is less than the typical local energy variation scale, the sources of pinning may include magnetostatic coupling of local magnetization at grain boundaries, interface strain, dislocations, and random local grain related anisotropies.

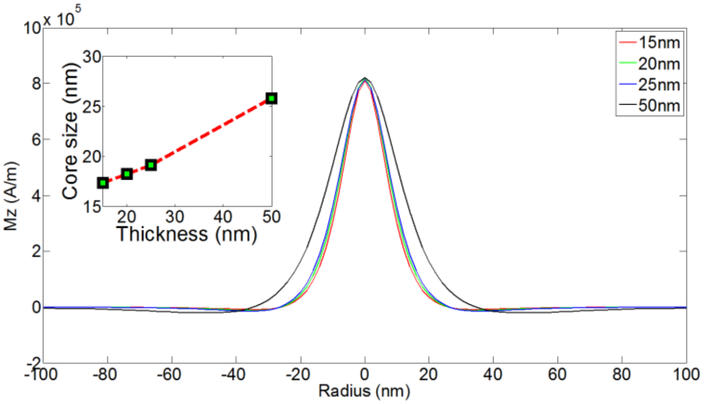

Figure 4.4 Numerically calculated variation of the cortex core size with dots thickness t (diameter 1036nm, cell size 2x2xt nm^3).

- **MFM measurements and simulations:**

VFMFM (Variable Field Magnetic Force Microscopy)[172] was used [††] to characterize the magnetic state of one of the measured samples, namely the 20nm thick Py dots, in remanence state and under an externally applied magnetic field. As we have seen, the static magnetization results (Figure 4.1,Figure 4.2) suggest formation of metastable DMV ground state at zero field in these dots. The MFM images have been obtained after the application of an in-plane field which is about two times bigger than the saturation field [173].

MFM microscopy is (especially given the sensitive nature of the metastable states) quite an invasive technique. The images obtained in this way reveal that the experimentally observed magnetic configuration depends on the type of magnetic tip used. The low moment commercial tip (Nanosensors PPP-LM-MFMR) seems to modify the magnetic state of the dots substantially because it always provides single vortex images (see Figure 4.5a).

[††] Done by A.Asenjo group [ICMM-CSIC- Madrid, Spain.]

A homemade tip with lower magnetic moment however, reveals the characteristic of the DMV state in its images (Figure 4.5b,c). Some of the images even reveal jumps between the DMV and single vortex states during the scanning process, demonstrating the influence of the tip on the metastability of the states (see Figure 4.5b which shows second scan of the marked in blue area). With sufficiently large external magnetic field (180 Oe) the shifted single vortex state is observed (Figure 4.5d). The fact that vortices shift in the opposite directions implies their opposite chirality.

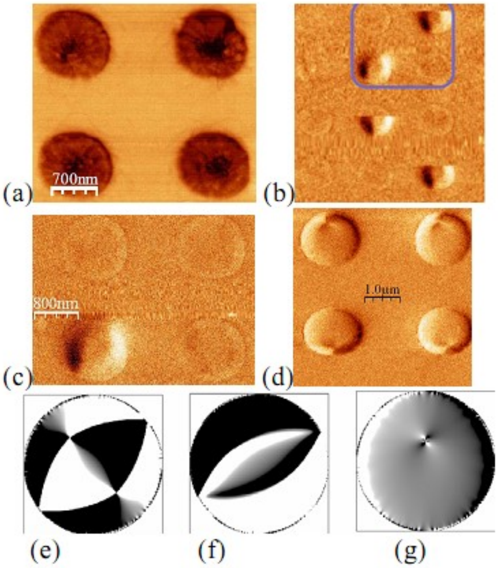

Figure 4.5 MFM images in zero field with commercial tip (a), with low magntic moment tip (b,c). Part (d) shows images of the shifted vortex in the field of 180 Oe. Parts (e-g) present correspondingly simulated (within approach[174], **in the absence of tip field) MFM images for DMV, S and shifted single vortex states.**

Figure 4.5e-f show simulated MFM images of the DMV (part e), S (part f) and shifted single vortex states which (in the absence of magnetic tip) are expected to depend on divergence of the magnetization[174]. The observed metastable states which are affected by the MFM imaging (parts b,c), more closely resemble DMV states than S- states [173].

Summarizing the static part; the presented experimental data reveal fundamental change in the ground state of Py dots with decreasing thickness starting from and below 25nm. Micromagnetic simulations and MFM images indicate that the new remanent state in which the thinnest Py dots remain blocked at zero magnetic field, is the double vortex metastable state. While in micromagnetic simulations the DMV state survives only on the nanosecond time scale unless imperfections in the form of random fluctuations are included, the experiments, in accordance with previous observations[47], [48], [160], indicate that the metastable double vortex state is stabilized at room temperature through vortex core pinning by spatial fluctuations of the local pinning potential [158].

As long as the vortex core size decreases with decreasing dots thickness [170], the enhanced vortex pinning in Py dots with thickness below 25 nm could be understood as a transition between the situation where the vortex core exceeds the typical size of the pinning centers (vortex delocalized) to the situation where the vortex core is smaller than the pinning size (localized vortex core and pinned metastable DMV state).

4.3.2 Double magnetic vortex dynamics

- **Measurements of the spin wave spectra**

In the experiments we have investigated the evolution of the broadband dynamic response of the dot as a function of a slowly (in steps of about 5 Oe) changed in-plane magnetic field. We first saturate the sample by applying a positive field that is two times larger than the positive vortex annihilation field (H_a). Subsequently we sweep the field downwards through vortex nucleation field (H_n) and after changing the field polarity we end above the negative vortex annihilation field.

The microwave field drive parallel to the external bias field, with an amplitude in several thousand times smaller than H_a, mainly couples to DW where the exchange energy is the highest. This permits precise detection of possible localized excitations in the DW[143] .

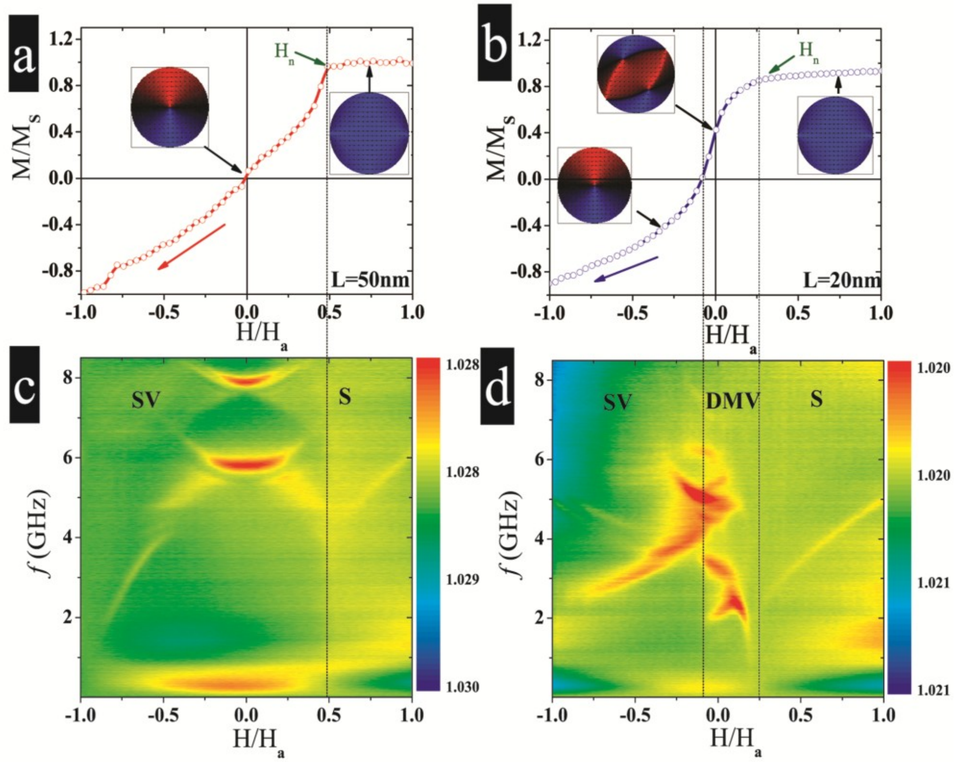

Figure 4.6 The figures (a,b) show the static magnetization of the Py dots with 1000 nm diameter and thicknesses of 50 and 20 nm respectively measured by sweeping field from H$_a$ to –H$_a$. Parts (c,d) show intensity plots of the measured spin excitation spectra for the Py dot arrays with the bias field swept down from saturation and the driving field applied parallel to the bias field. Magnetic field is normalized by the vortex annihilation field H_a. The vortex nucleation fields are marked as H_n, inserts and vertical lines indicate the saturated (SAT), DMV and SV magnetic states.

Figure 4.6 compares the static magnetization and dynamic response for dots with thicknesses L=50 nm (left) and 20 nm (right). The spin wave resonances in 50 nm thick dots for bias fields below vortex nucleation field $|H_n|$ correspond to the azimuthal modes [127], [147] and are symmetric with respect to the field direction, as expected for the single vortex SV state (Figure 4.6a,c). However, this low field response drastically changes for the Py dots with smaller L. Starting from 25 nm thick dots, the magnetization dynamics becomes asymmetric at low fields (Figure 4.6d). Besides, we find for a parallel excitation field and for bias fields just below H_n, additional peaks with frequencies between 2 and 5

GHz, which are lower than the first azimuthal mode frequency of the SV state, but much higher than the vortex gyrotropic frequency [157]. We claim that these unexpected modes originate from another, intermediate state. Namely, we believe that the Py dots in the array are in a metastable DMV state in the field interval indicated by vertical dashed lines in Figure 4.6. This metastable state is stabilized (as mention in the previous paragraphs) due to the reduction of the vortex core size and a decrease in the dot's thickness, accompanied by the enhancement of the effective damping. Existence of metastable DMV state is in agreement with previous measurements [47], [48], [51], [160].

Our broadband measurements reveal generally similar spin wave response for different Py dots with diameter of 1000nm and thicknesses below 25nm, as illustrated in Figure 4.7. Qualitatively similar results were obtained for the Py dots with diameter of 600 nm and thickness of 20 nm.

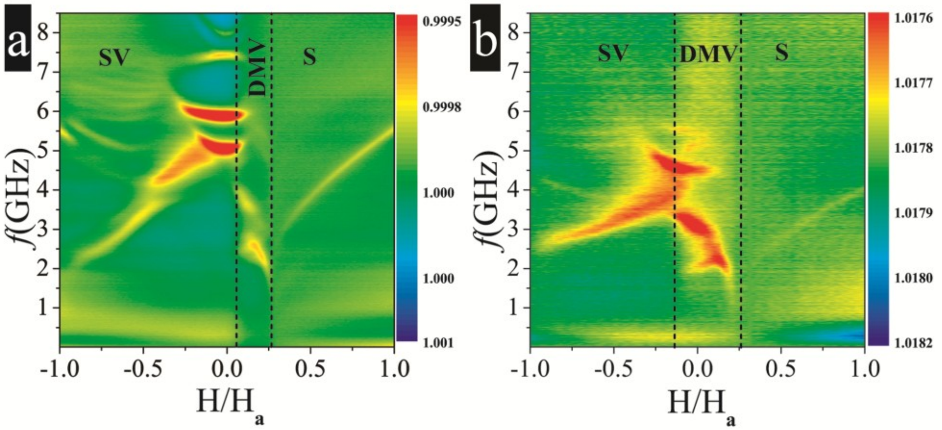

Figure 4.7 (a,b) Intensity plots of the spin-wave spectra for the for 25 (a) and 15nm (b) thick dots Py dots with a diameter of 1035 nm. The magnetic field is reduced from positive to negative values and the RF field is applied parallel to the external magnetic field.

• Long term stability of the DMV state

Once the DMV is nucleated in the dots, the measurements below the nucleation field show that the DMV can be captured and moved forwards and backwards. Below we show that the DMV state can be investigated for a long time (at least **a** few days).

Figure 4.8 shows the response, starting after nucleation the DMV. Once we have captured the DMV state, we sweep the fields within the different minor loop increasing its amplitude, namely between 50 Oe and 0 Oe (Figure 4.8a), 50 and -10 Oe (Figure 4.8b) and between 50 and -20 Oe (Figure 4.8c) for a huge number of field cycles (>200, about 24 hours). The obtained average response shows the characteristics of the DMV for the loops that sweep field down to 0 or -10 Oe. Going further down to -20 Oe, changes the dots ground state. The dots magnetization falls in the single vortex state and the spin wave response corresponds then to the azimuthal modes excited in the SV state. This results demonstrate the tenability of the DMV state and possibility to investigate its dynamics once the external drive is small.

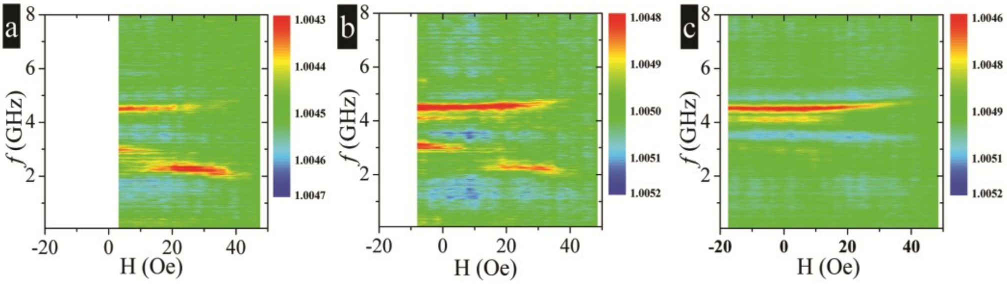

Figure 4.8 (a,b,c) Intensity plots of the measured spin-wave spectra for the 1035 nm Py dot of the 15nm thickness, with the field swept down from 50Oe to (a) 0 Oe, (b) -10 Oe and (c) -20 Oe for multiple measurements (cycles >200). The RF fields are applied parallel to the magnetic field.

- ## Identification of the eigenmodes

In order to investigate the excitation of the metastable states of the dots, we performed micromagnetic simulations. To excite magnetization dynamics, a variable driving field (Gaussian field pulse) with the amplitude of 1 Oe and FWHM of 1 ps was applied. We perform local Fourier transforms over all simulation cells and average these spectra to obtain the spin eigenfrequencies.

To identify the measured asymmetric eigenmodes in (Figure 4.6d); we make a comparison of the calculated spin excitation spectra for different metastable (S or DMV) states with the experimental results. The comparison of the dynamic simulations for the S-type and DMV states with experimental data reveals that the spin wave modes excited between the positive H_n and small negative bias fields are much closer to those expected for the DMV state (Figure 4.9).

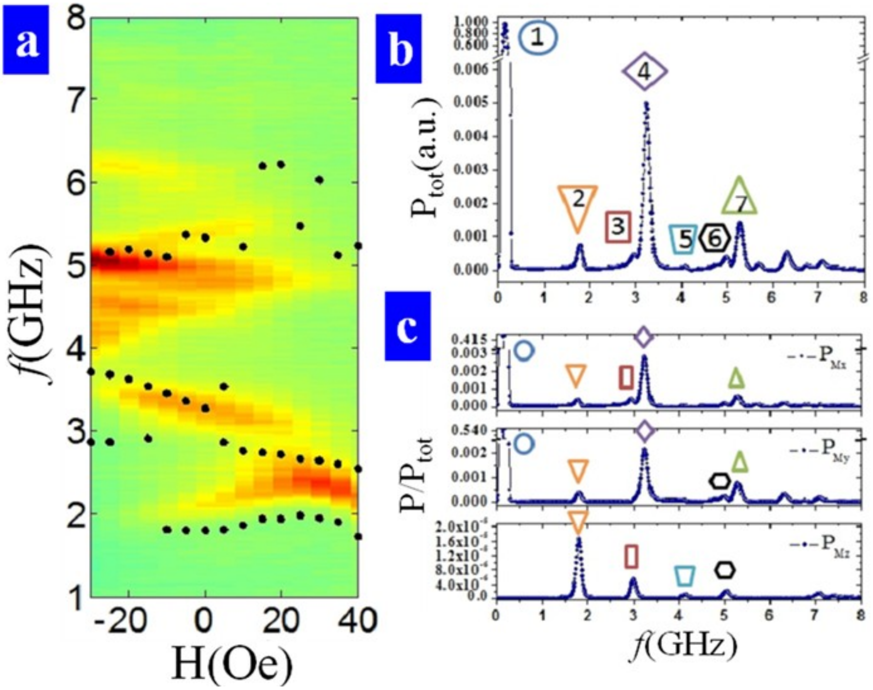

Figure 4.9 Left: Comparison of the simulations (closed circles) with the experiments (background, see marked part of Figure 4.6d). The simulated frequencies are obtained by taking the three strongest peaks at each applied field. Right: (b) Simulated spectrum at zero field for all the magnetization components M_X, M_Y and M_Z combined and for the separate magnetization components, respectively (c). In (b) the measured intensity peaks are marked by integers, corresponding to the first 7 excited spin eigenmodes (see Figure 4.10 for the spatial distributions of these modes). The dot sizes for both the simulations and experiment are 2R=1035 nm and L=20 nm.

It can be seen that the M_X, M_Y and M_Z magnetization components do not respond in the same way to a given field pulse. Some excited modes are more pronounced than others. This is due to the fact that odd modes in one direction will be filtered out by spatially averaging the magnetization. However, the modes that are even along the X direction are not necessarily even in the Y direction. Therefore, combining these three spectra mimics the experiment more adequately, where odd modes will show up as well. Although due to the nature of the present measurements they will be lower in amplitude than the even modes. Figure 4.9a shows the three strongest peaks (above the gyrotropic frequency) of the simulated spectra compared to the experiments. Clearly, there is a good match between the experiments and simulations.

- **Eigenmodes profile**

In order to get more insight into the spin dynamics in the DMV state we investigate the spatial distribution of the main eigenmodes. Knowing the local distribution of the phases and amplitudes for every cell for a selected eigenfrequency, we can reconstruct the eigenmode profiles [175].

Figure 4.10 identifies the main eigenmodes excited in the DMV state at zero applied field. The modes are numbered according to the spectra in Figure 4.9b. The first eigenmode is primarily a gyrotropic mode type excitation of the vortex cores. Modes 2,3,4 and 5 are localized along the domain walls that connect the vortex cores (VC) and edge localized half-antivortex cores. Mode 2 is of an optical type (the different DW´s connecting the V-AV-V-AV rhomb apexes are oscillating out-of-phase) and is localized closer to the dots edge, at the ends of the DWs. Mode 3 shows a node in the oscillation amplitude. The mode 4 (acoustic) reveals no nodes but a strong pinning at the AV positions near the dot edges. Eigenmode 5 is a running wave along V-AV-V-AV rhomb. The higher frequency modes 6 and 7 show strong features localized outside the domain walls. Supplementary movies in [176] provide time sequences of the variation of M_X component of magnetization corresponding to the spin wave modes 2 (at 1.8 GHz), mode 3 (2.9 GHz) and mode 4 (3.2 GHz) for the 1035x20 nm Py dot shown in Figure 4.10. The time evolution of the magnetization for these modes was obtained in the absence of bias field. While mode 2 weakly excites the vortex cores motion, mode 4 does not excite edge half-antivortex. Mode 3 excites motion of both the vortex cores and edge half-antivortices.

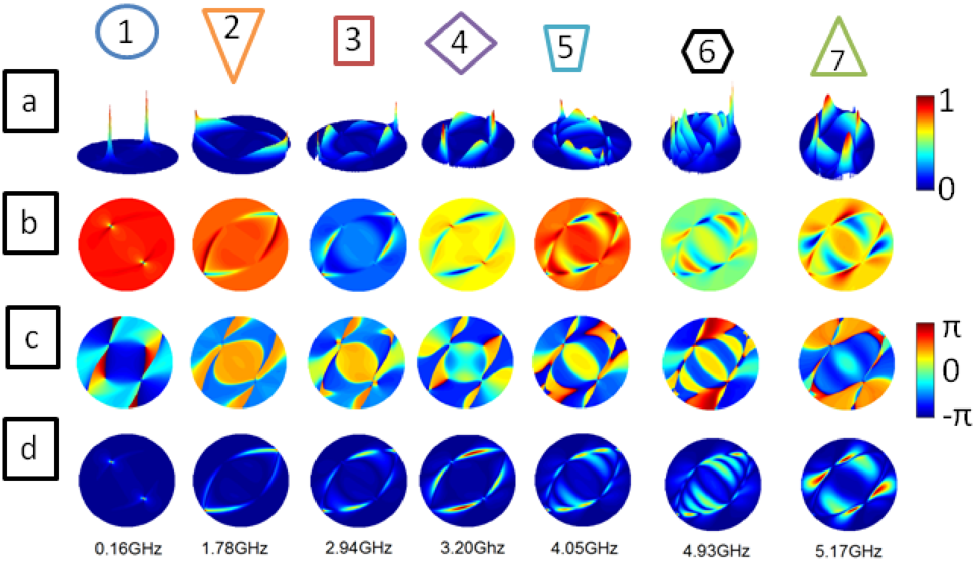

Figure 4.10 The spatial distributions of the first 7 spin eigenmodes at zero bias field corresponding to the frequency spectra of Fig. 4.9. The snapshots for the relative magnetization ΔM$_X$ component are as follows: (a) 3D-visualization of modulus (a.u.), (b) the real part (a.u.), (c) the phase and (d) 2D-visualization of the amplitude (a.u.). The dot sizes are 2*R*=1035 nm and *L*=20 nm. Supplementary movies[176] **show online 3D animations of the eigenmodes 2, 3 and 4.**

- ## Winter´s magnons

This paragraph discusses analytical approach describing the observed results in terms of excited Winter magnons in circular Py dots[177]. The approach was developed in ref. [177] in close collaboration with K. Guslienko.

There are two branches of the spin excitations in the presence of a DW: ¨free spin waves¨ with excitations resembling those in an infinite uniformly magnetized ferromagnet and wall-bounded spin excitations or Winter´s magnons [178], representing oscillations of the DW shape near the static equilibrium position which can be described as a plane. The DW displacement waves are analogous to the displacements that can propagate along elastic strings (e.g., violin strings) and to the capillary waves on the surface of liquids.

The Winter´s magnons were first considered for the Bloch type of the DW [178] in an infinite ferromagnet. But in our case of the flat soft magnetic dots, the spins lay in the dot plane (*xOy*) due to strong magnetostatic energy and a Néel DW should be considered as a ground state. To understand 1D spin waves confined along the Néel DW that is pinned by the V(AV) cores, ref. [177] determines spin excitations of the wall applying the approach by Slonczewski[179].

To describe the magnetization dynamics ref. [177] uses the Landau-Lifshitz equation of motion of the reduced magnetization $\mathbf{m}=\mathbf{M}/M_s$ ($|\mathbf{M}|=M_s$ is the saturation magnetization). Under the assumption that there is a Néel DW connecting the V and AV centers (*Oy* axis see the sketch of the experimental setup in methods) the DW excitations are expressed using **m** as a sum $\mathbf{m}=\mathbf{m}_0+\delta\mathbf{m}$ of the DW static magnetization and spin wave contribution. Further, one changes from the Cartesian to spherical coordinates. Taking into account that the DW length Δ is about the dot radius *R* and the dot is thin (*L*<<*R*), one neglects the magnetization dependence on *z*-coordinate (perpendicular to the dots plane) and applies for the static DW description in the infinite film 1D approximation. The flexural modes of the DW or so called Winter´s magnons[178] appear in [177] by introducing a strong pinning near the VC position in the DW (*y*=0) and no pinning or a strong pinning near the AV core ($y=\Delta, \Delta\approx R$). To satisfy these boundary conditions one uses the plane wave eigenfunctions $\propto\sin(k_n y)$, with discrete $k_n=(2n-1)\pi/2\Delta$ or $k_n=n\pi/2\Delta$, *n*=1,2,…, respectively, and consider the quantized frequencies of the Winter´s magnons $\omega_n=\omega(k_n)$. The magnon frequencies

$$\omega_n^2/\omega_M^2=p\int_0^\infty x\sinh^{-1}(\pi x)\left(\sqrt{x^2+k_n^2\delta^2}-x\right)dx+(4/\pi)\exp(-\Delta/\delta),$$

where $p=L/\delta$ with δ is the DW width, $k_nL<<1$, are calculated from the linearized equations of motion within the magnetostatic approximation following the method suggested by Guslienko et al.[180]. They are in a good agreement with the measured eigenfrequencies (here $\omega_M=4\pi\gamma M_s$, γ is the gyromagnetic ratio).

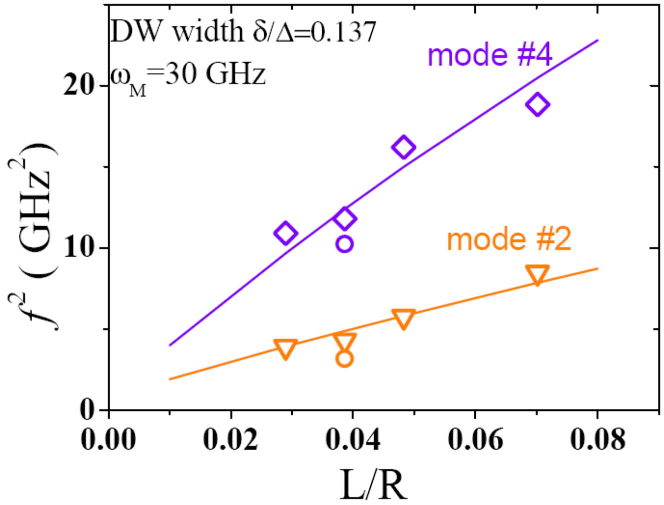

Figure 4.11 Comparison of the experimental (squares and triangles), analytical (lines) and simulated (circles) eigenfrequencies for the most intensive excited spin modes #2 and #4 as function of the dot aspect ratio (thickness over radius).

Applicability of the model to experiment is confirmed by considering variation of the eigenfrequencies for the spin modes 2 and 4 with the dot aspect ratio *L/R* (see above Figure 4.11). The Winter's magnon eigenfrequencies are $\omega_n \propto \sqrt{L/R}$ at *L/R*<<1 similarly to the frequencies of the magnetostatic radial and azimuthal spin waves in the flux closure single vortex state [18].

4.4 Conclusions

This chapter investigates static and dynamic properties of the metastable double vortex state in circular Py dots. It has been found that this metastable magnetic state exists at sufficiently long times even at zero field and therefore can be studied experimentally. The magnetization dynamics in the DMV state has been described in terms coupled vortex-domain walls oscillations.

We identified new type of quasi one-dimensional localized spin wave modes confined along the domain walls, connecting vortex cores with half-antivortices in circular magnetic dots. The frequencies measured by broadband ferromagnetic resonance are in good agreement with the DW flexural oscillation frequencies calculated in the magnetostatic approximation assuming Neel domain walls connecting the vortex and antivortex cores. In general*, similar spin waves could be excited by spin torque or microwave magnetic field in thin arbitrary shape (circular, triangular, rectangular, etc.) patterned magnetic nanostructures possessing magnetic domain walls.*

Besides, our findings may contribute to understanding of domain wall motion in magnetic stripes and rings induced by magnetic field or spin polarized current. Finally, our results introduce a scheme to investigate the high-frequency magnetization dynamics of symmetry breaking states in highly symmetric patterned magnetic elements.

To summarize the three new main observations presented in this chapter:

1) DMV state could be presented as long living metastable state in circular thin magnetic dots. This DMV could be described as spatially separated two magnetic vortices interconnected by domain walls (DWs).

2) Spin wave modes excited in the DMV state were detected and its dependence on the applied magnetic field and dots aspect ratio was investigated and understood.

3) New kind of spin waves, namely “Winter´s magnons” which are analogous to the displacement waves of strings has been detected. Relevant spin wave mode frequencies were found to be in a good agreement with theory which considers the DW flexural oscillation frequencies calculated in the magnetostatic approximation.

CHAPTER V: COUPLED VORTEX DYNAMICS

5.1 Introduction

Understanding of the coupled vortex systems is important both fundamental and the application points of view. Indeed, as we mentioned before, circular magnetic dots in the vortex state are the main elements of numerous proposed novel spintronic devices [181–183], capable of fascinating spin-based electronics applications, from extremely sensitive magnetic field sensors, to spin polarized current-tunable microwave vortex nano-oscillators[181] and vortex MRAM[183]. Examples range from a dense array of vortex state magnetic elements, to attempts to extract higher energy output from nano oscillators vortex based oscillators. Sincronization due to coupling between vortex oscillators is one of the most efficient ways to increase emitted power. All this implies a need to understand not only static, but also dynamic coupling between vortices.

Additionally, a new devices, so-called magnonic crystals (MC) [184], based on either one- (1D) or two-dimensional (2D) periodically modulated magnetic structures have been developed recently. Here, the artificially introduced periodicity and inter-element coupling may modify the spin excitation spectra in a controllable way. In particular, allowed and forbidden spin excitation frequency bands can appear [185]. This have opened a new branch in nanomagetisim physics where magnetic coupling have to be well understood.

In this chapter we explore, experimentally, and by simulations and analytical estimations, the dynamic properties of the lateral and afterwards the vertically coupled circular Permalloy (Py) dots with different separation (interdots distance for laterally coupled and spacer thickness for the vertically coupled dots). We investigate high-frequency response and how the coupling affects the frequencies and the splitting and whether the coupling changes or transforms the types of the modes by applying a bias in-plane field. We compare the results with the spin wave spectra of the uncoupled dots (presented en the previous chapters, see also refs. [127], [147]).

5.2 Samples, experimental setup and simulations

Square arrays of Permalloy (Py, $Ni_{80}Fe_{20}$) circular dots were fabricated by combination of lithography and lift-off techniques on a standard Si(100) substrate with a 2.5 nm oxide layer on top, as explained in details in chapter III. The set consists of three samples with different lattice periods a=2R+d of 1200, 1500 and 2500 nm. The dot thickness L is 50 nm and radius R is 500 nm. The excited in linear regime (in-plane driving rf field is below 0.2 Oe) spin modes have been studied in the frequency range from 100 MHz up to 20 GHz by using a broadband VNA–FMR spectrometer (see Methods) with a coplanar wave guide (CWG) in transmission configuration.

As to the vertically coupled dots, two sets of samples in the form of square arrays of tri-layer Py(25nm)/Cu(d)/Py(25nm) circular dots were fabricated by a combination of e-beam lithography and lift-off techniques on a standard Si(100) substrate (see chapter III). The samples have Py layers thickness of L=25 nm, diameter $2R$=600 nm and large interdot center-to-center distances of 1000 nm to minimize the dipolar lateral coupling. The thickness of the Cu spacer for the first type of samples is d=0.9 nm (we call it as IEC-interlayer exchange coupled tri-layer), while the second type of samples has d=20 nm (further- DIC, dipolar interlayer coupled tri-layer).

The spin wave spectra of these nanopillars have been also studied at room temperature by broadband vector network analyzer based VNA-FMR technique in the range up to 14 GHz where excitation of azimuthal spin wave modes is expected. Besides, a continuous reference layers have also been studied separately to characterize the interlayer coupling. The data on nanopillars were obtained and analyzed using parallel pumping scheme when both the bias dc field $\mathbf{H}_0 \parallel \mathbf{x}$ and oscillating pumping field $\mathbf{h}$ are in plane and parallel to each other (see Methods). The pumping field $\mathbf{h}$ excites only the spin eigenmodes localized in the areas where the torque $\mathbf{h} \times \mathbf{M}_0 \neq 0$, ($\mathbf{M}_0$ is the static magnetization) and quasi-uniform FMR-mode is suppressed. We shall further characterize the vortex in j-layer (j=1,2) by its core polarizations p_j and chirality C_j.

The main advantage of using symmetric (the same thickness and material) circular ferromagnetic layers is their unique opportunity to investigate the influence of the strength and character of interlayer coupling (i.e., interlayer exchange vs. dipolar) and relative vortex chiralities on spin wave dynamics in vortex-vortex coupled system without influence of additional factors.

The simulation was done by OOMMF [159]. The simulated cell size is 5 × 5 × 5 nm^3 for the DIC nanopillar and single dots and 5 × 5 × 1 nm^3 for IEC pillars. The gyromagnetic ratio $\gamma/2\pi = 2.96$ MHz/Oe, the exchange stiffness A = 1.4×10^{-11} J/m, the saturation magnetization $M_S = 830\times10^3$ A/m, and the Gilbert damping $\alpha = 0.01$.

5.3 Laterally Coupled Vortices

- **Brief review**

Multiple spin eigenmodes of a different nature can be excited in magnetic dots with a vortex ground state by an external perturbation. In the linear regime, the total dynamical response is described by a superposition of these modes. The excitation spectrum of a single circular dot in a vortex state consists of the low-frequency gyrotropic mode (typically well below 1 GHz [29], [32]), and high frequency spin wave modes of different symmetry. These are labelled by, m and the number of nodes of dynamical magnetization along azimuthal plane, n, along the dot radial direction [37], [39], [144]. The gyrotropic modes with $|m| = 1$ are associated with the displacement of the vortex core from the dot center. Due to topology of the vortex, the frequencies of azimuthal modes ($m \neq 0$) are splitted in doublets having indices $m = \pm|m|$, with the largest value of splitting for $|m| = 1$ [39], [147], [186]. For isolated micron and submicron sized soft magnetic dots, the spin wave eigenmode frequencies are determined by the dot aspect ratio $\beta = L/R$, and are proportional to the square root of β, whereas the gyrotropic frequency and the $m=\pm1$ doublet splitting are linear on β for thin dots ($\beta \ll 1$)[147], [148] as presented in the chapter III.

Most of the previous investigations of the magnetization dynamics have been focused on interacting nano-(micro-) stripe arrays (1D MC), where the propagating spin waves were observed by means of BLS [187–189]. Experimental investigations of the spin wave propagation in 2D MC of square Permalloy dots using BLS [190] indicated a strong dependence of the spin wave spectrum on the interdot distance. Influence of interdot coupling on the spectra in 2D MC of square arrays of circular dots using BLS was measured [191] and the observed four-fold magnetic anisotropy was attributed to non-uniform magnetization of the dots. A general approach to the induced magnetic anisotropy in arrays of non-uniformly magnetized dots was developed[192], and afterwards particular models [7], [151], [193] have been successfully applied to explain the FMR experimental data obtained on 2D dot arrays.

5.3.1 Experimental results

The variation of the modulus of the transmitted rf signal at zero magnetic field (the centred vortex ground state, see Figure 5.1), indicates the above-mentioned spin eigenmodes that are excited by uniform rf field.

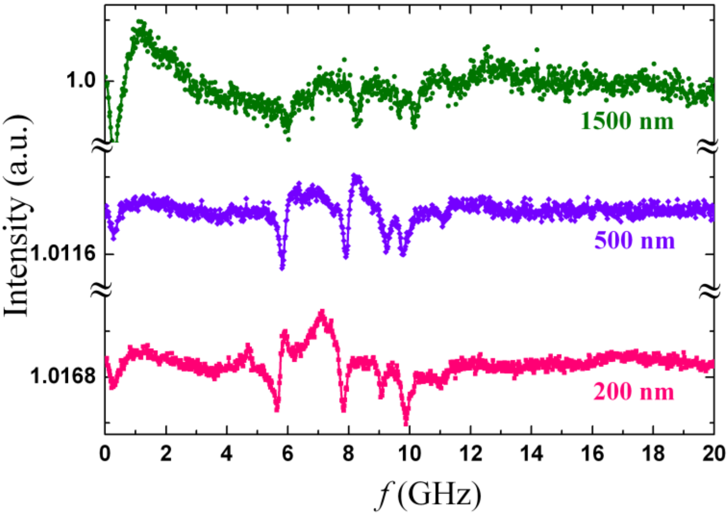

Figure 5.1 Zero in-plane bias field response of the three arrays of 50 nm thick, 1000nm diameter Py dots with different interdot separations *d*= 200, 500, 1500 nm.

A qualitatively similar set of the spin eigenmodes was observed in all the samples under study: a gyrotropic mode, two doublets of the high frequency azimuthal spin wave modes with n=0, 1 and $m = \pm 1$, and one low-intensity radial mode indexed as n=0, m=0. Estimation on the basis of equations of Ref.[37] yields for this radial mode frequency the value of 12.7 GHz.

The influence of the interdot separation value on the observed resonance peak positions is well noticeable for all the modes (Figure 5.2). It is most significant for the gyrotropic mode frequency ω_g, and for the values of the frequency splitting for $m = \pm 1$ doublets with n=0 and n=1, $\Delta\omega_0$ and $\Delta\omega_1$, respectively (Figure 5.3). Both the gyrotropic frequency and the splitting $\Delta\omega_0$ reveal well-pronounced non-monotonous dependence on the dot array period a, whereas the dependence $\Delta\omega_1(a)$ is monotonous.

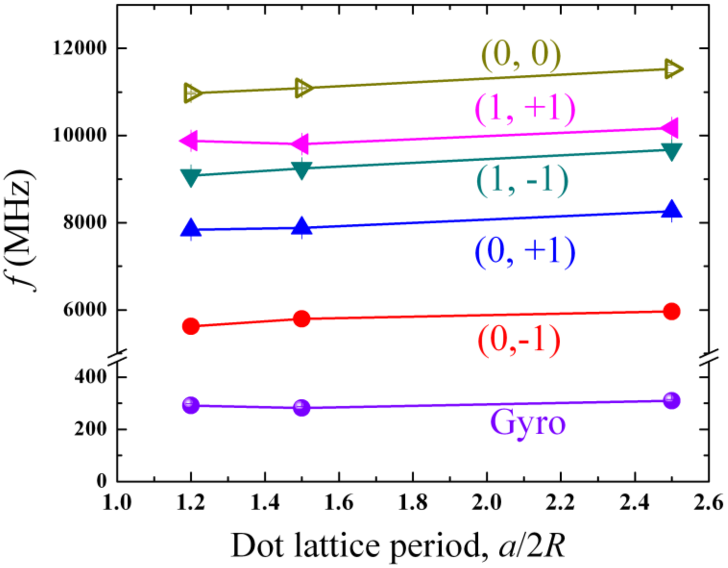

Figure 5.2 The detected spin excitation frequencies labelled by the mode indices (*n*, *m*) vs. the interdot separation.

To explain this complicated behaviour, we[‡‡] consider [Awad et al.,[194] the interdot coupling of the ground vortex state dots within an array. The only source of the coupling in our case is the magnetostatic interaction of the non-uniform dynamical magnetizations $\mathbf{m}(\mathbf{r},t)$ of the different dots. For an array of well separated dots, $R << a$, a theory of the

---

[‡‡] In collaboration with K.Y.Guslienko (UPV, Spain), G. N. Kakazei (U. Oporto, Portugal), B. A. Ivanov (IM, Kiev, Ukraine).

collective spin modes has been developed by expansion of the magnetostatic energy over the small parameter R/a[195] . Within this approach, the interdot interaction can be presented as a sum of different multipole contributions similar to a multipole expansion in classical electrodynamics. The first (dipolar) term is determined by oscillations of the total dot magnetic moments $\boldsymbol{\mu}(t)=\int d\mathbf{r}\,\mathbf{m}(\mathbf{r},t)$. This dipolar term leads to contributions to the eigenfrequencies that are proportional to $1/a^3$. The non-dipolar terms are determined mainly by the dot quadrupolar moments $q_{ij}=\int d\mathbf{r}\; m_i x_j$, $i,j=x,y,z$ [192]. The quadrupolar terms lead to $1/a^5$ dependence of the interdot interaction energy. Only the spin modes with $m=0,\pm1$ having non-zero $\boldsymbol{\mu}$ are affected by the interdot dipolar interactions. For the rest of the modes (with higher m) the sole source of the coupling is a non-dipolar coupling. On the other hand, the quadrupolar interaction can be essential even for the dipolarly-active modes (with $m=0,\pm1$) [195].

The particular excitation scheme of the FMR experiment, using an almost uniform in-plane rf field, corresponds to excitations of the modes with $m=\pm1$ only, i.e., the gyrotropic mode and azimuthal spin waves. However, a small out-of-plane component of the rf field due to the finite CWG lateral size results in excitation of a low-intensity radial mode (m =0, n=0) (as discussed in the chapter III) [147]. For our samples the parameter $2R/a$ is not small (it varies from 0.4 to 0.83). Nevertheless, our experimental data can be explained taking into account both the dipolar and quadrupolar interactions of the modes. Within this simple scheme, the spin eigenfrequencies can be described by the equation

$$\omega_\alpha=\omega_\alpha(0)-\Omega_{\alpha,d}\left(\frac{2R}{a}\right)^3+\Omega_{\alpha,q}\left(\frac{2R}{a}\right)^5, \qquad (5.1)$$

where ω_α with α= g, 0, 1 give the values of ω_g, $\Delta\omega_0$, and $\Delta\omega_1$, respectively. The quantities $\omega_\alpha(0)$ describe the frequency values for non-interacting dots, and the parameters $\Omega_{\alpha,d}$ and $\Omega_{\alpha,q}$ are the weights of the dipolar and quadrupolar contributions to the corresponding frequencies.

We discuss the experimental data on the ground of Eq. (5.1), with proper choice of the parameters $\Omega_{\alpha,d}$ and $\Omega_{\alpha,q}$.

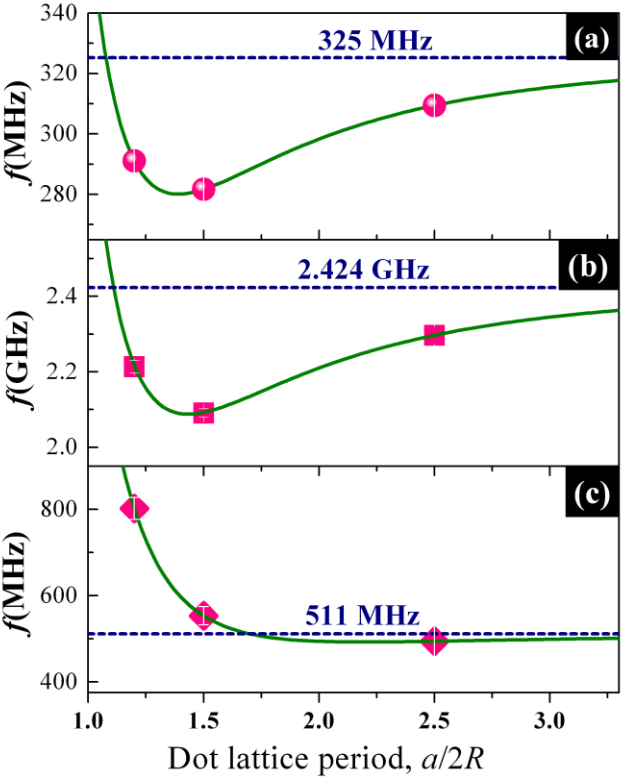

Figure 5.3 The dependence of the gyrotropic frequency ω_g (a) and the frequency splitting of the first $\Delta\omega_0$ (b) and the second $\Delta\omega_1$ (c) doublets of azimuthal spin waves on the dot array period a. Symbols represent the FMR experimental data, solid green lines give the description of the experimental data by Eq. (5.1). Horizontal dotted lines present the limit frequency values $\omega_\alpha(0)$ found for isolated dot, $(R/a)\to 0$.

First, for n=1, $m=\pm1$ azimuthal modes the amplitude of the dipolar moment $\boldsymbol{\mu}_{n,m}$ is much less than for n=0, $m=\pm1$ modes due to radial node of the eigenfunctions, the corresponding ratio is $\mu_{1,\pm1}/\mu_{0,\pm1}\approx 0.13$ [195]. Thus, the dipolar interaction is small for n=1 modes being of order of 2% of the value expected for n=0 modes. The quadrupolar interaction should be dominating for frequencies of the azimuthal modes with n=1, $m=\pm1$ and their frequency splitting. The observed value of $m=\pm1$, n=1 doublet splitting is well described by the dependence $\Delta\omega_1=\Delta\omega_1+\Omega_{1,q}(2R/a)^5$, with *positive* constant $\Omega_{1,q}$ (Figure 5.3c). Thus, the quadrupolar interaction provides the upward shift of the frequencies for n=1, $m=\pm1$ modes proportional to $(2R/a)^5$.

For both the gyrotropic mode, and the main spin wave frequency doublet (n=0, $|m|=1$) splitting, only the dipolar interaction was previously calculated giving the *negative* contribution with $\Omega_{0,d}=\pi\beta\gamma M_s\sigma(0)/72$ [195], where $\sigma(0)\approx9.03$ is the dipolar sum, γ is the gyromagnetic ratio, M_s is the saturation magnetization. Combining this dipolar contribution with the positive quadrupolar one of the same form as for n=1, a good description of the experimental data for ω_g and $\Delta\omega_0$ dependencies on $2R/a$ is obtained, see Figure 5.3a,b. Here the non-monotonous dependence of the frequencies on a naturally appears as a competition of two contributions, dipolar and quadrupolar, with different signs. Most intriguing is the experimental observation that for the coupled dot arrays the proportionality $\Delta\omega_0(a)\propto\omega_g(a)$ holds.

Thus, the simple phenomenological dependence (Eq. (5.1)) with proper choice of the coefficients $\Omega_{\alpha,d}$ and $\Omega_{\alpha,q}$ provides a good *qualitative* description for all the experimental data. As to a *quantitative* description of the data, the limiting value of $\omega_g/2\pi=325$ MHz (Figure 5.3a) is somewhat lower than 480 MHz expected from analytical theory[29], [32] and from our micromagnetic simulations (391 MHz) on an isolated Py dot with R=500 nm and L=50 nm (for simulation parameters see Methods). The simulated first azimuthal doublet (n=0, m=±1) frequencies 6.35 GHz, 8.40 GHz are very close to the experimentally detected frequencies 5.96 GHz, 8.26 GHz at d=1500 nm confirming their interpretation. The value of the dipolar interaction contribution to the gyrotropic frequency ω_g is much higher than in the theory [195]. The ratio between the measured values of the n=0, $m=\pm 1$ doublet frequency splitting $\Delta\omega_0$ (2.09–2.30 GHz) and gyrotropic frequency (282 - 310 MHz), namely $\Delta\omega_0/\omega_g \approx 7.4$, is twice higher than the ratio $\Delta\omega_0/\omega_g \approx 4$ calculated in Ref [186]. These discrepancies could be attributed to the fact that the corresponding calculations were performed in the main approximation on the small parameters, β and R/a, whereas these ratios are not small in our case. For example, the value of β=0.1 is higher than in previous experiments[29], [32], [39] . Note that the essential downward deviation from the linear dependence ω_g on β was reported [196] for β>0.1 due to a non-uniformity of **m** along the dot thickness. One more possible source of such discrepancies is lowering of the symmetry of the vortex ground state magnetization distribution for the dense dot arrays, as well as different directions of the vortex polarities [55].

5.4 Vertically Coupled Vortices

- **Brief review**

Layered magnetic nanopillars consisting of ferromagnetic (F) and nonmagnetic (N) layers are becoming the main “building blocks” in spintronics. However, the bulk of the current knowledge on magnetization dynamics of the vortex state dots (the gyrotropic and spin wave modes of different symmetry) is related to a single vortex state dot as presented in the two previous chapters, or laterally coupled vortex dots presented earlier in this chapter; see also ref.[54], [55], [194]. As to the vertically coupled magnetic vortices in F/N/F nanopillars, the scarce knowledge on dynamics is mainly restricted to investigation of the interlayer coupling effect on the vortex low frequency gyrotropic modes [181], [197] and little is known on the influence of character of the coupling[198] on the excited high frequency spin wave modes[199]. Besides, the major part of the previous studies of the vertically coupled vortex state dots in nanopillars has been done in asymmetric conditions by using the dots made of different materials (typically Co and Py)[199], [200] or having different thickness[201]. Previous experiments[63] showed that some conditions should be satisfied to stabilize a remanent double vortex state in F/N/F stack. If the F-layer thicknesses and radii are relatively small, the dots are in in-plane single domain state and only edge localized modes can be detected in the low frequency part of the spin excitation spectra[198].

5.4.2 Measurements and results

- **Static and dynamic measurements**

The DC magnetization for both IEC (interlayer exchange coupled) and DIC (dipolar coupled) trilayer nanopillars (measured at 300K by SQUID magnetometer, see Figure 5.4a,b) have a vortex like hysteresis and are in qualitative agreement with hysteresis loops for simulated coupled circular dots in F/N/F nanopillars with centred vortices present in both the F-layers at remanence [63].

We will denote the core polarization p_j and chirality C_j to characterize the vortex in j-layer. The loops simulated by OOMMF [159], made by reducing the field to zero from initial saturation of the dots magnetization, indicate a centred double vortex remanent state and are qualitatively similar to the measured ones. As we shall see below, however, magnetization dynamics of DIC nanopillars points out the existence of a statistical distribution of the antiparallel chiralities APC (APC, C_1C_2=-1) and parallel chirality (PC, C_1C_2=+1) states for both types of nanopillars. Magnetization reversal (Figure 5.4a,b) reveals that vortex annihilation H_a fields are larger for IEC than for DIC nanopillars. This indicates that the dipolar coupling, present in both IEC and DIC pillars, is strengthened by antiferromagnetic exchange in the IEC dots with ultra thin Cu spacer.

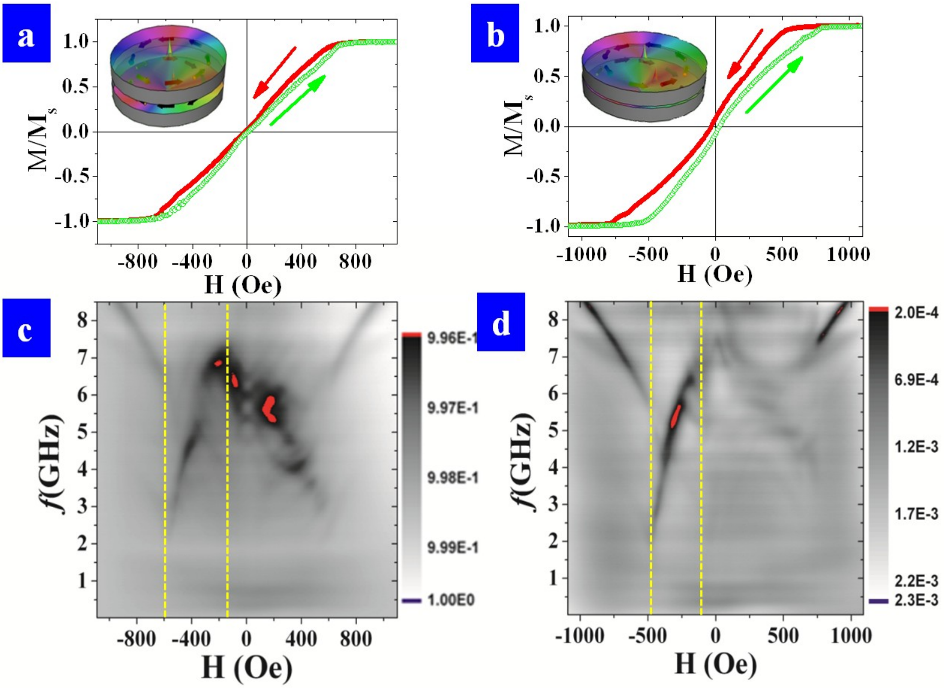

Figure 5.4 Magnetization hysteresis and dynamics experiment of double dots dipolar coupling Py/Cu(20nm)/Py, (a),(c) and with interlayer exchange coupling, Py/Cu(0.9nm)/Py, (a),(d). the insets shows schematic drawings of the nanopillars.

Two types of the broadband measurements have been carried out in order to detect both the low and high frequency spin wave modes. In *the first type of experiments* we initially saturated the magnetization and made a frequency sweep at fixed fields, starting from a negative field, and ending with a positive field, that forces the dots to be in a saturated state, and are larger than the annihilation field in both cases. In the saturated state we can detect the Kittel-like uniform spinwaves. These is the optical type mode [13], where the magnetization of both layer precesses at the same frequency and out of phase respect to each other, detected due to the parallel pumping scheme.

Below the saturation field (the nucleation field H_n) the trilayer dots pass through a metastable double vortex configuration in each of the coupled dots. The region (marked by the dotted yellow lines in Figure 5.4c,d) appears before entering into the vortex-vortex state. This state is characterized by the excitation of relatively low (few GHz) frequency spin waves, highly dependent on the field, that have a similar field dependence for both DIC and IEC samples but with frequencies shifted to higher values in the case of the thin spacer IEC sample. Those modes are known as “Winter's magnons” or flexural oscillations of the domain walls connecting the vortex and anti-vortex cores and have been extensively studied for single Py dots in the previous chapters and has been reported for single Py dots layer in the ref.[177].

Further reduction of the magnetic field close to zero reveals the emergence of the vortex-vortex modes. Further on we focus on high frequency modes only.

The high frequency spin waves reveal dramatic (more clear visible for DIC dots) changes in spin wave spectra in relatively small fields. Two doublets observed in the low field region, abruptly transform into multiple satellites with increasing fields above some critical value of about 40 Oe. This transition is more abrupt in the case of DIC trilayers than for IEC ones.

In order to investigate in more details the low field changes in broadband response of the coupled dots, we carried out a second type of the experiments by measuring the averaged broadband response using multiple scans within the minor loops (i.e. without annihilating any of the two vortices in the dots see Figure 5.5a,c). Both DIC and IEC dots reveal now more clearly strong changes of the spin wave response at low fields.

The symmetric spectra respect to the zero field which could be observed directly looking at the experimental results Figure 5.5a,c confirms the centred vortices in both samples.

We shall concentrate first on our main result: the spin wave excitations for the DIC dots (Figure 5.5a), where frequency doublets were observed in the small field region. With increasing bias field these doublets transform in multiple satellites above some critical value of about 40 Oe. The bias field induced changes of the eigefrequencies for DIC dots; those changes are more abrupt than for the IEC ones (Figure 5.5c).

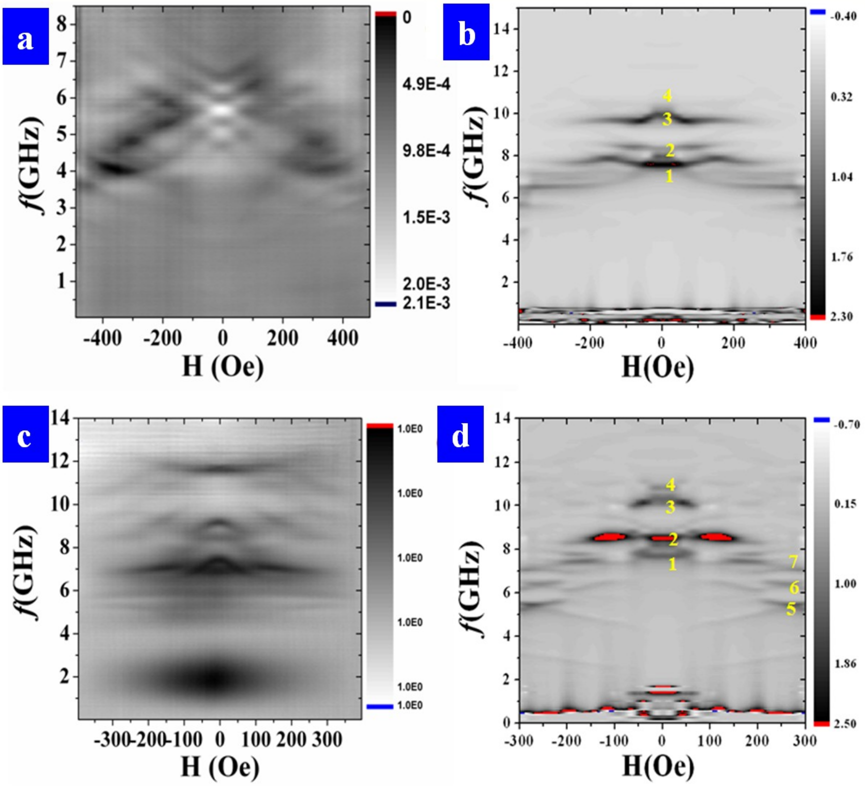

Figure 5.5 Measured absorption spectra as a function of applied field, for DIC (a) and IEC (c) measured at the minor loop. Simulated eigenfrequencies with for DIC (b) and IEC (d). Marked modes are explained in the text.

• Coupling effects on the eigenmodes[§§]

Before proceeding with the discussion of the results and the comparison with the simulation, we will try to discuss the effect of coupling on the modes and their splitting.

In zero approximation (no interlayer coupling) the high frequency part of the nanopillar spectrum consist of two peaks – azimuthal SW with $n=0$, $m = \pm 1$. And the frequency degeneracy of these SW is removed due to the

---

[§§] In collaboration with Prof.K. Y. Guslienko (UPV, Spain).

dynamic vortex-SW interaction resulting in forming of the doublets with the frequency splitting of 1.3 GHz (as we have shown in Chapter III [147], [186]) (L=25 nm, R=300 nm).

To identify the observed frequency peaks, we employ standard schematics describing the spin waves (SW) excited in nearly centred vortex state according to number of the nodes in dynamic magnetization observed along the azimuthal m and radial n directions. As the vortex core radius is about 10 nm and the dot radius is 300 nm, the spin wave modes are concentrated mainly outside the core. The SW can be described via dynamic magnetization $\boldsymbol{\mu} = (\mu_\rho, 0, \mu_z)$ components in the cylindrical coordinates (ρ, ϕ, z), $\mu_z(\rho, t) = a_{nm}(\rho)\cos(m\phi - \omega t)$, $\mu_\rho(\rho, t) = b_{nm}(\rho)\sin(m\phi - \omega t)$. Accounting that driving magnetic field $\mathbf{h}_{rf}$ is linearly polarized and oscillates in the dot plane *xOy*, only the azimuthal modes with $m = \pm 1$ (arbitrary n) can be excited. These spin waves correspond to rotating in plane average magnetization $\langle \mu_x(t) \rangle_V \sim C\langle b \rangle_\rho \sin(\omega t)$, $\langle \mu_y(t) \rangle_V = C\langle b \rangle_\rho m\cos(\omega t)$. So, maximum mode intensity corresponds to minimal number of oscillations of the mode profile $b(\rho)$ along the radial direction, *i.e.*, to the index n=0.

The interlayer coupling energy in the F/N/F stack consists of two parts: exchange (essential only if d< 2 nm) and magnetostatic coupling (for all d). The volume density of the exchange energy can be written as $w_{\text{int}}^{ex} = -(J/LM_S^2)\boldsymbol{\mu}_1 \cdot \boldsymbol{\mu}_2$ (J- exchange integral). The magnetostatic coupling energy density in the main approximation can be written via the F-layer dipole moments $w_{\text{int}}^{dip} = (V/(d+L)^3)\langle \boldsymbol{\mu}_1 \rangle \langle \boldsymbol{\mu}_2 \rangle$ placed in the centres of the dots of volume V. We see that the corresponding interaction fields H_{int}^{ex} and H_{int}^{dip} can be added to each other because they follow the same angular dependence $\sim \cos(\Theta)$, where Θ is the angle between the averaged layer dynamic magnetizations. Since for Cu the maximum value of J ~0.14 erg/cm^2 [202], estimation shows that the magnetostatic coupling dominates for both the Cu-spacer thicknesses d=0.9 and 20 nm explored. The dipolar interaction energy is $w_{\text{int}}^{dip} \propto \langle \boldsymbol{\mu}_1 \rangle \cdot \langle \boldsymbol{\mu}_2 \rangle \propto -C_1 C_2 m_1 m_2$ [203];

where $m_1, m_2 = \pm 1$ are the indices of the azimuthal SW forming the doublets in the 1st and 2nd layers. The product $m_1 m_2 = p_1 p_2$, because the sign of m_j is determined by sign of p_j of the j-th layer. The positive (negative) sign of $C_1 C_2 p_1 p_2$ corresponds to effective ferromagnetic (antiferromagnetic) interlayer coupling. Each of the $(0, m_j)$ -frequencies splits into the frequencies of in-phase and out-of-phase modes[13]. The in-phase (out-of-phase) mode frequency is lower for ferromagnetic (antiferromagnetic) coupling.

Summarizing, we can say that the eigenfrequency spectrum of F/N/F tri-layer pillars is formed mainly by the intralayer magnetostatic interaction yielding spin wave modes of the different symmetry. Then, the excited azimuthal SW with $m=\pm 1$ are splitted due to interaction with the dynamic vortex cores, and the resulting frequencies are renormalized by relatively weak interlayer coupling. But, nevertheless, this coupling is important because it distinguishes the modes excited in the C_1C_2=+/-1 chirality states and leads to formation of in-phase/out-of-phase modes in F-layers and to a strong dependence of the spectra on the external bias fields. We note that an opposite classification of the simulated SW spectra was done for Py(20nm)/Cu(10nm)/Py(10nm) nanopillars [204] assuming that the interlayer interaction is essentially larger than the azimuthal mode frequency splitting.

- **Simulated modes**[***]

Dynamic OOMMF simulations (see parameters in the corresponding paragraph) with parallel vortex cores show qualitative agreement with our main experimental observations. The simulations are done by applying a time dependent driving field (one ps Gaussian pulse of 5 Oe) to the relaxed state. We reconstruct the eigenmodes profiles of the main modes[175].

Simulations of the ground state at zero field for DIC dots show the lowest azimuthal modes that are splitted due to the dynamical vortex core – SW interaction in each F-layer. Zero field experiments reveal, however,

---

[***] In collaboration with A. Lara (Master student-MAGNETRANS-UAM group).

the existence of a pair of the doublets in the frequency range where the lowest azimuthal mode doublet is expected. The further splitting of the $(0,m_j)$ mode frequencies of the doublets is attributed to the coupling of the layers having the APC or PC chiralities in each of the DIC dots forming the tri-layers, as indicated by simulations (Figure 5.5b) by the numbers 1,2,3,4. As the eigenfrequencies of the isolated layers are degenerated, the splitting of the frequencies for different signs of C_1C_2 is a result of the interlayer coupling.

In agreement with experimental observations, the finite field simulations show an abrupt additional splitting and the relative phase changes in the SW azimuthal modes applying magnetic field exceeding 15 Oe. We need to assume a mixture of the C_1C_2=+1/-1 state nanopillars in the measured array to explain the splitting of the modes $(0,\pm1)$. The assumption about 50% mixture (we have checked with simulations that approximately half of the DIC tri-layers relaxes into PC state, and the other half - into APC state, starting from a random distribution of magnetization) of the APC and PC nanopillars describes qualitatively well the experimental observations with four weakly field dependent spin wave modes at small fields, which are transformed to multiple and strongly field dependent SW frequencies above some critical magnetic field (Figure 5.6b). The frequencies of nanopillars with C_1C_2 = -1 (higher frequency in-phase mode) experience splitting in smaller bias fields than one for nanopillars with C_1C_2 = +1 (lower frequency in-phase mode), i.e., the SW modes of nanopillars with C_1C_2 = +1 are less sensitive to change of the bias field.

Figure 5.6 shows in more details the frequency excitation spectra of the nanopillars presented before in (Figure 5.5a,b). A zoom of the measured broadband spinwave spectra shows clearly the abrupt change of the frequencies of the spin waves as field is increased. The simulated eigenfrequencies as function of in-plane bias field for APC and PC states of the Py layers marked by different colors for each magnetization state in Figure 5.6b. Additionally, the simulated excitation spectra as function of frequency is presented at low fields in the APC and in the PC configuration in Figure 5.6 c,d respectively.

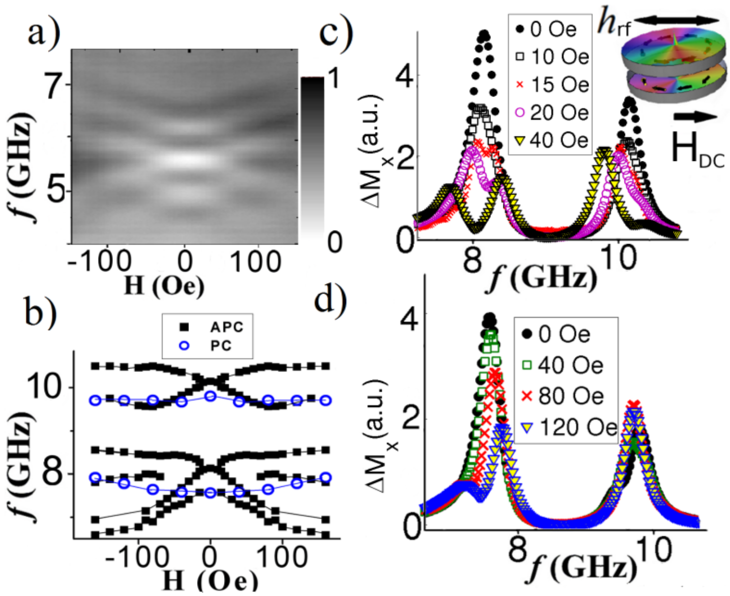

Figure 5.6 Frequency excitation spectra of Py/Cu(20nm)/Py nanopillars: a) measured broadband ferromagnetic resonance amplitude of the absorption spectra (a.u.) as a function of applied field. b) Simulated eigenfrequencies as function of in-plane bias field for APC and PC states of the Py layers. Simulated excitation spectra at low fields in the APC (c) and in the PC (d) states.

The simulated frequencies of DIC nanopillars are approximately in 50% higher than the experimentally measured frequencies. This could be due to few reasons: (i) the saturation magnetization of the Py-layers can be smaller than the value of $M_S=830\times10^3$ A/m used in simulations (done at zero temperature) and (ii) the lateral interdot dipolar coupling in the array typically leads to lowering of the isolated dot eigenfrequencies.

The results for IEC nanopillars show that they also contain a mixture of both APC and PC configurations. The main difference of the IEC nanopillars is that the frequency shift behaviour in the applied field shows more smooth dependence but generally is similar to the DIC dots. We shall see further from the modes classification, profiles and the change of the frequencies that behaviour in the higher fields for the IEC dots is more gradual than the abrupt one observed in DIC dots. Figure 5.7compares experiments and simulations for the low field response in IEC dots for 70% APC - 30% PC distributed chiralities.

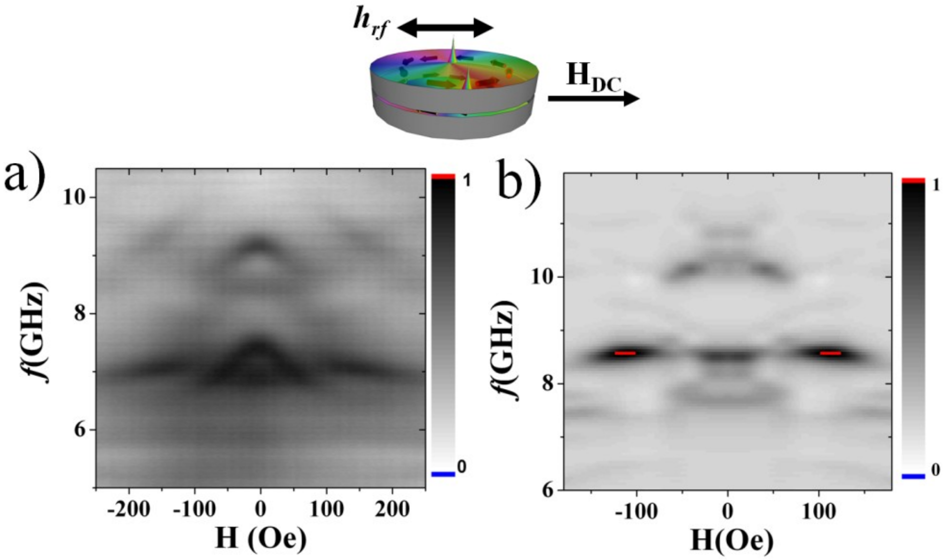

Figure 5.7 Spin wave excitation spectra of Py/Cu(0.9nm)/Py nanopillars vs. in-plane bias field: (a) experimental measurements of broadband ferromagnetic resonance amplitude of absorption (a.u.). (b) Dynamic micromagnetic simulations with 70% contribution from the APC nanopillars (a.u.). The inset above indicates the direction of the *rf* and the applied fields.

- **Modes classification and profiles**

DIC nanopillar modes

The changes in the modes can be seen from simulated spatial distributions of the dynamic magnetization in the DIC dots with PC (part b of Figure 5.8) and APC chiralities (part a of Figure 5.8), presented as ΔMx/Ms. We see that modes suffer strong changes above 15 Oe. At zero field, the main two modes are excited at 8.13 GHz (counter-clockwise (CCW) motion, n=0, *m*=+1) and at 10.15 GHz (clockwise (CW) motion, n=0, *m*=-1). Being of the acoustic type (i.e., the two layers response is nearly in-phase, it is shown for APC mode (Figure 5.8a); those modes are 2,4 in Figure 5.5b. The PC modes (Figure 5.8b) vary more gradually with bias field (those modes are 1,3 in Figure 5.5b)

The APC modes keep its profile and nature till reaching a small external magnetic applied field of above 15 Oe. Then the modes transform to be out-of-phase (in one layer respect to another) as seen in Figure 5.8a. The APS modes suffer the abrupt changes (modes with black squares in Figure 5.6d). We believe that this transformation, accompanied with the abrupt change in frequencies respect to field occurs because, at fields different from zero, each vortex is pushed towards a different part of the dot, and differences of phase appear as a result of the changes in the symmetry of the ground state with respect to the dot centre.

The zero field splitting of the APC and PC in-phase modes in Figure 5.8 (0.55 GHz and 0.41 GHz for the low/high doublet frequency) is a direct measure of the interlayer coupling.

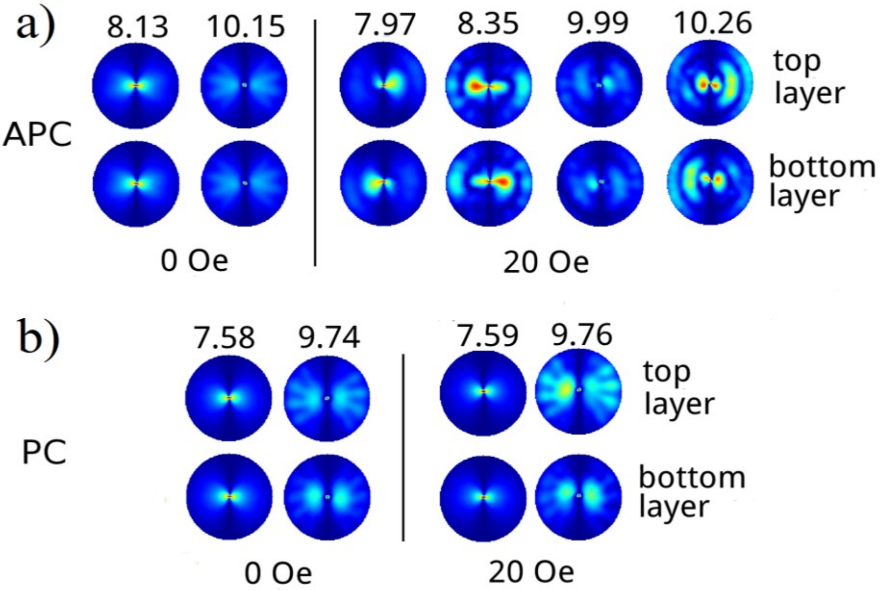

Figure 5.8 The simulated spin wave eigenmodes in the top and bottom layer of the tri-layer DIC Py/Cu(20nm)/Py nanopillars in (a) APC and (b) PC states (reduced dynamic magnetization component $\Delta M_x/M_S$ is presented). On the top of each mode image the corresponding frequency is specified (in GHz). When bias field is applied, there is 180° - phase shift of the moving mode profiles in the APC state, meanwhile in the PC state there is a mirror-like reflection of the phase along a central vertical line.

IEC nanopillar modes

The IEC modes at zero field are the qualitatively the same as the modes in DIC pillar but with different frequencies. Namely the modes are around 8 GHz (1,2 in Figure 5.5d are counter-clockwise (CCW) motion, n=0, *m*=+1) and modes 3,4 around 10 are clockwise (CW) motion, n=0, *m*=-1for PC (1,3) and APC (2,4) configurations as can be seen in Figure 5.9. We can notice that those modes at zero field are of acoustic type (i.e. the two layers response is nearly in-phase) and they are equal to the modes of the DIC nanopillar (Figure 5.8a with zero field),

At higher fields, similarly to observed for DIC dots, spin modes in IEC dots obtain out of phase character. As an example we show modes 5,6,7 in Figure 5.9 taken at field of 270Oe shows the shifted vortices and the optic type mode. All of these modes have low dependence on the field.

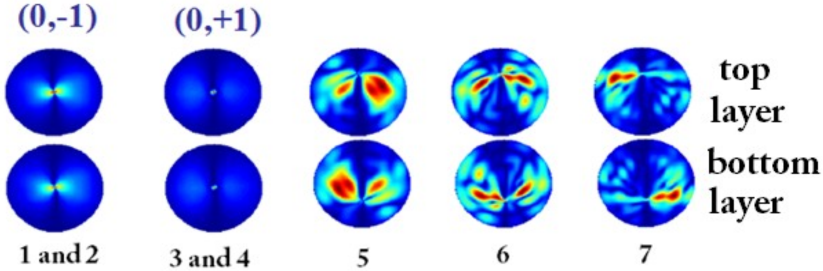

Figure 5.9 Simulated spatial distributions of the vortex dynamic magnetization in the samples (presented ΔMx/Ms) at different fields for IEC nanopillar dots with ACP chirality (numbers are the same modes in Figure 5.5d)

To summarize, magnetization dynamics in the coupled vortex dots in Py/Cu/Py tri-layer nanopillars subject to in plane magnetic field reveals substantial differences with respect to a single dot response. For APC dipolar coupled dots external in plane magnetic field exceeding small (few tens of Oe) critical value leads to excitation of multiple spin wave modes, characterized not only by their strong field dependence, but also their differences in relative phase of the dynamic response of the layers.

5.5 Conclusions:

Study of excited spin wave modes in the presence of lateral dipolar coupling in the vortex ground state of 2D dot arrays shows that it is quite different from one observed for saturated dots. For example, no four-fold anisotropy exists in the vortex ground state. Our measurements demonstrate the essential role of the dynamical magnetostatic interaction on the vortex dot spectra. Especially, the fine structure (the values ω_g, $\Delta\omega_0$ and $\Delta\omega_1$) of the spectra is found to be very sensitive to the interdot coupling. Accounting both the dipolar and quadrupolar contributions yields a good qualitative description of the complicated spin excitation spectra in coupled dot arrays. Contrary to previous believes, the excitation frequencies of the dipolarly-active modes are affected by the interaction for large enough dot separations. For example, even for the separation with the ratio $(a/2R)=2.5$, where dots are usually considered as uncoupled, values of the frequencies ω_g and $\Delta\omega_1$ differs from their limit (isolated vortex) values. The obtained results can serve as a basis for understanding of the propagation of spin excitations in 2D MC consisting of the vortex state magnetic dot arrays.

Broadband magnetization response of vertically coupled vortex state magnetic dots in layered nanopillars is explored as a function of in-plane magnetic field and interlayer separation. For dipolarly coupled circular Py(25nm)/Cu(20nm)/Py(25nm) nanopillars of 600 nm diameter a small in-plane field splits the eigenfrequencies of azimuthal spin wave modes inducing an abrupt transition between in-phase and out-of-phase kinds of the low-lying coupled spin wave modes. The critical field for this splitting is determined by antiparallel chiralities of the vortices in the layers. Qualitatively similar (although more gradual) changes occur also in the exchange coupled Py(25nm)/Cu(1nm)/Py(25nm) tri-layer nanopillars. These findings are in qualitative agreement with micromagnetic dynamic simulations.

To summarize the three new main observations presented in this chapter

1- For qualitative description of the azimuthal spin excitation spectra in coupled dot arrays both the dipolar and quadrupolar contributions should be taken into account. And this coupling is effective in even at big range of dot´s separation.

2- Coupling in the vertcial configuration changes substantially the eignmodes dependence with applied field, which is essentially dependent on the relative chiralities of the coupled layers and their frequencies depend on the spacer thickness between the ferromagnetic layers.

3- For dipolarly coupled nanopillar abrupt transition occurs as in-phase azimuthal modes eigenfrequencies splits to out-of-phase kinds of the low-lying coupled spin wave modes with the application of a small in-plane field. The critical field value for this splitting is determined by antiparallel chiralities of the vortices in the layers. Qualitatively similar (although more gradual) changes occur also in the exchange coupled tri-layer nanopillars.

All these findings are in qualitative agreement with micromagnetic dynamic simulations.

CHAPTER VI: VORTEX DYNAMICS IN NANOSTRUCTURED SUPERCONDUCTORS

6.1 Introduction

A superconducting vortex, similarly to a magnetic vortex in confined conditions, presents a topological magnetic anomaly. The main difference between descriptions of their electromagnetic responses is that, while a magnetic vortex has eigen frequencies, the microwave response of a superconducting vortex is similar to a damped oscillator. This thesis studies, separately, the microwave responses of magnetic (chapters III-V) and superconducting vortices (this chapter) as preliminary step to investigate the dynamics of coupled magnetic and superconducting vortices in ferromagnetic/superconducting FM/SC hybrid structures.

Superconductors with their unique properties, such as the extreme low dissipation, are implemented in many high frequency devices especially those working at high frequencies such as signal filters, receivers, resonators, etc. In the Meissner state the high frequency electrodynamics response can be described mainly by London penetration length and it is mainly real. The real conductivity describes the conductivity of the quasi-particles [205]. In the mixed state the penetration length could be presented as a complex parameter [see [80]] and the electromagnetic response of type II superconductors in a magnetic field is determined mostly by the dynamics of Abrikosov vortices [70].

In the mixed state the high frequency electromagnetic response of the superconductors presents rich features starting from flux creep at low frequencies and with transition from thermal activation to pinning regime at relatively intermediate frequencies where the vortices oscillate around the pining potential in the linear regime: so called ¨Campbell regime¨ [206–208]. Finally, at large drives, the flux flow regime appears where the dissipation is maximized. In real samples, without artificial pinning centers, pinning exists due to multiple sources as imperfections, defect, grain boundaries, lattice mismatch, strain, etc.

Another important phenomena related to collective response of vortices are vortex avalanches. The application of a finite current or step-like increase of the magnetic field, when sample is in the critical state, could destabilize vortex system leading to its collapse to new ground state mediated by vortex avalanches (see for details the introduction chapter).

This chapter will deal with broadband response of Pb films in the critical state. We shall study the microwave stimulated SC vortex depinning and subsequent development of avalanches. Our results allow developing a new method to determine the microwave vortex depining frequency. On the other side, from the exact knowledge of broadband response, we are capable of triggering precisely vortex avalanches in superconducting films.

As we have mentioned in the beginning of this paragraph, one of the main motivations for the inclusion of the study of the superconducting high frequency electromagnetic response in this thesis project was to gain knowledge on reference vortex systems (magnetic dots and superconducting films) before starting to explore the mutual dynamics between the coupled magnetic and the superconducting vortices.

6.1.1 Samples preparation

In order to study the vortex dynamics in superconductors we have chosen Lead films which are simple element type II superconductors. Bulk Lead (Pb) is known to be type-I superconductor with a $T_C = 7.2K$. However, it has been shown that thin Pb films are type-II superconductor. The transition from type I to type II for Pb films occurs below critical thickness of about 250 nm [209].

The Pb thin films were fabricated at the Katholieke Universiteit Leuven[†††]. The Pb was electron-beam evaporated onto liquid nitrogen-cooled Si/SiO_2 substrates. Films were covered with a 20nm-thick protective layer of amorphous Ge.

The 80nm thick Pb films were evaporated in a MBE Varian VT-118 system at a working pressure of 7×10^{-8} Torr with a source material in the crucible of 99.9999 % purity. In order to obtain a smooth film, the

---

[†††] Dr. Silhanek and prof. V. V. Moshchalkov , INPAC, K.U. Leuven

substrate was cooled to 77 K, with a growth rate of 5 Å/s, controlled by mass spectrometer. The average roughness estimated by AFM was 1.2 nm on an area of 1 μm^2. Low angle X-ray Diffraction (XRD) shows periodic oscillations of intensity as a function of angle, a characteristic of highly homogeneous films. High angle XRD shows that Pb has a preferential growth along the (111) direction of the fcc lattice. The structure of the films is textured, meaning that actually not all grains are oriented along (111) direction. Although the effects reported here were observed for Pb films with thickness between 50 and 90 nm and dimensions of 6*5 mm^2, we will concentrate below on representative set of data obtained on the 80nm thick Pb film samples.

It is shown in Figure 6.1a the temperature dependences of the real and imaginary contributions to the susceptibility, which yield the critical temperature T_c=7.2 K typical for Pb type II superconducting thin films [209], [210]. Magnetization curves (Figure 6.1b) indicate the presence of vortex avalanches at sufficiently low temperatures.

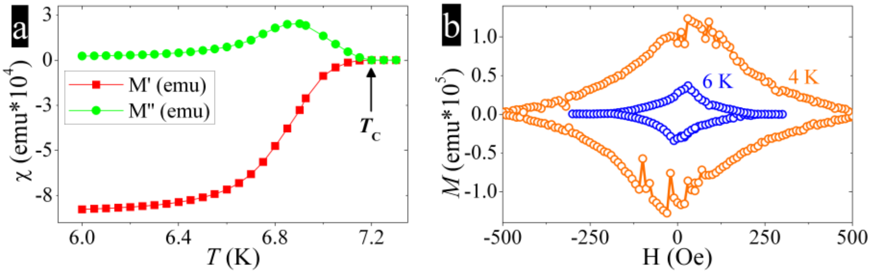

Figure 6.1 (a) Temperature dependence of the real and imaginary parts of the susceptibility (h = 1 Oe, f = 3837 Hz). (b) Typical magnetization hysteresis curves with vortex avalanche regime at low temperatures (4K).

Sample edges were obtained by cleaving after film deposition. The film was placed face-down on the CWG to locate the sample edge above the central conductor so that (h_{rf}) was parallel to the surface but nearly perpendicular to the film edge [microwave field profile for CWG has been described in Chapter 2]. The bias field (H) has been applied perpendicular to the surface and the measurement protocol was with frequency sweeps at a constant dc field.

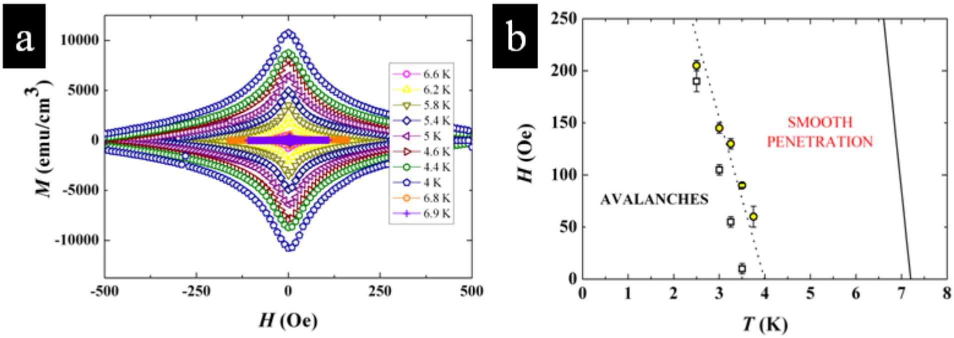

Figure 6.2 (a) Magnetization hysteresis curves at different temperatures. (b) Phase diagram of vortex penetration indicating the transition from smooth penetration to the vortex avalanche regime at low temperatures.

As the magnetization curves were obtained for wide range of tempratures, this permited to estimate the critical currents from bean model as well as to define the phase diagram of the vortex avalanches as shown in Figure 6.2. The phase diagram indicates the presence of vortex avalanches at sufficiently low temperatures below a threshold of tempreture of about 4K.

6.1.2 Methology

The broadband measurements were done in the transmission configuration by means of two ports (1,2) Vector Network Analyzer (VNA) (see methods at chapter II for more details). The microwave drive field (*h_{rf}*) up to 0.11Oe is provided by a coplanar wave guide (CWG) in the TEM mode, Figure 6.3. The signal from the CWG to VNA (after calibration of the external cables and correction for small field independent contributions due to geometric resonances) was analyzed with a model [6] based on the effective uncalibrated microwave permeability parameter:

$$U(f,H_n) = \pm i\left(\frac{\ln\left[S_{21-H_n}(f)\right]}{\ln\left[S_{21-H_{ref}}(f)\right]} - 1\right)$$

neglecting the effect of reflection. Here $S_{21\text{-}H}(f)$; with indexes H_n and H_{ref} are the frequency dependent forward transmissions between ports 1 and 2 measured correspondingly at the applied field H_n, and the reference field H_{ref} (usually the maximum applied field). The imaginary part, Im[U], describes the losses. In order to minimize the influence of field independent "ripples" from the standing waves due to multiple reflection from the connectors, we carried out a differential analysis of U(f,H) by using as H_{ref} the previous value of the magnetic field, H_{n-1}. Since $\ln[S_{21-H}(f)] \sim -\alpha(f,H)$, where α (f,H) is the signal attenuation between the ports 1 and 2, the so-defined function Im[U(f,H)] converts into: $\mathrm{Im}[U'(f,H)] \sim \alpha^{-1}\, \partial\alpha / \partial H$.

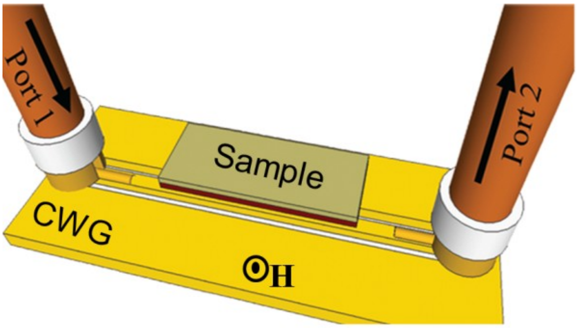

Figure 6.3 Sketch of the CWG with the sample and the magnetic field direction.

6.1.3 The electromagnetic broadband response

Properties of type-II superconductors at high frequencies are influenced by the dissipation and shielding and strongly dependent on the vortex dynamics. So, the broadband measurements depend on the pinning and motion of vortices in the mixed state and their results can be verified by comparing with existing models. Summary of the electromagnetic dynamics of the superconducting vortices has been given in the introduction chapter. Essentially, under the applied microwave current, the vortices would move and dissipate energy, unless they are pinned. The maximum current that a superconductor can stand, a critical current density J_c , is mainly defined by the properties of the pinning [211]. In the linear response regime one assumes that vortices are to be trapped by a pinning potential V(r) and oscillate under the applied a. c. field near its minimum r=0. In these conditions the pinning potential is quantified by the so called Labush constant $\alpha_L=(\partial^2 V/\partial r^2)_{r=0}$ characterizing its curvature at the minimum [81], [206], [212–215]. If the applied frequency is high enough and exceeds the so-called depinning frequency $f_d=\alpha_L/2\pi\eta$ (here η is viscous drag coefficient), the oscillating vortices cease to feel the detail of the pinning potential. This picture describes both, single vortices, in a single vortex pinning regime, and vortex bundles, where collective effects become essential [212]. Usually the information about the Labush constant was obtained from the data on the surface impedance on an assumption that only one kind of pinning is important [74], [120], [216–218], see also references in [82].

Furthermore, the vortex depinning would lead to triggering of avalanches of magnetic flux, which stochastically emerge at weakest pinning points close to the edges of the sample [90], [91], [210]. In thin films, irreproducible flux avalanches involving up to millions of vortices are usually observed. The avalanches are conventionally attributed to thermomagnetic instabilities induced by moving vortices [89–91], [95], [219], [220]. Indeed, the vortex motion locally heats the film, resulting in a local decrease in the pinning strengths and thus developing a positive feedback loop triggering instability [93], [221]. It is still not fully clear to what extent one can control the intermittent flux dynamics in type II superconductors (see, e.g.,[87], [222], [223]). However; recent experiments indicate that the microwave may induce avalanches. Some recent experiments indicate that those avalanches might have very specific frequency dependence containing pronounced peaks at a few specific excitation frequencies [224], indicating a complex microwave vortex depinning. Generally, there exist several ways to trigger avalanches, e.g., by laser [96] or current [97] pulses, due to microwave fields in superconducting resonators or coils [100], [101], [225], etc. The main feature of these methods is that the instability is triggered by a hot spot in the normal state generated by the external perturbation. Therefore, the detailed relationship between the characteristics of the excitation and those of flux pinning is not straightforward.

6.2 Experimental broadband response

In our experiments, the broadband response is proportional to the complex microwave permeability. Therefore we expect to detect the vortex dynamical response to the input *rf* signal. As long as electromagnetic dynamics of the vortices at high frequencies may be dissipative, one would expect the complex effective permeability μ and microwave surface impedance to be affected by the different regimes of vortex electromagnetic dynamics. The imaginary part μ'' conveys the microwave loss of dissipation whereas the real part μ' indicates the flux screening [80]. Microwave losses are expected to increase at the crossover in the flux flow regime due to vortex depinning. Besides, the dissipation may increase due to vortex avalanches as the flux jumps inside the superconductor.

The sample is placed in the experimental setup (insert) and fixed face-down on the CWG with the sample edge above the central conductor. The insert is cooled to about 10K in zero field cooling (ZFC). We start the measurements at a temperature $T=10K > T_c$ to assure that there is no unusual response in the setup (due to contact problems). Effectively, the broadband response shows almost constant signal as a function of the applied magnetic field with a small background ripple ¨noise¨. The broadband response is typically measured at a fixed input rf drive power and temperature, for several fixed magnetic fields from $H<1000$ Oe with steps of 5 Oe, by continuous rf frequency scans between 300kHz and 8 GHz.

After cooling the sample below T_c in ZFC conditions, one starts to notice that the imaginary part of the response Im[U(f,H)] shows decreased and nearly symmetric values in fields (respect zero field), that correspond to the entrance to superconducting state from the normal state.

When we cool the sample further far below T_c , we start to observe terrace like variation in the imaginary part of the response, Im[U(f,H)], and related spike-like anomalies (SLA) in the corresponding Im[U´(f,H)] (i.e. differential absorption as a function of frequency, see Figure 6.4). The comparison between Im[U(f,H)], where the reference field H_{ref} is 500 Oe, and Im[U´(f,H)] demonstrates the relation between these functions and confirms the validity of the differential analysis using Im[U´(f,H)]. These terrace like borders in the Im[U(f,H)] (i.e SLA in Im[U´(f,H)]) show an abrupt increase of the dissipation and have nearly symmetric shape in magnetic field.

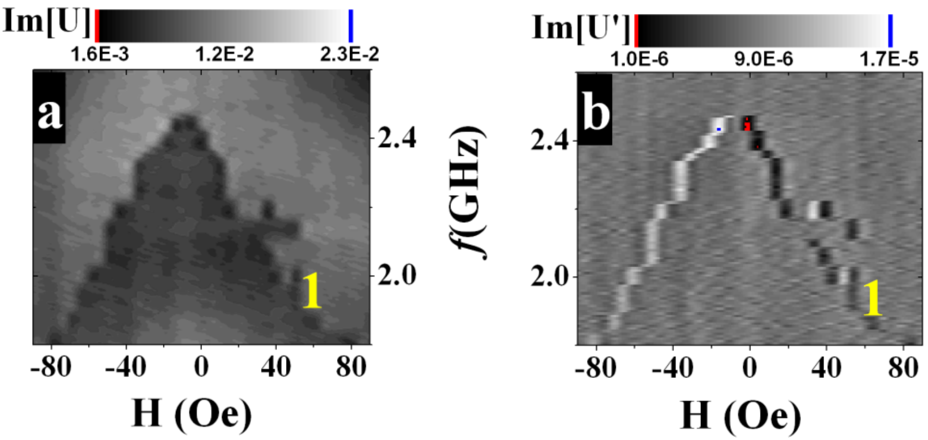

Figure 6.4 Counterplot of (a) the Im[U(f,H)] (H_{ref} is 500Oe)and (b) Im[U´(f,H)] measured for the mode i = 1 at T = 6.1K, h_{rf} = 0.06 Oe.

We attribute the observed SLAs to a microwave induced vortex depinning at the sample edges triggering vortex avalanches but not to *rf* induced vortex depinning itself. The reasons are the following:

(i) These SLAs appear only at low enough temperatures, typically, below 0.8 T_c. Our magnetization measurements, in accordance to the previous reports [92], indicate magnetization steps below (0.6-0.7) T_c (see Figure 6.2b, where the threshold is almost 4K)

(ii) These SLAs diminish when the maximum of the *rf* excitation is shifted from the edge to the film center or the sample is covered by thermal grease.

(iii) Last but not least, these SLAs are observed only above some threshold drive (see further below).

So, along with the broadband capabilities, as we shall demonstrate below, our method provides direct measurements of the vortex depinning frequencies through detection of avalanches triggered in a region of excitation powers, magnetic fields, temperatures, and through continuous frequency sweeps, previously inaccessible to other techniques [74], [75], [125], [217], [218], [226] and references within [82], [99].

Let us compare out experiments with previous ones which report on vortex depinning frequency, for example, with other wideband technique- Corbino disk geometry technique [125], [217], [218]. The above technique mainly provides *information on microwave vortex depinning inside the superconducting sample*, close to the centre of film where microwave field is largest. On the contrary, our metallic coplanar wave guide technique detects microwave vortex dynamics close to the film edge. In addition, the deposition of metallic pads in the Corbino disk geometry should prevent to some extent the creation of avalanches, making difficult the observation of *rf* induced vortex depinning via avalanche detection- subject of the present study.

6.2.4 Field and frequency dependences of the SLAs

As we discussed above, the continuous *rf* frequency scan, (from 300kHz to 8GHz) at fixed temperature and field, induces SLAs at certain drive frequencies. These SLA are spikes due to the anomalous variation of Im[U′(f,H)] as a function of microwave frequency. The corresponding frequencies will be denoted as f_0^i. Although these frequencies f_0^i have nearly symmetric dependence on the magnetic field, several SLAs have shown even more complicated dependences at high frequencies (see the branch i=3 and others SLAs in Figure 6.5). Generally, the values f_0^i show field dependence similar to that observed previously for vortex depinning frequencies (presented in the Introduction chapter).

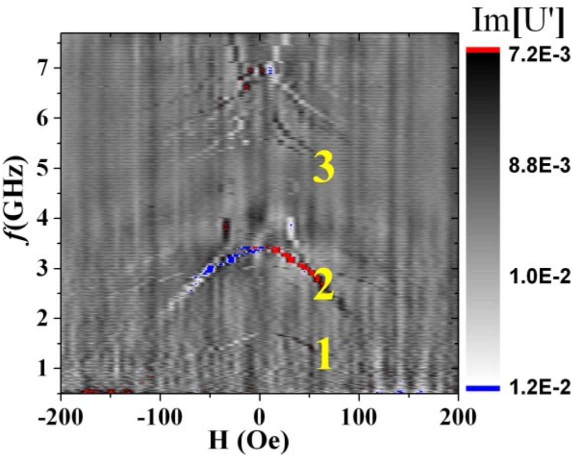

Figure 6.5 Counterplot of Im [U′(f,H)] versus external magnetic field for h_{rf} = 0.1Oe, T = 6.1 K. Marked branches are f_0^i ; with i = 1,2,3 will be further analyzed.

6.2.5 Temperature dependence of the SLA

We observed the SLA mainly at T<0.8T$_c$. Decreasing the temperature expands the magnetic field interval where SLAs are detected and generally increases the characteristic frequency f_0^i . Figure 6.6 shows the magnetic field dependences of the SLAs with i=1,2 $f_0^{1,2}(H)$ for different temperatures.

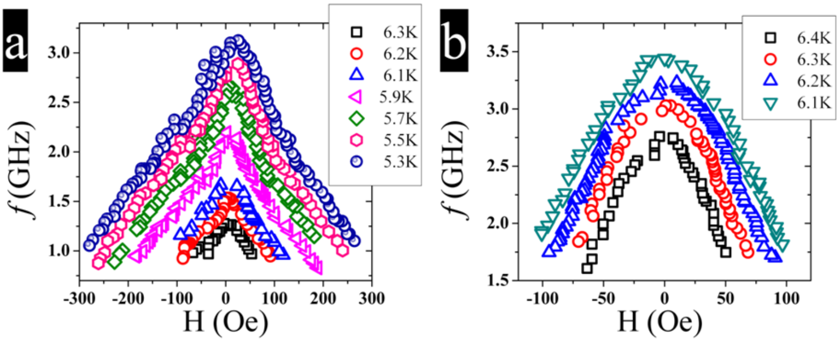

Figure 6.6 Temperature and magnetic field dependences of SLAs f_0^1 (a) and f_0^2 (b) for different temperatures measured at the drive intensity 5dBm.

In order to analyze the temperature dependences of the selected SLAs (i) we take the maximum frequency value at the lowest field at which we can detect the SLAs.Figure 6.7. represent temperature dependencies of SLAs' positions $f_0^i(T)$ for i=1,2,3. One notes that f_0^1 shows a clear tendency to decrease with temperature and vanish at T→T$_c$. At the same time, f_0^3 shows much weaker temperature dependence.

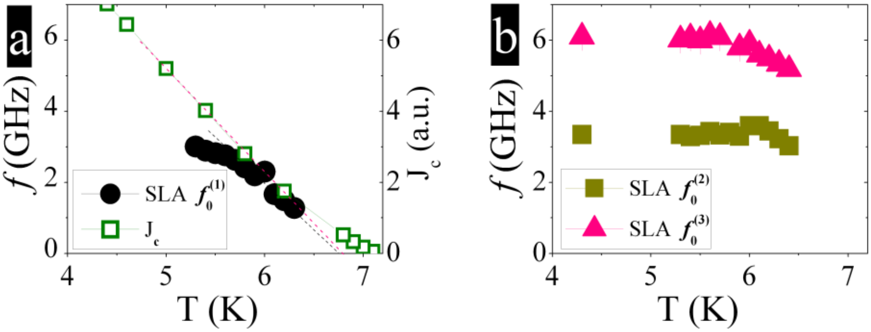

Figure 6.7 (a) Comparison of temperature dependence of low field frequencies f_0^1 and the estimated critical current density J$_c$(T). (b) Temperature dependences of $f^{2,3}(T)$ SLAs.

Interestingly, extrapolating $f_0^1(T)$ to $f = 0$ (see Figure 6.7a) gives a critical temperature very close to that obtained from extrapolating the experimentally measured J$_c$(T), at H=0, from magnetization loops. The similarity of $f_0^1(T)$ and J$_c$(T) supports the suggestion that the lowest frequency branch (i=1) in SLAs is due to avalanches induced by vortex depinning from the weakest pinning sites. Indeed, these thermally activated vortex depinning can limit the critical current. While lower depinning frequencies (f_0^1 branch) correspond to vortex depinning from weakest pinning sites with depinning barrier being strongly reduced as temperature approaches the T$_c$, the pinning sites with stronger pining barriers which correspond to branches $f_0^{2,3}$ are less affected by temperature.

6.2.6 Power dependence of the SLA

The power dependence of the SLA has been verified in order to elucidate the possible influence of *rf* heating on the vortex avalanches, and to investigate how the *rf* triggers the vortex depinning and avalanches. We have investigated the influence of the microwave power on the SLAs in two manners. The first one, by measuring the broadband frequency response with a set of different input powers and secondly, by making single frequency power sweeps. It is shown in Figure 6.8a the frequency dependences of the differential absorption for different microwave powers in the range (-20 to 5) dBm, the *rf* field amplitudes being (0.0067 to 0.11) Oe. Figure 6.8a shows how the SLA with i =0 emerge at lower input powers when rf frequency is swept at a fixed temperature.

Figure 6.8b shows the power dependence (presented in form of estimated *rf* excitation field) for the amplitude of f_0^1 SLA for two different temperatures. Within the precision of our technique we observe that, below some particular (for each branch i) threshold power, the *rf* drive does not depin vortices (Figure 6.8b) and the *SLAs* are absent below some critical amplitude. The threshold value shows a tendency to increase when the temperature is reduced. These experimental facts further confirm that SLAs are related with rf-triggered vortex avalanches induced by vortex depinning.

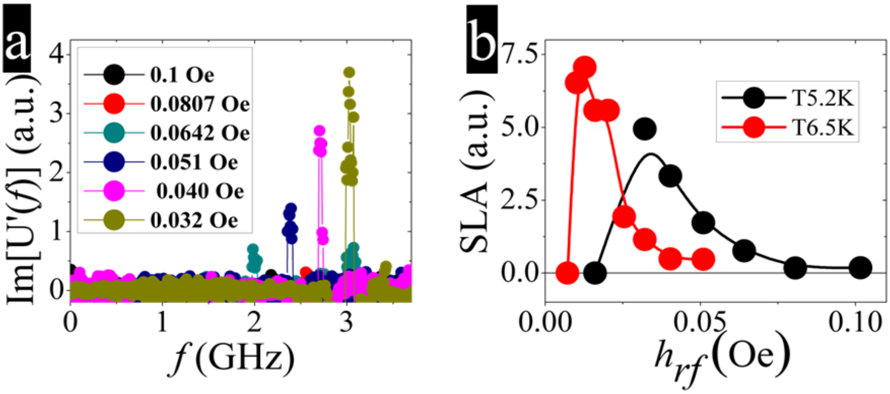

Figure 6.8 (a) Frequency dependence of microwave losses (SLA with i=0) measured with different rf drive fields at a temperature of 5.2K and bias field of 240 Oe. (b) Amplitude of SLA (i=1) as a function of *rf* power (*rf* magnetic field) measured at two different temperatures.

As we shall discuss in more details below, the microwave power exceeding a particular threshold depins specific (for each mode i) vortices at the sample edge which, in turn, facilitates the thermomagnetic instability resulting in flux avalanches (observed as SLAs). Further increase of the *rf* power seems to heat slightly the sample (estimated temperature increase at the maximum *rf* drive does not exceed 0.1K near T_c) decreasing in this way the magnitude of SLAs.

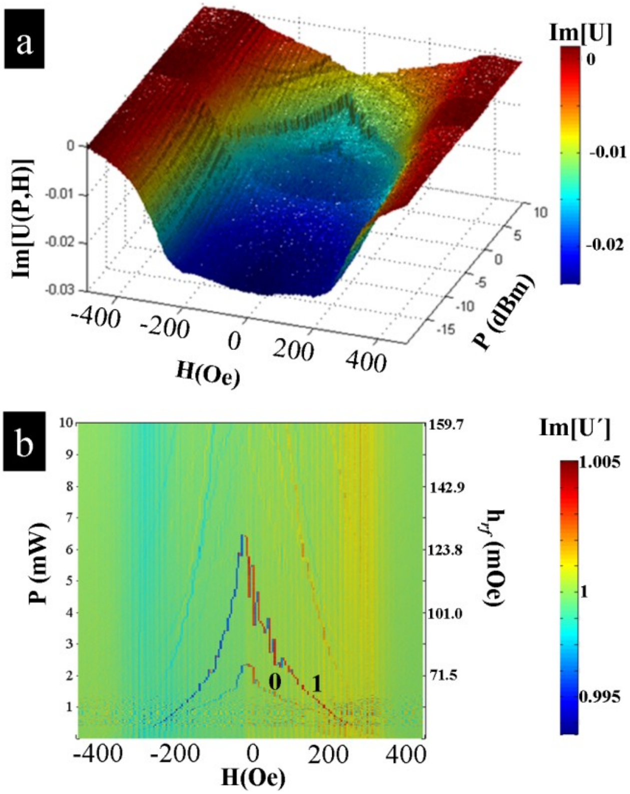

Figure 6.9 (a) 3D Counterplot of the power dependence (in dBm units) Im[U(f,H)] (H_{ref} is 500Oe) as a function of the applied field and the corresponding Im[U′(f,H)] at (b) (in linear mW units and the corresponding *rf* field values); measured for fixed frequency h_{rf} and fixed temperature 2.5 GHz, 5.2K respectively the mode i = 1 is the main dissipative mode.

We stress here that the dependence of the SLAs amplitudes on the rf power reflects abrupt changes in the losses due to avalanches triggered by the edge vortex depinning. This fact can be confirmed by different experimental design, namely by making power sweep at single *rf* frequency. In this manner we avoid influence of the geometrical and ripple peaks in the response. Figure 6.9a presents Im[U(f,H)] for the same temperature as shown inFigure 6.8a i.e. at T = 5.2K. The input power is presented in logarithmic scale (dBm). We note that dBm units are mainly used by engineering terms to present the losses and the noise:

$$\begin{aligned} P_{dBm} &= 10\log_{10}(1000P_W) \\ P_W &= 10^{(P_{dBm}-30)/10} \end{aligned} \tag{6.1}$$

The low microwave power response shows decreased dissipation compared to the normal state dissipation (see Figure 6.9b where the red color presents the maximum dissipation and the blue the lowest. One can notice that the vertical lines (more pronounced in Figure 6.9b), presenting the low dissipation due to the superconducting state, do not change at high powers emphasizing that the temperature of the sample is not substantially affected by the microwave power at these temperatures. Also the low power response does not affect the vortices and no further depinning producing avalanches could be detected unless the power exceeds a particular threshold. Above this field dependent threshold, a specific kind of pinned vortices at the sample edge is released, resulting in sudden increase of the dissipation as clearly seen from terrace-like variation of the imaginary part of microwave permeability. The main variation of dissipation between terraces corresponds to the f_0^1 branch as can be seen from comparison of Im[U(f,H)], reflecting in most contrast branch, and the Im[U′(f,H)] dependence (see Figure 6.9b).

6.2.7 Microwave vortex depinning and thermomagnetic instability: model

Within the linear response model, the vortices are trapped by a pinning potential and oscillate under the applied a. c. field around the pinning potential minimum. The Labush constant $\alpha_L=(\partial^2 V/\partial r^2)_{r=0}$ characterize the pinning potential curvature at the minimum r=0 [81], [206], [212–215]. When the *rf* frequency exceeds the depinning frequency $f_d=\alpha_L/2\pi\eta$, the vortex motion changes from weakly dissipative pinned to dissipative vortex motion regime. This picture describes both, single vortices in a single vortex pinning regime and vortex bundles, where collective effects become essential [212]. In the latter case η is a friction constant for the vortex system.

In accordance with the mentioned linear-response model [81], [206], [212–215], the absorbed power, $Q_{vm}(f)$, can be represented as:

$$Q_{vm} = Q_c \frac{f^2}{f^2 + f_d^2}, f_d = \frac{\alpha_L}{2\pi\eta}, Q_c \propto \frac{J_0^2}{\eta} \qquad (6.2)$$

Here J_0 is the microwave current amplitude while f_d is the so-called depinning frequency. Hence, the absorption is low at f « f_d and saturates at $f \geq f_d$. Therefore it is natural to expect that for a given drive intensity the conditions for nucleation of the thermomagnetic instability are frequency dependent. The depinning frequency f_d (similarly to critical current) is determined by the details of vortex pinning[82].

In particular, f_d is very different in bulk and film superconductors [227]. In the case of films, f_d strongly depends on the film thickness approaching from MHz (bulk superconductors) to GHz range for thin films [226]. Each type of defects has its own f_d, therefore one can expect successive depinning of different defects.

Along the simplified model [93] of the thermomagnetic instability (which ignores thermal conductance along the film) the onset of thermomagnetic instability is usually related to the so-called ¨stability parameter¨ :

$\beta = Q_{vm} /(\gamma C+C_S)\Delta T$. The absorbed microwave power, Q_{vm} , is balanced by heating of the Pb film, $\gamma C\Delta T$ (γ is the density of Pb), during the avalanche process in combination with heat removal into the substrate ($C_S\Delta T$) where C_S is the heat transfer coefficient of the metal-substrate interface. Our experimental observations could be qualitatively understood from the analysis of the dependence of the thermal stability factor β on the external microwave power and magnetic field. Since $Q_{vm}(f)$ rapidly increases at

$f_0 \approx f_d$ one can expect that at this frequency the thermo magnetic instability starts. For β =1 at some value Q_0 of the absorbed power and using Equation(6.2) we get that the instability threshold corresponds to the frequency

$$f_0 = f_d \sqrt{\frac{Q_C}{Q_C - Q_0}} \tag{6.3}$$

Therefore, increasing the microwave power (and the rf amplitude J_0) leads to a decrease of the signal frequency required for reaching the instability criterion, β =1. This is also in agreement with the experiment, see Figure 6.8.

The observed dependence of the critical frequency on the magnetic field can be explained as follows. On the one hand, $Q_{vm} \propto H$ through the total magnetic flux. On the other hand, the heat capacity can contain field independent (phonons) and can be proportional to magnetic field quasiparticle contributions [93], [228]. Therefore, the stability parameter could be expected to depend on the external field as $\beta \approx H/(H + const)$, which linearly increases at small fields and should consequently reduce the critical frequency with increasing magnetic field, as observed, see Figure 6.6a,b.

Let us compare the experimentally measured depinning frequencies with those one could expect based on average material characteristics. The typical value of $f_d = \alpha_L/2\pi\eta$[75] can be estimated using $k_p = \pi B_c^2/\mu_0$ (where k_p is the pinning constant (in some sense analogous to the Labusch constant), B_c is the thermodynamic critical field) and $\eta(T) = \Phi_0 B_{c2}(T)/\rho_n$[69]. Here Φ_0 is the magnetic flux quantum, B_{c2} is the upper critical field, ρ_n is the normal state resistivity. For the temperature range of interest (T=5-6K) with B_c =50Oe, B_{c2} =500Oe and ρ_n =4 μΩcm we get f_d =400MHz, which is a factor of 6–10 smaller than the SLA frequencies observed experimentally. This is, of course, a very crude estimate since the parameters used (particularly the resistivity) could be different at the film edge where the rf-induced vortex depinning takes place.

6.2.8 Reproducibility of the measurements

The presented above results are highly reproducible both with time and even changing slightly the experimental parameters. The same features could be obtained repeating the experiment in a few hours later provided that there was no substantial heating of the sample above critical temperature (see Figure 6.10).

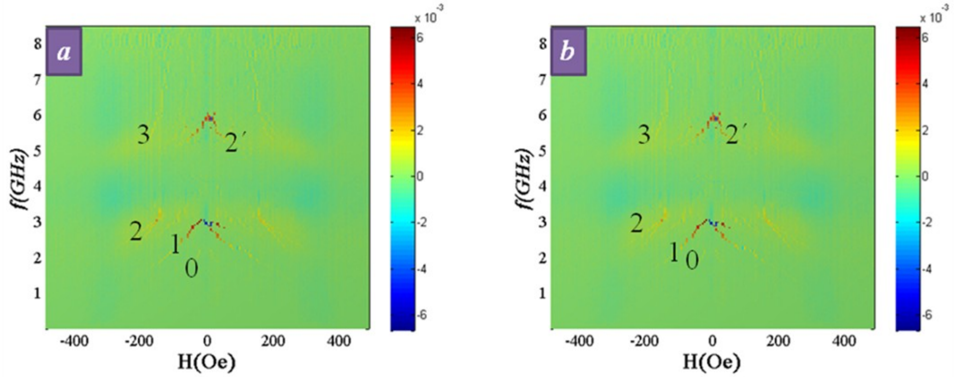

Figure 6.10 (a) Counterplot of Im [U′(f,H)] versus external magnetic field for h_{rf} = 0.1Oe, T = 5.2 K. Marked branches are f_0^i ; with i = 0,1,2,3 analyzed previously and new i=2′. (b) Same experiment as (b) repeated few hours later.

Therefore, a particular set of observed depinning frequencies is a kind of "fingerprint" of vortex pinning potential determined by details of the edge pinning in a given sample. Since the depinning frequencies for different defects are controlled by disorder, the value of f_d is expected to be sensitive to thermal annealing. Indeed, we found experimentally that increasing the temperature to 20K does not influence the observed effects. Heating to 150K keeps SLA modes continous dependence with field, while ¨annealing¨ of the defects with a thermal excursion to 300K during 5 h changes both the critical frequencies $f_0^{(i)}$ and their field dependences (see Figure 6.11).

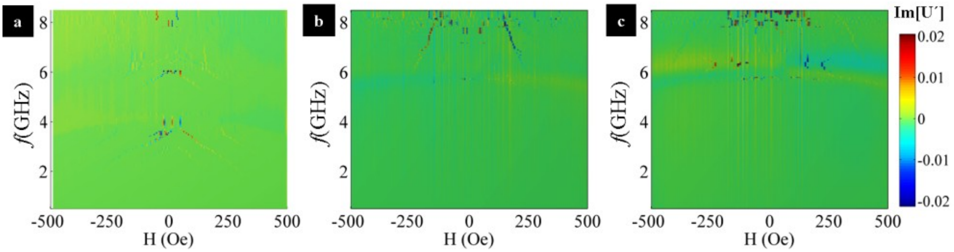

Figure 6.11 Counterplots of Im [U´(f,H)] versus external magnetic field for h_{rf} = 0.1Oe, T = 4, (a) . Plot (b) shows results after heating to 150K, while plot (c) shows results obtained after heating to 300 K.

6.3 Summary & Conclusions

In this Chapter, we presented observation of abrupt changes (SLAs) in the microwave permeability of thin type II superconducting Pb films as a function of frequency in the presence of an out of plane magnetic field. We interpret these changes as generated by flux avalanches triggered by microwave depinning of superconducting vortices at the sample edges. The experimental results are described in terms of the linear response model.

We suggest that the vortex avalanches are triggered by the edge vortex depinning occurring at well defined frequencies of the *rf* drive. The edge vortices are usually the most strongly pinned by the edge defects and therefore could act as "nails" for the rest of the vortex system keeping it in the critical state. The edges recover the superconducting state after the avalanches expand inside the film [98]. This scenario is also supported by the experimental fact that the observed effects are strongest and symmetric *vs.* applied external magnetic field when *rf* drive is applied across one of the film edges.

We show here that broadband measurements of the permeability at different microwave powers allow determining the vortex depinning frequencies in the cases when different types of defects are present. This method allows one to determine f_d for the different sources of pinning in a more-or-less model-free way.

Previous implementation of superconducting striplines and coplanar waveguides was aimed mainly at the improvement of microwave transmission [229]. Our results, however, show that in principle superconducting stripline based techniques [98], [229] might also be employed for broadband detection of vortex depinning frequencies due to generated avalanches, once impedance mismatch between normal rf launchers and superconducting transmission striplines is minimized. The presence of multiple depinning frequencies in the experiments with superconducting strips was probably observed in Ref.[229]; the authors there, however, did not consider reproducible spikes in the microwave losses as evidence of the vortex depinning frequencies.

In *Conclusion*, we have introduced a method to determine edge vortex depinning frequencies in superconducting films via broadband detection of rf-triggered avalanches. This method allows the detection of multiple depinning frequencies reflecting different pinning sources. Besides, our results indicate the possibility to effectively trigger vortex avalanches by using a specific set of microwave frequencies.

6.3.9 Perspectives

The knowledge of the vortex depinning frequencies opens the opportunity to control and manipulate superconducting vortices using relatively weak microwave excitations at specific frequencies. In the broader perspective, our work introduces a novel method to investigate depinning of the vortex system close to critical conditions.

Also, as future perspective, the work suggests to carry out the visualization of the avalanches induced by the rf vortex depinning a magneto-optic experiments in the presence of broadband microwave sweeps. The fine power control in such experiment could unveil details of avalanche processes triggered by vortex rf induced vortex depinning from samples edges.

Precise knowledge of the edge depinning frequencies of superconducting vortices is of importance for understanding vortex pinning, control over the vortex avalanches in high frequency applications of superconductors and could be effective way for noise reduction from trapped vortices in sensitive SQUID detectors through microwave assisted vortex depinning.

GENERAL CONCLUSION

In this thesis the vortex electromagnetic response of the systems with topological anomalies in the form of magnetic or superconducting vortices has been studied by means of a broadband microwave inductive technique.

In order to investigate the ***magnetic vortex dynamics***, the spin waves in the magnetic vortex state were studied in the simplest geometry of circular Py magnetic dots. For this model system the dependence of the vortex dynamics on different parameters such as aspect ratio, thickness, coupling (lateral or vertical), was investigated. The influence of the applied bias field on spin waves in the vortex state was studied in detail. Special attention has been paid to the dynamic and static response for the range of parameters when a metastable double vortex state is expected to emerge. The experimental results were compared with numerical or analytical studies.

As to the broadband response in ***superconducting vortex,*** in the mixed state, the experimental results allowed us to introduce a novel method to determine the vortex depinning frequency for edge vortices trapped in the superconducting films via detection of rf-triggered avalanches. This method determines directly a set of vortex depinning frequencies originated from different pinning source. It also permits to investigate various parameters affecting the depinning processes such as temperature, the magnetic field, and the applied rf power. Besides, our results indicate the possibility to effectively trigger vortex avalanches by using a specific set of microwave frequencies.

Below we summarize the most important original results of the thesis:

In ***Chapter III*** we have investigated the main spinwave eigenmodes excited in circular Permalloy dots with moderate aspect ratio range (0.03 - 0.1). We observed that the splitting of the azimuthal mode doublets is in a good agreement with the theoretical prediction which accounts the hybridization of the SW modes with the gyrotropic mode of the vortex.

We found that the splitting of the second azimuthal mode shows a maximum as a function of the dot´s aspect ratio.
We prove experimentally that the *main azimuthal modes exist only in the low field range below the vortex nucleation field*. We also present the first observation of the transformation of azimuthal modes to a qualitatively new type of spinwave modes with in plane bias field. We found the fundamental differences in the field dependence of spin wave modes excited with perpendicular (with abrupt change between the stable single vortex and shifted vortex states where spin waves are excited in whole dot) and parallel pumping (with the *spin waves are excited only close to the shifted vortex core*).

Chapter IV presents the investigation of spin waves in the metastable double vortex state in the circular Py dots. The response in this relatively long living state has been studied both statically and dynamically. The magnetization dynamics in this state is characterized by a *new kind of domain wall oscillations*. We have identified related quasi one-dimensional localized spin wave modes confined along the domain walls, connecting vortex cores with edge half-antivortices. These spinwave modes are the so-called "Winter´s magnons" - spin waves analogous to the displacement waves of strings¨. The observed eigen-frequencies were found to be in a good agreement with the DW flexural oscillation frequencies calculated in the magnetostatic approximation assuming Neel-type domain walls connecting the vortex and antivortex cores.

Chapter V presents the study the lateral coupling effect on spin excitation frequencies in the vortex ground state. We found that the coupling in the vortex state for the 2D magnetic dot arrays is quite different from the one found before for saturated or single domain dots. We demonstrate that *the dynamical magnetostatic interaction plays an essential role in the vortex dot excitation spectra*. Accounting both the dipolar and quadrupolar contributions yields a good qualitative description of the complicated spin excitation spectra in coupled dot arrays.
We also studied the influence of vertical coupling in layered nanopillars on spin waves. We explored the coupling effect for two types of nanopillar with different interlayer separation and investigated the influence of in-plane magnetic field on eigenmodes. For both types of the studied coupled

vortices (dipolar coupled and exchange coupled) we found that the dipolar interaction is the main contribution to the coupling. Its influence on the eigenmodes depends on the relative chiralities of the coupled vortices. A particularly interesting observation is that for the dipolar coupled circular nanopillars a *small in-plane field* splits the eigenfrequencies of the azimuthal spin wave modes *inducing an abrupt transition between in-phase and out-of-phase kinds of the low-lying coupled spin wave modes* excited in each of the coupled layers.

Dynamic simulations show that the critical field for this splitting is determined by antiparallel chiralities of the vortices in the layers. Qualitatively similar (although more gradual) changes occur also for the exchange coupled tri-layer nanopillars. These findings are in qualitative agreement with micromagnetic dynamic simulations.

Chapter VI presents the experimental results obtained for the broadband response in superconducting vortex state in plane Pb films. The main results are related to the development of a *new method to investigate vortex depinning frequency via broadband detection of rf-triggered avalanches*.

We observed that these vortex avalanches; triggered by the edge vortex depinning, occur at well defined frequencies of the electromagnetic excitation and may be detected experimentally as abrupt changes in the microwave permeability. We found that these abrupt changes are strongest and symmetric respect to the applied external magnetic field when an electromagnetic excitation is applied across the film´s edges. In addition we observed that the amplitude of the abrupt changes in the electromagnetic permeability has a non-monotonous dependence on the excitation power. Our method allows, for the first time, direct detection of multiple vortex depinning frequencies presented in real superconductors films. The experimental results have been described in terms of the linear response and thermal instability models. Finally, *our results indicate the possibility to trigger effectively the vortex avalanches in superconducting devices by using specific set of microwave frequencies*.

CONCLUSIONES GENERALES

La presente tesis estudia la respuesta electromagnética de banda ancha en sistemas magnéticos y superconductores con anomalías topológicas en forma de vórtices.

Con el fin de estudiar la dinámica de ***los vórtices magnéticos***, se ha investigado en una geometría lo más simplificada posible, las ondas de espín en el estado de vórtice magnético, en particular con la forma de puntos ¨discos¨ magnéticos circulares. Para estos sistemas-modelo, se ha investigado la dependencia de la dinámica de vórtice en función de diferentes parámetros, como son la relación entre el diámetro y el grosor de las muestras, y su acoplamiento (lateral o vertical). La influencia del campo magnético aplicado sobre las ondas de espín en el estado vórtice ha sido estudiada en detalle. Se ha puesto especial atención a la respuesta dinámica y estática en el estado metaestable de doble vórtice. Además, los resultados experimentales han sido comparados con estudios numéricos y analíticos.

Respecto a la respuesta en banda ancha de las sistemas de vórtices superconductores, gracias a los resultados experimentales, se ha introducido un nuevo método para determinar la frecuencia de desenganchamiento (depinning) de los ***vórtices superconductores***. Se trata de frecuencias de "depinning" de los vórtices atrapados en el borde de las películas superconductoras, que son determinadas a través de la detección del desencadenamiento de avalanchas en banda-ancha. Este método permite estudiar las frecuencias de desenganchamiento (depinning) de los vórtices que tienen su origin de diferentes fuentes de desenganchamiento. También nos permite investigar diversos parámetros que afectan a los procesos de desenganchamiento en función de la temperatura, de la frecuencia, del campo magnético y de la potencia de microondas aplicada. Además, nuestros resultados indican la posibilidad de desencadenar avalanchas de vórtices de forma eficaz mediante el uso de un conjunto de frecuencias específicas de microondas.

A continuación resumiremos los resultados originales más destacados de la tesis:

En el ***capítulo III***, hemos investigado los modos propios de las ondas de espín excitados en puntos circulares de Permalloy (Py), los cuales poseen una relación moderada ¨intermedio¨entre su grosor y su radio (0.03 – 0.1). En estos puntos circulares, hemos observado que el desdoblamiento de los modos azimutales está en un buen acuerdo con la predicción teórica que representa la hibridación de los modos de ondas de espín con el modo girotrópico del vórtice. Así como, que el desdoblamiento del segundo modo azimutal muestra un máximo en función de la relación ente el grosor y el radio.
También *hemos demostrado experimentalmente que los principales modos azimutales solo existen en un rango de campos magnéticos bajos, por debajo del campo de la nucleación del vórtice*. Hemos realizado la primera observación experimental de la transformación de los modos azimutales en un nuevo tipo de ondas de espín, aplicando el campo magnético en el plano de los puntos de Py.
En particular, *hemos encontrado diferencias fundamentales en la dependencia de los modos de onda de espín con el campo magnético externo aplicado*: estimulándolo con una excitación perpendicular al campo aplicado (con un cambio brusco entre el estado con un único vórtice estable y el estado de vórtice desplazado, en donde las ondas de espín están excitadas en todo el área del punto) y con una excitación paralelo al campo aplicado (con las ondas de espín están excitadas sólo cerca del núcleo del vórtice desplazado).

El ***capítulo IV*** presenta la investigación de las ondas de espín en el estado metaestable de doble vórtice en puntos circulares de Py. La respuesta en este estado, que tiene tiempo de vida relativamente largo, ha sido estudiada tanto estática como dinámicamente. La dinámica de la magnetización en este estado, se caracteriza por una nueva forma de oscilaciones en las paredes de dominio. *Hemos identificado modos de onda de espín localizados cuasi unidimensional y confinados a lo largo de las paredes de dominio,* que conectan los núcleos de los vórtices con los antivortices en el borde. Estos modos de ondas de espín son los llamados "Magnones de Winter", que son ondas de espín análogas a las ondas de desplazamiento en una cuerda. Se encontró que las frecuencias propias observadas están en un buen acuerdo con las frecuencias de oscilación flexibles de las paredes de dominio, calculadas dentro de la aproximación magnetostática, y asumiendo que las paredes de dominio, conectan a los vórtices y a los núcleos de las anti-vórtices, son de tipo Néel.

El ***V capítulo*** presenta un estudio detallado sobre el efecto del acoplamiento lateral y vertical sobre las frecuencias de excitación de ondas de espín en el estado fundamental del vórtice. Hemos descubierto que el acoplamiento lateral en el estado vórtice para redes 2D de puntos magnéticas es bastante diferente de la que se había encontrado antes para puntos saturados o mono-dominio. *Se ha demostrado que la interacción dinámica magnetostática, tiene un papel fundamental sobre el espectro de excitación vórtice en dichos puntos*. Teniendo en cuenta las contribuciones dipolares y cuadrupolares, hemos obtenido una buena descripción cualitativa de los espectros de excitación en redes de puntos acoplados de Permalloy.
También se ha estudiado la influencia del acoplamiento vertical, en nanopilares con varias capas, sobre las ondas de espín. Se exploró el efecto del acoplamiento en dos tipos de nanopilares, con diferente separación entre las capas ferromagneticas, y se ha investigado la influencia del campo magnético aplicado en el plano sobre los modos propios. Para ambos tipos de vórtices acoplados (acoplo dipolar y acoplo de canje) se encontró que la interacción dipolar es la principal contribución en el acoplo. Su influencia en los modos propios depende de las quiralidades relativas de los vórtices acoplados. Queremos destacar que hemos observado un efecto particularmente interesante para los nanopilares circulares con acoplo dipolar: *cuando aplicamos un pequeño campo en el plano, las frecuencias propias de los modos de onda de espín azimutal se desdoblan, induciendo una transición abrupta entre modos tipo en fase y modos tipo antifase entre las capas acopladas*. Las simulaciones dinámicas han mostrado que el campo crítico para este desdoblamiento está determinado por las quiralidades antiparalelas de los vórtices en las capas. Además, se producen cambios cualitativamente similares (aunque más graduales) en los nanopilares tri-capa con acoplo de canje. Estos resultados están en un buen acuerdo cualitativo con las simulaciones dinámicas micromagnéticas.

El ***capítulo VI*** presenta los resultados experimentales obtenidos en sistemas de vórtices superconductores. Se trata de las primeras medidas experimentales que directamente localizan las frecuencias de desenganchamiento (depinning) de los vórtices atrapados en el borde de las películas superconductoras a través de la detección en banda ancha. A dichas frecuencias tiene lugar el desencadenamiento de avalanchas inducidas.

Estas avalanchas, provocadas por el desenganchamiento de los vórtices de borde, producen en una excitación electromagnética a frecuencias bien definidas, que se detectan experimentalmente como cambios bruscos en la permeabilidad magnética.

Hemos estudiado estos cambios bruscos en función del campo magnético externo aplicado, cuando la excitación electromagnética se aplica a largo de los bordes de la película. Se ha observado que la amplitud de los cambios abruptos en la permeabilidad electromagnética tiene una dependencia no monótona respecto a la energía de excitación aplicada.

Los resultados experimentales obtenidos han permitido introducir un nuevo método para determinar la frecuencia de desenganchamiento de vórtices superconductores. Este método permite la detección directa de múltiples frecuencias de desenganchamiento.

Las medidas de permeabilidad de microondas, utilizando diferentes potencias de excitación, permiten la determinación directa de las frecuencias de desenganchamiento de los vórtices en los casos en que hay diferentes tipos de defectos. Los resultados experimentales han sido descritos en términos del modelo de respuesta lineal y de inestabilidad termomagnética. Finalmente, nuestros resultados indican la posibilidad de desencadenar avalanchas de vórtices superconductores atrapados en dispositivos comerciales de forma eficaz mediante el uso de frecuencias específicas de microondas.

REFERENCES

[1] L. Landau and E. Lifshitz, “On the theory of the dispersion of magnetic permeability in ferromagnetic bodies,” *Phys. Z. Sowietunion*, vol. 8, pp. 153–169, 1935.

[2] T. L. Gilbert, “Lagrangian formulation of the gyromagnetic equation of the magnetization field,” *Physical Review*, vol. 100, p. 1243, 1955.

[3] J. H. E. GRIFFITHS, “Anomalous High-frequency Resistance of Ferromagnetic Metals,” *Nature*, vol. 158, no. 4019, pp. 670–671, Nov. 1946.

[4] C. Kittel, “On the Theory of Ferromagnetic Resonance Absorption,” *Physical Review*, vol. 73, no. 2, pp. 155–161, Jan. 1948.

[5] C. Kittel, *Introduction to solid state physics*. Wiley, 1995, p. 688.

[6] S. S. Kalarickal, P. Krivosik, M. Wu, C. E. Patton, M. L. Schneider, P. Kabos, T. J. Silva, and J. P. Nibarger, “Ferromagnetic resonance linewidth in metallic thin films: Comparison of measurement methods,” *Journal of Applied Physics*, vol. 99, no. 9, p. 093909, 2006.

[7] G. N. Kakazei, Y. G. Pogorelov, M. D. Costa, T. Mewes, P. E. Wigen, P. C. Hammel, V. O. Golub, T. Okuno, and V. Novosad, “Origin of fourfold anisotropy in square lattices of circular ferromagnetic dots,” *Physical Review B*, vol. 74, no. 6, pp. 1–4, Aug. 2006.

[8] P. Grünberg, R. Schreiber, Y. Pang, M. Brodsky, and H. Sowers, “Layered magnetic structures: Evidence for antiferromagnetic coupling of Fe layers across Cr interlayers.,” *Physical review letters*, vol. 57, no. 19. pp. 2442–2445, Nov-1986.

[9] M. Salamon, S. Sinha, J. Rhyne, J. Cunningham, R. Erwin, J. Borchers, and C. Flynn, “Long-range incommensurate magnetic order in a Dy-Y multilayer,” *Physical Review Letters*, vol. 56, no. 3, pp. 259–262, Jan. 1986.

[10] A. Cebollada, J. Martnez, J. Gallego, J. de Miguel, R. Miranda, S. Ferrer, F. Batallán, G. Fillion, and J. Rebouillat, “Antiferromagnetic ordering in Co-Cu single-crystal superlattices,” *Physical Review B*, vol. 39, no. 13, pp. 9726–9729, May 1989.

[11] P. Grünberg, “Layered magnetic structures in research and application,” *Acta Materialia*, vol. 48, no. 1, pp. 239–251, Jan. 2000.

[12] A. Layadi, “Effect of biquadratic coupling and in-plane anisotropy on the resonance modes of a trilayer system,” *Physical Review B*, vol. 65, no. 10, pp. 1–7, Feb. 2002.

[13] J. Lindner and K. Baberschke, “Ferromagnetic resonance in coupled ultrathin films,” *Journal of Physics: Condensed Matter*, vol. 15, no. 5, pp. S465–S478, Feb. 2003.

[14] J. Ben Youssef and a. Layadi, “Ferromagnetic resonance study of Permalloy/Cu/Co/NiO spin valve system,” *Journal of Applied Physics*, vol. 108, no. 5, p. 053913, 2010.

[15] A. Wachowiak, J. Wiebe, M. Bode, O. Pietzsch, M. Morgenstern, and R. Wiesendanger, “Direct observation of internal spin structure of magnetic vortex cores.,” *Science (New York, N.Y.)*, vol. 298, no. 5593, pp. 577–80, Oct. 2002.

[16] R. p. Cowburn, D. K. Koltsov, A. O. Adeyeye, M. E. Welland, and D. M. Tricker, “Single-domain circular nanomagnets,” *Physical Review Letters*, vol. 83, p. 1042, 1999.

[17] T. Shinjo, T. Okuno, R. Hassdorf, K. Shigeto, and T. Ono, “Magnetic Vortex Core Observation in Circular Dots of Permalloy,” *Science*, vol. 289, no. 5481, pp. 930–932, Aug. 2000.

[18] K. Y. Guslienko, “Magnetic Vortex State Stability , Reversal and Dynamics in Restricted Geometries,” *Journal of Nanoscience and Nanotechnology*, pp. 2745–2760, 2008.

[19] J. Shibata, K. Shigeto, and Y. Otani, “Dynamics of nano-scale magnetic vortices in ferromagnetic dot arrays,” *Journal of Magnetism and Magnetic Materials*, vol. 272–276, pp. 1688–1689, May 2004.

[20] K. Y. Guslienko and V. Novosad, “Vortex state stability in soft magnetic cylindrical nanodots,” *Journal of Applied Physics*, vol. 96, no. 8, p. 4451, 2004.

[21] K. L. Metlov and K. Yu, “Stability of magnetic vortex in soft magnetic nano-sized circular cylinder,” *Journal of Magnetism and Magnetic Materials*, vol. 245, pp. 1015–1017, 2002.

[22] K. Y. Guslienko, V. Novosad, Y. Otani, H. Shima, and K. Fukamichi, “Field evolution of magnetic vortex state in ferromagnetic disks,” *Applied Physics Letters*, vol. 78, no. 24, p. 3848, 2001.

[23] K. Guslienko, V. Novosad, Y. Otani, H. Shima, and K. Fukamichi, “Magnetization reversal due to vortex nucleation, displacement, and annihilation in submicron ferromagnetic dot arrays,” *Physical Review B*, vol. 65, no. 2, pp. 1–10, Dec. 2001.

[24] M. Kammerer, M. Weigand, M. Curcic, M. Noske, M. Sproll, A. Vansteenkiste, B. Van Waeyenberge, H. Stoll, G. Woltersdorf, C. H. Back, and G. Schuetz, “Magnetic vortex core reversal by excitation of spin waves.,” *Nature communications*, vol. 2, p. 279, Jan. 2011.

[25] S. Bader, “Colloquium: Opportunities in nanomagnetism,” *Reviews of Modern Physics*, vol. 78, no. 1, pp. 1–15, Jan. 2006.

[26] V. S. Pribiag, I. N. Krivorotov, G. D. Fuchs, P. M. Braganca, O. Ozatay, J. C. Sankey, D. C. Ralph, and R. A. Buhrman, “Magnetic vortex oscillator driven by d.c. spin-polarized current,” *Nature Physics*, vol. 3, no. 7, pp. 498–503, May 2007.

[27] G. N. Kakazei, P. E. Wigen, K. Y. Guslienko, R. W. Chantrell, N. a. Lesnik, V. Metlushko, H. Shima, K. Fukamichi, Y. Otani, and V. Novosad, “In-plane and out-of-plane uniaxial anisotropies in rectangular arrays of circular dots studied by ferromagnetic resonance,” *Journal of Applied Physics*, vol. 93, no. 10, p. 8418, 2003.

[28] A. A. Thiele, “Steady-State motion of magnetic Domains,” *Physical Review Letters*, vol. 30, p. 230, 1973.

[29] K. Y. Guslienko, B. a. Ivanov, V. Novosad, Y. Otani, H. Shima, and K. Fukamichi, “Eigenfrequencies of vortex state excitations in magnetic submicron-size disks,” *Journal of Applied Physics*, vol. 91, no. 10, p. 8037, 2002.

[30] J. Park, P. Eames, D. Engebretson, J. Berezovsky, and P. Crowell, “Imaging of spin dynamics in closure domain and vortex structures,” *Physical Review B*, vol. 67, no. 2, pp. 1–4, Jan. 2003.

[31] V. Novosad, M. Grimsditch, K. Guslienko, P. Vavassori, Y. Otani, and S. Bader, “Spin excitations of magnetic vortices in ferromagnetic nanodots,” *Physical Review B*, vol. 66, no. 5, pp. 2–5, Aug. 2002.

[32] V. Novosad, F. Fradin, P. Roy, K. Buchanan, K. Guslienko, and S. Bader, “Magnetic vortex resonance in patterned ferromagnetic dots,” *Physical Review B*, vol. 72, no. 2, pp. 1–5, Jul. 2005.

[33] K. Guslienko, X. Han, D. Keavney, R. Divan, and S. Bader, "Magnetic Vortex Core Dynamics in Cylindrical Ferromagnetic Dots," *Physical Review Letters*, vol. 96, no. 6, pp. 1–4, Feb. 2006.

[34] K. Y. Guslienko, "Low-frequency vortex dynamic susceptibility and relaxation in mesoscopic ferromagnetic dots," *Applied Physics Letters*, vol. 89, no. 2, p. 022510, 2006.

[35] A. Vogel, A. Drews, T. Kamionka, M. Bolte, and G. Meier, "Influence of Dipolar Interaction on Vortex Dynamics in Arrays of Ferromagnetic Disks," *Physical Review Letters*, vol. 105, no. 3, pp. 1–4, Jul. 2010.

[36] M. Buess, R. Höllinger, T. Haug, K. Perzlmaier, U. Krey, D. Pescia, M. Scheinfein, D. Weiss, and C. Back, "Fourier Transform Imaging of Spin Vortex Eigenmodes," *Physical Review Letters*, vol. 93, no. 7, pp. 1–4, Aug. 2004.

[37] K. Guslienko, W. Scholz, R. Chantrell, and V. Novosad, "Vortex-state oscillations in soft magnetic cylindrical dots," *Physical Review B*, vol. 71, no. 14, pp. 1–9, Apr. 2005.

[38] X. Zhu, Z. Liu, V. Metlushko, P. Grütter, and M. Freeman, "Broadband spin dynamics of the magnetic vortex state: Effect of the pulsed field direction," *Physical Review B*, vol. 71, no. 18, pp. 2–5, May 2005.

[39] J. Park and P. Crowell, "Interactions of Spin Waves with a Magnetic Vortex," *Physical Review Letters*, vol. 95, no. 16, pp. 1–4, Oct. 2005.

[40] B. Ivanov and C. Zaspel, "High Frequency Modes in Vortex-State Nanomagnets," *Physical Review Letters*, vol. 94, no. 2, pp. 23–26, Jan. 2005.

[41] F. Hoffmann, G. Woltersdorf, K. Perzlmaier, A. N. Slavin, V. S. Tiberkevich, A. Bischof, D. Weiss, and C. H. Back, "Mode

degeneracy due to vortex core removal in magnetic disks," *Physical Review B*, pp. 1–5, 2007.

[42] K. Y. Guslienko, "Magnetic Vortex State Stability, Reversal and Dynamics in Restricted Geometries," *Journal of Nanoscience and Nanotechnology*, vol. 8, no. 6, pp. 2745–2760, Jul. 2008.

[43] I. Neudecker, G. Woltersdorf, B. Heinrich, T. Okuno, G. Gubbiotti, and C. Back, "Comparison of frequency, field, and time domain ferromagnetic resonance methods," *Journal of Magnetism and Magnetic Materials*, vol. 307, no. 1, pp. 148–156, Dec. 2006.

[44] I. Neudecker, K. Perzlmaier, F. Hoffmann, G. Woltersdorf, M. Buess, D. Weiss, and C. Back, "Modal spectrum of permalloy disks excited by in-plane magnetic fields," *Physical Review B*, vol. 73, no. 13, pp. 1–9, Apr. 2006.

[45] G. de Loubens, A. Riegler, B. Pigeau, F. Lochner, F. Boust, K. Guslienko, H. Hurdequint, L. Molenkamp, G. Schmidt, A. Slavin, V. Tiberkevich, N. Vukadinovic, and O. Klein, "Bistability of Vortex Core Dynamics in a Single Perpendicularly Magnetized Nanodisk," *Physical Review Letters*, vol. 102, no. 17, pp. 1–4, May 2009.

[46] M. Lai and C. Liao, "Size dependence of C and S states in circular and square Permalloy dots," *Journal of Applied Physics*, vol. 103, no. 7, p. 07E737, 2008.

[47] C. Vaz, M. Kläui, L. Heyderman, C. David, F. Nolting, and J. Bland, "Multiplicity of magnetic domain states in circular elements probed by photoemission electron microscopy," *Physical Review B*, vol. 72, no. 22, pp. 1–8, Dec. 2005.

[48] I. L. Prejbeanu, M. Natali, L. D. Buda, U. Ebels, A. Lebib, Y. Chen, and K. Ounadjela, "In-plane reversal mechanisms in circular Co dots," *Journal of Applied Physics*, vol. 91, no. 10, pp. 10–12, 2002.

[49] M. Demand, M. Hehn, K. Ounadjela, R. L. Stamps, E. Cambril, A. Cornette, and F. Rousseaux, “Magnetic domain structures in arrays of submicron Co dots studied with magnetic force microscopy,” *Journal of Applied Physics*, vol. 87, no. 9, p. 5111, 2000.

[50] R. Mattheis, D. Berkov, and N. Gorn, “Magnetic reversal in ultra-thin nanoshaped magnetic dots: numerical simulations and Kerr observation,” *Journal of Magnetism and Magnetic Materials*, vol. 199, pp. 216–218, 1999.

[51] M. Rahm, M. Schneider, J. Biberger, R. Pulwey, J. Zweck, and D. Weiss, “Vortex nucleation in submicrometer ferromagnetic disks,” *Applied Physics Letters*, vol. 82, no. 23, pp. 4110–4112, 2003.

[52] M. J. Pechan, C. Yu, D. Owen, J. Katine, L. Folks, and M. Carey, “Vortex magnetodynamics: Ferromagnetic resonance in permalloy dot arrays,” *Journal of Applied Physics*, vol. 99, no. 8, p. 08C702, 2006.

[53] J. Shibata and Y. Otani, “Magnetic vortex dynamics in a two-dimensional square lattice of ferromagnetic nanodisks,” *Physical Review B*, vol. 70, no. 1, pp. 2–5, Jul. 2004.

[54] S. Sugimoto, Y. Fukuma, S. Kasai, T. Kimura, A. Barman, and Y. Otani, “Dynamics of Coupled Vortices in a Pair of Ferromagnetic Disks,” vol. 197203, no. May, pp. 11–14, 2011.

[55] O. V. Sukhostavets, J. M. Gonzalez, and K. Y. Guslienko, “Magnetic Vortex Excitation Frequencies and Eigenmodes in a Pair of Coupled Circular Dots,” *Applied Physics*, vol. 4, pp. 4–6, 2011.

[56] A. Fert and E. Al, “Recent developments and emerging directions in spintronics,” *Proceed. Magnetic Single Nano-Object Workshop & School*, pp. 4–5.

[57] N. Locatelli, V. V. Naletov, J. Grollier, G. de Loubens, V. Cros, C. Deranlot, C. Ulysse, G. Faini, O. Klein, and a. Fert, “Dynamics of

two coupled vortices in a spin valve nanopillar excited by spin transfer torque,” *Applied Physics Letters*, vol. 98, no. 6, p. 062501, 2011.

[58] K. Y. Guslienko, K. S. Buchanan, S. D. Bader, and V. Novosad, “Dynamics of coupled vortices in layered magnetic nanodots,” *Applied Physics Letters*, vol. 86, no. 22, p. 223112, 2005.

[59] S. Wintz, T. Strache, M. Ko□rner, M. Fritzsche, D. Markó, I. Mo□nch, R. Mattheis, J. Raabe, C. Quitmann, J. McCord, a. Erbe, and J. Fassbender, “Direct observation of antiferromagnetically oriented spin vortex states in magnetic multilayer elements,” *Applied Physics Letters*, vol. 98, no. 23, p. 232511, 2011.

[60] G. Gubbiotti, M. Madami, S. Tacchi, G. Carlotti, and T. Okuno, “Field dependence of spin excitations in NiFe/Cu/NiFe trilayered circular dots,” *Physical Review B*, vol. 73, no. 14, pp. 1–6, Apr. 2006.

[61] P. Vavassori, V. Bonanni, a. Busato, G. Gubbiotti, M. Madami, a. O. Adeyeye, S. Goolaup, N. Singh, C. Spezzani, and M. Sacchi, “Static and dynamical properties of circular NiFe/Cu/Co nanodisks,” *Journal of Applied Physics*, vol. 103, no. 7, p. 07C512, 2008.

[62] K. Buchanan, K. Guslienko, A. Doran, A. Scholl, S. Bader, and V. Novosad, “Magnetic remanent states and magnetization reversal in patterned trilayer nanodots,” *Physical Review B*, vol. 72, no. 13, pp. 1–8, Oct. 2005.

[63] K. Buchanan, K. Guslienko, A. Doran, A. Scholl, S. Bader, and V. Novosad, “Magnetic remanent states and magnetization reversal in patterned trilayer nanodots,” *Physical Review B*, vol. 72, no. 13, pp. 1–8, Oct. 2005.

[64] V. Naletov, G. de Loubens, G. Albuquerque, S. Borlenghi, V. Cros, G. Faini, J. Grollier, H. Hurdequint, N. Locatelli, B. Pigeau, A. Slavin, V. Tiberkevich, C. Ulysse, T. Valet, and O. Klein,

"Identification and selection rules of the spin-wave eigenmodes in a normally magnetized nanopillar," *Physical Review B*, vol. 84, no. 22, pp. 1–23, Dec. 2011.

[65] H. K. Onnes, "The resistance of pure mercury at helium temperatures," *Commun. Phys. Lab. Univ. Leiden*, vol. 12, 1911.

[66] F. London and H. London, "The Electromagnetic Equations of the Supraconductor," *Proceedings of the Royal Society A Mathematical Physical and Engineering Sciences*, vol. 149, no. 866, pp. 71–88, 1935.

[67] W. Meissner and R. Ochsenfeld, "Ein neuer Effekt bei Eintritt der Supraleitfähigkeit," *Naturwissenschaften*, vol. 21, no. 44, pp. 787–788, 1933.

[68] V. L. Ginzburg and L. D. Landau, "On the theory of superconductivity," *Zh. Eksp. Teor. Fi.*, vol. 20, pp. 1064–1082, 1950.

[69] J. Bardeen and M. Stephen, "Theory of the Motion of Vortices in Superconductors," *Physical Review*, vol. 140, no. 4A, pp. A1197–A1207, Nov. 1965.

[70] A. A. Abrikosov, "On the magnetic properties of superconductors of the second group," *Zh. Eksp. Teor. Fiz.*, vol. 32, p. 1442, 1957.

[71] J. F. Sierra, "Magnetization Dynamics in Magnetic and Superconducting Nanostructures," Ph.D Thesis, UAM, 2008.

[72] J. Pearl, "Current distribution in superconducting films carrying quantized fluxoids," *Applied Physics Letters*, vol. 5, no. 4, p. 65, 1964.

[73] E. Brandt, "Vortex-vortex interaction in thin superconducting films," *Physical Review B*, vol. 79, no. 13, pp. 1–9, Apr. 2009.

[74] M. Golosovsky, M. Tsindlekht, and D. Davidov, “High-frequency vortex dynamics in,” *Superconductor Science and Technology*, vol. 9, no. 1, pp. 1–15, Jan. 1996.

[75] J. Gittleman and B. Rosenblum, “Radio-Frequency Resistance in the Mixed State for Subcritical Currents,” *Physical Review Letters*, vol. 16, no. 17, pp. 734–736, Apr. 1966.

[76] Z. D. Wang, Q. Wang, and P. C. W. Fung, “Electromagnetic and thermomagnetic properties of high- superconductor in its mixed state: the single-vortex-motion model,” *Superconductor Science and Technology*, vol. 9, no. 5, pp. 333–346, May 1996.

[77] M. Tinkham, *Introduction to superconductivity*. Dover Publications, 2004, p. 454.

[78] P. Anderson and Y. Kim, “Hard Superconductivity: Theory of the Motion of Abrikosov Flux Lines,” *Reviews of Modern Physics*, vol. 36, no. 1, pp. 39–43, Jan. 1964.

[79] N. Pompeo and E. Silva, “Reliable determination of vortex parameters from measurements of the microwave complex resistivity,” *Physical Review B*, vol. 78, no. 9. pp. 094503–, 2008.

[80] M. Coffey and J. Clem, “Unified theory of effects of vortex pinning and flux creep upon the rf surface impedance of type-II superconductors,” *Physical Review Letters*, vol. 67, no. 3, pp. 386–389, Jul. 1991.

[81] E. Brandt, “Penetration of magnetic ac fields into type-II superconductors,” *Physical Review Letters*, vol. 67, no. 16, pp. 2219–2222, Oct. 1991.

[82] M. Bonura, a Agliologallitto, M. Livigni, and a Martinelli, “Depinning frequency in a heavily neutron-irradiated MgB2 sample,” *Physica C: Superconductivity*, vol. 468, no. 24, pp. 2372–2377, Dec. 2008.

[83] C. P. Bean, “Magnetization of High-Field Superconductors,” *Reviews of Modern Physics*, vol. 36, no. 1, pp. 31–39, Jan. 1964.

[84] E. H. Brandt, “Superconductors and Vortices at Radio Frequency Magnetic Fields,” in *talk presented in (Padova) Italy*, 2010.

[85] E. H. Brandt, M. V. Indenbom, and A. Forkl, “Type-II Superconducting Strip in Perpendicular Magnetic Field,” *Europhysics Letters (EPL)*, vol. 22, no. 9, pp. 735–740, Jun. 1993.

[86] E. Zeldov, J. Clem, M. McElfresh, and M. Darwin, “Magnetization and transport currents in thin superconducting films,” *Physical Review B*, vol. 49, no. 14, pp. 9802–9822, Apr. 1994.

[87] E. Altshuler and T. H. Johansen, “Colloquium: Experiments in vortex avalanches,” *Reviews of Modern Physics*, vol. 76, no. 2, pp. 471–487, Apr. 2004.

[88] U. Bolz, B. Biehler, D. Schmidt, B.-U. Runge, and P. Leiderer, “Dynamics of the dendritic flux instability in YBa 2 Cu 3 O 7 − δ films,” *Europhysics Letters (EPL)*, vol. 64, no. 4, pp. 517–523, Nov. 2003.

[89] D. V. Denisov, a. L. Rakhmanov, D. V. Shantsev, Y. M. Galperin, and T. H. Johansen, “Dendritic and uniform flux jumps in superconducting films,” *Physical Review B*, vol. 73, no. 1, pp. 1–7, Jan. 2006.

[90] I. S. Aranson, A. Gurevich, M. S. Welling, R. J. Wijngaarden, V. K. Vlasko-Vlasov, V. M. Vinokur, and U. Welp, “Dendritic Flux Avalanches and Nonlocal Electrodynamics in Thin Superconducting Films,” *Physical Review Letters*, vol. 94, no. 3, pp. 1–4, Jan. 2005.

[91] V. V. Yurchenko, T. H. Johansen, and Y. M. Galperin, “Dendritic flux avalanches in superconducting films,” *Low Temperature Physics*, vol. 35, no. 8, p. 619, 2009.

[92] H. Radovan and R. Zieve, “Vortex microavalanches in superconducting Pb thin films,” *Physical Review B*, vol. 68, no. 22, pp. 1–6, Dec. 2003.

[93] E. R. Nowak, O. W. Taylor, L. Liu, H. M. Jaeger, and T. I. Selinder, “Magnetic flux instabilities in superconducting niobium rings: Tuning the avalanche behavior,” *Physical Review B*, vol. 55, no. 17, pp. 11702–11705, May 1997.

[94] S. S. James, C. D. Dewhurst, R. A. Doyle, D. M. Paul, Y. Paltiel, E. Zeldov, and A. M. Campbell, “Flux pinning , surface and geometrical barriers in YNi 2 B 2 C,” *Physica C*, pp. 173–177, 2000.

[95] I. Aranson, A. Gurevich, and V. Vinokur, “Vortex Avalanches and Magnetic Flux Fragmentation in Superconductors,” *Physical Review Letters*, vol. 87, no. 6, pp. 6–9, Jul. 2001.

[96] P. Leiderer, J. Boneberg, P. Brüll, V. Bujok, and S. Herminghaus, “Nucleation and growth of a flux instability in superconducting YBa2Cu3O7-x films,” *Physical Review Letters*, vol. 71, no. 16, pp. 2646–2649, Oct. 1993.

[97] A. V. Bobyl, D. V. Shantsev, T. H. Johansen, W. N. Kang, H. J. Kim, E. M. Choi, and S. I. Lee, “Current-induced dendritic magnetic instability in superconducting MgB2 films,” *Applied Physics Letters*, vol. 80, no. 24, p. 4588, 2002.

[98] G. Ghigo, F. Laviano, L. Gozzelino, R. Gerbaldo, E. Mezzetti, E. Monticone, and C. Portesi, “Evidence of rf-driven dendritic vortex avalanches in MgB[sub 2] microwave resonators,” *Journal of Applied Physics*, vol. 102, no. 11, p. 113901, 2007.

[99] G. Ghigo, R. Gerbaldo, L. Gozzelino, F. Laviano, G. Lopardo, E. Monticone, C. Portesi, and E. Mezzetti, “Local thermal bistability in MgB[sub 2] microwave coplanar resonators: Opposite jumpwise

response to weak-link switching and to vortex avalanches," *Applied Physics Letters*, vol. 94, no. 5, p. 052505, 2009.

[100] P. D. J. Cuadra-Solís, J. M. Hernández, A. García-Santiago, J. Tejada, J. Noskovic, A. Pidik, and M. Grajcar, "Vortex Avalanches Induced by Single High-Frequency Pulses in MgB2 Films," *Journal of Superconductivity and Novel Magnetism*, vol. 24, no. 1–2, pp. 395–400, Oct. 2010.

[101] G. Ghigo, F. Laviano, L. Gozzelino, R. Gerbaldo, E. Mezzetti, E. Monticone, and C. Portesi, "Evidence of rf-driven dendritic vortex avalanches in MgB[sub 2] microwave resonators," *Journal of Applied Physics*, vol. 102, no. 11, p. 113901, 2007.

[102] G. Ghigo, R. Gerbaldo, L. Gozzelino, F. Laviano, and E. Mezzetti, "Switching response of MgB_{2} thin-film microwave resonators due to local nonlinear Joule heating," *Physical Review B*, vol. 82, no. 5, pp. 1–7, Aug. 2010.

[103] B. Hillebrands and K. Ounadjela, Eds., *Spin Dynamics in Confined Magnetic Structures I*, vol. 83. Berlin, Heidelberg: Springer Berlin Heidelberg, 2002.

[104] C. Bilzer, "Microwave susceptibility of thin ferromagnetic films: metrology and insight into magnetization dynamics," Universite Paris-Sud 11, France, 2007.

[105] W. Dietrich, W. E. Proebster, and P. Wolf, "Nanosecond Switching in Thin Magnetic Films," *IBM Journal of Research and Development*, vol. 4, no. 2, pp. 189–196, Apr. 1960.

[106] T. J. Silva, C. S. Lee, T. M. Crawford, and C. T. Rogers, "Inductive measurement of ultrafast magnetization dynamics in thin-film Permalloy," *Journal of Applied Physics*, vol. 85, no. 11, p. 7849, 1999.

[107] S. S. Kalarickal, P. Krivosik, M. Wu, C. E. Patton, M. L. Schneider, P. Kabos, T. J. Silva, and J. P. Nibarger, “Ferromagnetic resonance linewidth in metallic thin films: Comparison of measurement methods,” *Journal of Applied Physics*, vol. 99, no. 9, p. 093909, 2006.

[108] B. Hillebrands and A. Thiaville, *Spin Dynamics in Confined Magnetic Structures III*, vol. 101. Springer Berlin Heidelberg, 2006, p. 345.

[109] G. Gubbiotti, G. Carlotti, T. Okuno, T. Shinjo, F. Nizzoli, and R. Zivieri, “Brillouin light scattering investigation of dynamic spin modes confined in cylindrical Permalloy dots,” *Physical Review B*, vol. 68, no. 18, pp. 1–7, Nov. 2003.

[110] B. Argyle, E. Terrenzio, and J. Slonczewski, “Magnetic Vortex Dynamics Using the Optical Cotton-Mouton Effect,” *Physical Review Letters*, vol. 53, no. 2, pp. 190–193, Jul. 1984.

[111] M. R. Freeman and J. F. Smyth, “Picosecond time-resolved magnetization dynamics of thin-film heads,” *Journal of Applied Physics*, vol. 79, no. 8, p. 5898, 1996.

[112] M. H. Kryder and F. B. Humphrey, “A Nanosecond Kerr Magneto-Optic Camera,” *Review of Scientific Instruments*, vol. 40, no. 6, p. 829, 1969.

[113] “http://www.physik.uni-regensburg.de/forschung/back/magnet/more1.php.” [Online]. Available: http://www.physik.uni-regensburg.de/forschung/back/magnet/more1.php.

[114] S. Tamaru, J. A. Bain, R. J. M. van de Veerdonk, T. M. Crawford, M. Covington, and M. H. Kryder, “Imaging of quantized magnetostatic modes using spatially resolved ferromagnetic resonance,” *Journal of Applied Physics*, vol. 91, no. 10, p. 8034, 2002.

[115] G. Schütz, W. Wagner, W. Wilhelm, P. Kienle, R. Zeller, R. Frahm, and G. Materlik, “Absorption of circularly polarized x rays in iron,” *Physical Review Letters*, vol. 58, no. 7, pp. 737–740, Feb. 1987.

[116] B. H. Kamel, *Spin Dynamics in Confined Magnetic Structures II*, vol. 87. Berlin, Heidelberg: Springer Berlin Heidelberg, 2003.

[117] D. A. Bonn, D. C. Morgan, and W. N. Hardy, “Split-ring resonators for measuring microwave surface resistance of oxide superconductors,” *Review of Scientific Instruments*, vol. 62, no. 7, p. 1819, 1991.

[118] F. Zuo, M. Salamon, E. Bukowski, J. Rice, and D. Ginsberg, “Microwave dissipation in single-crystal high-Tc superconductors,” *Physical Review B*, vol. 41, no. 10, pp. 6600–6604, Apr. 1990.

[119] J. Owliaei, S. Sridhar, and J. Talvacchio, “Field-dependent crossover in the vortex response at microwave frequencies in YBa_{2}Cu_{3}O_{7-δ} films,” *Physical Review Letters*, vol. 69, no. 23, pp. 3366–3369, Dec. 1992.

[120] M. Golosovsky, M. Tsindlekht, H. Chayet, and D. Davidov, “Vortex depinning frequency in YBa2Cu3O7-x superconducting thin films: Anisotropy and temperature dependence,” *Physical Review B*, vol. 50, no. 1, pp. 470–477, Jul. 1994.

[121] S. Revenaz, D. Oates, D. Labbé-Lavigne, G. Dresselhaus, and M. Dresselhaus, “Frequency dependence of the surface impedance of YBa2Cu3O7-δ thin films in a dc magnetic field: Investigation of vortex dynamics,” *Physical Review B*, vol. 50, no. 2, pp. 1178–1189, Jul. 1994.

[122] N. Pompeo, “Microwave complex response in superconducting thin films in magnetic fields,” Ph.D thesis, Universit`a degli Studi Roma Tre, 2005.

[123] E. Ritz, “Dynamic behavior of correlated electrons in the insulating doped semiconductor Si: P,” Ph.D thesis, Justus-Liebig-Universität Gießen, 2009.

[124] A. Schwartz, M. Scheffler, and S. Anlage, “Determination of the magnetization scaling exponent for single-crystal La0.8Sr0.2MnO3 by broadband microwave surface impedance measurements,” *Physical Review B*, vol. 61, no. 2, pp. R870–R873, Jan. 2000.

[125] J. C. Booth, D. H. Wu, and S. M. Anlage, “A broadband method for the measurement of the surface impedance of thin films at microwave frequencies,” *Review of Scientific Instruments*, vol. 65, no. 6, p. 2082, 1994.

[126] E. Silva, N. Pompeo, and S. Sarti, “Wideband microwave measurements in Nb/Pd 84 Ni 16 /Nb structures and comparison with thin Nb films,” *Superconductor Science and Technology*, vol. 24, no. 2, p. 024018, Feb. 2011.

[127] F. Aliev, J. Sierra, A. Awad, G. Kakazei, D.-S. Han, S.-K. Kim, V. Metlushko, B. Ilic, and K. Guslienko, “Spin waves in circular soft magnetic dots at the crossover between vortex and single domain state,” *Physical Review B*, vol. 79, no. 17, pp. 1–7, May 2009.

[128] J. F. Sierra, V. V. Pryadun, F. G. Aliev, S. E. Russek, M. García-Hernández, E. Snoeck, and V. V. Metlushko, “Temperature dependent dynamic and static magnetic response in magnetic tunnel junctions with Permalloy layers,” *Applied Physics Letters*, vol. 93, no. 17, p. 172510, 2008.

[129] D. Chumakov, J. McCord, R. Schäfer, L. Schultz, H. Vinzelberg, R. Kaltofen, and I. Mönch, “Nanosecond time-scale switching of permalloy thin film elements studied by wide-field time-resolved Kerr microscopy,” *Physical Review B*, vol. 71, no. 1, Jan. 2005.

[130] D. H. Kim, H. H. Kim, C.-Y. You, and H.-S. Kim, “Optimization of Ferromagnetic Resonance Spectra Measuring Procedure for

Accurate Gilbert Damping Parameter in Magnetic Thin Films Using a Vector Network Analyzer,” *Journal of Magnetics*, vol. 16, no. 3, pp. 206–210, Sep. 2011.

[131] “Rogers Corporation, RO4000® series high frequency Circuit materials manuel.”

[132] “Rogers Corporation, MWI-2010 Transmission line modeling software, (Version 2.2).”

[133] C. Bilzer, T. Devolder, P. Crozat, C. Chappert, S. Cardoso, and P. P. Freitas, “Vector network analyzer ferromagnetic resonance of thin films on coplanar waveguides: Comparison of different evaluation methods,” *Journal of Applied Physics*, vol. 101, no. 7, p. 074505, 2007.

[134] B. Kuanr, R. Camley, and Z. Celinski, “Extrinsic contribution to Gilbert damping in sputtered NiFe films by ferromagnetic resonance,” *Journal of Magnetism and Magnetic Materials*, vol. 286, pp. 276–281, Feb. 2005.

[135] C. Bilzer, T. Devolder, P. Crozat, and C. Chappert, “Open-Circuit One-Port Network Analyzer Ferromagnetic Resonance,” *IEEE Transactions on Magnetics*, vol. 44, no. 11, pp. 3265–3268, Nov. 2008.

[136] C. Bilzer, T. Devolder, J.-V. Kim, G. Counil, C. Chappert, S. Cardoso, and P. P. Freitas, “Study of the dynamic magnetic properties of soft CoFeB films,” *Journal of Applied Physics*, vol. 100, no. 5, p. 053903, 2006.

[137] R. P. Cowburn, “Room Temperature Magnetic Quantum Cellular Automata,” *Science*, vol. 287, no. 5457, pp. 1466–1468, Feb. 2000.

[138] P. R. Krauss, “Fabrication of planar quantum magnetic disk structure using electron beam lithography, reactive ion etching, and chemical mechanical polishing,” *Journal of Vacuum Science &*

Technology B: Microelectronics and Nanometer Structures, vol. 13, no. 6, p. 2850, Nov. 1995.

[139] F. Rousseaux, “Study of large area high density magnetic dot arrays fabricated using synchrotron radiation based x-ray lithography,” *Journal of Vacuum Science & Technology B: Microelectronics and Nanometer Structures*, vol. 13, no. 6, p. 2787, Nov. 1995.

[140] A. Fernandez, P. J. Bedrossian, S. L. Baker, S. P. Vernon, and D. R. Kania, “Magnetic force microscopy of single-domain cobalt dots patterned using interference lithography,” *IEEE Transactions on Magnetics*, vol. 32, no. 5, pp. 4472–4474, 1996.

[141] G. N. Kakazei, P. E. Wigen, K. Y. Guslienko, V. Novosad, a. N. Slavin, V. O. Golub, N. a. Lesnik, and Y. Otani, “Spin-wave spectra of perpendicularly magnetized circular submicron dot arrays,” *Applied Physics Letters*, vol. 85, no. 3, p. 443, 2004.

[142] X. Zhu, Z. Liu, V. Metlushko, P. Grütter, and M. Freeman, “Broadband spin dynamics of the magnetic vortex state: Effect of the pulsed field direction,” *Physical Review B*, vol. 71, no. 18, pp. 2–5, May 2005.

[143] K. Y. Guslienko, B. a. Ivanov, V. Novosad, Y. Otani, H. Shima, and K. Fukamichi, “Eigenfrequencies of vortex state excitations in magnetic submicron-size disks,” *Journal of Applied Physics*, vol. 91, no. 10, p. 8037, 2002.

[144] M. Buess, T. P. J. Knowles, R. Höllinger, T. Haug, U. Krey, D. Weiss, D. Pescia, M. R. Scheinfein, and C. H. Back, “Excitations with negative dispersion in a spin vortex,” *Physical Review B*, pp. 1–6, 2005.

[145] F. Giesen, J. Podbielski, T. Korn, and D. Grundler, “Multiple ferromagnetic resonance in mesoscopic permalloy rings,” *Journal of Applied Physics*, vol. 97, no. 10, p. 10A712, 2005.

[146] B. Van Waeyenberge, A. Puzic, H. Stoll, K. W. Chou, T. Tyliszczak, R. Hertel, M. Fähnle, H. Brückl, K. Rott, G. Reiss, I. Neudecker, D. Weiss, C. H. Back, and G. Schütz, “Magnetic vortex core reversal by excitation with short bursts of an alternating field.,” *Nature*, vol. 444, no. 7118, pp. 461–4, Nov. 2006.

[147] A. A. Awad, K. Y. Guslienko, J. F. Sierra, G. N. Kakazei, V. Metlushko, and F. G. Aliev, “Precise probing spin wave mode frequencies in the vortex state of circular magnetic dots,” *Applied Physics Letters*, vol. 96, no. 1, p. 012503, 2010.

[148] K. Y. Guslienko, A. N. Slavin, V. Tiberkevich, and S.-K. Kim, “Dynamic origin of azimuthal modes splitting in vortex-state magnetic dots.,” *Physical review letters*, vol. 101, no. 24, p. 247203, Dec. 2008.

[149] G. Gubbiotti, M. Conti, G. Carlotti, P. Candeloro, E. D. Fabrizio, K. Y. Guslienko, A. Andre, C. Bayer, and a N. Slavin, “Magnetic field dependence of quantized and localized spin wave modes in thin rectangular magnetic dots,” *Journal of Physics: Condensed Matter*, vol. 16, no. 43, pp. 7709–7721, Nov. 2004.

[150] H. Ding, a. Schmid, D. Li, K. Guslienko, and S. Bader, “Magnetic Bistability of Co Nanodots,” *Physical Review Letters*, vol. 94, no. 15, pp. 20–23, Apr. 2005.

[151] K. Rivkin, W. Xu, L. E. De Long, V. V. Metlushko, B. Ilic, and J. B. Ketterson, “Analysis of ferromagnetic resonance response of square arrays of permalloy nanodots,” *Journal of Magnetism and Magnetic Materials*, vol. 309, no. 2, pp. 317–325, Feb. 2007.

[152] M. Fitzsimmons, T. Silva, and T. Crawford, “Surface oxidation of Permalloy thin films,” *Physical Review B*, vol. 73, no. 1, pp. 1–7, Jan. 2006.

[153] S. Kaka, M. R. Pufall, W. H. Rippard, T. J. Silva, S. E. Russek, and J. a Katine, "Mutual phase-locking of microwave spin torque nano-oscillators.," *Nature*, vol. 437, no. 7057, pp. 389–92, Sep. 2005.

[154] K. Yamada, S. Kasai, Y. Nakatani, K. Kobayashi, H. Kohno, A. Thiaville, and T. Ono, "Electrical switching of the vortex core in a magnetic disk.," *Nature materials*, vol. 6, no. 4, pp. 269–3, Apr. 2007.

[155] A. Dussaux, B. Georges, J. Grollier, V. Cros, A. V. Khvalkovskiy, A. Fukushima, M. Konoto, H. Kubota, K. Yakushiji, S. Yuasa, K. A. Zvezdin, K. Ando, and A. Fert, "Large microwave generation from current-driven magnetic vortex oscillators in magnetic tunnel junctions.," *Nature communications*, vol. 1, p. 8, Jan. 2010.

[156] A. Ruotolo, V. Cros, B. Georges, A. Dussaux, J. Grollier, C. Deranlot, R. Guillemet, K. Bouzehouane, S. Fusil, and A. Fert, "Phase-locking of magnetic vortices mediated by antivortices.," *Nature nanotechnology*, vol. 4, no. 8, pp. 528–32, Aug. 2009.

[157] K. S. Buchanan, P. E. Roy, M. Grimsditch, F. Y. Fradin, K. Y. Guslienko, S. D. Bader, and V. Novosad, "Soliton-pair dynamics in patterned ferromagnetic ellipses," *Nature Physics*, vol. 1, no. 3, pp. 172–176, Dec. 2005.

[158] R. Compton and P. Crowell, "Dynamics of a Pinned Magnetic Vortex," *Physical Review Letters*, vol. 97, no. 13, pp. 2–5, Sep. 2006.

[159] M. J. Donahue and D. G. Porter, "OOMMF User's Guide, Version 1.0," Gaithersburg, MD, 1999.

[160] T. Pokhil, D. Song, and J. Nowak, "Spin vortex states and hysteretic properties of submicron size NiFe elements," *Journal of Applied Physics*, vol. 87, no. 9, p. 6319, 2000.

[161] A. Tonomura, T. Matsuda, J. Endo, T. Arii, and K. Mihama, “Direct Observation of Fine Structure of Magnetic Domain Walls by Electron Holography,” *Physical Review Letters*, vol. 44, no. 21, pp. 1430–1433, May 1980.

[162] M. Hehn, K. Ounadjela, J.-P. Bucher, F. Rousseaux, D. Decanini, B. Bartenlian, and C. Chappert, “Nanoscale Magnetic Domains in Mesoscopic Magnets,” *Science*, vol. 272, no. 5269, pp. 1782–1785, Jun. 1996.

[163] J. Raabe, C. Quitmann, C. Back, F. Nolting, S. Johnson, and C. Buehler, “Quantitative Analysis of Magnetic Excitations in Landau Flux-Closure Structures Using Synchrotron-Radiation Microscopy,” *Physical Review Letters*, vol. 94, no. 21, pp. 1–4, Jun. 2005.

[164] M. Jaafar, R. Yanes, a Asenjo, O. Chubykalo-Fesenko, M. Vázquez, E. M. González, and J. L. Vicent, “Field induced vortex dynamics in magnetic Ni nanotriangles.,” *Nanotechnology*, vol. 19, no. 28, p. 285717, Jul. 2008.

[165] E. Saitoh, H. Miyajima, T. Yamaoka, and G. Tatara, “Current-induced resonance and mass determination of a single magnetic domain wall.,” *Nature*, vol. 432, no. 7014, pp. 203–6, Nov. 2004.

[166] L. Thomas, M. Hayashi, X. Jiang, R. Moriya, C. Rettner, and S. S. P. Parkin, “Oscillatory dependence of current-driven magnetic domain wall motion on current pulse length.,” *Nature*, vol. 443, no. 7108, pp. 197–200, Sep. 2006.

[167] D. Bedau, M. Kläui, S. Krzyk, U. Rüdiger, G. Faini, and L. Vila, “Detection of Current-Induced Resonance of Geometrically Confined Domain Walls,” *Physical Review Letters*, vol. 99, no. 14, pp. 5–8, Oct. 2007.

[168] O. Lemcke, “University of Hamburg.” [Online]. Available: http://www.nanoscience.de/group_r/stm-spstm/projects/temperature/ download.shtml .

[169] J. García-Palacios and F. Lázaro, “Langevin-dynamics study of the dynamical properties of small magnetic particles,” *Physical Review B*, vol. 58, no. 22, pp. 14937–14958, Dec. 1998.

[170] A. Hubert and R. Schäfer, *Magnetic domains: the analysis of magnetic microstructures*, 1st ed. Springer, 1998, p. 686 p.

[171] R. Zarzuela, S. Vélez, J. Hernandez, J. Tejada, and V. Novosad, “Quantum depinning of the magnetic vortex core in micron-size permalloy disks,” *Physical Review B*, vol. 85, no. 18, May 2012.

[172] M. Jaafar, J. Gómez-Herrero, A. Gil, P. Ares, M. Vázquez, and A. Asenjo, “Variable-field magnetic force microscopy.,” *Ultramicroscopy*, vol. 109, no. 6, pp. 693–9, May 2009.

[173] F. G. Aliev, D. Dieleman, A. A. Awad, A. Asenjo, O. Iglesias-, M. Garcia-Hernandez, and V. Metlushko, “Probing ground state in circular magnetic dots: Single vs. double magnetic vortex,” in *2010 International Conference on Electromagnetics in Advanced Applications*, 2010, pp. 160–163.

[174] J. M. García, A. Thiaville, J. Miltat, K. J. Kirk, J. N. Chapman, and F. Alouges, “Quantitative interpretation of magnetic force microscopy images from soft patterned elements,” *Applied Physics Letters*, vol. 79, no. 5, p. 656, 2001.

[175] R. D. McMichael and M. D. Stiles, “Magnetic normal modes of nanoelements,” *Journal of Applied Physics*, vol. 97, no. 10, p. 10J901, 2005.

[176] “Supplementary materials, Videos 1–3, time dependent variation of the Mx component of magnetization corresponding to the modes 2–

4 (1035 × 20nm Py dot).” [Online]. Available: http://link.aps.org/supplemental/10.1103/PhysRevB.84.144406 .

[177] F. Aliev, A. A. Awad, D. Dieleman, A. Lara, V. Metlushko, and K. Guslienko, “Localized domain-wall excitations in patterned magnetic dots probed by broadband ferromagnetic resonance,” *Physical Review B*, vol. 84, no. 14, pp. 1–5, Oct. 2011.

[178] J. Winter, “Bloch Wall Excitation. Application to Nuclear Resonance in a Bloch Wall,” *Physical Review*, vol. 124, no. 2, pp. 452–459, Oct. 1961.

[179] J. C. Slonczewski, “Direct excitation of standing-wave vibrations of domain walls,” *Journal of Magnetism and Magnetic Materials*, vol. 31–34, pp. 663–664, Feb. 1983.

[180] K. Guslienko, S. Demokritov, B. Hillebrands, and a. Slavin, “Effective dipolar boundary conditions for dynamic magnetization in thin magnetic stripes,” *Physical Review B*, vol. 66, no. 13, pp. 8–11, Oct. 2002.

[181] N. Locatelli, V. V. Naletov, J. Grollier, G. de Loubens, V. Cros, C. Deranlot, C. Ulysse, G. Faini, O. Klein, and a. Fert, “Dynamics of two coupled vortices in a spin valve nanopillar excited by spin transfer torque,” *Applied Physics Letters*, vol. 98, no. 6, p. 062501, 2011.

[182] P. M. Braganca, B. a Gurney, B. a Wilson, J. a Katine, S. Maat, and J. R. Childress, “Nanoscale magnetic field detection using a spin torque oscillator.,” *Nanotechnology*, vol. 21, no. 23, p. 235202, Jun. 2010.

[183] Y.-S. Yu, H. Jung, K.-S. Lee, P. Fischer, and S.-K. Kim, “Memory-bit selection and recording by rotating fields in vortex-core cross-point architecture,” *Applied Physics Letters*, vol. 98, no. 5, p. 052507, 2011.

[184] V. V. Kruglyak, S. O. Demokritov, and D. Grundler, “Magnonics,” *Journal of Physics D: Applied Physics*, vol. 43, no. 26, p. 264001, Jul. 2010.

[185] V. V. Kruglyak and R. J. Hicken, “Magnonics: Experiment to prove the concept,” *Journal of Magnetism and Magnetic Materials*, vol. 306, no. 2, pp. 191–194, Nov. 2006.

[186] K. Guslienko, A. Slavin, V. Tiberkevich, and S. Kim, “Dynamic Origin of Azimuthal Modes Splitting in Vortex-State Magnetic Dots,” *Physical Review Letters*, vol. 101, no. 24, p. 247203, Dec. 2008.

[187] M. Kostylev, P. Schrader, R. L. Stamps, G. Gubbiotti, G. Carlotti, a. O. Adeyeye, S. Goolaup, and N. Singh, “Partial frequency band gap in one-dimensional magnonic crystals,” *Applied Physics Letters*, vol. 92, no. 13, p. 132504, 2008.

[188] A. V. Chumak, a. a. Serga, B. Hillebrands, and M. P. Kostylev, “Scattering of backward spin waves in a one-dimensional magnonic crystal,” *Applied Physics Letters*, vol. 93, no. 2, p. 022508, 2008.

[189] G. Gubbiotti, S. Tacchi, G. Carlotti, N. Singh, S. Goolaup, a. O. Adeyeye, and M. Kostylev, “Collective spin modes in monodimensional magnonic crystals consisting of dipolarly coupled nanowires,” *Applied Physics Letters*, vol. 90, no. 9, p. 092503, 2007.

[190] S. Tacchi, M. Madami, G. Gubbiotti, G. Carlotti, H. Tanigawa, T. Ono, and M. Kostylev, “Anisotropic dynamical coupling for propagating collective modes in a two-dimensional magnonic crystal consisting of interacting squared nanodots,” *Physical Review B*, vol. 82, no. 2, pp. 1–8, Jul. 2010.

[191] C. Mathieu, C. Hartmann, M. Bauer, O. Buettner, S. Riedling, B. Roos, S. O. Demokritov, B. Hillebrands, B. Bartenlian, C. Chappert, D. Decanini, F. Rousseaux, E. Cambril, A. Mu□ller, B.

Hoffmann, and U. Hartmann, “Anisotropic magnetic coupling of permalloy micron dots forming a square lattice,” *Applied Physics Letters*, vol. 70, no. 21, p. 2912, 1997.

[192] K. Y. Guslienko, “Magnetic anisotropy in two-dimensional dot arrays induced by magnetostatic interdot coupling,” *Physics Letters A*, vol. 278, no. 5, pp. 293–298, Jan. 2001.

[193] K. Metlov, “Quasiuniform In-Plane Magnetization State of Thin Cylindrical Dots in a Square Array and Related Anisotropy,” *Physical Review Letters*, vol. 97, no. 12, pp. 2–5, Sep. 2006.

[194] A. A. Awad, G. R. Aranda, D. Dieleman, K. Y. Guslienko, G. N. Kakazei, B. a. Ivanov, and F. G. Aliev, “Spin excitation frequencies in magnetostatically coupled arrays of vortex state circular Permalloy dots,” *Applied Physics Letters*, vol. 97, no. 13, p. 132501, 2010.

[195] a. Galkin, B. Ivanov, and C. Zaspel, “Collective modes for an array of magnetic dots in the vortex state,” *Physical Review B*, vol. 74, no. 14, pp. 1–12, Oct. 2006.

[196] F. Boust and N. Vukadinovic, “Micromagnetic simulations of vortex-state excitations in soft magnetic nanostructures,” *Physical Review B*, vol. 172408, pp. 1–4, 2004.

[197] K. Y. Guslienko, K. S. Buchanan, S. D. Bader, and V. Novosad, “Dynamics of coupled vortices in layered magnetic nanodots,” *Applied Physics Letters*, vol. 86, no. 22, p. 223112, 2005.

[198] G. Gubbiotti, M. Madami, S. Tacchi, G. Carlotti, and T. Okuno, “Field dependence of spin excitations in NiFe⁄Cu⁄NiFe trilayered circular dots,” *Physical Review B*, vol. 73, no. 14, pp. 1–6, Apr. 2006.

[199] P. Vavassori, V. Bonanni, a. Busato, G. Gubbiotti, M. Madami, a. O. Adeyeye, S. Goolaup, N. Singh, C. Spezzani, and M. Sacchi,

"Static and dynamical properties of circular NiFe⁄Cu⁄Co nanodisks," *Journal of Applied Physics*, vol. 103, no. 7, p. 07C512, 2008.

[200] S. Wintz, T. Strache, M. Ko□rner, M. Fritzsche, D. Markó, I. Mo□nch, R. Mattheis, J. Raabe, C. Quitmann, J. McCord, a. Erbe, and J. Fassbender, "Direct observation of antiferromagnetically oriented spin vortex states in magnetic multilayer elements," *Applied Physics Letters*, vol. 98, no. 23, p. 232511, 2011.

[201] V. Naletov, G. de Loubens, G. Albuquerque, S. Borlenghi, V. Cros, G. Faini, J. Grollier, H. Hurdequint, N. Locatelli, B. Pigeau, A. Slavin, V. Tiberkevich, C. Ulysse, T. Valet, and O. Klein, "Identification and selection rules of the spin-wave eigenmodes in a normally magnetized nanopillar," *Physical Review B*, vol. 84, no. 22, pp. 1–23, Dec. 2011.

[202] Y. Choi, D. R. Lee, J. W. Freeland, G. Srajer, and V. Metlushko, "Layer-resolved study of magnetic interaction effects in heterostructure dot arrays," *Applied Physics Letters*, vol. 88, no. 11, p. 112502, 2006.

[203] A. A. Awad, A. Lara, V. Metlushko, K. Y. Guslienko, and F. G. Aliev, "Broadband probing magnetization dynamics of the coupled vortex state Permalloy layers in nanopillars," *Applied Physics Letters*, vol. accepted, 2012.

[204] F. Montoncello, L. Giovannini, and F. Nizzoli, "Soft spin modes and magnetic transitions in trilayered nanodisks in the vortex state," *Journal of Applied Physics*, vol. 105, no. 7, p. 07E304, 2009.

[205] N. Klein, "High-frequency applications of high-temperature superconductor thin films," *Reports on Progress in Physics*, vol. 65, no. 10, p. 1387, 2002.

[206] A. M. Campbell, "The response of pinned flux vortices to low-frequency fields," *Journal of Physics C: Solid State Physics*, vol. 2, no. 8, pp. 1492–1501, Aug. 1969.

[207] A. M. Campbell and J. E. Evetts, “Flux vortices and transport currents in type II superconductors,” *Advances in Physics*, vol. 21, no. 90, pp. 199–428, Mar. 1972.

[208] E. H. Brandt, “The flux-line lattice in superconductors,” *Reports on Progress in Physics*, vol. 58, no. 11, pp. 1465–1594, Nov. 1995.

[209] G. Dolan and J. Silcox, “Critical Thicknesses in Superconducting Thin Films,” *Physical Review Letters*, vol. 30, no. 13, pp. 603–606, Mar. 1973.

[210] M. Menghini, R. J. Wijngaarden, A. V. Silhanek, S. Raedts, and V. V. Moshchalkov, “Dendritic flux penetration in Pb films with a periodic array of antidots,” *Physical Review B*, vol. 71, no. 10, pp. 1–7, Mar. 2005.

[211] G. Blatter, V. B. Geshkenbein, A. I. Larkin, and V. M. Vinokur, “Vortices in high-temperature superconductors,” *Reviews of Modern Physics*, vol. 66, no. 4, pp. 1125–1388, Oct. 1994.

[212] A. E. Koshelev and V. M. Vinokur, “Frequency response of pinned vortex lattice,” *Physica C: Superconductivity*, vol. 173, no. 5–6, pp. 465–475, Feb. 1991.

[213] A. M. Campbell, “The interaction distance between flux lines and pinning centres,” *Journal of Physics C: Solid State Physics*, vol. 4, no. 18, pp. 3186–3198, Dec. 1971.

[214] E. Brandt, “The flux-line lattice in superconductors,” *Reports on Progress in Physics*, vol. 58, pp. 1465–1594, 1995.

[215] A. M. Campbell and J. E. Evetts, “Flux vortices and transport currents in type II superconductors,” *Advances in Physics*, vol. 50, no. 8, pp. 1249–1449, 2001.

[216] E. Silva, “Microwave resistivity at 48 GHz in high- T c superconductor films in magnetic fields,” *Superconductor Science and Technology*, vol. 13, no. 8. pp. 1186–, 2000.

[217] E. Silva, N. Pompeo, and S. Sarti, “Wideband microwave measurements in Nb/Pd 84 Ni 16 /Nb structures and comparison with thin Nb films,” *Superconductor Science and Technology*, vol. 24, no. 2, p. 024018, Feb. 2011.

[218] N. Pompeo and E. Silva, “Reliable determination of vortex parameters from measurements of the microwave complex resistivity,” *Physical Review B*, vol. 78, no. 9. pp. 094503–, 2008.

[219] A. L. Rakhmanov, D. V. Shantsev, Y. M. Galperin, and T. H. Johansen, “Finger patterns produced by thermomagnetic instability in superconductors,” *Physical Review B*, vol. 70, no. 22, pp. 1–8, Dec. 2004.

[220] D. Denisov, D. Shantsev, Y. Galperin, E.-M. Choi, H.-S. Lee, S.-I. Lee, A. Bobyl, P. Goa, A. Olsen, and T. Johansen, “Onset of Dendritic Flux Avalanches in Superconducting Films,” *Physical Review Letters*, vol. 97, no. 7, pp. 18–21, Aug. 2006.

[221] R. Mints and A. Rakhmanov, “Critical state stability in type-II superconductors and superconducting-normal-metal composites,” *Reviews of Modern Physics*, vol. 53, no. 3, pp. 551–592, Jul. 1981.

[222] A. Silhanek, S. Raedts, and V. Moshchalkov, “Paramagnetic reentrance of ac screening: Evidence of vortex avalanches in Pb thin films,” *Physical Review B*, vol. 70, no. 14, pp. 5–7, Oct. 2004.

[223] R. Zieve, T. Rosenbaum, H. Jaeger, G. Seidler, G. Crabtree, and U. Welp, “Vortex avalanches at one thousandth the superconducting transition temperature,” *Physical Review B*, vol. 53, no. 17, pp. 11849–11854, May 1996.

[224] P. Cuadrasolis, J. Hernandez, a Garciasantiago, J. Tejada, J. Vanacken, and V. Moshchalkov, “Magnetic moment relaxation studies by swept and pulsed microwave technique in LaSrCuO epitaxial thin film,” *Physica C: Superconductivity*, vol. 468, no. 7–10, pp. 805–808, Apr. 2008.

[225] G. Ghigo, R. Gerbaldo, L. Gozzelino, F. Laviano, G. Lopardo, E. Monticone, C. Portesi, and E. Mezzetti, “Local thermal bistability in MgB2 microwave coplanar resonators: Opposite jumpwise response to weak-link switching and to vortex avalanches,” *Applied Physics Letters*, vol. 94, no. 5, p. 052505, 2009.

[226] M. Golosovsky, M. Tsindlekht, H. Chayet, and D. Davidov, “Vortex depinning frequency in YBa2Cu3O7-x superconducting thin films: Anisotropy and temperature dependence,” *Physical Review B*, vol. 50, no. 1, pp. 470–477, Jul. 1994.

[227] J. et al, “Microwave response of thin niobium films under perpendicular static magnetic fields,” *Physical Review B*, vol. 74, no. 10. pp. –, 2006.

[228] A. Carr, J. Trafton, S. Dukan, and Z. Tešanović, “Low-temperature specific heat of an extreme type-II superconductor at high magnetic fields,” *Physical Review B*, vol. 68, no. 17, pp. 1–6, Nov. 2003.

[229] Y. Wang, H. T. Su, F. Huang, and M. J. Lancaster, “Wide-band superconducting coplanar delay lines,” *IEEE Transactions on Microwave Theory and Techniques*, vol. 53, no. 7, pp. 2348–2354, Jul. 2005.

[230] D. M. Pozar, *Microwave and RFf design of wireless systems*, 1st ed. John Wiley, 2000, p. 366.

APPENDIX A

7.1 Transmission line theory

In order to understand the notion used in the measurement process in the VNA FMR techniques, some basic of microwave knowledge is needed about the models and notations used for analyzing the data, such as S-parameter and transmission line, and the network analyzer itself.

Transmission line is used frequently in the microwave engineering where the dimensions of the circuit components are important due to the fact that normally it becomes of the order of the signal wavelength. The transmission lines essentially are used to transfer the electromagnetic wave from one point to another in the circuit. A transmission line is often schematically represented as a two-wire line as can be seen in Figure A.1.

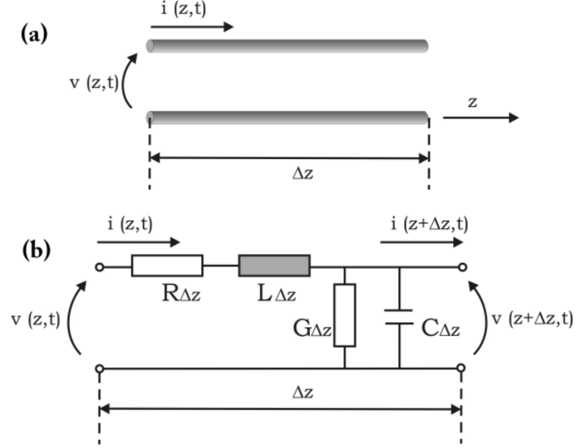

Figure A.1 (a) schematic representation of transmission line, (b) Transmission line circuit section of length Δz and have the four fundamental parameters R, L, G and C [adapted from [230]**].**

7.1.1 Telegrapher equations of transmission lines

Applying Kirchhoff's voltage and current laws to the equivalent lumped element circuit the length Δz (see Figure A.1), which is small compared to the wavelength λ, represented in Figure A.1. We consider the infinitely small length (Δz→ 0) which leads to the telegrapher or the time-domain form of the transmission line equations:

$$\frac{\partial V(z,t)}{\partial z} = -Ri(z,t) - L\frac{\partial i(z,t)}{\partial t} \tag{A.1}$$

$$\frac{\partial i(z,t)}{\partial z} = -Gv(z,t) - C\frac{\partial v(z,t)}{\partial t} \tag{A.2}$$

If we consider the sinusoidal time dependence of the signal as:

$V(z,t) = V(z).e^{jwt+\varphi_1}; I(z,t) = I(z).e^{jwt+\varphi_2}$

The telegrapher equations transform to:

$$\frac{\partial^2 V(z)}{\partial z^2} - \gamma^2 V(z) = 0 \tag{A.3}$$

$$\frac{\partial^2 I(z)}{\partial z^2} - \gamma^2 I(z) = 0 \tag{A.4}$$

The solutions of those telegrapher equations have the following form:

$$V(z) = V_0^+.e^{-\gamma z} + V_0^-.e^{\gamma z} \tag{A.5}$$

$$I(z) = I_0^+.e^{-\gamma z} + I_0^-.e^{\gamma z} \tag{A.6}$$

Where: $\gamma = \alpha + j\beta = \sqrt{(R + j\omega L)(G + j\omega C)}$ is the complex propagation constant, α attenuation constant and β is the phase constant. So we can get from equations (A.1) and (A.5) the current:

$$I(z) = \frac{\gamma}{R + j\omega L}(V_0^+.e^{-\gamma z} - V_0^-.e^{\gamma z}) \tag{A.7}$$

This will give directly comparing with the telegrapher equations (A.6):

$$I_0^+ = \frac{\gamma}{R + j\omega L}V_0^+; I_0^- = -\frac{\gamma}{R + j\omega L}V_0^- \tag{A.8}$$

So the impedance $Z = \frac{V}{I}$ can be presented as the characteristic impedance of the transmission line:

$$Z_0 = \frac{V_0^+}{I_0^+} = -\frac{V_0^-}{I_0^-} = \sqrt{\frac{R + j\omega L}{G + j\omega C}}$$

Some particular cases, when the transmission line losses can be neglected (R = G = 0) are named lossless. At very high frequencies the characteristic impedance tends towards this lossless constant value (ωL»R):

$$Z_0 = \sqrt{\frac{L}{C}}$$

The electromagnetic wavelength and the wave phase velocity then can be written:

$$\lambda = \frac{2\pi}{\beta} = \frac{2\pi}{\omega\sqrt{LC}}; v_P = \frac{\omega}{\beta} = \frac{1}{\sqrt{LC}}$$

7.1.2 Scattering parameters

The vector network analyzer measures the scattering parameters called S-parameters, which relate incident and reflected electromagnetic waves. These parameters describe the electrical behavior of linear electrical networks; and they are all about power because signal power and energy considerations are more easily to quantify than currents and voltage at high frequencies.

For a two port network (port is defined as every access line to a component consisting of a pair of terminals) one of the ports is connected to the input of the device under test (DUT) and the other one to the output of the microwave device under study. Here a_i and b_i are normalized incident and reflected voltages defined as for the *i* port:

$$a_i = \frac{V_i + Z_i I_i}{2\sqrt{Z_i}}, b_i = \frac{V_i - Z_i I_i}{2\sqrt{Z_i}}$$

From Equations (A.5) and (A.6);

$$a_i = \frac{V_i^+ .e^{-\gamma z}}{\sqrt{Z_i}}, b_i = \frac{V_i^- .e^{\gamma z}}{\sqrt{Z_i}}$$

The relation between $a_{1;2}$ and $b_{1;2}$ and the S-parameters can be presented schematically as shown in figure A.2 and can be expressed as:

$$\begin{pmatrix} b_1 \\ b_2 \end{pmatrix} = \overline{S}\begin{pmatrix} a_1 \\ a_2 \end{pmatrix} = \begin{bmatrix} S_{11} & S_{12} \\ S_{21} & S_{22} \end{bmatrix}\begin{pmatrix} a_1 \\ a_2 \end{pmatrix}$$

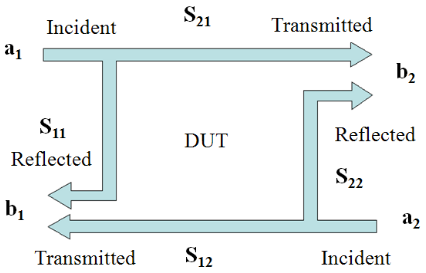

Figure A.2 Representation of the relation between the S-parameters of the two-port device under test DUT.

If we assume that each port is terminated in impedance Z_0, we can define the four S-parameters of the 2-port network as:

$$S_{11} = \left.\frac{b_1}{a_1}\right|_{a_2=0} ,S_{21} = \left.\frac{b_2}{a_1}\right|_{a_2=0} ,S_{22} = \left.\frac{b_2}{a_2}\right|_{a_1=0} ,S_{12} = \left.\frac{b_1}{a_2}\right|_{a_1=0}$$

APPENDIX B

8.1 New setup LT-FMR II:

The insert (LT-FMR II) presneted in the thesis were homebuilt enterially as a part of the thesis work. This setup works till 32 GHz and down to 1.8K figure B.1 shows photographs of some parts of the insert.

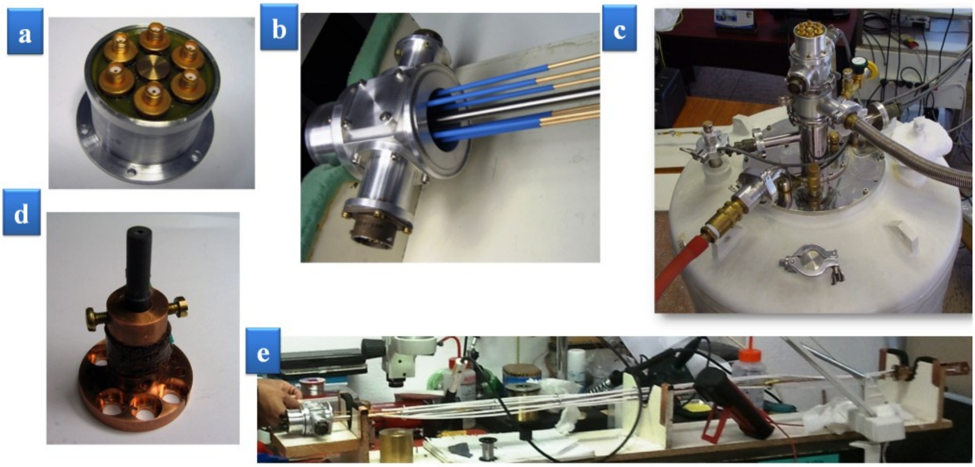

Figure B.1 (a,b) Photograph of the upper pert of the insert; (a) The Head with the RF vaccum conectores, (b) the head with the cabeles and the temperature control and the DC conectores. (c) The Cryostat with the insert. (d) 25 ohm heater. (e) The Microwave insert (LT-FMR II).

8.1.1 Thermometer calibration

The thermometer installed in the insert (LT-FMR II) is Cernox resistor thermometer (CX-1050-SD, serial: X44217) and was calibrated by means of other commercial calibrated Carbon-Ceramic CCS/A2 from 1.3-300K). The thermometer Carbon-Ceramic CCS/A2, was fixed on the sampled holder in this form the obtained calibration curve would permits to deduce directly the temperature of the sample. The temperature is sent afterwards to the lakeshore 340 temperature controller and assigned to the thermometer loop.

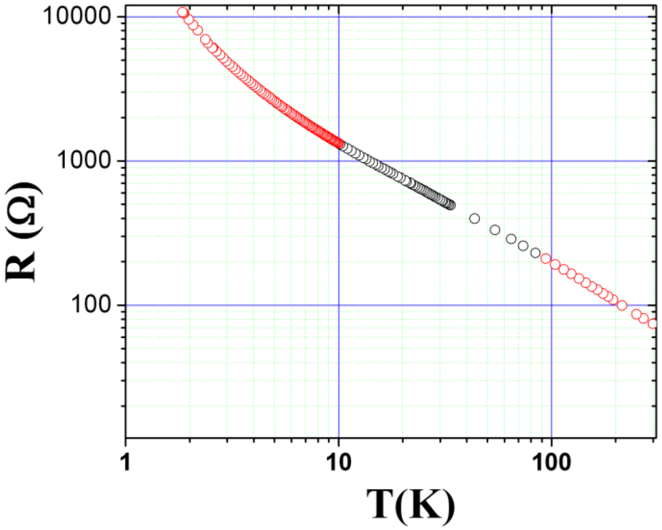

Figure B.2 The calibration curve obtained for the thermometer (Log Ohm Vs Log T) of insert (LT-FMR II), Cernox resistor thermometer (CX-1050-SD, serial: X44217).

8.2 VNA-FMR room temperature New Setup:

This set-up (see figure B.3) was elaborated in the course of the thesis and work up to 40GHz by using new Agilent network analyzer (PNA E8363C) and the implementation of new set of Rosenberger commercial cables with 2.92mm connectors working up to 40GHz. A microwave commercial nonmagnetic custom Picoprobe probes (K-type with tips in a GSG (Ground-Signal-Ground) geometry and 150 µm pitch size (separation between Ground-Signal pads) is used to contact on chip coplanar waveguides. These microwave coaxial probes, lead to a low insertion loss. They are similar to the K-type cables and work up to 40 GHz.

In addition two xyz manipulators (non-magnetic also) one to adjust the probe (Picoprobe) and the other to mount the sample/calibration (as can be seen in figure B.3,b) substrate to avoid the displacement of the probes and the cables preventing changes of phase due to their displacement after calibration. A homely adjusted webcam is mounted on the optical microscope permits direct visualisation and the connection between the picoprobe and the coplanar on the substrate.

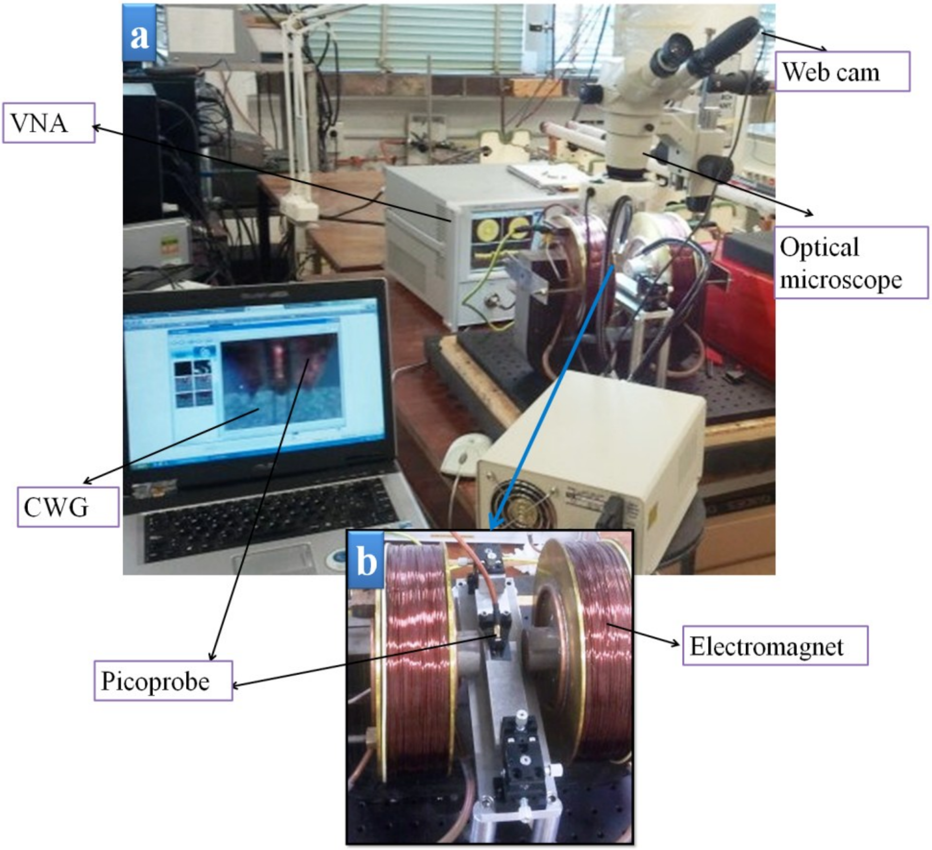

Figure B.3 The photograph is the VNA-FMR reflection setup with on-wafer coplanar wave guide CWG. (b) Zoom of the electromagnet and the probe head with the sample.

8.3 Samples images:

The samples studied in the thesis were all imaged using scanning electron microscopy (SEM) to ensure the good quality (sharpness of the edges , cylindrical geometry of the dots and the reproducibility of the dots) here we present in figure B.4 additional images of the presented dots.

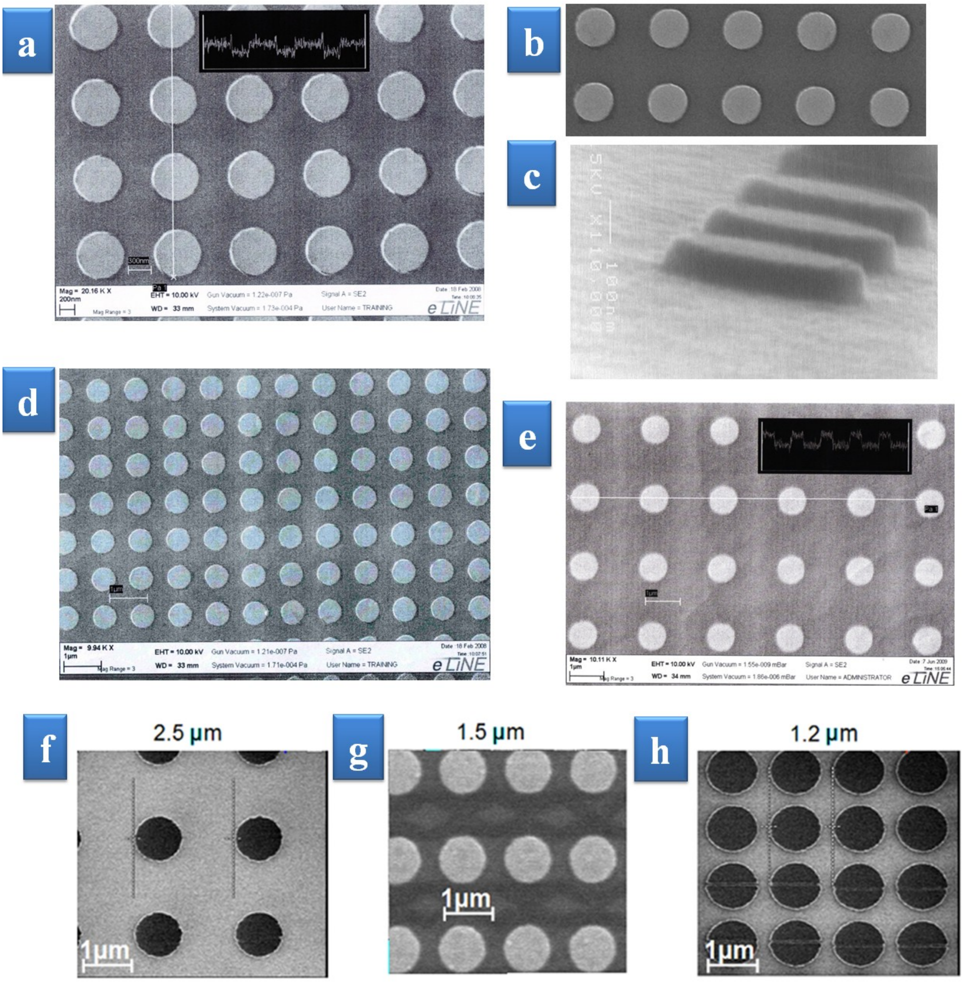

Figure B.4 SEM and AFM images of some of some of the measured arrays of Py dots, (a,b,c,d,e) with SEM for dots with R=500nm and L=15nm (a), 25nm (b), 50nm (c,f,g,h) and R=300nm, L=15nm(d). (F,g,h) Samples with same aspect ratio, but with different centre to centre distance of 2500, 1200 and 1500 nm respectively.

8.4 Simulations:

Besides the experimental studies, the micromagnetic simulations using precompiled OOMMF code [see http://math/nist.gov/oommf] were used to carry out to validate our hipothesis as well as to understand better the expermintal results and the mode profiles.

For the main part of our simulations we used (*:mif) input file the Spinvalve example exsist in the OOMMF examples modifying the structure to either a single layer or spinvalve, depending on the used structre. The main changes in the *.mif file is to change the square defind symmetry of the dots to the circular one. Bellow the script used,

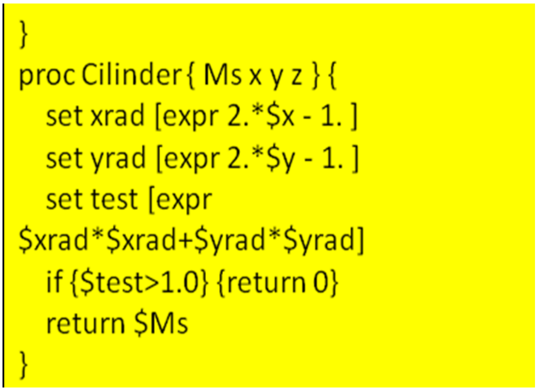

```
}
proc Cilinder{ Ms x y z } {
   set xrad [expr 2.*$x - 1. ]
   set yrad [expr 2.*$y - 1. ]
   set test [expr
$xrad*$xrad+$yrad*$yrad]
   if {$test>1.0} {return 0}
   return $Ms
}
```

The circular Py dot having having the deserved physical parameters of the individual cells of normally 5×5×A nm3 were A is the thickness of the dot if the dots thickness is lower than 25nm, and is in the case of thicker dots.

The material parameters used usually are the exchange stiffness constant A = 1.4 x 10^{-11} (J/m), the saturation magnetization Ms = 830×103 A/m, γ /2π = 2.96 MHz/Oe taken from the measurements, and the Gilbert damping constant of α = 0.01. To excite the magnetization a gussian pulse is applied and the script used to generet the puls:

$$H_X(t) = ae^{-\frac{(t-\mu^2)^2}{2\sigma^2}}$$

Where:

The application time is the expected value μ (mu) and variance σ2. The corresponding parameters and (a) is the amplitude Amp.

And the funcition is defined in the script as:

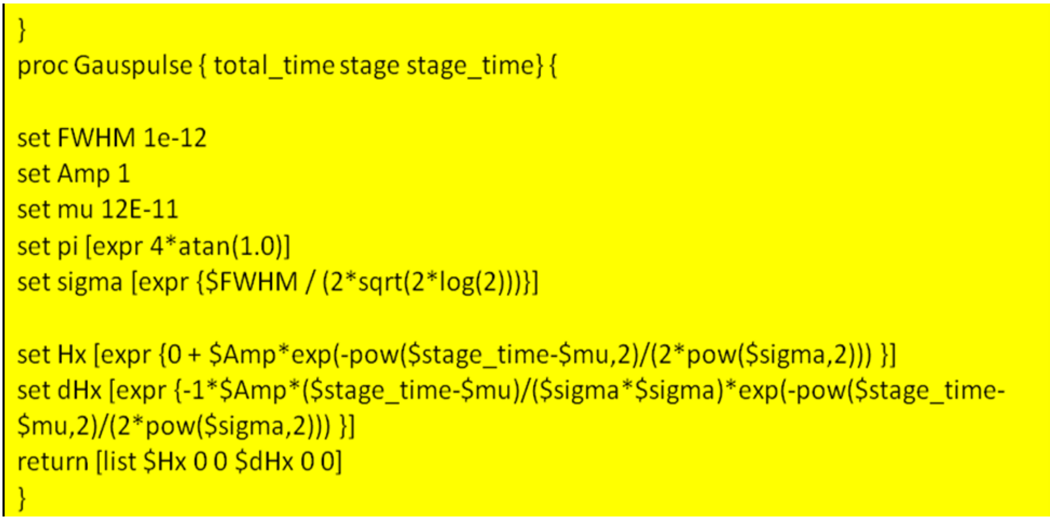

```
}
proc Gauspulse { total_time stage stage_time} {

set FWHM 1e-12
set Amp 1
set mu 12E-11
set pi [expr 4*atan(1.0)]
set sigma [expr {$FWHM / (2*sqrt(2*log(2)))}]

set Hx [expr {0 + $Amp*exp(-pow($stage_time-$mu,2)/(2*pow($sigma,2))) }]
set dHx [expr {-1*$Amp*($stage_time-$mu)/($sigma*$sigma)*exp(-pow($stage_time-
$mu,2)/(2*pow($sigma,2))) }]
return [list $Hx 0 0 $dHx 0 0]
}
```

After this variable driving field (Gaussian field pulse) with the amplitude of 1 Oe and FWHM of 1 ps was applied. We perform local Fourier transforms over all simulation cells and average these spectra to obtain the spin eigenfrequencies.

In order to get more insight into the spin dynamics and the modes profile the spatial distribution of the main eigenmodes is obtained; Knowing the local distribution of the phases and amplitudes for every cell for a selected eigenfrequency, we can reconstruct the eigenmode profiles as explained in Ref. [175].